INTERNATIONAL CENTER FOR NUMERICAL METHODS IN ENGINEERING

Numerical Modeling of Crack Formation in Power Compaction Processes

J.A. Hernández
X. Oliver
J.C. Cante

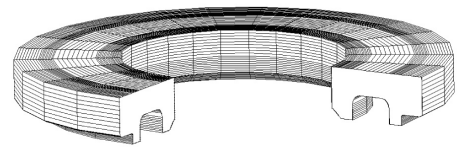

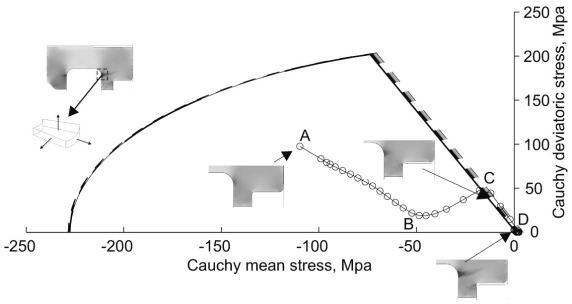

Monograph CIMNE Nº-114, November 2009

Numerical Modeling of Crack Formation in Power Compaction Processes

Joaquín A. Hernández Ortega
Xavier Oliver Olivella
Juan Carlos Cante Terán

Monograph CIMNE Nº 114, November 2009

INTERNATIONAL CENTER FOR NUMERICAL METHODS IN ENGINEERING
Gran Capitán s/n, 08034 Barcelona, España

INTERNATIONAL CENTER FOR NUMERICAL METHODS IN ENGINEERING
Edificio C1, Campus Norte UPC
Gran Capitán s/n
08034 Barcelona, Spain
www.cimne.upc.es

First edition: November 2009

NUMERICAL MODELING OF CRACK FORMATION IN POWER COMPACTION PROCESSES
Monograph CIMNE M114

ISBN: 978-84-96736-79-5

Dep. legal:

Abstract

Powder metallurgy (P/M) is an important technique of manufacturing metal parts from metal in powdered form. Traditionally, P/M processes and products have been designed and developed on the basis of practical rules and trial-and-error experience. However, this trend is progressively changing. In recent years, the growing efficiencies of computers, together with the recognition of numerical simulation techniques, and more specifically, the *finite element method* , as powerful alternatives to these costly trial-and-error procedures, have fueled the interest of the P/M industry in this modeling technology. Research efforts have been devoted mainly to the analysis of the pressing stage and, as a result, considerable progress has been made in the field of density predictions. However, the numerical simulation of the ejection stage, and in particular, the study of the formation of *cracks* caused by elastic expansion and/or interaction with the tool set during this phase, has received less attention, notwithstanding its extreme relevance in the quality of the final product.

The primary objective of this work is precisely to fill this gap by developing a constitutive model that attempts to describe the mechanical behavior of the powder during both pressing and ejection phases, with special emphasis on the representation of the cracking phenomenon. The constitutive relationships are derived within the general framework of rate-independent, isotropic, finite strain elastoplasticity. The yield function is defined in stress space by three surfaces intersecting non-smoothly, namely, an elliptical cap and two classical Von Mises and Drucker-Prager yield surfaces. The distinct irreversible processes occurring at the microscopic level are macroscopically described in terms of two internal variables: an internal hardening variable, associated with accumulated compressive (plastic) strains, and an internal softening variable, linked with accumulated (plastic) shear strains. The innovative part of our modeling approach is connected mainly with the characterization of the latter phenomenological aspect: strain softening. Incorporation of a softening law permits the representation of macroscopic cracks as high gradients of inelastic strains (strain localization). Motivated by both numerical and physical reasons, a *parabolic plastic potential function* is introduced to describe the plastic flow on the linear Drucker-Prager failure surface. A thermodynamically consistent calibration procedure is employed to relate material parameters involved in the softening law to fracture energy values obtained experimentally on Distaloy AE specimens.

The discussion of the algorithmic implementation of the model is confined ex-

clusively to the time integration of the constitutive equations. Motivated by computational robustness considerations, a non-conventional integration scheme that combines advantageous features of both implicit and explicit method is employed. The basic ideas and assumptions underlying this method are presented, and the stress update and the closed-form expression of the algorithmic tangent moduli stemming from this method are derived. This integration scheme involves, in turn, the solution at each time increment of the system of equations stemming from a classical, implicit backward-Euler difference scheme. An iterative procedure based on the decoupling of the evolution equations for the plastic strains and the internal variables is proposed for solving these return-mapping equations. It is proved that this apparently novel method converges unconditionally to the solution regardless of the value of the material properties.

To validate the proposed model, a comparison between experimental results of diametral compression tests and finite element predictions is carried out. The validation is completed with the study of the formation of cracks due to elastic expansion during ejection of an overdensified thin cylindrical part. Both simulations demonstrate the ability of the model to *detect evidence of macroscopic cracks*, *clarify and provide reasons* for the formation of such cracks, and evaluate *qualitatively* the influence of variations in the input variables on their propagation. Besides, in order to explore the possibilities of the numerical model as a tool for assisting in the design and analysis of P/M uniaxial die compaction (including ejection) processes, a detailed case study of the compaction of an axially symmetric multilevel part in an advanced CNC press machine is performed. Special importance is given in this study to the accurate modeling of the geometry of the tool set and the external actions acting on it (punch platen motions). Finally, the potential areas for future research are identified.

Table of Contents

List of Figures

List of Tables

Chapter 1

Introduction

1.1 Motivation

It is a widely known fact that technical progress develops faster than the corresponding science. For example, the wheel was invented thousands of years ago, yet it was not until relatively recent times that we possess the mathematical knowledge to understand its intricacies and predict its behavior. Likewise, magnificent cathedrals were designed and raised in the Middle Ages without the support of any predictive engineering theory, but rather based on observations of performance of earlier constructions.

The powder metallurgy industry is perharps one of the technology-based industries in which this paradox is more pronounced. Not even a single step of the P/M processes has been susceptible to theoretical prediction in the past [100]. Trial-and-error processes and accumulated practical experience have been traditionally the principal source of useful information for designing the tool set and the fabrication route. The bewildering complexity of the material behavior, that, during the pressing stage, evolves from a free-flowing powered state to an extremely brittle solid form, not to mention the difficulty in accurately controlling the performance of the compacting press - especially before the advent of advanced CNC press machines - have helped to create the impression that the manufacturing by P/M techniques of free-defect green parts with both the required dimensions and mechanical properties is an art mastered only by a few experienced, skilled practitioners.

The last two decades have witnessed a gradual reduction of this lag between practice and theory in the P/M industry. The general availability of fast computers with large memories, together with the recognition of numerical simulation methods, and more specifically, *finite element*-based technologies, as indispensable design tools in other engineering fields, has stimulated the development of phenomenological models that attempt to replicate the behavior of the powder during the compaction process. Although considerable progress has been achieved, especially in the prediction of density, the existing modeling tools have not matured to a point where numerical simulations can completely replace trial-and-error procedures. There is still a long way to go before this desirable goal is reached. Aside

from computational cost barriers, which, due to the ever increasing storage capacity and speed of computers, will be gradually surmounted as time progresses, one of the main deficiencies that limit extensive take-up of simulation by industry [13] is the inability of the existing simulation softwares to predict *the formation of cracks* during the compaction process. The route to identify cracks in computational simulations made with conventional finite element-based models is by scrutinizing density distributions, so as to find "suspiciously" intense gradients that may indicate the presence of shear cracks. However, a substantial part of the cracks detected in green compacts is generated during the pressure release and ejection stages. Density distributions remain practically unchanged during these process steps and, therefore, examination of density fields can hardly reveal these post-pressing defects.

Crack prevention is one of the major concerns of P/M manufacturers, specially for ferrous structural parts. When, upon visual or microscopic inspection of the green compact, a crack is detected, it often takes painstaking efforts to clarify the root cause of the crack so that corrective measures can be taken. If the part is conventional, the P/M designer has the benefit of an inventory of previously manufactured, similar parts to consult for relevant information. However, if the part is unconventionally complex, the design cannot be thoroughly guided by past experience, and the only solution is to undertake costly -they may involve the changeover of the entire tool set or elements thereof- and time-consuming trial-and-error procedures. Accordingly, to come into line with the demands of the P/M industry [13], the simulation tool should have the ability of not only predicting final density distributions, but also anticipating with a certain degree of accuracy the integrity (presence of cracks) of the part after ejection. This would undoubtedly contribute to consolidate a philosophy of design more rational and not exclusively grounded on practical rules and experience.

The above considerations, together with the ever appealing, exciting and rewarding challenge of delving into relatively unexplored topics, constitute solid, compelling reasons to pursue this line of research .

1.2 Objective and scope

The central goal of this work is to *construct, validate and implement in a finite element program a constitutive model that attempts to describe the mechanical behavior of metallic powders in cold die compaction processes, including both pressing and ejection stages, with special emphasis on the representation of crack formation.* Constitutive equations for the powder are derived within the general framework of rate-independent, isotropic, finite strain elastoplasticity. Although, in principle, these equations can be applied to any powder composition, the calibration presented here is carried out on the basis of a *ferrous alloy.* On the other hand, the discussion of the mathematical structure underlying the algorithmic solution is confined exclusively to the *time integration of the constitutive equations* (stress update and algorithmic tangent moduli). General details of the global finite element implementation, such as the spatial discretization of the momentum equation, are

omitted.

However, the research is not limited to the development and validation of the constitutive model for the powder. In the last part of the work, we adopt a more technical perspective, and explore some relevant aspects of the performance of CNC press machines. The aim in regarding the problem from this broader perspective is, on the one hand, to convey the *relevance of accurately characterizing the tool set and the external loads acting on it* - the boundary conditions of the governing differential equations -, since ignorance or unawareness of basic details in this respect may cause errors far overshadowing those introduced by deficiencies in the constitutive model or in the corresponding algorithmic solution procedure, and, on the other hand, to *evaluate the possibilities of the proposed finite element-based model as a potential tool for assisting in the design and analysis of PM uniaxial die compaction processes* (including also the ejection phase and the formation of cracks during this process step).

1.3 Modeling viewpoint

The first step towards the modeling of any process is to settle the *target system* whose behavior is represented. This system, if complicated, may be aggregated into several *sub-systems*, each one of them having its own sub-model. The accuracy in the characterization of each sub-system depends on the scope of the model, giving more emphasis to those phenomena we are interested in. In our case, the main goal is to *analyze the formation of cracks during the manufacturing of P/M parts.* Experimental results show that cracks can be formed at any point during the P/M process, but are primarily formed during the pre-sintering stages [112]. The pre-sintering stages refer to the pressure release, ejection and post-handling of the green specimen. Those operations are often the weakest link in the manufacturing process. Even if the compaction route has been optimal, an improper movement or layout of the tooling may lead to a mechanical deterioration, or eventually, fracture in the specimen. Therefore, our *target system must include at least two sub-systems: the powder (raw material) and the tooling* . The global model must be capable of describing the behavior of both sub-systems and their interaction with the optimal (from an industrial point of view) degree of detail. Other components involved in the process are excluded or substituted by some external actions. For instance, punches move driven by the action of mechanical or hydraulic devices, but for practical reasons the action of these devices is reduced to a uniform displacement of the boundary punches or a distributed pressure over them.

1.3.1 Powder sub-system

The behavior of the powder sub-system could be explained typically by two different approaches: the micro-mechanical and the macro-mechanical approaches. The first approach attempts to study the physics of each individual grain. Such a framework encompasses the local behavior between the particles, such as contact, sliding, crushing and segregation. In the second approach, the macro-mechanical, one

considers the powder system as a continuum medium occupying a certain region of physic space. In this approach, we agree to ignore the discrete composition of the powder. The continuum concept of matter allows to ascribe field quantities associated with the internal structure such as density and stress to each and every point of the region of space which the body occupies [65].

Continuum approach versus micro-mechanical approach

It may be tempting to use the micro-mechanical point of view for describing the crack phenomena since fracture could be interpreted directly as a break in the interparticle bonds between powder grains. This idea, although elegant, at this time suffers from the limitation that the particle-level response is difficult to measure and characterize [30]. Furthermore, the discrete nature of the powder gives rise to difficulties in applying such models because a representative part of a realistic problem will comprise many millions of particles. Micromechanical models, under the assumption of powder particle sphericity, have been developed only for the early stages of compaction. Models for the later stages of compaction, when the porosity is closed and the material approaches full density, are less well developed within this approach [22]. In the pre-sintering stages e.g., ejection, in which cracks are likely to occur, the behavior resembles that of a consolidated solid, for which the macro-mechanical or continuum approach is well-established. For this and other practical and computational reasons, *we adopt the macro-modeling, also termed phenomenological, approach for the powder sub-system.* The other sub-system in study, the tooling, will be also analyzed from the continuum point of view.

As mentioned above, the continuum or phenomenological approach enables us to define certain field quantities, such as density, stress and velocity, that describe the behavior of our system Establishing mathematical relationships between these relevant variables is the next step in the definition of the model. We have to distinguish between the *fundamental equations or balance principles*, based upon universal laws of physics such as the conservation of mass and the principles of energy and momentum, that hold for any continuum body, and the so-called constitutive equations, specific for each material. Such is the importance of these constitutive relationships that the modeling process is often reduced to the establishment of these equations, therefore referred to as *constitutive models.*

1.3.1.1 Basic aspects of the constitutive model for the powder

The bulk of this work is devoted to the development of constitutive equations for the powder sub-system. We will make no attempt to define a constitutive law that covers a wide range of loading situations. Such an effort would lead to unnecessarily complex relationships containing a large number of state variables and material parameters difficult to validate experimentally. Rather, we restrict ourselves to the case of *cold compaction*, which takes place in a temperature range, generally at ambient temperature, within which deformation mechanisms like dislocation or diffusional creep can be neglected (purely mechanical problem) [100]. We consider that the loose powder is confined in a cavity defined by a set of rigid punches,

core rods and dies. It is common to assume *homogeneous fill density distributions*, except for the case of multilevel parts, in which this assumption does not seem to reflect reality, and it is convenient to define different packing densities for each thickness level [52]. This partial homogeneity supposes a reduction of the spectrum of cracks detectable by the proposed model. Description of cracks due to impurities or air entrapment will fall beyond the scope of our phenomenological approach. Furthermore, although it is known that small anisotropy develops locally at high densities, it is assumed here that the compacted powder remains globally *isotropic* during the whole process [20]. The material *rate-independence* hypothesis is also applicable provided that punch velocity is not too high.

A common representative feature of the compaction behavior of different kinds of powder is that *large irrecoverable deformations* take place during pressing, regardless of the different types of densification mechanisms that may operate. In particular, compaction of metal powders results mainly from *plastic deformation* of the particles [95]. We shall thus adopt an *elasto-plastic model*, defined by a *multisurface yield function* which evolves as the material deforms plastically. In an isothermal problem, the (stress) response at any point is uniquely determined by the deformation history, or equivalently, by the current values of the deformation (external variable) and a finite set of *internal (or hidden) variables*, which are thermodynamic state variables that are supposed to describe aspects of the internal structure of the powder[46]. In our case, the evolution of the internal variables must capture at least *two phenomenological aspects*:

I. *Increase of strength under increasing compressive loads (strain hardening).* From a micro-structure point of view, when a pressure is applied to the loose powder confined in the die cavity the fraction of large voids or packing defects is reduced by restacking events. As the particle contacts become flattened by elastic and plastic deformation, the frictional forces are increased by cold welding and interlocking of rough particle surfaces, resulting in a higher macroscopic strength [100]. We shall follow the conventional continuum models that use *density as the internal variable* to account for this hardening phenomenon.

II. *Limited strength when subjected to tensile or shear stress state.* Interparticle welding or bonding are weak compared with the sintered fully dense material. Tensile forces, lateral shear forces or a combination of these two types may pull apart powder particles that have been locked together during compaction. In our constitutive model, this debonding process will be reflected by the *diminishing of a cohesion-like macroscopic variable.*

The description of the first phenomenological aspect (hardening behavior under compressive stress states) has been privileged in the literature, due to its relevance within the consolidation process [2, 37, 22, 52]. Earlier studies in this field attempted typically to establish empirically pressure-density relationships for several powders. The main ingredient in the constitutive model reflecting this aspect is a *cap yield surface* (typically elliptic) which bounds the elastic behavior domain

and expands in the stress space according to a specific hardening rule. Previous works of Oliver, Cante, Weyler et al. [109, 16, 81] constitute the base of our model concerning this aspect.

Modeling of the cracking phenomenon: strain localization

Less attention has been devoted to the second phenomenological feature, closely related to the onset and formation of cracks. The use of a failure surface, that represents the limit stress states beyond which fracture of the powder compact may occur [21], to capture the nonsymmetry in the compressive-tensile behavior is well established. A growth in the macroscopic cohesion ruling the failure surface is expected when yielding occurs on the cap surface [31]. But there is still lack of agreement of how this surface evolves in stress space when yielding occurs on it.

In some models [55, 16, 109] the failure envelope remains fixed and the mechanical strength during plastic straining on this surface does not change (null softening). But one may introduce in the model a deterioration of the mechanical properties via a strain softening law [59, 26]. It is well known that in materials exhibiting such a behavior, concentration of strains in narrow bands, the so-called *strain localization*, may arise. The strain-localization phenomenon has frequently been envisaged as a way to model displacement discontinuities [75] and therefore, it could be also interpreted as the presence of a macroscopic crack in the affected band. This continuum approach of crack formation is known as the *smeared crack approach*. The nucleation of each individual crack is translated into a deterioration of the mechanical strength in the affected area, thus "smearing out" the cracks over the localization band [11].

There are other methodologies for tackling the modeling of fracture process. Fracture mechanics uses discrete approaches wherein jumps in the displacement field across a discontinuity interface are introduced along with propagation and crack growth direction criteria [66]. Bridging the gap between discrete techniques and the smeared crack approach -in which the intense strain gradient in the localization band is translated into a *weak discontinuity* in the displacement field-, the *Continuum Strong Discontinuity Approach* (CSDA) appears as a strategy in which, on the basis of continuum constitutive models (stress vs. strain), the multiscale character of the underlying problem is taken into account by decomposing the displacement field, in the localization band, into a continuous and a discontinuous part [75, 76, 91].

However, the aim of modern non-linear Fracture Mechanics and the hybrid technologies developed under its influence is to give a detailed insight of the crack formation phenomena. A physical discontinuity (an initial crack or a flaw) is typically assumed to exist from the onset and the attention is focused in how the presence of such defects affects the mechanical properties of the component under characteristic loading conditions. Questions such as what is the largest sized crack that a structure or mechanism can contain for failure to be avoided or how long before a crack which was safe becomes unsafe have to be answered [72]. Our objective is slightly different. It is not relevant for our purpose to analyze under which

conditions a defective component will fail during its performance in service. Our attention is focused only on intermediate manufacturing operations (compaction and die ejection). *If any sign of cracking is detected at the end of these operations, the product will be rejected for the following sintering stage, regardless of how the defect was formed.* Our phenomenological description, thus, must capture any evidence of macroscopic cracking but *without the necessity of giving an accurate and detailed description of the growth conditions.* A reasonable similarity between the crack (diffuse) pattern predicted by the model and that observed experimentally would suffice to consider the prediction as reliable.

Taking into consideration all these factors, the smeared crack model turns out to be the more appealing approach due mainly to its conceptual simplicity. We have to bear in mind that our description attempts to give a unified framework for both the compaction and the failure phenomena, which may overlap during the pressing stage if the consolidation route is not optimal. In the smeared crack model, both constitutive laws (compaction and failure) have the same structure and its unified manipulation does not imply any significant difficulty.

One of the weakest aspects of the smeared crack approach is that the width of the localization zone is not well defined and the energy dissipation within this zone can not be uniquely determined [58]. This problem may be circumvent to some extent by the introduction, in the constitutive equation, of a *characteristic length* depending on the spatial discretization, so as to ensure conservation of the energy dissipated by the material upon mesh-size refinements [74].

References in the literature to the use of continuum constitutive softening laws to capture strain localization in powder metallurgy processes are relatively scarce. Coube and Riedel [26] consider the possibility of softening by making the cohesive strength and cohesion slope of a Drucker-Prager yield criterion state dependent variables. Lewis and Khoei [59] study the prediction of localization phenomenon at the final stage of compaction by applying an isochoric (Von Mises) yield criterion. However, none of these works deals with the characteristic length concept above mentioned. Furthermore, in Coube and Riedel the evolution equations of the variables governing the failure surface are derived without acknowledging the thermodynamic requirement of positive dissipation, and in Lewis and Khoei the assumption of a Von Mises yield criterion introduces a symmetry in the compressive-tensile behavior which is unrealistic for the characterization of a green compact. It is worth mentioning the experimental work carried out by Jonsén [48] which provides fracture energy values measured in diametral compression tests. These fracture energy values (which are strongly density dependent) will be used in our model to calibrate the softening law.

1.3.2 Tooling sub-system

The other major feature of our global system is the tooling. In the pressure-assisted forming operations, one usually distinguishes between axial (die) pressing and isostatic pressing. In axial pressing, which is by far the most widely used method and is considered as the conventional technique, the powder is compacted in rigid dies by axially loaded punches. In isostatic pressing, pressure is applied

from all directions against the powder that is contained in a flexible die [39]. In this work, we will focus our attention on the former process, the *axial pressing (or axial die compaction) technique*. In the axial pressing technique, the term tooling (or tool set) refers to the set of upper and lower punches, die and core rods used for forming the powder into the required shape. The die normally controls the outer peripheral shape and size of the compacting part. Core rods are extensions of the die that controls the inner peripheral shape and size of the part. Upper and lower punches carry the full load of the compressive force required to compact the PM part.

Rigid versus elastic characterization of the tooling

The tooling set is frequently referred as "rigid tooling", emphasizing that tools undergo negligible dimensional changes in comparison with the powder confined in the cavity. This large difference between the deformability of the tools and the powder material, aided by simplicity reasons, has motivated classically a rigid body characterization of the tooling sub-system. The rigidity of the tools implies that the top and bottom faces of the punches undergo the same displacement. This assumption constitutes a source of discrepancies when fitting experimental data for a given pressing kinematics, since punch strokes do not correspond exactly with displacements of punch faces in contact with the powder. But it is in the subsequent pressure release and ejection stages when the deformation of the tool equipment becomes crucial and cannot be ignored. The die experiences some lateral expansion during compaction, and a certain amount of potential (elastic) energy is stored in the die. When the desired position is reached, the pressing punches are withdrawn and the pressure applied by the mechanical or hydraulic press tends to zero. However, due to the elastic recovery of the die, the compact is held back in the cavity die, and friction with die walls obliges to exert an external upward force for stripping the trapped part from the cavity. Considerable tensile and/or shear stress states, and consequently fracture, may take place in some critical points of the part if the stripping movement is not designed properly (tooling misalignment, uneven tooling deflection, non-simultaneous tool ejection timing, etc.). Thus, *taking into account the deformation of the tooling is vital for capturing the onset and formation of cracks during the pressure release and ejection processes*. A purely rigid die cannot possess deformation energy and, hence, cannot do work on the compact after the punch removal. As a result, the radial pressure acting upon the die wall would tend to zero as the punches are removed and the compact could be stripped from the cavity without any effort, which is physically unrealistic.

Tool design and production is a highly specialized field in itself. Exploring phenomena such as wear on die walls, fatigue, buckling in long thin-walled punches, etc. goes beyond the scope of this work. We will assume that the tooling sub-system is composed of continuum elastic bodies. The action of the mechanical or hydraulic press will be replaced by a boundary displacement or a distributed pressure over the punch faces in contact with clamp rings. Stationary punches will be modeled by imposing zero displacement on the punch faces contiguous to supports. The longer punches deform more elastically than the shorter ones when subjected to a load.

Hence, considering the actual dimension of the punches is also crucial, since uneven punch deflections is a common cause of cracks in the pressure releasing stage.

1.3.3 Interaction powder-tooling

Our systemic modeling setting ends up with the definition of the interaction between the components (powder and tooling) of our global system. Magnetic, electric or thermal effects are omitted in our approach and, thus, only a purely mechanical interaction is considered. The choice of phenomenological continuum approaches for both the powder and the tooling places a limit in the precision to resolve the mechanical behavior in the contact interface. The rough microscopic character of surfaces in contact will be ignored, and they will be treated as smooth surfaces. Contact condition in the normal direction will be imposed by enforcing the purely non-penetration geometrical constraint, leaving aside thus any attempt of modeling normal contact via a constitutive relation stemming from micromechanical analyzes.

Relative tangential movement on the contact interface demands more insight, since density distributions on compacts are seriously affected by the frictional forces developed at the die wall.Of equal importance is the friction between the green compact and the die wall during the ejection of the compact from the die, which may generate a pull off force and high tensile stress on the compact [112].

In our approach, the underlying dissipative events occurring on the contact interface are characterized macroscopically by a classical dry friction model, which comprises a set of evolution equations derived in analogy with elasto-plastic constitutive laws (splitting the tangential relative displacement into a stick-elastic part and a slip-plastic part [110]).

1.4 Outline

The remainder of this text is organized in five chapters. Chapter 2 is entirely devoted to the derivation of the constitutive equations that describe the powder behavior. The introductory section 2.1 is provided to aid the reader unfamiliar with continuum fracture mechanics to grasp the notion of *strain localization*, crucial to understand how an inherently discontinuous phenomena as cracking can be represented by a continuum approach. Section 2.2 gives a brief account of large strain kinematics. The formal thermodynamic framework for the construction of the constitutive equations is established in section 2.3. The remaining sections of chapter 2 discuss the details of the elastic and plastic responses, including the stress-elastic strain relationship, yield criteria, flow rule and the hardening and softening laws.

In order not to interrupt the continuity of chapter 2, the consistency of the proposed constitutive model with the second law of thermodynamics is discussed in appendix C. For similar reasons, lengthy mathematical derivations have been relegated to appendix A.1. A remark concerning notation is in order here. Whereas in chapter 2 (and also in chapter 3) , direct notation is predominantly used, in appendix A.1, both direct and indicial notation are employed. The convention index

adopted in this appendix follows Marsden and Hughes [63], in which the nature of the tensorial quantity (covariant-contravariant) changes depending of the placement of the suffix (superindex or subindex). Considering that our developments are embedded in the setting of a cartesian representation, to some readers, such a refined, admittedly convoluted notational scheme might seem utterly pretentious and unnecessary. However, rather than pretentiousness or extravagant claims to generality, we adopt this notation because, in our opinion, it enables us to go through some subtle steps of large strain plasticity theory that very often are inadvertently overlooked when using simpler notational schemes.

Appendix B is also connected with the contents of chapter 2. It contains an analytical study of the frictionless compaction of a cylindrical specimen. This appendix will allow the reader not steeped in the intricacies of large strain plasticity to gain some insight into this theory and acquire familiarity with terms like deformation gradient, rate of deformation tensor or plastic flow rule, which certainly are not of common usage in the daily engineering practice.

Chapter 3 deals with the time integration of the constitutive laws. In section 3.1, the basic ideas underlying the implicit-explicit (IMPLEX) integration scheme and the arguments in support of such non-conventional method are provided. Section 3.2 discusses the solution of the return-mapping equations, and in section 3.3 the stress update and algorithmic tangent moduli expressions stemming from the IMPLEX scheme are presented. The derivation of the algorithmic tangent moduli takes tedious algebra and hence is addressed in appendix A.4. Those readers not actively involved or interested in the numerical implementation of the model can perfectly skip chapter 3. However, they are advised to, at least, skim the chapter and read the brief overviews given at the outset of each section, so that they can capture, without the finer detail, the essence of the proposed integration procedures.

Chapter 4 is concerned with the assessment of the formulation and numerical implementation of the model. First, an abridged overview of some aspects of the global numerical implementation are provided in the introductory section. The two remaining sections present the example used for the validation, namely, a *Brazilian or diametral compression test* and the *pressing and ejection of a thin cylindrical part*.

Chapter 5 contains a detailed case study of the compaction of an axially symmetric multilevel adapter in an advanced CNC press machine. Sections 5.1 and 5.2 concentrate on the modeling of the tool set and the external loads acting. Section 5.3 deals with the simulation of the pressing stage; the effect of innacuracies in the input data in terms of final density distribution receives special attention. The question of optimization of the pressing sequence is addressed in section 5.3.3, and the analysis of the ejection process is discussed throughly in section 5.4.

Finally, Chapter 6 provides some concluding remarks and identifies areas for future research.

Chapter 2

Continuum modeling of the powder behavior

In the previous introductory chapter, the breaking up of the global system into its parts and the more relevant observable occurrences were described. We detailed there briefly the phenomenological aspects of the *powder sub-system* relevant to our goal, namely, the work hardening tendency of confined powder at high pressures, and the initiation and growth of cracks in localized zones due to inappropriate compaction schemes or improper tooling deflection. In this chapter, we first present (section 2.1) a brief overview of the analysis of these phenomena, with emphasis placed on the characterization of failure. To this end, we consider two simple tests: the double compaction of a cylindrical part, for describing the hardening behavior, and the tensile test, for analyzing the fracture phenomenon. Both tests allow a *one dimensional representation* of the above-mentioned phenomenological features and provide a fairly comprehensive introduction without requiring further insight into the mathematical background.

In the remainder of the chapter, attention is restricted to the development of a formal framework for describing mathematically the abovementioned physical events observed in the powder sub-system. Although the origins of these physical changes are to be sought in microstructural aspects, our analysis is based on the continuum approach and consequently we ascribe these physical changes to the relative motion of continuous distributed portions of material (continuum *particles*). Section 2.2 is devoted thus to carry out a purely *kinematic* analysis by providing adequate means of measuring the status of deformation at a given particle without concern of the exterior factors provoking such deformation. Since thermal effects are ignored, it is evident, therefore, that physical properties associated to a particle of the medium are solely determined by the history of deformation at this point. To judge whether a particular deformation process induces permanent changes in the physical structure of the medium or not, the history of deformation path for a material point at a fixed instant is related to the stress state via the *constitutive equation* or *constitutive law*. Roughly, if the stress in a given point of the medium

is beyond a critical value, mechanical properties vary permanently in a fashion dictated by the constitutive equation. From section 2.3 onwards, we concentrate on deriving the proposed constitutive model for the powder.

In order to preserve the phenomenological character of our discussion, mathematical derivations and concepts which are not crucial for the understanding of the underlying physics, yet may be relevant for a deeper and detailed analysis, are relegated to Appendix A.

2.1 Phenomenological aspects within a one dimensional setting

2.1.1 Densification phenomenon

In the double compaction of a cylindrical part (figure 2.1), the powder is compacted by applying simultaneously an equal amount of pressure and movement by both the upper and lower punches. The compaction pressure P_u is defined as the force exerted by the punches, divided by the cross section of the compact perpendicular to the pressure direction. An overall mathematical characterization of the hardening phenomenon is provided by the so-called *compressibility curve* (average density against compaction pressure). It describes the extent to which a mass of powder can be densified by the application of pressure. Physical mechanisms of deformation indicate an increasing resistance of the compact against further densification, and this is translated in the compressibility curve into a steadily decreasing slope approaching asymptotically a final density (see figure 2.1c), referred as full density, which is below the theoretical density of the sintered material.

Die surface roughness reduces the extent of bulk particle movement and a lower density is attained in regions furthest away from the pressing punches. These gradients in the axial direction can be estimated easily by means of a one dimensional analysis, which is commonly used for calibrating some useful parameters, such as the friction coefficient [83]. All variables are considered constant over the cylindrical cross section. The radial pressure exerted on the die wall by the compact is related to the axial stress in each cylindrical section through a constant k_{tr}, sometimes referred as pressure transmission coefficient [31, 28], which takes always a value less than one. Frictional forces developed at the die wall are accounted via a typical Coulomb law. A force balance on the infinitesimal slice of height dz shown in figure 2.1 yields

$$\pi R^2(-p(z+dz)+p(z))+(2\pi R dz)\tau_{fr}=0, \tag{2.1.1}$$

where p is the axial pressure, R is the radius of the cylindrical part, z is the axial coordinate and τ_{fr} is the tangential stress due to the interaction with the die wall. Taking a uniform friction coefficient μ throughout the contact surface, we arrive at the boundary value problem

$$\frac{dp}{dz}=\frac{2\pi k_{tr}}{R}p(z), \quad z\in[-\frac{L}{2},\frac{L}{2}], \quad p(|L/2|)=P_u, \tag{2.1.2}$$

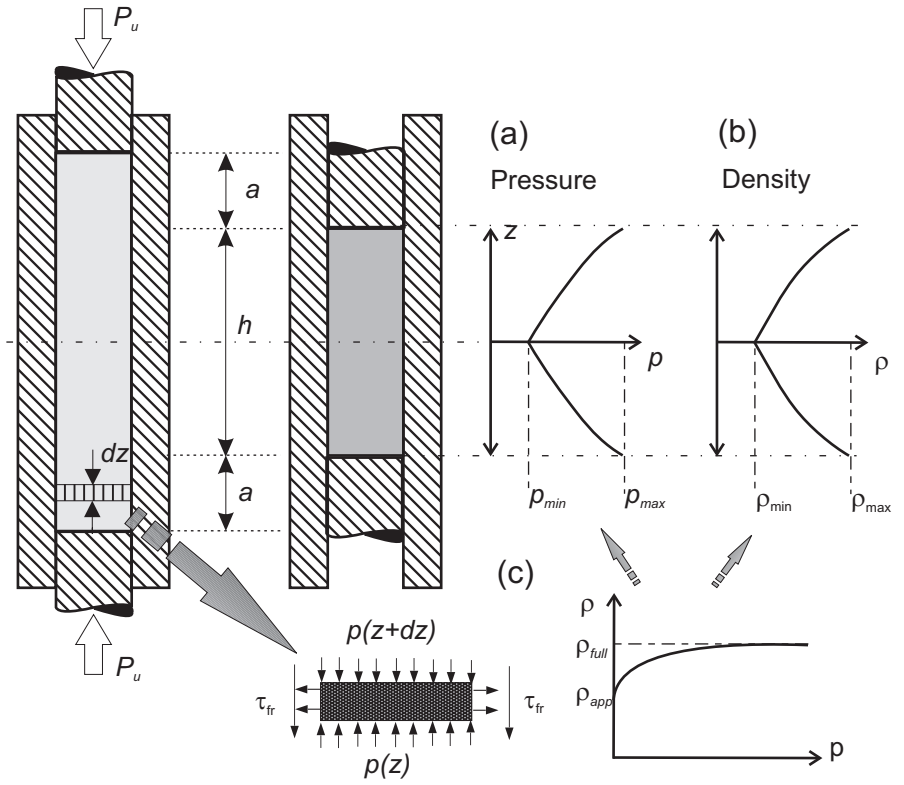

Figure 2.1 *Two step compaction procedure. (a) Pressure distribution (b) Density distribution f(c) Compressibility curve*

whose solution is the symmetric exponential function, shown in figure 2.1a,

$$p(z) = P_u e^{-\frac{2\mu k_{tr}}{R}(L/2-|z|)}. \tag{2.1.3}$$

Thus, axial pressure on the powder mass decreases with increasing distance to the face of the pressing punches, attaining its minimum at $z = 0$. Density distribution presents a similar profile, as illustrated in figure 2.1b. The extent of these gradients is promoted by *the length to diameter ratio* $h/2R$ and by friction between die and powder, which assesses the importance of reducing both factors in the common practice of green compact manufacturing.

2.1.2 Cracking phenomena and their modelling

Prior to proceeding with the analysis, it is worthwhile to point out some notions about the terminology used for describing the phenomenon we are interested in. In the context of the manufacturing of green compacts, we consider a source of *failure* any defect that either motivates the rejection of the compact, or remain in

the part after sintering and affects the final properties and performance. Hence, the situation of *failure* is relative to a particular material and its technical aspects. For instance, for structural P/M materials, a high level of porosity is considered as a defect due to its undesirable effects on mechanical properties, whereas for self-lubricant parts, porosity is crucial for meeting their oil retaining requirements. Defects in green compacts span a wide range of imperfections. They may be very visible to the naked eye or very fine and extremely difficult to detect. *Cracks* are the most common defects. The classical conception of *crack* entails the onset and propagation of microdefects along a discontinuity line, which is not necessarily straight or smoothly oriented [3]. Other representative defects, whose definitions do not fit completely into the above-mentioned conception of *crack*, are the *crumbling* of the edges and corners of the compact and the appearance of *surface bulges*, due to inadequate removal of air during the compaction [43]. On the other hand, *fracture* implies the breaking of the compact into two or more parts and it is induced mainly by *cracking*. With some abuse of terminology, we occasionally may use indiscriminately throughout the text the terms *cracking*, *fracture* and *failure* to refer to the appearance of any evidence of mechanical damage.

In order to describe mathematically the cracking phenomenon, we have first to understand the connection between the interplay of dissipative actions that take place at the grain scale in the affected area and the macroscopic behavior of the material. Cracking implies a breakage of the mechanical bonds between powder particles [112], and this loss of particle cohesion becomes manifest at the macrolevel in gradual local degradation of the effective green strength. Since we are using a continuum-based description, it is required a constitutive model with *softening*, i.e., a decrease in strength with additional deformation.

2.1.2.1 Strain localization

A controversial issue of the continuum approach we have invoked for describing our system is its inability, without any further enhancements, of handling spatial discontinuities, which are intrinsic to the cracking phenomena. This limitation may seem to render the chosen approach questionable on fundamental grounds. However, the underlying mathematical aspects of stress-strain plastic softening relationships permit to model the discontinuity surface associated to a crack as a *high gradient of inelastic strains concentrated along a band of finite thickness (strain localization).* As is customary in the related literature [10], a one dimensional analysis of a tensile test will provide the guidance to understand this feature.

Let us consider for this purpose that the green compact obtained in the double action compaction described previously is ejected from the die and placed between two supports, using adhesive, and subjected to a gradually increasing axial displacement δ on its top surface. All properties are assumed to be constant through the cross section.

As a direct consequence of die frictional forces during pressing, the level of intergranular cohesion is not uniform throughout the specimen, attaining its minimum at the middle plane, as it indicates the density distribution shown in figure 2.1b. For the sake of clarity, let us assume that the material within a central band Ω_a

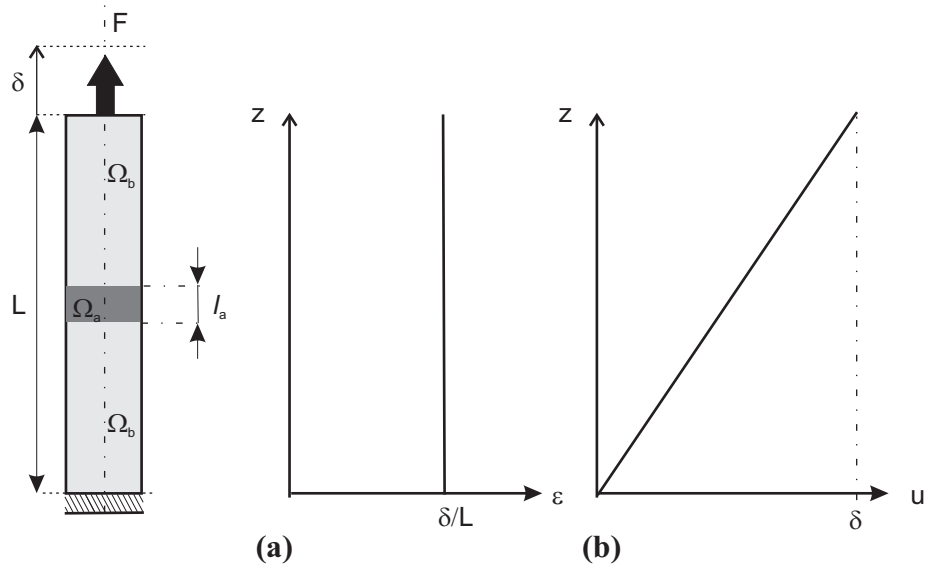

Figure 2.2 *Tensile test. Pre-peak distribution of: (a) strain (b) displacement.*

of width l_a possesses a tensile strength lower than in the surrounding material Ω_b, i.e., $\sigma_a^y > \sigma_b^y$. Prior to reaching σ_a^y in the central band Ω_a, a Hooke's law is obeyed and stress, σ, or load F, is proportional to strain ϵ, or displacement δ. Assuming a uniform Young's modulus E, we find

$$\text{For} \quad \delta \leq \frac{\sigma_y^a}{EL} \Longrightarrow \begin{cases} \epsilon(z) = \dfrac{\delta}{L}, & \forall z \in [0, L], \\ \sigma(z) = E\epsilon = \dfrac{E\delta}{L}, & \forall z \in [0, L]. \end{cases} \tag{2.1.4}$$

Therefore, the specimen exhibits a uniform strain field up to the yield strength σ_a^y (figure 2.2). Immediately after the yield strength σ_a^y is reached, softening starts in Ω_a, i.e. a gradual degradation of mechanical strength accompanying an increase in strain, as it indicates the descending branch BC of the stress-strain curve shown in figure 2.3, and plastic yielding is confined to that domain.

At a given instant t after onset of yielding, the stress in domain Ω_a has decreased from σ_a^y to $\sigma_a(t)$. Obvious equilibrium considerations require uniformity of stress in the entire domain $\sigma_a(t) = \sigma_b(t)$. Inasmuch as the material outside the band has a greater yield strength $\sigma_b^y > \sigma_b(t)$, under increasing external prescribed displacement $\dot{\delta} > 0$, its mechanical properties remain unaltered and it simply unloads in an elastic manner along path AB (figure 2.3). Thus, at any time after the onset of yielding there exist, for the same stress level, two different strain levels along the specimen ($\epsilon_a \neq \epsilon_b$) (figure 2.4). This tendency towards plastic yielding in localized regions accompanied by elastic unloading in the surrounding material is a distinctive feature of strain softening constitutive models, and it is referred to as *strain localization.* The mathematical explanation of this bifurcation of the strain field is to be sought

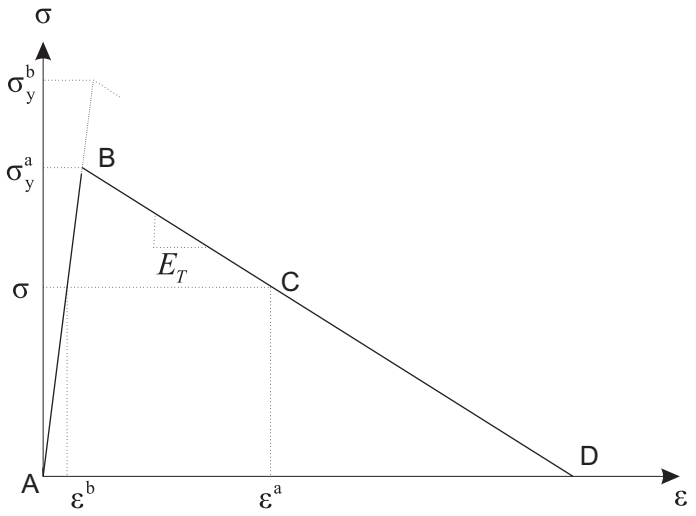

Figure 2.3 *Stress-strain response.*

in the local change of character of the governing set of differential equations, which cease to be elliptic for the static case [70]. In the one-dimensional setting, loss of ellipticity occurs when the tangent modulus E_T becomes negative.

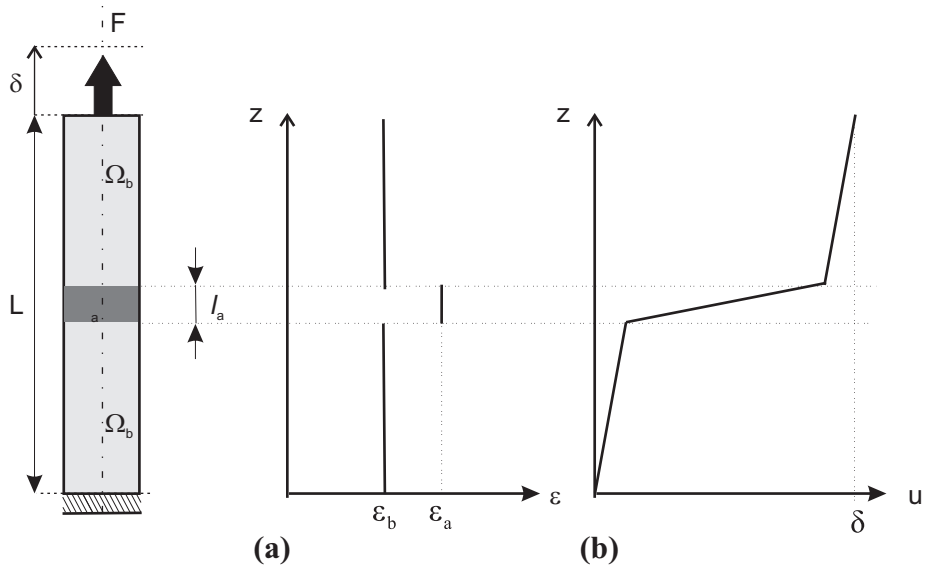

Figure 2.4 *Tensile test. Post-peak distribution of: (a) strain (b) displacement.*

The post-peak rate of change of the strain $\dot{\epsilon}_a$ in Ω_a as a function of $\dot{\sigma}_a$ is given

by

$$\dot{\sigma}_a = E\left(\dot{\epsilon}_a - \dot{\epsilon}_a^p\right) = E\left(\dot{\epsilon}_a - \frac{\dot{\sigma}_a}{H}\right) \Longrightarrow \dot{\epsilon}_a = \frac{EH}{E+H}\dot{\sigma}_a = E_T\,\dot{\sigma}_a. \tag{2.1.5}$$

For deriving the equation above, we have used some basic considerations embodied in the classical theory of plasticity [42, 51, 53], namely, the additive decomposition of the strain ϵ into elastic ϵ^e and plastic part ϵ^p, and the evolution of stress during plastic loading in terms of the plastic strain rate $\dot{\epsilon}^p$. Material brittleness is characterized by the so called isotropic *softening modulus* $H \leq 0$, and E_T is the slope of the descending branch of the stress-strain curve shown in figure 2.3. Note that the range of values within which softening modulus may lie is restricted by the requirement that E_T is negative, hence $|H| < E$.

Likewise, rate of change of the strain $\dot{\epsilon}_b$ in the undamaged material is obtained straightforwardly as

$$\dot{\sigma}_b = E\dot{\epsilon}_b \Longrightarrow \dot{\epsilon}_b = \frac{\dot{\sigma}_b}{E}. \tag{2.1.6}$$

By substituting equations 2.1.5 and 2.1.6 in the equilibrium condition $\dot{\sigma}_a = \dot{\sigma}_b$, one obtains the relationship between strain rates in both domains

$$\dot{\epsilon}_a = \frac{E+H}{H}\dot{\epsilon}_b. \tag{2.1.7}$$

Expression 2.1.7 shows that whereas in Ω_a strain increases ($\dot{\epsilon}_a > 0$), there is a strain release in Ω_b ($\dot{\epsilon}_b < 0$). Using the compatibility requirement $\dot{\epsilon}_a l_a + \dot{\epsilon}_b(L - l_a) = \dot{\delta}$ and equations 2.1.7, 2.1.6 and 2.1.5 we obtain, upon rearrangement, the force-displacement rate response after yielding

$$\dot{F} = \frac{EA}{L\left(1 + \dfrac{E}{H}\dfrac{l_a}{L}\right)}\dot{\delta}. \tag{2.1.8}$$

From equation 2.1.8, we can deduce that different values of l_a yield different post-peak paths. The smaller the value of l_a, the steeper the slope of the path. For $l_a \to 0$ the softening branch BC of the force-displacement curve (figure 2.5) approaches the initial elastic branch AB, which is not acceptable from the physical point of view. This fact highlights the relevance of the role played by the size of the localization zone in the material response. Although physical interpretations may be suggested (e.g., average distance between inhomogeneities or micro-pores in the green compact), they are meaningless in the context of the standard continuum smeared-crack approach we have adopted, in which l_a is determined by the minimum element size of the spatial discretization used in the subsequent numerical resolution.

The absence of a physically grounded intrinsic width l_a, thus, spans a space of infinite continuum solutions. When choosing a particular spatial discretization, one of this solution is obtained. This strong mesh dependence can be partially alleviated by reinterpreting the role of the continuum softening modulus H in the

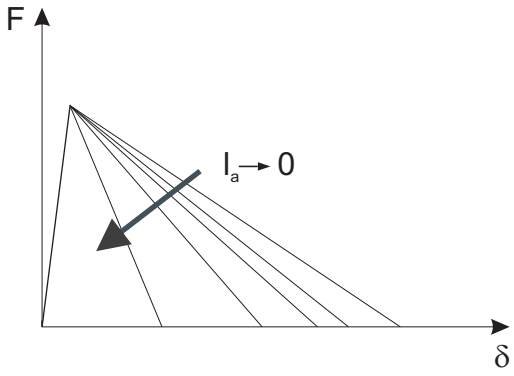

Figure 2.5 *Force-displacement response.*

formulation of the constitutive model. Consider next the energy consumed during the interval $[0, t_\infty]$, where t_∞ denotes the time when the load carrying-capacity of the bar is totally exhausted:

$$\begin{aligned}
\mathcal{W}^{\text{ext}} &= \int_0^{t_\infty}\!\!\int_\Omega \sigma\dot{\epsilon}\, d\Omega\, dt = \int_0^{t_\infty}\!\!\int_{\Omega_a} \sigma\dot{\epsilon}\, d\Omega + \overbrace{\int_0^{t_\infty}\!\!\int_{\Omega_b} \sigma\dot{\epsilon}\, d\Omega}^{=0} \\
&= \int_0^{t_\infty} \sigma\dot{\epsilon}\,(A\, l_a)\, dt = \int_0^{t_\infty} \sigma\,(\dot{\epsilon}_e + \dot{\epsilon}_p)\; l_a\, dt \\
&= \int_0^{t_\infty} \sigma\dot{\epsilon}_p\,(A\, l_a)\, dt = \int_0^{t_\infty} \sigma \frac{\dot{\sigma}}{H}\,(A\, l_a)\, dt = \left[\frac{1}{2}\frac{\sigma^2}{H}\,(A\, l_a)\right]_{\sigma_y}^{0} \\
&= \frac{1}{2}\frac{\sigma_y^2}{|H|}\,(A\, l_a).
\end{aligned} \tag{2.1.9}$$

Energy dissipation is, thus, exclusively due to plastic flow in the localization band, since the surrounding material remains in the elastic state throughout the process. If we divide the amount of energy dissipated $\mathcal{W}^{\text{ext}}$ by the cross sectional area A, we obtain the energy necessary to achieve fully exhaustion of the load-carrying capacity of a bar of unit area. This concept of energy is tantamount to the so-called *fracture energy* $\mathcal{G}_f$, defined, in the context of classical fracture mechanics, as the mechanical energy required for the formation of a unit of fracture surface. The fracture energy can be calibrated experimentally for each *fracture mode*(figure 2.6), and thus it can be interpreted as material property. Enforcing that the energy dissipated along the localization band equals the fracture energy, we have

$$\mathcal{G}_f = \frac{\mathcal{W}^{\text{ext}}}{A} = \frac{1}{2}\frac{\sigma_y^2}{|H|} l_a\,. \tag{2.1.10}$$

Equation 2.1.10 suggests that, for avoiding dependency to mesh refinement, softening modulus H has to be also a function of the mesh size and not a uniformly

distributed local variable, as it was presumed. Then, rephrasing equation 2.1.10, we obtain

$$|H| = \left(\frac{1}{2} \frac{\sigma_y^2}{\mathcal{G}_f} \right) l_a = |\hat{H}| l_a, \tag{2.1.11}$$

where the material property $|\hat{H}|$ is denominated the *intrinsic softening modulus*. A reliable choice of the numerical localization bandwidth l_a for more complicated spatial discretizations is dictated not only by the size of the mesh elements, but also by the orientation of the crack within the mesh [74].

A further sophisticated alternative within the continuum framework which avoids this drawback is the *Strong Discontinuity Approach* [91], in which the negligible character of the intrinsic length scale justifies the mathematical simplification of assuming zero band thickness. The Strong Discontinuity Approach allows the representation of displacement jumps across the localization band, which are precluded in our description since standard finite elements can only exhibit finite jumps of strain across the element boundaries (figure 2.4).

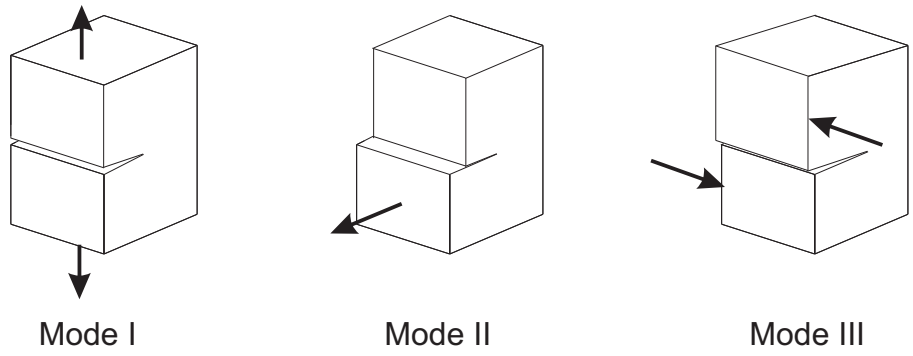

Figure 2.6 *Fracture modes. In the opening mode or mode I the loads inducing fracture are perpendicular to the plane of the crack, as in the tensile test we are describing. Modes II and III are shearing modes, with loads acting on the crack plane.*

2.2 Kinematics of plastic large deformations

Consider the powder sub-system as a deformable body $\mathcal{B}$ consisting of continuously distributed material occupying, at a reference time t_0, a region Ω_0 of $\mathbb{R}^n$ $(n = 2, 3)$. Deformation is measured from this *reference configuration*, which does not coincide necessarily with the loose powder state. We assume that the deformation at time t relative to the reference configuration is given by the one-to-one $\mathcal{C}^2$ mapping $\boldsymbol{\varphi} : \Omega_0 \to \Omega_t \subset \mathbb{R}^n$. The position vector, with respect to a fixed origin o, of particle $X \in \mathcal{B}$ in the so-called *current configuration* Ω_t is given by

$$\mathbf{x} = \boldsymbol{\varphi}(\mathbf{X}, t), \tag{2.2.1}$$

or in component form

$$x^a = \varphi^a(\mathbf{X}, t)\,, \tag{2.2.2}$$

where $\mathbf{x} = x^a \bar{\mathbf{e}}_a$, being $\{\bar{\mathbf{e}}_a\}$, $(a = 1 \dots n)$ an orthogonal basis vector. An alternative Cartesian basis $\{\bar{\mathbf{E}}_A\}$ $(A = 1 \dots n)$ is used for describing the position of material[1] points $\mathbf{X} = X^A \bar{\mathbf{E}}_A$.

The deformation gradient of mapping (2.2.1), defined as

$$\mathbf{F}\,(\mathbf{X}, t) = \frac{\partial \boldsymbol{\varphi}\,(\mathbf{X}, t)}{\partial \mathbf{X}} \qquad \text{or} \qquad F^a_A(\mathbf{X}, t) = \frac{\partial \varphi^a(\mathbf{X}, t)}{\partial X^A}, \tag{2.2.3}$$

plays a crucial role in characterizing the local deformation at $\mathbf{X}$. However, the deformation gradient itself is not a suitable means of measuring straining. The physical interpretation of the polar decomposition of $\mathbf{F}$ (see Eq.(A.1.6) in Appendix A), suggests that the local rigid rotation must be purged from any measure of strain, since a rigid rotation maintains the distance between particles and hence does not alter physical properties of the body. A wide range of possible strain tensors, with the common characteristic of being independent of the rotational part of $\mathbf{F}$, can be established in both the reference configuration Ω_0 and the current configuration Ω_t. We shall employ as material strain measure the *Green-Lagrange* strain tensor, defined in the reference configuration Ω_0 as

$$\mathbf{E}(\mathbf{X}) = \frac{1}{2}\left(\mathbf{C}(\mathbf{X}) - \mathbf{1}\right), \tag{2.2.4}$$

where $\mathbf{C} = \mathbf{F}^T \cdot \mathbf{F}$ is the right Cauchy-Green tensor, and $\mathbf{1}$ is the second order identity tensor[2] in Ω_0. In analogous manner, the strained state is characterized in the current configuration Ω_t by the so-called Almansi strain tensor

$$\mathbf{e}(\mathbf{x}) = \frac{1}{2}\left(\mathbf{1} - \mathbf{b}^{-1}(\mathbf{x})\right), \tag{2.2.5}$$

where $\mathbf{b}^{-1}$ is called the *Finger* deformation tensor $\mathbf{b}^{-1} = \mathbf{F}^{-T} \cdot \mathbf{F}^{-1}$. A useful relationship between the spatial and material strain tensors is given by

$$\mathbf{e} = \varphi_*(\mathbf{E}) = \mathbf{F}^{-T} \cdot \mathbf{E} \cdot \mathbf{F}^{-1}, \tag{2.2.6}$$

where the operator $\varphi_*(\bullet)$ is referred to as the *push-forward* transformation induced by $\boldsymbol{\varphi}$ (see Eq.(A.1.12) in Appendix A).

Inasmuch as plastic deformations are governed by rate form constitutive equations, it is pertinent to summarize some expressions for the rates of deformation tensor. The spatial *velocity gradient* $\mathbf{l}$ is given by

$$\mathbf{l}(\mathbf{x}) = \dot{\mathbf{F}} \cdot \mathbf{F}^{-1}, \tag{2.2.7}$$

being $\dot{\mathbf{F}}$ the derivative of $\mathbf{F}$ with respect to time holding $\mathbf{X}$ fixed. Its symmetric part:

[1] Upper case indices refer to the reference configuration Ω_0 and lower case indices are related to the current configuration. See Appendix A for more details.

[2] More precisely, $\mathbf{1}$ can be interpreted, for this equation, as the metric tensor in Ω_0 (see Eq.(A.1.9) in Appendix A).

$$\mathbf{d} = \frac{1}{2}(\mathbf{l} + \mathbf{l}^T), \tag{2.2.8}$$

is called the rate of deformation tensor, and it turns out to be the *Lie derivative* (see Eq.(A.1.20) in Appendix A) of the spatial strain tensor $\mathbf{e}$, i.e. $\mathbf{d} = \mathcal{L}_v\mathbf{e}$.

2.2.1 Multiplicative decomposition

So far, we have presented some tensorial fields expressions for characterizing the deformation of our powder continuum sub-system at any time, regardless of the extent and nature of this deformation. A further step in the kinematic description is to analyze separately the elastic and plastic contributions to the deformation state. As is customary in the literature of compaction modeling [15, 81, 7, 90], we introduce the standard local multiplicative decomposition of the deformation gradient into plastic and elastic parts:

$$\mathbf{F} = \hat{\mathbf{F}}_e \cdot \mathbf{F}_p, \tag{2.2.9}$$

where $\mathbf{F}_p$ accounts for a pure plastic local deformation from Ω_0 to a fictitious[3] stress-free *intermediate configuration* $\hat{\Omega}_t$ and $\hat{\mathbf{F}}_e$ represents a pure elastic loading from the intermediate state $\hat{\Omega}_t$ to the current configuration Ω_t. Observe that the elastic counterpart of the deformation gradient, $\hat{\mathbf{F}}_e$, is defined in the intermediate configuration $\hat{\Omega}_t$, whereas $\mathbf{F}_p$ maps objects in the reference configuration Ω_0 to $\hat{\Omega}_t$. An elastic strain measure in Ω_t can be established, by analogy with Eq.(2.2.6), as

$$\mathbf{e}_e = \frac{1}{2}(\mathbf{1} - \mathbf{b}_e^{-1}), \tag{2.2.10}$$

where $\mathbf{b}_e^{-1}$ is the elastic *Finger* deformation tensor, $\mathbf{b}_e^{-1} = \hat{\mathbf{F}}_e^{-T} \cdot \hat{\mathbf{F}}_e^{-1}$. The same similarity can be exploited for deriving an expression of a plastic strain tensor in $\hat{\Omega}_t$:

$$\hat{\mathbf{e}}_p = \frac{1}{2}(\mathbf{1} - \hat{\mathbf{b}}_p^{-1}), \tag{2.2.11}$$

with $\hat{\mathbf{b}}_p^{-1} = \hat{\mathbf{F}}_p^{-T} \cdot \hat{\mathbf{F}}_p^{-1}$. Furthermore, it can be proved (see A.1.30 in Appendix A) that

$$\mathbf{e} - \mathbf{e}_e = \hat{\mathbf{F}}_e^{-T} \cdot \hat{\mathbf{e}}_p \cdot \hat{\mathbf{F}}_e^{-1}, \tag{2.2.12}$$

i.e., the difference between the spatial strain $\mathbf{e}$ and the elastic spatial strain $\mathbf{e}_e$ is equal to the tensor resulting of transforming, via $\hat{\mathbf{F}}_e^{-1}$, the plastic tensor $\hat{\mathbf{e}}_p$ defined in $\hat{\Omega}_t$ to the spatial configuration Ω_t. This means that a physical meaning of pure spatial strain tensor cannot be attached to the difference $\mathbf{e} - \mathbf{e}_e$, since both elastic and plastic effects are involved in its definition.

[3] Note that, despite its seemingly resemblance with the state reached upon pressure release in a ordinary compaction process, the *intermediate configuration* $\hat{\Omega}_t$ may be physically unachievable, since residual stress are unavoidable.

2.2.1.1 Extent of plastic and elastic deformations

Kinematic relationships deduced hitherto are valid regardless of the extent of plastic and elastic deformation experienced by the body during its motion. However, in order to keep the subsequent derivations as simple as possible, it is worth inquiring whether some approximations might be introduced in the particular case of cold axial compaction of a standard metallic powder. For example, for pure cooper PM parts, the ratio of the volume of loose powder in a die to that of the final compact made from it at the end of the pressing stage ranges between 2.6 and 2.8 [96]. This means that, if we choose the reference configuration Ω_0 of the continuum body as the region occupied by the powder in its loose state, and the deformed configuration Ω_t as the region occupied by the green compact before punch removal, then an infinitesimal volume elemental placed in Ω_0 shrinks to a factor 2.7 in Ω_t, as it emanates from the conservation of mass local equation $det(\mathbf{F}) \sim 1/2.7$. In addition to this large strains, large local rotations may also be involved, especially in multilevel parts in which material flow around corners is pronounced. A deeper insight into the nature (elastic or plastic) of these considerable straining shows that the behavior of the powder is basically plastic. Compacted parts undergo slight expansions (spring-back) in both pressing and radial direction upon pressure release [100]. The magnitude of these dimensional changes are three to four orders smaller than the characteristic dimension of the compact [106], which suggests that a vast portion of the deformation experienced by the powder during pressing is basically unrecoverable, i.e. plastic[4]. A common assumption in modeling the pressing stage [16, 81, 109] is thus to consider that *elastic strains are small compared to unity during the pressing stage.*

On the other hand, during the subsequent ejection from the die, apart from the above mentioned partial[5] recovery of the (small) elastic strains developed in the pressing stage, the green compact may undergo deformation states entailing softening plastic behavior in localized zones of the body (see Section 2.1.2). Since unsintered parts are considered to be quasi-brittle, the extent of plastic strains developed in this zones are also assumed to be small. Furthermore, the motion of the compact through the die cavity during ejection involves no solid rigid rotations, since punches push only in the (vertical) pressing direction[6]. These kinematics assumptions (small elastic and plastic strains accompanied of negligible rotations) indicates that, if we take as reference configuration the deformed state at the end of compaction, an *approximated description of the deformation of the powder subsystem during the pressure release and ejection stages may be carried out employing an infinitesimal plastic strain theory.*

In summary, the kinematic description based on the multiplicative decomposition (A.1.21) admits two approximations. During the pressing stage, large plastic

[4] An alternative method of demonstrating the extent and importance of plastic deformation during compaction is to measure the increases in the microhardness of individual particles after varying amounts of compaction [43].

[5] Residual stresses upon pressure release may be presented in non-homogeneous plastic deformation states [48].

[6] This assumption holds only for conventional axial pressing processes. Splitting die system or isostatic pressing would require revision of this hypothesis.

deformations are presented accompanied by small elastic strains, whereas during pressure release and ejection, the magnitude of both plastic and elastic strains are relatively small. Since the former approximation constitutes a broader framework encompassing both cases, attention is restricted henceforth to detail the strain measures derived from this particular approach of *finite plastic deformations and small elastic strains*.

The methodology for obtaining the strain measure in this case parallels that followed in the classical infinitesimal theory. The difference between the intermediate configuration $\hat{\Omega}_t$ and the current configuration Ω_t becomes insignificant. Tensorial fields defined in $\hat{\Omega}_t$ can be transformed directly into spatial tensorial fields. In particular, $\hat{\mathbf{e}}_p \approx \mathbf{e}_p$, which implies, in accordance with Eq.(2.2.12), the additive decomposition of the spatial strain tensor[7]:

$$\mathbf{e}(\mathbf{x}) = \mathbf{e}_e(\mathbf{x}) + \mathbf{e}_p(\mathbf{x}). \tag{2.2.13}$$

Another valuable consequence of the assumption of infinitesimal elastic strains is that $\mathbf{e}_e$ can be regarded as a linearized strain tensor:

$$\mathbf{e}_e(\mathbf{x}) = \frac{1}{2}(\mathbf{J}_e(\mathbf{x}) + \mathbf{J}_e^T(\mathbf{x})), \tag{2.2.14}$$

wherein $\mathbf{F}_e = \mathbf{1} + \mathbf{J}_e$.

The same reasoning (see Appendix A) applies for the rate of deformation tensor, which inherits the additive structure shown above:

$$\mathbf{d} = \mathbf{d}_e + \mathbf{d}_p. \tag{2.2.15}$$

Furthermore, it can be easily verified that the plastic and elastic parts of the rate of deformation tensor are the Lie derivatives of the plastic and elastic Almansi strain tensors, i.e.

$$\mathbf{d}_p = \mathcal{L}_v \mathbf{e}_p \qquad \text{and} \qquad \mathbf{d}_e = \mathcal{L}_v \mathbf{e}_e \ , \tag{2.2.16}$$

respectively.

2.3 Thermodynamic consistency

After establishing adequate tensors for characterizing the deformation at the neighborhood of each material particle X, attention is now turned to describe mathematically the effects of such deformation processes on the physical attributes of the powder sub-system. The preliminary step in this mathematical description is to select the appropriate set of independent scalar and tensorial fields whose values at a given time allow to determine uniquely the Cauchy stress field and other state functions. Since thermal effects are ignored, all these variables can be expressed in terms of the deformation history through adequate functional relationships. We set as the basic state variable the deformation itself, expressed by the current value

[7] In Appendix A (Eq.(A.1.34)), this simplification is carried out in a more rigorous manner.

(at time t) of the deformation gradient $\mathbf{F}$. The elastic part of the deformation gradient, $\hat{\mathbf{F}}_e$, is regarded as another tensorial state variable, linked to the recoverable deformation of the powder sub-system. The remaining fields are the so-called *internal* or *hidden* variables [61], denoted collectively by $\boldsymbol{\xi}$. Since the evolution of these variables are related with irreversible mechanisms, it seems reasonable to classify $\boldsymbol{\xi}$ according to the nature of the internal physical changes associated with each mechanism. Specifically, we categorize the set of internal variables into internal *hardening* variables, $\boldsymbol{\xi}^h$, and internal *softening* variables, $\boldsymbol{\xi}^s$, a classification that discloses the phenomenological aspects discussed in section 2.1. Without loss of generality, we assume that the as yet unspecified internal variables are all scalar variables. Hence, the α-th hardening mechanism, for instance, is characterized by the scalar field $\xi^h_\alpha = \xi^h_\alpha(\mathbf{x}, t)$. Furthermore, it follows from the inherent irreversibility of the hardening and softening phenomena that $\dot{\xi}^h_\alpha \geq 0,\ \alpha = 1, 2 \ldots n_{ih}$, and $\dot{\xi}^s_\beta \geq 0,\ \beta = 1, 2 \ldots n_{is}$, i.e., the internal variables have the non-decreasing property. Later, it will be discussed further the physical meaning of each internal variable and their evolution equations in terms of plastic deformation paths.

The Cauchy stress field, denoted by $\boldsymbol{\sigma}(\mathbf{x}, t)$, and other state functions, are related to the state variables $\{\mathbf{F}, \hat{\mathbf{F}}_e, \boldsymbol{\xi}^h, \boldsymbol{\xi}^s\}$ through a set of *constitutive* equations. We shall attempt to derive the mathematical form of these constitutive relationships within a rational thermodynamic framework, although it might prove expedient a shift towards pragmatism in some aspects of the derivation. We postulate the existence of a Helmholtz free energy function ψ, defined per unit reference volume. In the absence of thermal variations, ψ coincides with the internal energy per unit reference volume, and it includes the elastic strain energy and all other forms of energy that do not contribute to kinetic energy. We adopt here the hypothesis, favored by Mandel and others (see Ref. [61]), in which the free energy depends on the current value of the deformation gradient $\mathbf{F}$ solely through its elastic part, $\hat{\mathbf{F}}_e$. In the small elastic strain regime and assuming isotropic elastic response, we may legitimately write[8]:

$$\psi = \psi(\mathbf{e}_e, \boldsymbol{\xi}^h, \boldsymbol{\xi}^s). \tag{2.3.1}$$

2.3.1 Physical interpretation of changes in the value of the internal energy

To appreciate the effect of a change in the state variables in the value of the internal energy, we take the time derivative of Eq.(2.3.1):

$$\dot{\psi} = \overbrace{\frac{\partial \psi}{\partial \mathbf{e}_e} : \mathbf{d}_e}^{\dot{\psi}_d} + \overbrace{\frac{\partial \psi}{\partial \xi^h_\alpha} \dot{\xi}^h_\alpha}^{\dot{\psi}_h} + \overbrace{\frac{\partial \psi}{\partial \xi^s_\beta} \dot{\xi}^s_\beta}^{\dot{\psi}_s}, \tag{2.3.2}$$

where $\mathbf{d}_e$ is the elastic part of the rate of deformation tensor[9].

[8] See section (A.1.1) in Appendix A for further details.
[9] See Proposition (A.1.1) in Appendix A.

2.3.1.1 Changes due to elastic deformation

The first term of the right-hand side of Eq.(2.3.2), $\dot{\psi}_d$, represents the rate of change in internal energy due to *elastic deformation of the body*. During pressing, typically $\dot{\psi}_d > 0$, which means that a portion of the energy supplied to the powder sub-system is stored in the form of recoverable deformation. As it is suggested by the success in predicting density distributions by using rigid-plastic constitutive models, in which elastic effects are neglected [104], the elastic behavior of the powder particles plays a relatively minor role in the macroscopic response of the compact during the pressing operation. In the subsequent unloading, however, the way in which this elastic energy is released ($\dot{\psi}_d < 0$) is of central importance for the final mechanical properties of the compact, since it controls the degree of spring-back [64].

2.3.1.2 Changes associated with strain hardening

The term $\dot{\psi}_h$ is the rate at which mechanical energy, per unit reference volume, is stored in the powder sub-system due to interlocking of rough grains, plastic deformation and cold welding of particles, and other microscopic events macroscopically correlated with a *strain-hardening tendency*. These events are likely to occur only under compressive load states. Hence, during pressing it is expected $\dot{\psi}_h > 0$, whereas in the following pressure release and ejection $\dot{\psi}_h = 0$.

2.3.1.3 Changes associated with (inelastic) release of energy

The last term accounts for the release of energy ($\dot{\psi}_s \leq 0$) associated with the breakage of bonds between particles under tensile/shear straining. It was discussed in section (2.1.2) that material softening implicates localization of inelastic strains. Hence, the release of energy tends to occur in concentrated regions, in contrast to the overall manifestation of $\dot{\psi}_d$ and $\dot{\psi}_h$. The body may experience this type of microstructural alterations during both pressing and post-pressing operations, although they are more frequent in the latter.

Early stages of compaction

The physical interpretation of $\dot{\psi}_s$ in the early stages of the pressing operation requires further consideration. At this point of the compaction route, densification takes place principally by rearrangement of the powder particles [36], and therefore the body does not possess a significant cohesive strength. In the event of pressing of multilevel parts, corner regions, characterized by pronounced material flow, are prone to shear conditions with low levels of hydrostatic pressure, which eventually would activate the softening mechanisms. Nevertheless, the lack of adhesion of powder particles renders the role of softening, interpreted as deterioration of strength, dubious in this particular situation, because there are no measurable strength to be degraded. We shall make the assumption, thus, that the *strain-softening mechanism is not active until certain level of densification*, characterized by certain value of the hardening variables $\boldsymbol{\xi}^{h^*}$, has been reached, or expressed mathematically:

$$\boldsymbol{\xi}^h < \boldsymbol{\xi}^{h^*} \;\Rightarrow\; \dot{\psi}_s(\mathbf{X},t) = 0, \quad \forall\, \mathbf{X} \in \Omega_0. \tag{2.3.3}$$

An additional argument in support of this assumption is the lack of experimental data for fracture energy (a material parameter which is intimately tied to the rate of energy release $\dot{\psi}_s$) in the range of low densities. Indeed, in order to ensure adequate green strength for further handling, tests conducted to determine fracture energy can be only performed on specimens compacted to densities greater than a certain value, say 5 g/cm^3 for iron based powder [48]. Therefore, motivated by the dubious role of the softening mechanism for lower densities, and in the absence of experimental data for fracture energy, assumption (2.3.3), which in turn is equivalently to consider *perfect plasticity* under tensile/shear stress conditions, appears reasonable.

2.3.2 Decomposition of the free energy function

In Section 2.2.1, we introduced the additive decomposition of the spatial strain tensor into elastic and plastic parts. It is natural to inquiry at this point whether a similar decomposition might hold for the free energy. Large strain plasticity literature abounds with references to the hypothesis of additive decomposition of the free energy into (uncoupled) elastic and plastic parts [61, 92, 93], and it has been also advocated by some authors in the specific field of powder compaction modeling [81, 109, 7, 62]. This assumption implicates that the elastic response is not influenced by the structural changes experienced by the powder during the pressing stage or, in other words, the elastic parameters do not depend on the level of densification. Experimental evidence, however, confirms the opposite trend. As in the case of porous and granular material, the *elastic properties of the powder are observed to be strongly dependent on volumetric strain* [89, 84, 86]. Thus, the energy stored in the powder sub-system is described in more realistic terms using the following additive decomposition:

$$\psi(\mathbf{e}_e, \boldsymbol{\xi}^h, \boldsymbol{\xi}^s) = \psi_0 + \psi_e(\mathbf{e}_e, \boldsymbol{\xi}^h) + \psi_p(\boldsymbol{\xi}^h, \boldsymbol{\xi}^s). \tag{2.3.4}$$

The independent term of the right-hand side of *Eq.*(2.3.4), ψ_0, can be interpreted as the inelastic energy stored (in form of cold welding, interparticle locking, etc.) in the undeformed body. If the reference configuration Ω_0 coincides with the loose powder state, then we assume $\psi_0 = 0$, for all points $\mathbf{X} \in \Omega_0$[10]. The *elastic* counterpart, ψ_e, depends on both the elastic strain tensor and the hardening variables, for the reasons outlined above, whereas the value of the *plastic* free energy ψ_p is determined by the current value of the set of hardening and softening internal variables.

The stress power measured per unit reference volume is given by $\mathcal{P}_i = \boldsymbol{\tau} : \mathbf{d}$ and the local dissipation (assuming isothermal processes) $\mathcal{D}$ is the difference between the stress power and the rate of change in internal energy, $\mathcal{D} = \boldsymbol{\tau} : \mathbf{d} - \dot{\psi}$, where $\boldsymbol{\tau}$ is

[10] ψ_0 is included in the definition of ψ only for avoiding negative values of ψ, which may arise due to the release of energy associated with softening $\dot{\psi}_s < 0$. However, it only plays a conceptual role and its value is irrelevant for the subsequent numerical integration.

the spatial Kirchhoff stress. Using the additive splitting of the rate of deformation tensor and factoring common terms, the dissipation function reads

$$\mathcal{D} = (\boldsymbol{\tau} - \frac{\partial \psi_e}{\partial \mathbf{e}_e}) : \mathbf{d}_e + \boldsymbol{\tau} : \mathbf{d}_p - \frac{\partial \psi_e}{\partial \xi_\alpha^h}\dot{\xi}_\alpha^h - \frac{\partial \psi_p}{\partial \xi_\alpha^h}\dot{\xi}_\alpha^h - \frac{\partial \psi_p}{\partial \xi_\beta^s}\dot{\xi}_\beta^s. \tag{2.3.5}$$

The second law of thermodynamics, i.e. $\mathcal{D} \geq 0$, must be satisfied in all conceivable motions, hence the coefficient of $\mathbf{d}_e$ must vanish (Coleman-Noll procedure) [61], which implies that the Kirchhoff stress tensor is the derivative of the free energy with respect to the elastic strain tensor.

$$\boldsymbol{\tau} = \frac{\partial \psi_e}{\partial \mathbf{e}_e}. \tag{2.3.6}$$

The dissipation inequality then becomes

$$\mathcal{D} = \boldsymbol{\tau} : \mathbf{d}_p - (\frac{\partial \psi_e}{\partial \xi_\alpha^h} + \frac{\partial \psi_p}{\partial \xi_\alpha^h})\dot{\xi}_\alpha^h - \frac{\partial \psi_p}{\partial \xi_\beta^s}\dot{\xi}_\beta^s. \tag{2.3.7}$$

The most crucial aspects of the model remains to be addressed. On the one hand, an expression for ψ_e is needed to completely determined the elastic response. We deal with this topic in the following section. On the other hand, evolution equations for the set of internal variables, $\boldsymbol{\xi}^h$ and $\boldsymbol{\xi}^s$, and for $\mathbf{d}_p$ have to be derived, as well as constitutive relationships (consistent with inequality (2.3.7)) between internal variables $\boldsymbol{\xi}^h$ and $\boldsymbol{\xi}^s$ and their *conjugate* variables (in the sense of dissipation per unit reference volume). This task entails considerable complexity and will confine our attention in the remainder of the chapter.

2.4 Elastic response

Motivated by the smallness of the elastic strains, the structure of the elastic free energy function is borrowed from that of classical infinitesimal theory:

$$\psi_e(\mathbf{e}_e, \boldsymbol{\xi}^h) = \frac{1}{2}(3\kappa^e \mathrm{tr}^2\, \mathbf{e}_e + 2\mu^e\, dev\, \mathbf{e}_e : dev\, \mathbf{e}_e), \tag{2.4.1}$$

where $\mathrm{tr}\, \mathbf{e}_e$ denotes the trace of the spatial elastic tensor $\mathbf{e}_e$, $\mathrm{tr}\, \mathbf{e}_e = \delta^{ab}(\mathbf{e}_e)_{ab}$, and $dev\, \mathbf{e}_e = \mathbf{e}_e - \frac{1}{3}\mathrm{tr}\, \mathbf{e}_e \mathbf{1}$ is the deviator of $\mathbf{e}_e$. The bulk modulus κ^e and shear modulus μ^e are expressible in terms of the Young's modulus E^e and the Poisson's ratio ν^e, which are not constant but dependent on the hardening internal variables:

$$\kappa^e = \frac{E^e(\boldsymbol{\xi}^h)}{3(1-2\nu^e(\boldsymbol{\xi}^h))} \quad \text{and} \quad \mu^e = \frac{E^e(\boldsymbol{\xi}^h)}{2(1+\nu^e(\boldsymbol{\xi}^h))}, \tag{2.4.2}$$

a fact that reflects the aforementioned coupling between the elastic response and the hardening mechanism. Observe that ψ_e depends on $\mathbf{e}_e$ only through the tensorial invariants $\mathrm{tr}\, \mathbf{e}_e$ and $\|dev\, \mathbf{e}_e\|^2 = dev\, \mathbf{e}_e : dev\, \mathbf{e}_e$, which implicates an *isotropic* elastic response. The adoption of the isotropic assumption is a somewhat controversial issue. Ultrasound velocity measurements, collected by Coube et al. [26], show that

anisotropy develops at high densities, resulting in die pressed parts which are stiffer in the transverse direction than in the pressing direction. However, presumably because the predominance of plastic deformation masks the effects of elastic events, a precise knowledge of how to characterize this induced elastic anisotropy is still lacking, and recourse to the isotropy hypothesis is very common in continuum modeling of powder compaction [81, 7, 15, 12]. The price of this simplistic approach is that, say E^e employed in Eq.(2.4.2) is calibrated in the pressing direction, then the degree of radial spring-back may result underestimated.

An important implication of using the elastic free energy function 2.4.1 is that, at a constant $\boldsymbol{\xi}^h$, the *relation between stresses and elastic strains is linear*. This issue is also marked by controversy. Experiments conducted by Mosbah et al.[69] have revealed that a non-linear elasticity law is more adequate for describing the behavior during unloading and ejection phases. In the work of Pavier [83], this conclusion is also corroborated. However, it is claimed there that, as a first approximation, the dependence of the elastic secant modulus on the stress state can be disregarded.

For later purposes, it is convenient to express 2.4.1 as the contraction of tensorial quantities:

$$\psi_e(\mathbf{e}_e, \boldsymbol{\xi}^h) = \frac{1}{2}\mathbf{e}_e : \boldsymbol{c_e}(\boldsymbol{\xi}^h) : \mathbf{e}_e, \tag{2.4.3}$$

where $\boldsymbol{c_e}$ denotes the fourth-order elasticity tensor in the current configuration, defined as

$$\boldsymbol{c_e} = \kappa^e \mathbf{1} \otimes \mathbf{1} + 2\mu^e(\boldsymbol{I}_{\text{sym}} - \frac{1}{3}\mathbf{1} \otimes \mathbf{1}), \tag{2.4.4}$$

wherein $\mathbf{1} = \delta^{ab}\bar{\mathbf{e}}_a \otimes \bar{\mathbf{e}}_b$ denotes the second-order identity tensor and $\boldsymbol{I}_{\text{sym}} = \frac{1}{2}(\delta^{ac}\delta^{bd} + \delta^{ad}\delta^{bc})\,\bar{\mathbf{e}}_a \otimes \bar{\mathbf{e}}_b \otimes \bar{\mathbf{e}}_c \otimes \bar{\mathbf{e}}_d$ is the fourth-order symmetric tensor. According to Eq.(2.3.6), the spatial Kirchhoff stress tensor at time t is then given by

$$\boldsymbol{\tau}(\mathbf{x}, t) = \frac{\partial \psi}{\partial \mathbf{e}_e} = \boldsymbol{c_e} : \mathbf{e}_e. \tag{2.4.5}$$

It is important to note that the validity of (2.4.1) and (2.4.5) is restricted to the case of a stress-free reference configuration. The derivation of a more general expression can be found in section A.1.1 of Appendix A.

A complete description of the elastic response necessitates that explicit dependence of Young's modulus E^e and Poisson's ratio ν^e on the hardening variables is determined. As we have not yet specified the set of internal hardening variables, this task will be properly accomplished in section 2.5.4.

2.5 Plastic response

As stated earlier, the unequivocal definition of the physical attributes at $\mathbf{X} \in \Omega_0$ and at time $t \in [t_0, t_f]$, after experiencing a deformation process given by $\mathbf{x} = \boldsymbol{\varphi}(\mathbf{X}, t)$, involves the knowledge of the current values of the set of independent state variables $\{\mathbf{F}, \hat{\mathbf{F}}_e, \boldsymbol{\xi}^h, \boldsymbol{\xi}^s\}$. The deformation gradient $\mathbf{F}$ (the primary or *driving*

variable) at any $\hat{t} \in [t_0, t]$ can be directly obtained by differentiation of the mapping $\boldsymbol{\varphi}$. If no plastic deformation occurs, then $\mathbf{F} = \hat{\mathbf{F}}_e$. In this case, the powder sub-system maintains its initial physical attributes and the Kirchhoff stress tensor depends only of the *point value* of $\mathbf{F}$.

On the contrary, if dissipative processes take place, physical attributes are altered, and to obtain the correct final state of the body, the deformation path must be traced from the reference configuration. It is precisely here where the usefulness of the internal variables is brought to light. They can be regarded as mathematical objects introduced for avoiding an explicit dependence of the stress state and other properties on the history of deformation. Thus, additional equations are needed to relate the current values of the internal variables $\boldsymbol{\xi}$ with the plastic deformation trajectory. Based on the mathematical statement that any curve is fully described by its differential equation (with adequate initial conditions), these relationships are given in *rate form*. Another set of differential equations is provided by the *flow rule*, which define the plastic rate of deformation tensor $\mathbf{d}_p$ as a function of the stress and other state variables. An essential element in the definition of these evolution equations is the *yield function*, which, in conjunction with the *loading/unloading conditions*, governs the onset and continuance of plastic deformation.

In summary, obtaining the local *plastic response* in the domain of interest $[t_0, t_f]$ entails the resolution of a system of (first-order) ordinary differential equations supplemented by suitable initial conditions, with the time t as the independent variable, the components of $\hat{\mathbf{F}}_e$ (or $\mathbf{F}_p$) and $\boldsymbol{\xi}$ as dependent variables[11], and a function of time of the deformation gradient $\mathbf{F}(t)$ as the source term. The highly non-linear character of this ODE renders impossible to get a closed-form solution. Therefore, the aim of this section is to formulate the corresponding differential equations in a form amenable to a subsequent numerical implementation.

2.5.1 Internal variables

For consistency with the rest of state variables, it is reasonable to give a dimensionless character to $\boldsymbol{\xi}$, hence they are termed *strain-like* internal variables[12]. A judicious selection of $\boldsymbol{\xi}$ involves a compromise between accuracy of the description and complexity of the resulting system of governing equations, and it is further influenced by the availability of experimental data supporting the choice.

2.5.1.1 Hardening variables

Concerning the set of internal hardening variables $\boldsymbol{\xi}^h$, a review of the vast literature on the subject shows that the proposal of using a single scalar internal variable, for

[11] In practice, the dependent variables are neither $\mathbf{F}_p$ nor $\hat{\mathbf{F}}_e$ (they do not even appear in the numerical formulation, as we shall see in the next chapter), but any related strain measure, as $\mathbf{e}_e$ or $\mathbf{e}_p$. The reasoning behind this is that the isotropy assumption renders irrelevant the role of the plastic spin $\mathbf{w}_p = \frac{1}{2}(\mathbf{l}_p - \mathbf{l}_p^T)$ [92].

[12] Note that with this particular choice of dimensions for $\boldsymbol{\xi}$, their *conjugated forces* in the sense of rate of plastic free energy (see Eq.(2.3.7)): $\boldsymbol{\Xi} = \frac{\partial \psi_p}{\partial \boldsymbol{\xi}}$, can be interpreted as *stress-like* internal variables.

capturing the inelastic behavior under compressive load states, prevails over more complex theories. It has been found that this pragmatic approach yields realistic descriptions for the majority of loading conditions that occur in practical pressing schedules. The definition of such variable in terms of the plastic deformation path, however, is marked by much controversy. The most common assumption is formulated in terms of the compressive volumetric plastic strain accumulated during the deformation [21, 104, 33, 16]. The overridden argument in support of this particular assumption comes from the fact that the internal variable defined in this way can be practically identified with the density itself, thereby being very easy to monitor and measure experimentally. A plausible objection, however, is that when the compact approaches the theoretical density, its properties, in some aspects, parallel those of the dense metal, in which plastic flow is activated mainly by distorsional deformation, rather than volumetric deformation. Hence, it is felt that the internal variable should depend also on the deviatoric part of the accumulated plastic strain. This alternative hypothesis is theoretically substained and experimentally confirmed in the work of Cocks et al. [22]. More specifically, they show that an adequate description of the compaction process is better provided by an internal variable intimately connected with the work done during the compaction, thereby including both deviatoric and volumetric plastic strains.

Pursuing this line of discussion, however, is not the prevailing goal of our work, therefore we simply adopt the former classical hypothesis of a single internal hardening variable ($n_{ih} = 1$) associated with the accumulated volumetric plastic strain. Suppose that the material is subjected to a monotonically increasing compressive load, such that $\operatorname{tr} \mathbf{d}_p(t) < 0$, for all $t \in [t_0, t_f]$. The internal hardening variable, henceforth denoted by ξ^h, at time $t \in [t_0, t_f]$ is defined as

$$\xi^h(t) = \xi^{h0}\, e^{-\int_{t_0}^{t} \operatorname{tr} \mathbf{d}_p \, dt}, \tag{2.5.1}$$

where $\xi^{h0} = \xi^h(t_0)$. The equivalent rate form expression is achieved by deriving with respect to time:

$$\dot{\xi}^h = -\xi^h \operatorname{tr} \mathbf{d}_p. \tag{2.5.2}$$

Definitions (2.5.1) and (2.5.2) are valid only in this particular case of a compressive stress state always at yield. Later on, once the rule governing the plastic flow is addressed, a general rate form definition of ξ^h will be provided.

Resemblance between ξ^h and the *relative density* becomes readily apparent by expressing the equation for conservation of mass:

$$\rho(\mathbf{X}, t) = \frac{\rho_0(\mathbf{X})}{J(\mathbf{X}, t)}, \tag{2.5.3}$$

where ρ and ρ_0 stands for the current and initial density, respectively and $J = \det \mathbf{F}$ is the Jacobian determinant, in rate form. Using the chain rule, derivation with respect to time of the above equation leads to

$$\frac{\partial \rho}{\partial t} = \rho_0 \frac{\partial J^{-1}}{\partial t} = -\rho \frac{1}{J} \frac{\partial J}{\partial \mathbf{F}} \dot{\mathbf{F}}. \tag{2.5.4}$$

Introducing the expression

$$\frac{\partial J}{\partial \mathbf{F}} = J\mathbf{F}^{-T} \tag{2.5.5}$$

in Eq.(2.5.3) and using the definition (2.2.7) of the velocity gradient, it yields

$$\frac{\partial \rho}{\partial t} = -\rho \mathrm{tr}\, \mathbf{d}. \tag{2.5.6}$$

To get a dimensionless expression, the above equation is divided by the *theoretical density*, denoted by ρ_{th}. Thus,

$$\dot{\eta} = -\eta \mathrm{tr}\, \mathbf{d}, \tag{2.5.7}$$

being $\eta = \rho/\rho_{th}$ the *relative density*. Finally, substitution of the decomposition (2.2.15) of the rate of deformation tensor in Eq.(2.5.7) and the assumption of negligible elastic strains leads to

$$\dot{\eta} = -\eta \mathrm{tr}\, (\mathbf{d}_p + \mathbf{d}_e) \approx -\eta \mathrm{tr}\, (\mathbf{d}_p). \tag{2.5.8}$$

Comparison of the rate form equations Eq.(2.5.8) and Eq.(2.5.2) substantiates the similarity between ξ^h and η in loading histories with a steady accumulation of compressive plastic strains.

2.5.1.2 Softening variables

The specification and discussion of the role played by the other group of internal state variables $\boldsymbol{\xi}^s$ deserve particular attention, since it is one of the novelties of the proposed approach. Indeed, the majority of the continuum modeling efforts in the powder manufacturing field has been devoted to characterize the hardening behavior, leaving unaddressed the other phenomenological facet, softening, at least within a formal thermodynamic framework with internal variables.

Similarly to the hardening variables $\boldsymbol{\xi}^h$, the definition of the softening state variables $\boldsymbol{\xi}^s$ is cast in terms of the plastic strain trajectory, particularly as a function of combined dilatational/shear accumulated plastic strains:

$$\dot{\boldsymbol{\xi}}^s = \dot{\boldsymbol{\xi}}^s(dev\, \mathbf{d}_p, \mathrm{tr}\, \mathbf{d}_p), \quad \text{with} \quad \mathrm{tr}\, \mathbf{d}_p > 0. \tag{2.5.9}$$

However, there is a striking difference between hardening and softening behavior in regards to the experimental recording of such plastic strain trajectories. Strain hardening involves normally an overall manifestation, which means that in a standard compaction test, for example, every point $\mathbf{X} \in \Omega_0$ of the powder is *at yield* during the pressing stage. This fact, in conjunction with negligible die wall friction, ensures a fairly uniform strain pattern during the experiment. Hence, the internal variable ξ^h (which may be thought of as the relative density) is obtained at each time by simply recording *average* density values.

By contrast, experimental tests involving softening, i.e. fracture tests, are characterized by localized yielding, as briefly discussed in section 2.1.2. Consequently, after bifurcation of the response, the plastic strain field cannot be represented by a

single (tensorial) value and average values are meaningless. To monitor the inelastic strain in the localization band, it would be necessary to mount a displacement transducer across this band, which is not possible in practice.

Therefore, in the absence of this experimental measurements, the selection and definition of a particular group of softening internal variables $\boldsymbol{\xi}^s$ must be based on physically plausible assumptions, many of them borrowed from constitutive models of cohesive-frictional materials. In addition, this task is further facilitated by introducing the concept of *yield function*, formulated herein in the spatial Kirchhoff stress space. The evolution of $\boldsymbol{\xi}^s$ can be interpreted in stress space as changes in size, location and shape of the locus of critical points defined by the yield function. It is difficult to picture such geometric transformations without a particular yield locus in mind. Hence, the definition of $\boldsymbol{\xi}^s$ is deferred until later, and attention is focused in the following in the characterization of the proposed yield function.

2.5.2 Yield function

The condition defining the yield locus in the Kirchhoff stress space is expressed as

$$\phi(\boldsymbol{\tau}, \xi^h, \boldsymbol{\xi}^s) = 0, \tag{2.5.10}$$

explicitly indicating the dependence on both ξ^h and $\boldsymbol{\xi}^s$. However, for the reasons outlined above, only the functional form

$$\phi|_{\boldsymbol{\xi}^s=\mathbf{0}} = \phi_h(\boldsymbol{\tau}, \xi^h) \tag{2.5.11}$$

(supposing that $\boldsymbol{\xi}^s(t_0) = \mathbf{0}$), is actually supported by experimental tests. This parametric family of surfaces is taken as the point of departure for defining the form of the yield locus in a general case $\boldsymbol{\xi}^s > 0$. In particular, we assume that the yield locus determined by $\phi(\boldsymbol{\tau}, \xi^h, \boldsymbol{\xi}^s) = 0$, with $\boldsymbol{\xi}^s > 0$, can be obtained as a combination of affine transformations on the yield locus $\phi_h(\boldsymbol{\tau}, \xi^h) = 0$, or portions thereof, the number of independent transformations being limited by the number of internal softening variables n_{is}. For instance, should the yield surface be an ellipse for $\boldsymbol{\xi}^s = 0$ then it will keep this elliptical shape for $\boldsymbol{\xi}^s > 0$, but with a variation of its size (contraction) and location in stress space.

By invoking the isotropy assumption[13], the yield function can be written as a function of the invariants of $\boldsymbol{\tau}$. The formulation in terms of the first invariant (I_1) of the stress tensor and the second invariant (J_2) of its deviatoric part, extensively used in powder compaction modeling, is adopted herein. Particularly, to simplify the algebra, the yield condition is expressed as a function of the mean stress $p = \frac{1}{3} I_1 = \frac{1}{3} \mathrm{tr}\, \boldsymbol{\tau}$, and the norm of the deviatoric part of $\boldsymbol{\tau}$, i.e. $q = \sqrt{2J_2} = \sqrt{dev\, \boldsymbol{\tau} : dev\, \boldsymbol{\tau}}$. The influence of a third invariant is ignored and, consequently, the parametric family of yield loci $\phi(\boldsymbol{\tau}, \xi^h, \boldsymbol{\xi}^s) = 0$ can be fully characterized in the p-q Kirchhoff space.

[13] Experimental and theoretical studies have revealed that small anisotropy is induced at high densities in close die compaction processes [97]. However, we are not concerned in this work with such effects on the plastic response.

The proposed yield surface is determined by three surfaces which intersect non-smoothly. In Fig. 2.7 , the relative position of these three surfaces is depicted for two different states. For moderate levels of densification (Fig. 2.7.a), the elastic domain is bounded by a *Drucker-Prager* envelope and a *elliptical* cap (centered at the origin). This two-surface yield criterion captures some of the essential features of the powder behavior, such as the pressure-sensitive character of the plastic response, and the large contrast between compressive and tensile strength. The equation of the ellipse is given by

$$\phi^e = q^2 + s_2^2 p^2 - s_1^2 s_2^2 = 0, \tag{2.5.12}$$

where s_1 is the major axis and s_2 the eccentricity (see figure 2.7.a). Both quantities are regarded as state functions, hence $s_1 = s_1(\xi^h, \boldsymbol{\xi}^s)$ and $s_2 = s_2(\xi^h, \boldsymbol{\xi}^s)$. The Drucker-Prager surface is a straight line in the p-q plane:

$$\phi^d = q + \alpha p - c = 0, \tag{2.5.13}$$

where $c = c(\xi^h, \boldsymbol{\xi}^s)$, customarily referred to as *cohesion*[14], stands for the intersection with the q-axis , and $\alpha = \alpha(\xi^h, \boldsymbol{\xi}^s)$, termed the *parameter of internal friction*, is the slope (figure 2.7.a). For higher levels of densification, a third surface comes

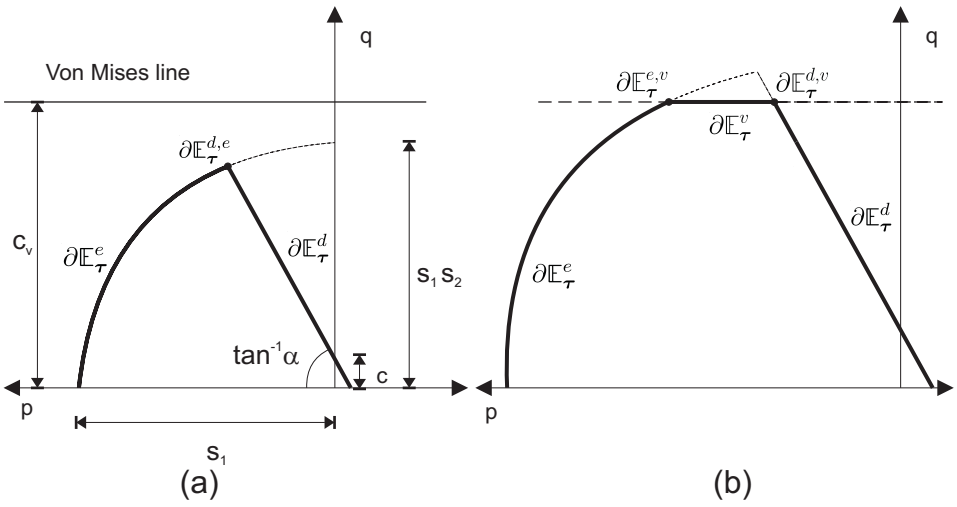

Figure 2.7 *Yield surfaces for two different states. (a) Drucker-Prager + elliptical cap, for moderate level of compaction (b) Drucker-Prager + elliptical cap + Von Mises, for high level of compaction (close to full density)*

into play, as depicted in Fig. 2.7.b. The horizontal line in the (p,q) plane represents a classical pressure-independent Von Mises criterion, whose expression is given by

$$\phi^v = q - c_v = 0. \tag{2.5.14}$$

[14]The state varialbe c is so named because it is reminiscent of the *cohesion* defined in a Mohr-coulomb model rather than because its physical meaning. It can be regarded as the shear strength under zero hydrostatic stress.

This additional surface is introduced to account for the fact that the deviatoric stress measure q cannot exceed the yield strength of the fully dense material (see Coube [26]). In other *cap* models, this restriction is accommodated by recourse to ellipsoidal shaped yield functions which tend to a Von-Mises line when the compact approaches full density [108, 109]. The constitutive parameter c_v (see figure 2.7.b) and the yield strength of the fully dense material, denoted by σ_y, are related by

$$c_v = \sqrt{\frac{2}{3}} J \sigma_y. \tag{2.5.15}$$

As the Drucker-Prager and ellipse parameters, c_v is regarded as a state function, $c_v = c_v(\xi^h, \boldsymbol{\xi}^s)$.

The elastic domain in the stress space is defined formally as

$$\mathbb{E}_{\boldsymbol{\tau}} = \left\{ \boldsymbol{\tau} \mid \phi^\alpha(\boldsymbol{\tau}, \xi^h, \boldsymbol{\xi}^s) \leq 0, \text{ for all } \alpha \in \{e, d, v\} \right\}. \tag{2.5.16}$$

Since our developments are embedded in the contex of rate-independent plasticity, the stress state must remain on the boundary of $\mathbb{E}_{\boldsymbol{\tau}}$, denoted by $\partial\mathbb{E}_{\boldsymbol{\tau}}$, during plastic deformation intervals, the so-called *consistency condition*. The nature of the phenomenological events associated with such plastic deformation is different depending on the location of the stress state on $\partial\mathbb{E}_{\boldsymbol{\tau}}$. The following division of $\mathbb{E}_{\boldsymbol{\tau}}$ is, hence, of considerable assistance in enhancing the understanding of these events. For the case depicted in Fig. 2.7.a, for instance, we have

$$\partial\mathbb{E}_{\boldsymbol{\tau}} = \partial\mathbb{E}^e_{\boldsymbol{\tau}} \cup \partial\mathbb{E}^d_{\boldsymbol{\tau}} \cup \partial\mathbb{E}^{d,e}_{\boldsymbol{\tau}}, \quad \text{with} \quad \partial\mathbb{E}^d_{\boldsymbol{\tau}} \cap \partial\mathbb{E}^e_{\boldsymbol{\tau}} = \emptyset, \tag{2.5.17}$$

where $\partial\mathbb{E}^e_{\boldsymbol{\tau}}$ corresponds to the elliptical cap, $\partial\mathbb{E}^d_{\boldsymbol{\tau}}$ stands for the Drucker-Prager envelope and $\partial\mathbb{E}^{d,e}_{\boldsymbol{\tau}}$ is the intersection of both surfaces. Yielding at $\partial\mathbb{E}^e_{\boldsymbol{\tau}}$ implicates hardening behavior, whilst $\partial\mathbb{E}^d_{\boldsymbol{\tau}}$ is linked to the softening response, hence the denomination of *failure* surface. The nature of the behavior at the *singular* point $\partial\mathbb{E}^{d,e}_{\boldsymbol{\tau}}$ is somewhat less transparent and deserves some scrutiny.

2.5.3 Flow rule

To carry out the analysis further, it is necessary to provide evolution equations for the plastic strains. As is customary in the framework of incremental plasticity theory, the plastic rate of deformation tensor $\mathbf{d}_p$ is presumed to be aligned to the gradient of a certain *plastic potential function*. More precisely, each surface of the elastic boundary is associated to a particular plastic potential function. Thus, if the stress state is located on the yield surface $\alpha \in \{e, d, v\}$, i.e. $\boldsymbol{\tau} \in \partial\mathbb{E}^\alpha_{\boldsymbol{\tau}}$, the plastic rate of deformation tensor is obtained by

$$\mathbf{d}_p = \dot{\lambda}^\alpha \boldsymbol{m}^\alpha = \dot{\lambda}^\alpha \frac{\partial Q^\alpha}{\partial \boldsymbol{\tau}} \quad \text{for} \quad \boldsymbol{\tau} \in \partial\mathbb{E}^\alpha_{\boldsymbol{\tau}}, \tag{2.5.18}$$

where $\boldsymbol{m}^\alpha$ stands for the *plastic flow vector*, $\dot{\lambda}^\alpha$ is a positive scalar factor, referred to as *consistency parameter* or *plastic multiplier* and Q^α is the plastic potential function associated to $\partial\mathbb{E}^\alpha_{\boldsymbol{\tau}}$. The *flow rule* (2.5.18), so named because it resembles

the constitutive equation of a viscous fluid, does not hold for the situation $\boldsymbol{\tau} \in \partial\mathbb{E}^{\alpha,\beta}_{\boldsymbol{\tau}}$, $\alpha, \beta \in \{e, d, v\}$, that is, if the stress state is on the interception of two yield surfaces. The gradient at this singular point is not unique, and (2.5.18) is conveniently replaced by

$$\mathbf{d}_p = \sum_{\gamma\in\{\alpha,\beta\}} \dot{\lambda}^{\gamma} \boldsymbol{m}^{\gamma}, \quad \text{for} \quad \boldsymbol{\tau} \in \partial\mathbb{E}^{\alpha,\beta}_{\boldsymbol{\tau}}, \tag{2.5.19}$$

an expression which goes by the name of *Koiter's rule*. The consistency parameters obey the standard *Karush-Kuhn-Tucker* loading/unloading conditions [92]:

$$\dot{\lambda}^{\alpha} \geq 0, \quad \phi^{\alpha}(\boldsymbol{\tau}, \xi^h, \boldsymbol{\xi}^s) \leq 0, \tag{2.5.20}$$

and

$$\dot{\lambda}^{\alpha}\phi^{\alpha}(\boldsymbol{\tau}, \xi^h, \boldsymbol{\xi}^s) = 0, \qquad \text{(no sum on } \alpha), \tag{2.5.21}$$

along with the consistency condition:

$$\dot{\lambda}^{\alpha}\dot{\phi}^{\alpha}(\boldsymbol{\tau}, \xi^h, \boldsymbol{\xi}^s) = 0, \qquad \text{(no sum on } \alpha). \tag{2.5.22}$$

2.5.3.1 Elliptical cap ($\partial\mathbb{E}^{e}_{\boldsymbol{\tau}}$)

The assumption of *associated* flow rule on the elliptical surface has proved to be reasonably accurate for modeling most pressing processes [22]. This assumption postulates that the functional forms of the yield locus and the plastic potential function coincides. Hence, in view of Eq.(2.5.12), the plastic potential function for $\boldsymbol{\tau} \in \partial\mathbb{E}^{e}_{\boldsymbol{\tau}}$ can be written as

$$Q^e(\boldsymbol{\tau}, \xi^h, \boldsymbol{\xi}^s) = q^2 + s_2^2 p^2. \tag{2.5.23}$$

The plastic flow vector,

$$\boldsymbol{m}^e = \frac{\partial Q^e}{\partial \boldsymbol{\tau}} = 2dev\,\boldsymbol{\tau} + \frac{2}{3}s_2^2 p\,\mathbf{1}, \tag{2.5.24}$$

is thus normal to the cap surface, as displayed in Fig.2.8.a[15]. According to Eq.(2.5.18) and Eq.(2.5.24), $\mathbf{d}_p$ is obtained by

$$\mathbf{d}_p = \dot{\lambda}^e \left(2dev\,\boldsymbol{\tau} + \frac{2}{3}s_2^2 p\mathbf{1}\right), \quad \text{for} \quad \boldsymbol{\tau} \in \partial\mathbb{E}^{e}_{\boldsymbol{\tau}}. \tag{2.5.25}$$

Experimental data for calibrating the yield surface parameters s_1, s_2, c, α and c_v, which will be presented later, show that the elliptical cap lies in the second

[15] For illustration purposes, $\boldsymbol{m}^e$ is plotted in the p-q plane *perpendicular* to the cap surface. But one has to bear in mind that the condition of normality is defined in the 6D Kirchhoff stress space, by virtue of Eq.(2.5.24), which means that $\mathbf{d}_p$ is a vector in the 6D stress space perpendicular to the surface $Q^e = K$, with K constant. However, the projection onto the p-q plane of such entities does not inherit this normality condition, since the p-q stress space is not *isomorphic* to 6D tensor stress space [98], and therefore the actual angle subtended by $\boldsymbol{m}^e$ and $Q^e = K$ in the p-q plane is not right.

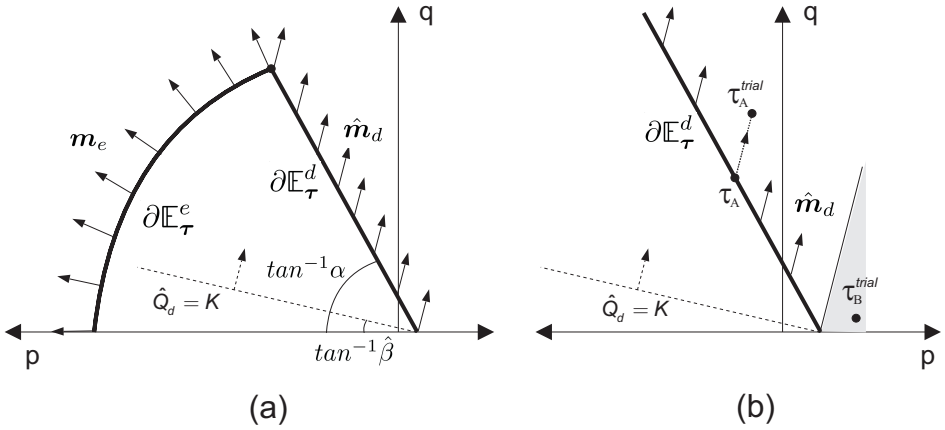

Figure 2.8 *Direction of the plastic flow. (a) Associated flow (ellipse) + linear plastic potential function (b) Singularity at the vertex.*

quadrant of the p-q plane ($p < 0$) for the whole range, supported by experiments, of such parameters. Stated otherwise,

$$\boldsymbol{\tau} \in \partial\mathbb{E}^e_{\boldsymbol{\tau}} \Rightarrow p < 0. \tag{2.5.26}$$

A useful result can be extracted from this condition. Taking the trace of both sides of Eq.(2.5.25), it yields

$$\mathrm{tr}\,\mathbf{d}_p = \dot{\lambda}^e 2 s_2^2 p \quad \text{for} \quad \boldsymbol{\tau} \in \partial\mathbb{E}^e_{\boldsymbol{\tau}}. \tag{2.5.27}$$

Hence, by virtue of condition (2.5.26) and the positiveness of $\dot{\lambda}^e$, expression (2.5.27) reveals that plastic strain increments are compressive ($\mathrm{tr}\,\mathbf{d}_p < 0$) whenever yielding occurs in the stress range determined by the elliptic surface. Furthermore, it follows from the above condition and from Eq.(2.5.2) that the *general expression for the evolution of the hardening variable* ξ^h takes the form

$$\dot{\xi}^h = -\xi^h \dot{\lambda}^e 2 s_2^2 p. \tag{2.5.28}$$

Thus, stress states on $\partial\mathbb{E}^e_{\boldsymbol{\tau}}$ are unequivocally correlated with hardening behavior, being precluded the occurrence of a different phenomenological trend.

2.5.3.2 Drucker-Prager yield surface ($\partial\mathbb{E}^d_{\boldsymbol{\tau}}$)

Whereas the hypothesis of associated flow rule is generally accepted, and almost tacitly invoked, in the case of the elliptical cap $\partial\mathbb{E}^e_{\boldsymbol{\tau}}$, the direction of $\mathbf{d}_p$ when the stress point lies on the Drucker-Prager envelope $\partial\mathbb{E}^d_{\boldsymbol{\tau}}$ is plagued by much controversy. Some authors simply extend the validity of the associative assumption and consider that $\mathbf{d}_p$ is normal to the failure line [20, 90, 33]. However, this hypothesis is clearly at odds with reality (it over-predicts the dilatational response), as experimental studies carried out by Pavier [83] and Sinka [94] evidence. These studies

reveal that the direction of $\mathbf{d}_p$ is only adequately described by the normality condition in the cap portion $\partial\mathbb{E}^e_{\boldsymbol{\tau}}$. As the stress state approaches the interception with the Drucker-Prager envelope, the plastic strain increment becomes steeper. Eventually, at the interception point $\partial\mathbb{E}^{e,d}_{\boldsymbol{\tau}}$, $\mathbf{d}_p$ turns vertical and the nature of the plastic flow ceases to be compressive. Furthermore, according to Pavier [83], $\mathbf{d}_p$ maintains this vertical orientation in the Drucker-Prager stress range, or, in other words, the material flows at *constant volume* when yielding occurs on the Drucker-Prager surface $\partial\mathbb{E}^d_{\boldsymbol{\tau}}$, being precluded the occurrence of dilatation. Motivated by these observations, some authors have favored the assumption of *isochoric* ($\operatorname{tr}\mathbf{d}_p = 0$) plastic flow on the failure surface [17, 109].

Apart from the above mentioned studies, the characterization of the plastic flow in the failure region does not feature in the literature on powder compaction modeling, whereby recourse is to be made to models developed for other granular material, such as soils, to further guide our analysis in this respect. Frictional effects in a granular material are manifested by volumetric dilatancy, especially in the low confinement regime [105]. Therefore, it is plausible to expect also a similar behavior, in some extent, in the powder. To accommodate this dilatancy in the flow rule, when using the Drucker-Prager yield criterion (2.5.13), the most common plastic potential function employed is formulated as

$$\hat{Q}^d = q + \hat{\beta}p, \tag{2.5.29}$$

and the corresponding flow vector is given by

$$\hat{\boldsymbol{m}}_d = \frac{\partial\hat{Q}^d}{\partial\boldsymbol{\tau}} = \frac{dev\,\boldsymbol{\tau}}{\|dev\,\boldsymbol{\tau}\|} + \frac{1}{3}\hat{\beta}\mathbf{1}. \tag{2.5.30}$$

Note that the equation $\hat{Q}^d = K$, with K constant, also defines a straight line, as the yield criterion (2.5.13), in the p-q plane. The material parameter $\hat{\beta}$, the slope of such line, is often called *dilatancy factor* [60], and it represents the ratio of the volumetric and shear (deviatoric) part of the plastic rate of deformation, i.e.

$$\hat{\beta} = \frac{\operatorname{tr}\mathbf{d}_p}{\|dev\,\mathbf{d}_p\|}. \tag{2.5.31}$$

With a vanishing dilatancy factor ($\hat{\beta} = 0$), the isochoric plastic flow is recovered, and associated plasticity results if $\hat{\beta} = \alpha$.

Nevertheless, it has been long known that, when a backward Euler integration scheme is applied to solve the resulting differential equations, the use of the plastic potential function (2.5.29) gives rise to numerical difficulties. A complete understanding of the reasons behind such difficulties requires some notions of the structure of the integration scheme. Skipping for now the derivation details, which will be addressed in Chapter 3, we can roughly say that the stress update algorithm resulting from this time-integration procedure is based on, first, the computation of a certain elastic predictor or *trial stress*, by assuming elastic behavior throughout a given step. If such trial stress lies outside the elastic domain, that is, if it violates the algorithmic counterpart of Eq.(2.5.20), then the updated stress is obtained by projecting the trial state back to the yield surface (return map). The

return direction depends basically on the direction of the plastic flow vector $\hat{\boldsymbol{m}}_d$, but they do not necessarily coincide. For illustration purposes, however, suppose that the return direction is aligned with $\hat{\boldsymbol{m}}_d$, and furthermore, that the yield surface is fixed. In Fig. 2.8.b, the orientation of $\hat{\boldsymbol{m}}_d$, which is constant, is sketched for a value of the dilatancy factor $\hat{\beta} < \alpha$. The return map would bring a trial stress such as $\boldsymbol{\tau}_A^{tr}$, lying on the left hand side of the Drucker-Prager apex (intersection of $\partial\mathbb{E}_{\boldsymbol{\tau}}^d$ with the abscissa), back to a point $\boldsymbol{\tau}_A \in \partial\mathbb{E}_{\boldsymbol{\tau}}^d$. Difficulties are encountered, however, when the trial state lies in the shaded region on the right hand side of the apex (Fig. 2.8(b)). Clearly, the return direction that would project the trial stress $\boldsymbol{\tau}_B^{tr}$ back to the yield surface (to the apex) is not derived from the potential function (2.5.29). This singularity might seriously affect the rate of convergence of the iterative scheme which accompanies the incremental analysis, and hence the robustness and reliability of the numerical predictions.

Parabolic plastic potential function

It can be readily concluded from the foregoing explanation that the root cause of these difficulties is the non-smoothness of the plastic potential surface defined by (2.5.29) at the apex. The solutions proposed to alleviate this shortcoming are basically of two types. On one hand, one may introduce an additional cap to "round off" the linear potential function at that point [32]. On the other hand, one may resort to a different potential function meeting the requirement of smoothness at the apex [105, 56]. Here the latter approach is adopted. The proposed *parabolic* plastic potential function, expressed as

$$Q^d(\boldsymbol{\tau}, \xi^h, \boldsymbol{\xi}^s) = q^2 + \beta(\xi^h, \boldsymbol{\xi}^s)\, p, \tag{2.5.32}$$

with $\beta > 0$, is adequate to this end, since the corresponding flow vector:

$$\boldsymbol{m}^d = \frac{\partial Q^d}{\partial \boldsymbol{\tau}} = 2\, dev\, \boldsymbol{\tau} + \frac{1}{3}\beta \mathbf{1}, \tag{2.5.33}$$

is horizontal, in the p-q plane, at the apex ($q = 0$), and, consequently, the normals to the potential surface cover all possible return directions.

The equation $Q^d = K$, with K constant, defines a parabola in the p-q plane, hence the name of *parabolic* potential. The use of parabolic plastic potential functions can be traced back to the work of Willam et al.[34], and it is frequently utilized for the characterization of failure mechanisms for cohesive frictional materials [38]. However, there is a fundamental difference between these constitutive models and the one presented here. Willam's model is a parabolic extension of both the yield criterion and the potential function, i.e., both the yield and the potential functions are parabolic-shaped. The essence of our approach, by contrast, is to introduce a parabolic potential function, but maintaining the classical (linear) Drucker-Prager yield criterion (see Fig. 2.9). In this way, the singularity at the vertex is circumvented and, at the same time, the simplicity and the computational convenience of using a linear yield criterion is retained. It should be remarked that claims with regard to the necessity of "rounding off" the Drucker Prager yield surface at the apex for avoiding the singularity are unfounded, and might be ascribed to an over-exposure to associated plasticity.

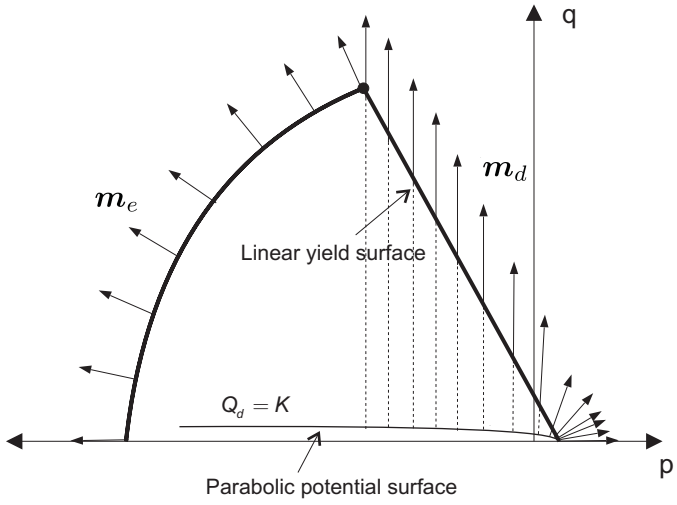

Figure 2.9 *Parabolic plastic potential surface, for γ close to zero.*

Thermodynamic consistency

With such an approach, which appears to be a truly novel element of the present development, one is faced with the unexplored task of determining a functional form for the state function $\beta = \beta(\xi^h, \boldsymbol{\xi}^s)$. In order to avoid thermodynamically unreasonable results, the functional form of β must be consistent with the dissipation inequality (2.3.7), which, for the case in which only the Drucker-Prager yield surface is active ($\dot{\xi}^h = 0$), reduces to

$$\mathcal{D} = \boldsymbol{\tau} : \mathbf{d}_p - \dot{\psi}_s = \boldsymbol{\tau} : \mathbf{d}_p - \frac{\partial \psi_p}{\partial \boldsymbol{\xi}^s} \dot{\boldsymbol{\xi}}^s \geq 0. \tag{2.5.34}$$

As outlined in section (2.3), the term $\dot{\psi}_s$ is associated with a release of energy, i.e. $\dot{\psi}_s \leq 0$. Hence, the worst conceivable circumstances for the satisfaction of inequality (2.5.34) correspond to the case $\dot{\psi}_s = 0$. A sufficient condition for ensuring the positiveness of $\mathcal{D}$ is therefore

$$\boldsymbol{\tau} : \mathbf{d}_p \geq 0. \tag{2.5.35}$$

According to Eq.(2.5.18) and Eq.(2.5.33), the plastic rate of deformation tensor takes the form

$$\mathbf{d}_p = \dot{\lambda}^d (2\, dev\, \boldsymbol{\tau} + \frac{1}{3}\beta \mathbf{1}), \quad \text{for} \quad \boldsymbol{\tau} \in \partial \mathbb{E}^d_{\boldsymbol{\tau}}. \tag{2.5.36}$$

with $\dot{\lambda}^d \geq 0$. Substitution of (2.5.36) in (2.5.35) leads to:

$$\boldsymbol{\tau} : \mathbf{d}_p = \dot{\lambda}^d \left(2 dev\, \boldsymbol{\tau} : \boldsymbol{\tau} + \frac{1}{3}\beta \mathbf{1} : \boldsymbol{\tau} \right) = \dot{\lambda}^d \left(2q^2 + \beta p \right) \geq 0. \tag{2.5.37}$$

The bracketed term of Eq.(2.5.37) is expressible as a polynomial in q by enforcing the yield condition (2.5.13):

$$\boldsymbol{\tau} : \mathbf{d}_p = \dot{\lambda}^d \left(2q^2 - \frac{\beta}{\alpha} q + \frac{\beta}{\alpha} c \right). \tag{2.5.38}$$

It is straightforward to show that the above inequality is fullfiled for all $q \geq 0$ provided that

$$\left(\frac{\beta}{\alpha} \right)^2 - 8 \frac{c\beta}{\alpha} \leq 0 \quad \Rightarrow \quad \beta \leq 8c\alpha. \tag{2.5.39}$$

It follows from the above condition, hence, that a logical choice for the functional form of β is

$$\beta = \gamma \, c \, \alpha, \quad \text{with} \quad 0 \leq \gamma \leq 8. \tag{2.5.40}$$

The material parameter γ controls the plastic dilatancy, and it is considered constant over the whole stress range. In order to reproduce the behavior described by Pavier [83], γ is set to values close to zero, so that the the plastic flow is practically isochoric in the whole range of stresses, except in a small neighborhood at the apex, wherein the flow vector rotates until becoming purely dilatational for $q = 0$ (see Fig. 2.9).

2.5.3.3 Von Mises surface ($\partial \mathbb{E}^d_{\boldsymbol{\tau}}$)

The Von Mises yield surface represents a theoretical threshold in stress space beyond which inelastic volumetric deformation ceases and only deviatoric flow can occur. In this aspect, the behavior of the powder at this stress range parallels that of the fully dense material. The direction of plastic flow is obtained, thus, from the following potential function:

$$Q^v(\boldsymbol{\tau}) = q^2. \tag{2.5.41}$$

The plastic flow vector is, hence, purely deviatoric:

$$\boldsymbol{m}^v = \frac{\partial Q^v}{\partial \boldsymbol{\tau}} = 2 dev \, \boldsymbol{\tau}. \tag{2.5.42}$$

Note that the definition (2.5.2) of internal hardening variable indicates that hardening is precluded when yielding takes place at $\partial \mathbb{E}^v_{\boldsymbol{\tau}}$:

$$\dot{\xi}^h = -\xi^h \mathrm{tr} \, \mathbf{d}_p = 0. \tag{2.5.43}$$

2.5.4 Hardening laws

Using the standard chain rule for the partial derivatives of a function of several variables, we can write

$$\dot{s}_1 = \overbrace{\frac{\partial s_1}{\partial \xi^h} \dot{\xi}^h}^{\dot{s}_{1\mathrm{h}}} + \overbrace{\frac{\partial s_1}{\partial \boldsymbol{\xi}^s} \dot{\boldsymbol{\xi}}^s}^{\dot{s}_{1\mathrm{s}}} = \dot{s}_{1\mathrm{h}} + \dot{s}_{1\mathrm{s}} \, . \tag{2.5.44}$$

The same holds for the other state variables:

$$\dot{s}_2 = \frac{\partial s_2}{\partial \xi^h}\dot{\xi}^h + \frac{\partial s_2}{\partial \boldsymbol{\xi}^s}\dot{\boldsymbol{\xi}}^s = \dot{s}_{2\mathrm{h}} + \dot{s}_{2\mathrm{s}}\,, \tag{2.5.45}$$

$$\dot{c} = \frac{\partial c}{\partial \xi^h}\dot{\xi}^h + \frac{\partial c}{\partial \boldsymbol{\xi}^s}\dot{\boldsymbol{\xi}}^s = \dot{c}_h + \dot{c}_s\,, \tag{2.5.46}$$

$$\dot{\alpha} = \frac{\partial \alpha}{\partial \xi^h}\dot{\xi}^h + \frac{\partial \alpha}{\partial \boldsymbol{\xi}^s}\dot{\boldsymbol{\xi}}^s = \dot{\alpha}_{\mathrm{h}} + \dot{\alpha}_{\mathrm{s}}\,, \tag{2.5.47}$$

$$\dot{c}_v = \frac{\partial c_v}{\partial \xi^h}\dot{\xi}^h + \frac{\partial c_v}{\partial \boldsymbol{\xi}^s}\dot{\boldsymbol{\xi}}^s = \dot{c}_{vh} + \dot{c}_{vs} \tag{2.5.48}$$

Here the subscripts h and s denote *hardening* and *softening* respectively. This decomposition is particularly appealing since it permits a separate description of both phenomena. Relationships between the hardening counterparts of each state variable, i.e. c_{h}, and the internal hardening variable are called *hardening laws*, $\dot{c}_h = \dot{c}(\boldsymbol{\xi}^h)_{\boldsymbol{\xi}^s=cte}$. Conversely, *softening laws* are relations of the type $\dot{c}_s = \dot{c}(\boldsymbol{\xi}^s)_{\xi^h=cte}$, i.e. relating the softening counterpart of the state variables and the internal softening variables. Attention is restricted in this section to describe the former group of relationships, the hardening laws. Dependence of the elastic parameters on ξ^h is also addressed herein.

2.5.4.1 Elliptical surface parameters ($s_{1\mathbf{h}}$, $s_{2\mathbf{h}}$)

Major axis (s_{1h})

In Section B.1 of Appendix B, some useful expressions are drawn from an approximated (ignoring elastic effects) analysis of triaxial loading on a cylindrical specimen. According to these expressions, the functional form of $s_{1\mathrm{h}}(\xi^h)$ can be obtained by monitoring the pressure required for achieving different levels of density[16] when a specimen is compacted isostatically, or, in other words, it corresponds to the *hydrostatic yield stress in compression*. For iron-based powders, the expression of $s_{1\mathrm{h}}$ is found to be given by [83]:

$$s_{1\mathrm{h}} = Js_{1\mathrm{h}}^{cy} = \frac{\rho_0}{\rho} A_{s_1} \left(ln\left(\frac{1-\eta_{app}}{1-\xi^h} \right) \right)^{\frac{1}{N_{s_1}}}. \tag{2.5.49}$$

The parameters A_{s_1} and N_{s_1} are empirically adjusted for each alloy composition. The *relative apparent density* η_{app} is defined as

$$\eta_{app} = \frac{\rho_{app}}{\rho_{th}}, \tag{2.5.50}$$

where ρ_{app} and ρ_{th} are, respectively, the apparent and theoretical density of the powder. Note that $s_{1\mathrm{h}}^{cy}$ denotes the mayor axis of the elliptical yield surface in the

[16] In conformance with definition (2.5.1) of hardening internal variable, density herein refers to the overall density of the specimen measured after being extracted from the mold.

Cauchy stress space. The Jacobian determinant J is introduced to put in correspondence experimental (true) stress data with Kirchhoff stress values. For purposes of simplification in the subsequent numerical integration, it proves advantageous to invoke again the assumption of negligible elastic strains and approximate, in expression (2.5.49), the Jacobian determinant as

$$J = \frac{\rho_0}{\rho} = \frac{\rho_0/\rho_{th}}{\rho/\rho_{th}} \approx \frac{\eta_0}{\xi^h}, \tag{2.5.51}$$

where

$$\eta_0 = \frac{\rho_0}{\rho_{th}}. \tag{2.5.52}$$

Approximation (2.5.51) permits to cast $s_{1\mathrm{h}}$ solely in terms of the internal hardening variable ξ^h:

$$s_{1\mathrm{h}}(\xi^h) = \frac{\eta_0}{\xi^h} A_{s_1} \left(ln \left(\frac{1-\eta_{app}}{1-\xi^h} \right) \right)^{\frac{1}{N_{s_1}}}. \tag{2.5.53}$$

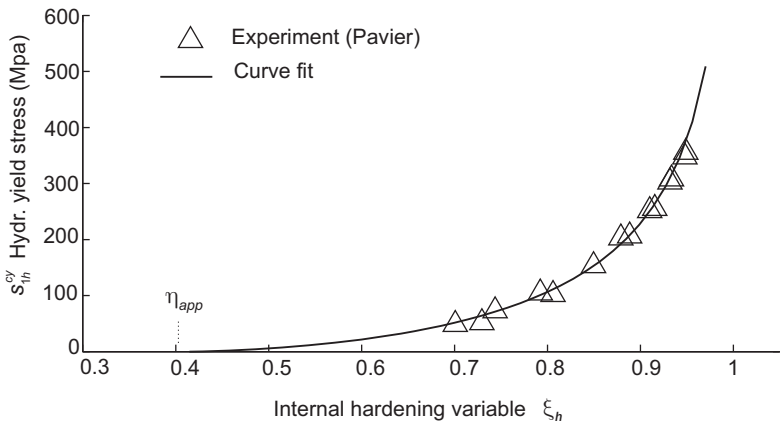

Figure 2.10 *Hydrostatic yield stress in compression $s^{cy}_{1_h}$ versus internal hardening variable ξ^h. Stress data represented in Cauchy (true) stress space. Experimental data from isostatic compression tests carried out by Pavier [83] on Distaloy AE powder specimens.*

In figure 2.10, values of $s^{cy}_{1\mathrm{h}}$, obtained in hydrostatic compression tests carried out by Pavier [83], are plotted versus ξ^h for an iron base powder (Distaloy AE) with parameters $\rho_0 = 3.04 g/cm^3$ and $\rho_{th} = 7.33 g/cm^3$. Fitting Eq.(2.5.49) to these experimental data we have $A_{s_1} = 95.4439 MPa$ and $N_{s_1} = 0.6506$. The curve fit bears close similarity to a typical compressibility curve (see figure 2.1.c), strictly its inverse, with a steadily increasing slope, in such a way that the hydrostatic yield strength asymptotes to infinity when ξ^h approaches unity.

Eccentricity (s_{2h})

The state variable $s_{2\mathrm{h}}$ is related to the radial to axial stress ratio k_{tr}, also known

as pressure transmission coefficient, through the following expression:

$$s_{2\mathrm{h}}(\xi^h) = \sqrt{\frac{3(1 - k_{tr}(\xi^h))}{1 + 2k_{tr}(\xi^h)}}, \tag{2.5.54}$$

as deduced in Appendix B.1. In figure 2.11, radial to axial stress ratio measures, collected by Sinka [94] on a Distaloy AE powder specimen, are displayed for several relative (inelastic) densities. Two regions can be distinguished in this plot. Experimental data points from approximately $\xi^h = 0.65$ show a clear increasing tendency, whereas data for low relative densities $(0.55 - 0.65)$ are widely scattered. These discrepancies at low densities are attributable to the lack of accuracy in monitoring stress values at this density range on powder materials. Furthermore, experimental information is available only for $\xi^h > 0.55$, hence the behavior for densities close to η_{app} is also uncertain.

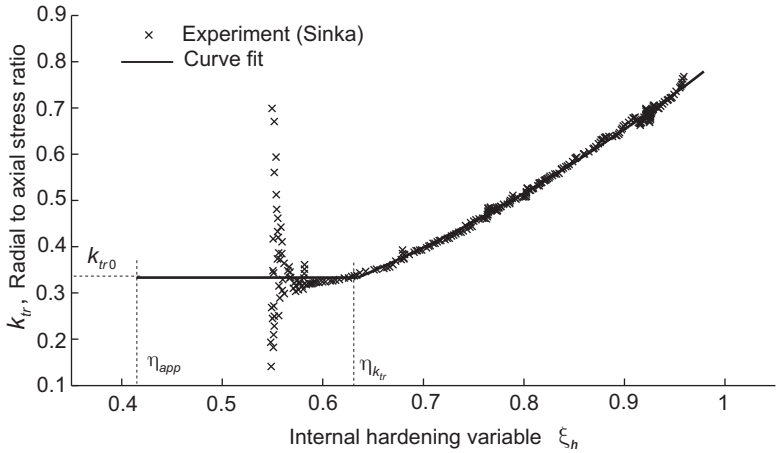

Figure 2.11 *Radial to axial stress ratio versus internal hardening variable ξ^h. Experimental data obtained from simulated closed die compactions conducted by Sinka et al. [94] on Distaloy AE powder specimens.*

In view of this lack of experimental evidence, it proves advantageous to employ predictions of micromechanical models for the early stages of compaction. Those predictions assert that the initial radial to axial stress ratio is $k_{tr0} = 1/3$ [22]. Note that this assertion is at odds with other descriptions found in the literature. Cante et al.[17] claimed that the eccentricity of the elliptical cap approaches zero, or equivalently $k_{tr} \to 1$, at values close to the apparent density. However, this assumption implies that the bulk powder cannot sustain any shear stress or, equivalently, it ascribes a fluid-like behavior to the cohesionless powder, which is not totally realistic.

The following empirical equation is proposed here for the radial to axial stress ratio (see figure 2.11):

$$k_{tr}(\xi^h) = \begin{cases} k_{tr0}, & if\ \xi^h \leq \eta_{k_{tr}}, \\ (\xi^h - \eta_{k_{tr}})(A_{k_{tr}}\xi^h + B_{k_{tr}}) + k_{tr0}, & if\ \xi^h > \eta_{k_{tr}}. \end{cases} \tag{2.5.55}$$

Note that the proposed functional form for k_{tr} acknowledges the abovementioned facet of powder characterization by fixing k_{tr} in a constant value $k_{tr0} = 1/3$ for densities below $\eta_{k_{tr}}$. Calibration of the parameters for this particular Distaloy AE alloy gives $A_{k_{tr}} = 1.074$, $B_{k_{tr}} = 0.242$ and $\eta_{k_{tr}} = 0.635$. In figure 2.12, the curve $s_{2\mathrm{h}} = s_{2\mathrm{h}}(\xi^h)$ obtaining by introducing Eq.(2.5.55) in Eq.(2.5.54) is shown.

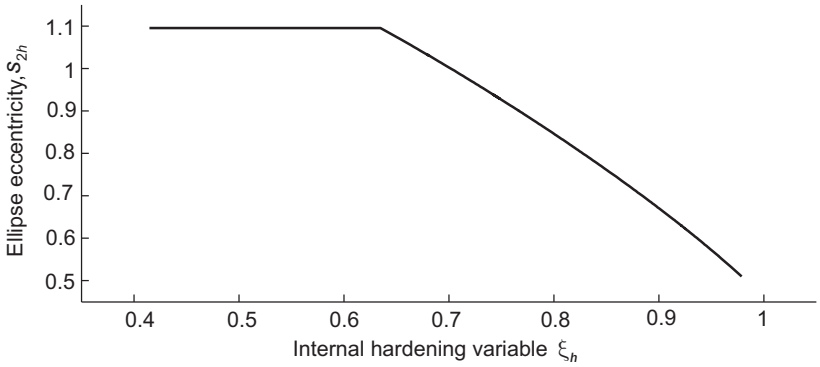

Figure 2.12 *Values of the elliptical cap yield surface eccentricity (s_{2h}), obtained by substituting the fitting equation (2.5.55) for k_{tr} in Eq.(2.5.54), versus the internal hardening variable ξ^h.*

2.5.4.2 Drucker-Prager yield surface parameters (c_{h}, α_{h})

The location of the Drucker-Prager failure line in the $p-q$ plane for several densities is obtained by performing, at least, two sets of fracture tests, namely a uniaxial compression test and and a Brazilian disc or diametral compression test. The failure line is then plotted by connecting fracture stress points corresponding to the same density.

Cohesion (c_h)

Coube [25] followed the above procedure to collect values of cohesion, shown in figure 2.13, and values of the parameter of internal friction α_{h}, displayed in figure 2.14.a, as a function of ξ^h for a Distaloy AE powder. The curve fit for the cohesion is given by the equation[17]

$$c_{\mathrm{h}}(\xi^h) = \sqrt{\frac{2}{3}}\frac{\eta_0}{\xi^h}c_{\mathrm{h}}^{cy} = \sqrt{\frac{2}{3}}\frac{\eta_0}{\xi^h}A_{c_{\mathrm{h}}}e^{B_{c_{\mathrm{h}}}\xi^h}. \tag{2.5.56}$$

[17]Notice that the factor $\sqrt{2/3}$ accounts for the fact that the deviatoric stress $q = \|dev\,\boldsymbol{\tau}\|$ is not a Von Mises effective stress measure.

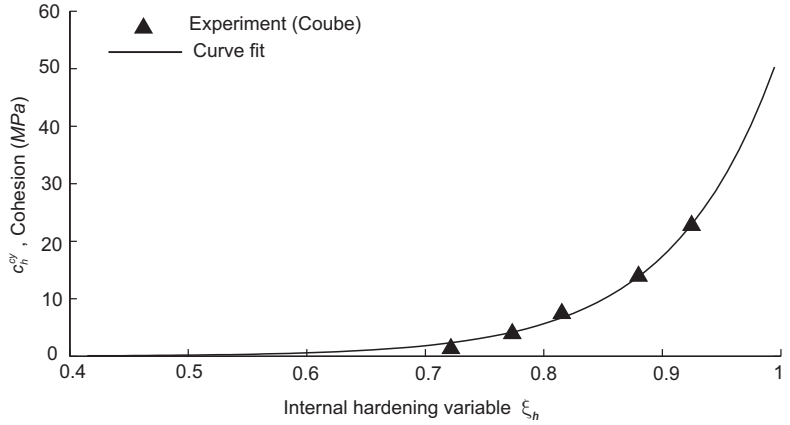

Figure 2.13 *Cohesion, in Cauchy (true) stress space, against internal hardening variables ξ^h. Experimental data obtained by experiments carried out by Coube [25] on Distaloy AE powder specimens.*

Calibration of this equation for the data shown in figure 2.13 yields $A_{c_\mathrm{h}} = 0.001MPa$ and $B_{c_\mathrm{h}} = 11.2368$.

Inspection of the cohesion c_h, which can be regarded as the shear strength under zero hydrostatic stress, and the hydrostatic yield stress in compression $s_{1\mathrm{h}}$ attained at a given value of the relative density, say $\xi^h = 0.9$, indicates that the green compact is notably weaker in tension/shear than in compression, up to a factor $s_{1\mathrm{h}}/c_\mathrm{h} \approx 24$.

Internal friction parameter (α_h)

Two curve fits for the parameter of internal friction $\alpha_\mathrm{h}(\xi^h)$ are shown in figure 2.14.a. From a regression analysis standpoint, the best fit is obviously the linear one. From a physical point of view, however, the values of α_h predicted by this linear fit in the range of low densities ($\xi^h < 0.65$) are meaningless. The reasoning underlying these unsatisfactory predictions is that, in order to ensure a finite value for the yield stress in uniaxial compression, the parameter of internal friction cannot exceed the slope (in absolute value) of the stress path in the $p - q$ plane corresponding to a uniaxial compression test (see figure 2.14.b) [60]. It can be easily deduced that the slope of the uniaxial compression stress path is $-\sqrt{6}$, hence we have the condition

$$\alpha_\mathrm{h} < \sqrt{6}. \tag{2.5.57}$$

For $\xi^h = 0.6$, we can see in figure 2.14.a that the linear fit estimates $\alpha_\mathrm{h} \approx \sqrt{2/3} \cdot 3.05 = 2.49$, which is greater than $\sqrt{6} \approx 2.45$.

Thus, the appropriate fit is a constant one, also shown in figure 2.14.a:

$$\alpha_\mathrm{h} = \alpha_{h0}, \tag{2.5.58}$$

with $\alpha_{h0} = \sqrt{2/3} \cdot 2.81 = 2.29$.

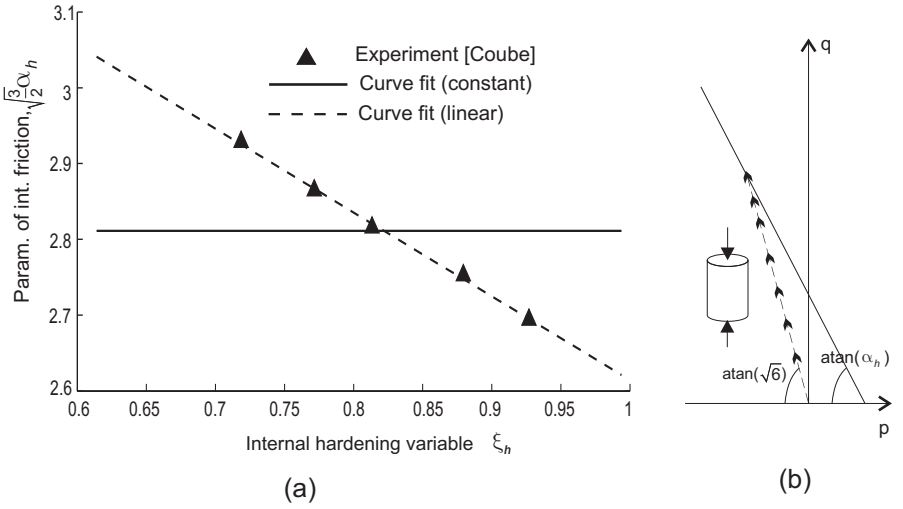

Figure 2.14 *(a) Parameter of internal friction α_h versus internal hardening variable ξ^h. Experimental data obtained by experiments carried out by Coube [25] on Distaloy AE powder specimens. (b) Representation of the stress path corresponding to a uniaxial compression test. The parameter of internal friction α_h cannot exceed the slope of such stress path.*

As in the case of $s_{2\mathrm{h}}$, empirical observations concerning the evolution of α_{h} for the range of low densities are not available, since an unavoidable requirement for undertaking fracture tests is that the specimen must posses some degree of consolidation, so as to be ejected from the die cavity without rupture. It seems more suitable in this regard to undertake flowability tests and other experiments in which the behavior of the powder in its cohesionless state can be characterized. Exploring such subject goes beyond the scope of this work. Hence, the assumption of a constant parameter of internal friction over the whole range of density will be adopted.

2.5.4.3 Von Mises yield surface parameter ($c_{v\mathbf{h}}$)

Experimental isodensity yield stress points in $p-q$ space are presented in figure 2.15. The tests for obtaining such information were conducted by Pavier[83] by subjecting cylindrical powder (Distaloy AE) specimens to different triaxial loading paths (consolidated and over-consolidated compression tests). In figure 2.15.a, isodensity contours are constructed by using an elliptical cap together with a Drucker-Prager failure line. On the other hand, in figure 2.15.b, isodensity contours are modified by introducing an additional horizontal straight line (Von Mises surface).

It is readily seen here that the best fit to the stress data points is provided by the isodensity contours plotted in figure 2.15.b, in which the Von Mises yield surface is considered. The failure line and the hardening cap on their own (see figure 2.15.a) overpredict the yield stress of the material in the vicinity of the their

intersection, to such an extent that the physically unattainable threshold σ_y (the yield strength of the full dense material) is clearly exceeded at a relative density $\eta = 0.982$.

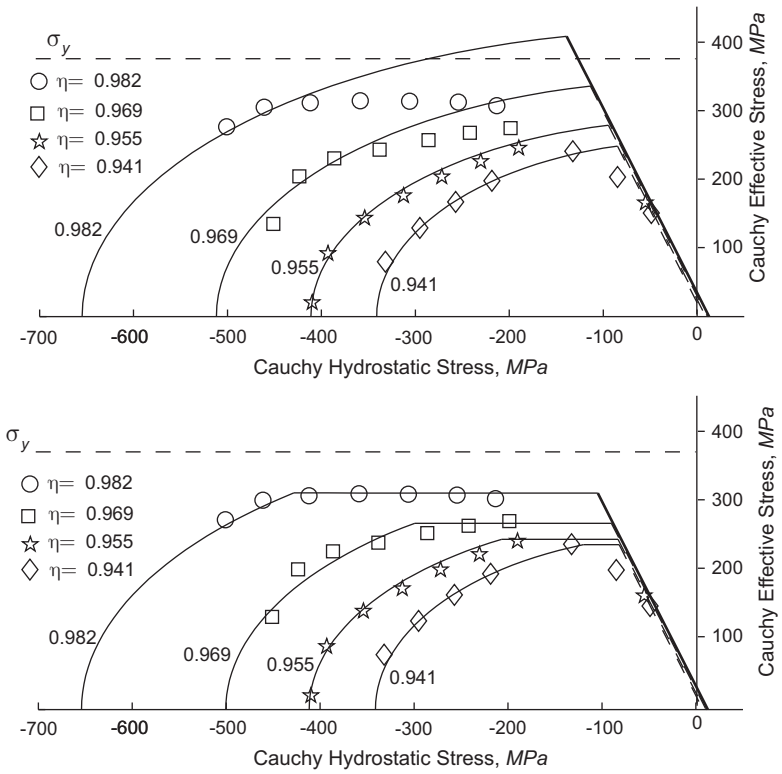

Figure 2.15 *Experimental data from consolidated and over-consolidated compression tests (Pavier [83]) on Distaloy AE powder specimens. Isodensity contours employing (a) Drucker-Prager + Elliptical cap, (b) Drucker-Prager + Elliptical cap + Von-Mises*

The comparison displayed in figure 2.15 conveys the relevance of the role played by the Von-Mises yield surface in the later stages of compaction. To proceed with the calibration of the hardening counterpart of the Von Mises parameter, $c_{v\mathrm{h}}$, we identify, as usual, relative density and hardening internal variable ($\xi^h \approx \eta$), on the basis that the slight difference between them (due to volumetric elastic strain) is of the same order as the measurement error. In figure 2.16.b, the values of $c_{v\mathrm{h}}$ resulting from the fit shown in figure 2.15.b are plotted versus ξ^h . The curve ABC represents the path traced by the deviatoric stress measure q_{int}^{cy} (see figure 2.15.a) at the intersection of the Drucker-Prager and the elliptical cap ($\partial \mathbb{E}_{\boldsymbol{\tau}}^{d,e}$). The curve BD is the quadratic fit to the data points obtained from figure 2.15.b. In order to put the evolution of $c_{v\mathrm{h}}$ in a mathematically suitable form, we assume that the curve $c_{v\mathrm{h}} = c_{v\mathrm{h}}(\xi^h)$ is composed of the branches AB and BD. From the apparent density up to η_{v0}, the Von Mises surface is *reduced* to a point, the

intersection $\partial\mathbb{E}^{d,e}_{\boldsymbol{\tau}}$. In practice, this means that the Von Mises yield surface is not considered for computational purposes for $\xi^h < \eta_{v0}$. It is only for densities above η_{v0} when it actually comes into play. The following empirical correlation reflects these considerations:

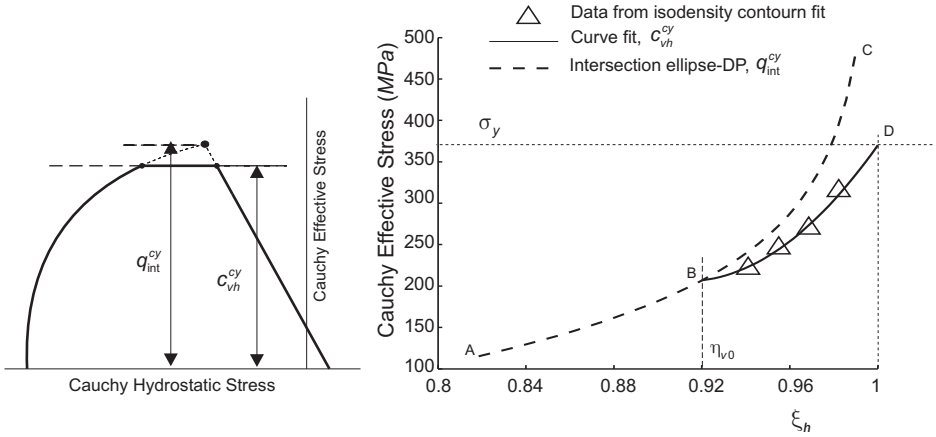

Figure 2.16 *(a) Definition of q^{cy}_{int} as the deviatoric stress measure at the intersection of the Drucker-Prager and the elliptical cap ($\partial\mathbb{E}^{d,e}_{\boldsymbol{\tau}}$. (b) Von Mises parameter c_{vh} vs internal hardening variable ξ^h. The curve AC corresponds to $q^{cy}_{int} = q^{cy}_{int}(\xi^h)$, whereas BD is the quadratic fit to the data points obtained from the isodensity contours shown in 2.15.b.*

$$c_{vh}(\xi^h) = \begin{cases} q_{int} = \sqrt{\dfrac{2}{3}}\dfrac{\eta_0}{\xi^h} q^{cy}_{int}, \quad if\, \xi^h \leq \eta_{v0}, \\ \sqrt{\dfrac{2}{3}}\dfrac{\eta_0}{\xi^h}\sigma_y(1 - A_{c_{vh}}(\xi^h - B_{c_{vh}})(1-\xi^h)), \quad if\, \xi^h > \eta_{v0}. \end{cases} \tag{2.5.59}$$

The fitted parameters for the Distaloy AE powder are $A_{c_{vh}} = 58.160$, $B_{c_{vh}} = 0.8252$, $\sigma_y = 370\, MPa$ and $\eta_{v0} = 0.92$.

The relative merits of employing an additional surface, to enhance the calibration of experimental stress data point, instead of, say, a unique yield function, will become manifest later. Indeed, inspection of Eqs. (2.5.18), (2.5.36) and (2.5.42) reveals that the plastic flow vector on $\partial\mathbb{E}^d_{\boldsymbol{\tau}}$, $\partial\mathbb{E}^e_{\boldsymbol{\tau}}$ and $\partial\mathbb{E}^v_{\boldsymbol{\tau}}$, respectively, is linear in $\boldsymbol{\tau}$, a feature that will offer a remarkable aspect of simplicity in the subsequent numerical integration.

2.5.4.4 Elastic parameters (E^e,ν^e)

As mentioned in section (2.4), the neglect of anisotropy effects renders the elastic response governed only by two parameters, the Young's modulus E^e and the Poisson's ratio ν^e. Experimental measures of the Poisson's ratio show a high variability with density, but without a clear trend [83]. This high variability is due to the difficulty in measuring accurately stresses in the radial direction. Hence, the

hypothesis of constant Poisson's ratio, of a value equal to that of the fully dense material ($\nu^e = 0.29$), is regarded as a reliable approximation.

Experimental data of Young's Modulus as a function of density, provided by Pavier [83], are shown in figure 2.17. The following exponential fit is proposed

$$E^e(\xi^h) = \frac{\eta_0}{\xi^h} E_0 e^{B_E(\xi^h - \eta_0)}, \tag{2.5.60}$$

with $E_0 = 1360.92\ MPa$ and $B_E = 8.82$ for a Distaloy AE[18].

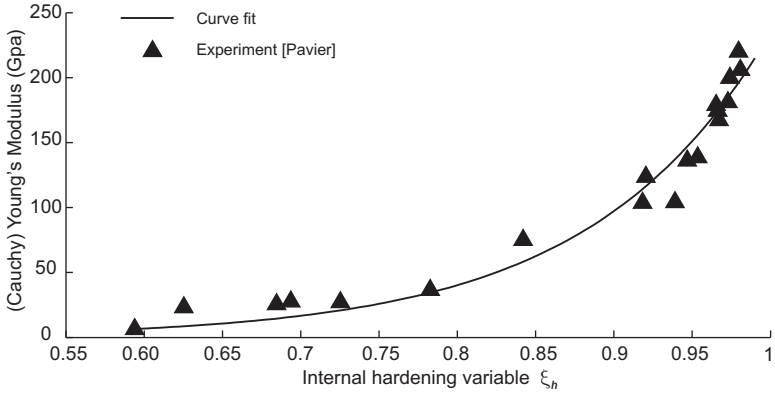

Figure 2.17 *Young's Modulus E^e vs internal hardening variable ξ^h. Experimental data obtained by tests conducted by Pavier [83] on Distaloy AE powder specimens.*

In using the above expression, we should bear in mind that this experimental correlation was obtained in triaxial tests by subjecting a cylindrical specimen to cycles of axial loading and unloading at *different levels of (constant) radial pressure*. Although it was observed that the relation between increments of axial stress and axial strain depends on the level of radial pressure, Pavier [83] suggested that, as a first approximation, this dependence may be disregarded.

On the other hand, by measuring the velocity of sound in the pressing direction on previously compacted Distaloy AE cylindrical specimens, Coube [25] concluded that an estimation for the elastic modulus in a *stress-free situation* is given by the following linear equation

$$E^e(\xi^h) = \frac{\eta_0}{\xi^h}(Y_{E1} + Y_{E2}\xi^h), \tag{2.5.61}$$

where $Y_{E1} = -16383.47\,MPa$ and $Y_{E2} = 39073.95\,MPa$.

In view of the experimental procedures from which Eqs. 2.5.60 and 2.5.61 are drawn, it seems more reasonable to employ Pavier's empirical law 2.5.60 in describing the elastic behavior in *situations of confinement*, whereas, in circumstances closer to unstressed configurations, Coube's relation (Eq.(2.5.61)) seems more adequate. A comparison of the values obtained by evaluating 2.5.60 and 2.5.61 at, say

[18]Note that the elastic free energy function (2.4.1) was defined per unit reference volume, hence the necessity of the (approximated) Jacobian factor η_0/ξ^h.

$\xi^h = 0.9$, reveals that the Young's Modulus predicted by the former is up to five times larger than the one predicted by the latter. Obviously, these two notoriously different estimations can be reconciled by using a unique *non-linear elastic law*, as the one presented in Mosbah [69], in which the elastic secant modulus E^e (the denomination "Young's modulus" would be a misnomer in this case) depends further on the stress state. Such generality, however, would complicate substantially the subsequent numerical integration.

2.5.5 Softening laws

The softening constitutive laws are relationships between the softening counterpart of the state variables defining the size, shape and location of the yield condition, and the as yet unspecified set of internal softening variables $\boldsymbol{\xi}^s$. Each affine transformation of the surfaces defining the yield condition in stress space is associated with a particular physical meaning. On this basis, we shall discern which variables should come into play for achieving a sufficient degree of realism, and, on the other hand, which can be disregarded. Note that the number of relationships that can be considered is constrained by the availability of experimental data to support such relations.

2.5.5.1 Elliptical surface parameters ($s_{1\mathbf{s}}$, $s_{2\mathbf{s}}$)

It will be assumed that the compressive strength of the material remains unaltered in the course of failure events, i.e.:

$$\dot{s}_{1\mathrm{s}} = 0 \quad \rightarrow \quad s_1(\xi^h, \boldsymbol{\xi}^s) = s_1(\xi^h) = s_{1\mathrm{h}}(\xi^h), \tag{2.5.62}$$

$$\dot{s}_{2\mathrm{s}} = 0 \quad \rightarrow \quad s_2(\xi^h, \boldsymbol{\xi}^s) = s_2(\xi^h) = s_{2\mathrm{h}}(\xi^h). \tag{2.5.63}$$

Hence, *the shape and size of the elliptical cap are completely determined by the internal hardening variable* ξ^h. At first sight, this hypothesis may appear too stringent from a physical standpoint. However, from a practical point of view, for replicating the behavior of interest insofar as determination of cracks is concerned, it suffices to account for the decay of mechanical strength in the tensile/shear regime, since the compact is more prone to failure in the pressure release and ejection stages, when these conditions prevail. Furthermore, the benefits arising in the subsequent numerical integration of the constitutive equation, due to the simplicity afforded by this assumption, outweighs any slight lack of accuracy that might result.

2.5.5.2 Von-Mises yield surface parameter (c_{vs})

The Von Mises yield surface only plays an active role under circumstances of high degree of confinement. Upon pressure release, the stress state at every point of the compact moves away from the cap and the Von Mises yield surfaces to the tensile/shear region. It seems reasonable, therefore, to disregard also the influence, as far as failure analysis is concerned, of the Von Mises yield surface. This implies to extend the hypothesis made above for the state variables s_1 and s_2, and assume that

$$\dot{c}_{vs} = 0 \quad \rightarrow \quad c_v(\xi^h, \boldsymbol{\xi}^s) = c_v(\xi^h) = c_{v\mathrm{h}}(\xi^h). \tag{2.5.64}$$

i.e. *the Von Mises parameter c_v is insensitive to changes of the softening internal variable $\boldsymbol{\xi}^s$.*

We must note emphatically that a general constitutive softening law $\dot{c}_{vs} = \dot{c}_{vs}(\boldsymbol{\xi}^s)$ can be accommodated in the formulation without any conceptual difference. The guidelines would be the same as the ones that we shall describe in the ensuing discussion (Drucker-Prager yield surface parameters). The only substantial change would arise in the numerical integration, since the integration of any constitutive law involving softening poses a great mathematical challenge, as it will be discussed in Chapter 3. Besides, any constitutive relation must be substainted by the corresponding experimental tests, and empiric observations, concerning fracture energy measurements, in tests in which the stress path involves yielding on the Von Mises surface are not available at present.

2.5.5.3 Drucker-Prager yield surface parameters (c_s, α_s)

We focus now on the details concerning the evolution of the Drucker-Prager failure envelope in stress space when softening takes place. This surface bounds the tensile and shear, for low degree of confinement, regions, hence a decrease of mechanical strength is reflected by a motion towards the origin of the Drucker-Prager yield surface in the p-q plane. We shall assume that the uniaxial tensile strength, which is related to the Drucker-Prager parameters through the expression

$$\sigma_t = \sqrt{\frac{3}{2}} \frac{\sqrt{6} c}{\sqrt{6} + \alpha}, \tag{2.5.65}$$

(see figure 2.18) decays at the same rate as the cohesion c. It follows from Eq.(2.5.65), and considering relation (2.5.58), that this assumption is tantamount to assert the constancy of α. Therefore, the parameter of internal friction α is independent of both ξ^h and $\boldsymbol{\xi}^s$ and α *can be regarded as a material constant* , i.e.

$$\dot{\alpha}_\mathrm{s} = 0 \quad \rightarrow \quad \alpha = \alpha_{h0}. \tag{2.5.66}$$

Therefore, in view of Eqs. (2.5.62), (2.5.63), (2.5.64) and (2.5.66), the task of establishing the set of softening laws is reduced to find the relationship $c_s = c_s(\boldsymbol{\xi}^s)$. To take developments a step forward, we have first to specify the set of internal softening variables. As it was pointed out in Eq.(2.5.9), the assumption of *strain softening* is adopted, which means that the amount of softening depends only on the length of the trajectory in the plastic strain space but *not* on the strain path itself [53], i.e.:

$$\xi_1^s = \int_{t_0}^{t} \| dev\, \mathbf{d}_p \|\, dt, \quad \text{for} \quad \boldsymbol{\tau} \in \partial \mathbb{E}_{\boldsymbol{\tau}}^{d} \cup \partial \mathbb{E}_{\boldsymbol{\tau}}^{d,e} \cup \partial \mathbb{E}_{\boldsymbol{\tau}}^{d,p}, \tag{2.5.67}$$

$$\xi_2^s = \int_{t_0}^{t} \mathrm{tr}\, \mathbf{d}_p\, dt, \quad \text{for} \quad \boldsymbol{\tau} \in \partial \mathbb{E}_{\boldsymbol{\tau}}^{d} \cup \partial \mathbb{E}_{\boldsymbol{\tau}}^{d,e} \cup \partial \mathbb{E}_{\boldsymbol{\tau}}^{d,p}, \tag{2.5.68}$$

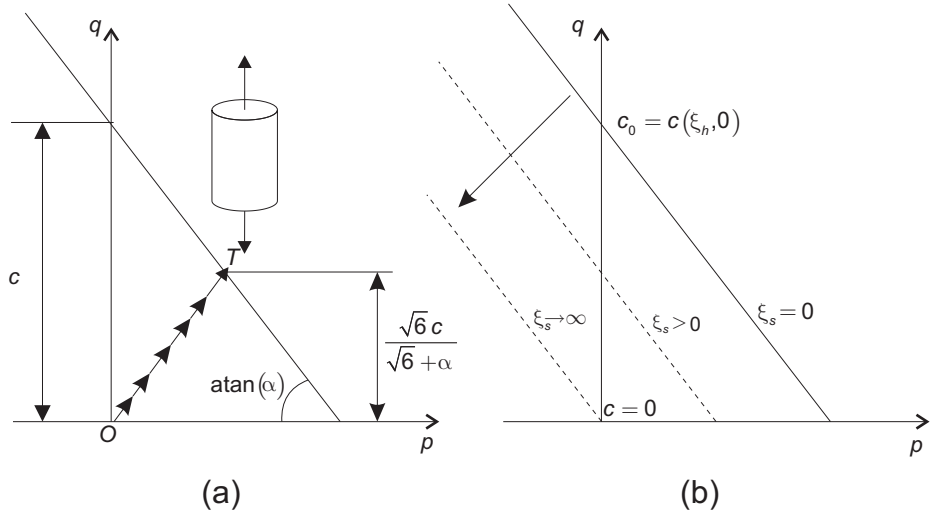

Figure 2.18 *(a) Tensile region in the p-q plane. Path OT represents the (elastic) stress trajectory in a uniaxial tensile test (b) Decrease of cohesion due to the accumulation of plastic shear strain*

or in rate form:

$$\dot{\xi}_1^s = \|dev\,\mathbf{d}_p\|, \quad \text{for} \quad \boldsymbol{\tau} \in \partial\mathbb{E}_{\boldsymbol{\tau}}^d \cup \partial\mathbb{E}_{\boldsymbol{\tau}}^{d,e} \cup \partial\mathbb{E}_{\boldsymbol{\tau}}^{d,p}, \tag{2.5.69}$$

$$\dot{\xi}_2^s = \operatorname{tr}\mathbf{d}_p, \quad \text{for} \quad \boldsymbol{\tau} \in \partial\mathbb{E}_{\boldsymbol{\tau}}^d \cup \partial\mathbb{E}_{\boldsymbol{\tau}}^{d,e} \cup \partial\mathbb{E}_{\boldsymbol{\tau}}^{d,p}. \tag{2.5.70}$$

Note that in Eqs. (2.5.67) to (2.5.70), it is explicitly remarked that ξ_1^s and ξ_2^s only evolve during intervals of plastic loading in which the stress state remains on the Drucker-Prager failure line. Therefore, the rate form definitions (2.5.69) and (2.5.70) can be rephrased in terms of the plastic flow vector on $\partial\mathbb{E}_{\boldsymbol{\tau}}^d$:

$$\dot{\xi}_1^s = \|dev\,\mathbf{d}_p\| = 2\dot{\lambda}^d q, \tag{2.5.71}$$

$$\dot{\xi}_2^s = \operatorname{tr}\mathbf{d}_p = \dot{\lambda}^d \gamma\alpha c. \tag{2.5.72}$$

In Eq.(2.5.46), it was assumed the additive decomposition of the cohesion rate, $\dot{c} = \dot{c}_h + \dot{c}_s$. The usefulness of this decomposition will become apparent in the numerical integration. A close inspection of the definitions of ξ^h, ξ_1^s and ξ_2^s reveals that the simultaneous occurrence of both hardening and softening is only possible when the stress state lies on the intersection $\partial\mathbb{E}_{\boldsymbol{\tau}}^{d,e}$ of the elliptical cap and Drucker-Prager line, where precisely more numerical difficulties are encountered[19]. However,

[19] In the subsequent numerical integration, the coupling between hardening and softening when the stress state is located at the intersection point $\partial\mathbb{E}_{\boldsymbol{\tau}}^{d,e}$ will be eliminated by modifying the evolution equation for ξ_1^s, that will take the form $\dot{\xi}_1^s = (1 - \mathcal{H}(\dot{\lambda}^e))(2\dot{\lambda}^d q)$, where $\mathcal{H}(\bullet)$ denotes the Heaviside function. Hence, it will be assumed that the occurrence of softening is precluded at $\partial\mathbb{E}_{\boldsymbol{\tau}}^{d,e}$.

for the sake of clarity, we preclude this possibility from our current analysis and presume that yielding takes place only at $\partial\mathbb{E}^d_{\boldsymbol{\tau}}$. Therefore, we can legitimately write

$$\dot{c} = \dot{c}_s, \quad \rightarrow \quad c(t) = c_0 + \int_{t_{is}}^{t} \dot{c}_s dt. \tag{2.5.73}$$

where t_{is} denotes the time at which yielding at $\partial\mathbb{E}^d_{\boldsymbol{\tau}}$ is initiated and c_0 is the cohesion at this time:

$$c_0 = c(\xi^h(t_{is}), \xi^s_{10}, \xi^s_{20}). \tag{2.5.74}$$

Observe that the *initial cohesion* c_0 depends on the degree of hardening, characterized by $\xi^h(t_{is})$, achieved in previous compacting processes. If $\xi^s_\beta(t_{is}) = 0, \beta = 1, 2$, the initial cohesion c_0 coincides with the cohesion[20] that one would obtain from the curve of *virgin* material $c_{\rm h}(\xi^h)$.

We are now faced with the task of setting a correlation between c_s and $\boldsymbol{\xi}^s$. Motivated by the exponential structure of the majority of empirical hardening laws seen in the previous section, the following softening law is adopted

$$c_s(\xi^s_1, \xi^s_2) = c_0(e^{\frac{1}{c_0}(H_{01}(\xi^s_1 - \xi^s_{10}) + H_{02}(\xi^s_2 - \xi^s_{20}))} - 1). \tag{2.5.75}$$

Recall that we only have at our disposal experimental fracture energy values, measured in a single test, for calibrating the parameters H_{01} and H_{02}, hereafter referred to as *softening parameters*. Thus, we are confronted with the dilemma of whether to neglect the influence of one of the internal variables or to calibrate one of these parameters, say H_{01}, and consider the other one as a dependent variable $H_{02} = H_{02}(H_{01})$. The dilemma can be resolved if we take into account the relative influence of both internal variables in the material response. Dividing *Eq.*(2.5.72) by *Eq.*(2.5.71), we get

$$\frac{\dot{\xi}^s_2}{\dot{\xi}^s_1} = \gamma \frac{\alpha c}{2q}. \tag{2.5.76}$$

It was set forth in section (2.5.3) that, in order to reproduce the behavior observed experimentally , the dilatancy parameter γ is set to values close to zero. This fact, according to Eq.(2.5.76), brings into prominence the effect of shear plastic strain in the material response, i.e.:

$$\dot{\xi}^s_1 \gg \dot{\xi}^s_2. \tag{2.5.77}$$

Therefore, it will be assumed that $\dot{\xi}^s_2 = 0$, and *the set of internal softening variables is reduced to the single scalar variable* $\xi^s = \xi^s_1$.

However, one has to be aware of the limitations imposed by hypothesis (2.5.77). Its validity hinges on assuming that q is greater, or of the same order, as c. This condition, although seldom, may fail in some circumstances. For instance, in an hypothetical hydrostatic *tensile* test, in which the stress state is such that $q = 0$, variable $\dot{\xi}^s_1$ would not evolve, and hence no failure would be predicted unless the degrading effect of dilatational deformations (ξ^s_2) is acknowledged.

[20] In practice, (see Eq.(3.2.89) in chapter 3), we simply make $c_0 = c_{\rm h}$.

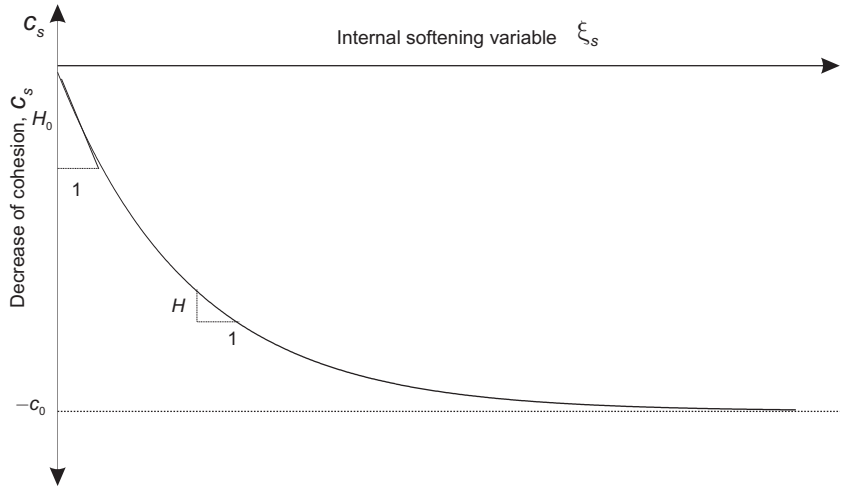

Figure 2.19 *Softening counterpart of the cohesion variable c_s vs internal softening variable ξ^s. The continuum softening modulus H is the tangential slope of this curve. The softening parameter H_0 is the tangential slope for $\xi^s = \xi^{s0}$.*

With only one internal softening variable, the softening law (2.5.75) can be then written as:

$$c_s(t) = c_0(e^{\frac{H_0(\xi^s - \xi^{s0})}{c_0}} - 1). \tag{2.5.78}$$

The remaining softening parameter H_0 is the initial slope of the plot c_s vs ξ^s (see figure 2.19). The tangential slope H at any value of ξ^s, defined by the following rate equation:

$$\dot{c}_s = H\dot{\xi}^s, \tag{2.5.79}$$

is termed the *continuum softening modulus* [76]. By differentiation of Eq.(2.5.78), H can be expressed as:

$$H = H_0\frac{c_0 + c_s}{c_0} = H_0\frac{c}{c_0}. \tag{2.5.80}$$

Calibration of the softening parameter

The procedure to calibrate the softening parameter H_0 was outlined in a simplified manner in section 2.1.2, within a one-dimensional setting. We shall now address this topic more in depth, since it constitutes one of the novelties of our modeling approach. For this purpose, consider the work $\mathsf{g_f}$, per unit reference volume, that has to be expended to decrease the cohesion from a value c_0 to zero:

$$\mathsf{g_f} = \int_{t_{is}}^{t_\infty} \boldsymbol{\tau} : \mathbf{d}\, dt. \tag{2.5.81}$$

where t_{is} denotes the time at which yielding is initiated.

Using the additive decomposition of the rate of deformation tensor (Eq.(2.2.15)), we get

$$\mathsf{g}_{\mathsf{f}} = \int_{t_{is}}^{t_\infty} \boldsymbol{\tau} : \mathbf{d}_e \, dt + \int_{t_{is}}^{t_\infty} \boldsymbol{\tau} : \mathbf{d}_p \, dt. \tag{2.5.82}$$

In virtue of Eq.(2.3.6), the first integral of the right hand side of the above equation takes the form:

$$\int_{t_{is}}^{t_\infty} \boldsymbol{\tau} : \mathbf{d}_e \, dt = \int_{t_{is}}^{t_\infty} \frac{\partial \psi_e}{\partial \mathbf{e}_e} : \mathbf{d}_e \, dt. \tag{2.5.83}$$

where ψ_e is the elastic free energy function, defined in Eq.(2.4.1). As proved in Proposition A.1.1 of Appendix A, the rate of change of ψ_e is given by

$$\dot{\psi}_e = \frac{\partial \psi_e}{\partial \mathbf{e}_e} : \mathbf{d}_e + \frac{\partial \psi_e}{\partial \xi^h} \dot{\xi}^h. \tag{2.5.84}$$

Employing Eq.(2.5.84) in Eq.(2.5.83), we get

$$\int_{t_{is}}^{t_\infty} \boldsymbol{\tau} : \mathbf{d}_e \, dt = \int_{t_{is}}^{t_\infty} (\dot{\psi}_e - \frac{\partial \psi_e}{\partial \xi^h} \dot{\xi}^h) \, dt. \tag{2.5.85}$$

We now suppose that, during intervals of plastic loading, the stress state remains on $\partial \mathbb{E}^d_{\boldsymbol{\tau}}$. This implies that the cap yield surface is not active, $\dot{\lambda}^e = 0$, and according to the rate equation (2.5.28), the internal hardening variable ξ^h does not evolve, i.e $\dot{\xi}^h = 0$. This observation permits to simplify Eq.(2.5.85) and omit the hardening term, resulting:

$$\int_{t_{is}}^{t_\infty} \boldsymbol{\tau} : \mathbf{d}_e \, dt = \int_{t_{is}}^{t_\infty} \dot{\psi}_e \, dt = \psi_e(\mathbf{e}_e(t_\infty)) - \psi_e(\mathbf{e}_e(t_{is})). \tag{2.5.86}$$

Assuming that the initial elastic strains are zero, we have

$$\psi_e(\mathbf{e}_e(t_{is})) = \psi_e(\mathbf{0}) = \frac{1}{2} \mathbf{e}_e : \boldsymbol{c_e} : \mathbf{e}_e = 0. \tag{2.5.87}$$

The term $\psi_e(\mathbf{e}_e(t_\infty))$ vanishes if we presume that the stresses are fully released at time t_∞, i.e.:

$$\psi_e(\mathbf{e}_e(t_\infty)) = \frac{1}{2} \mathbf{e}_e(t_\infty) : \boldsymbol{c_e} : \mathbf{e}_e(t_\infty) = \frac{1}{2} \mathbf{e}_e(t_\infty) : \overbrace{\boldsymbol{\tau}(t_\infty)}^{\mathbf{0}} = 0. \tag{2.5.88}$$

Then, Eq.(2.5.82) reduces to the integral over the interval $[t_{is}, t_\infty]$ of the rate of plastic work (per unit reference volume):

$$\mathsf{g}_{\mathsf{f}} = \int_{t_{is}}^{t_\infty} \boldsymbol{\tau} : \mathbf{d}_p \, dt. \tag{2.5.89}$$

Using the flow rule (2.5.36), the above equation is rephrased as:

$$\mathsf{g}_{\mathsf{f}} = \int_{t_{is}}^{t_\infty} \dot{\lambda}^d (2q^2 + \gamma \alpha c p) \, dt. \tag{2.5.90}$$

Employing Eqs. (2.5.71), (2.5.79) and (2.5.80), the plastic multiplier $\dot{\lambda}^d$ can be expressed in terms of the cohesion variable and the norm of deviatoric stress:

$$\dot{\lambda}^d = \frac{\dot{\xi}^s}{2q} = \frac{c_0}{2H_0 cq}\dot{c}. \tag{2.5.91}$$

Substitution of Eq.(2.5.91) in Eq.(2.5.90) yields

$$\begin{aligned} \mathsf{g}_\mathsf{f} &= \int_{t_{is}}^{t_\infty} \frac{c_0}{2H_0 cq}(2q^2 + \gamma\alpha cp)\dot{c}\, dt \\ &= \frac{c_0}{2H_0}\int_{c_0}^{0} \frac{2q^2 + \gamma\alpha cp}{cq}\, dc. \end{aligned} \tag{2.5.92}$$

To proceed with the integration of (2.5.92), we need an additional ingredient: the path followed by the stress state during the process. This ingredient, in conjunction with the yield condition, permits the expression of the integrand of (2.5.92) as a function of the cohesion[21].

We turn now our attention to describe the diametral compression test that will allow us to calibrate parameter H_0. These tests were carried out by Jonsén [50] on Distaloy AE powder cylindrical specimens, previously compacted at various densities, by applying two diametrically opposite forces (see figure 2.20.a). These forces induce at the center of the disc a tensile stress state which eventually leads to the initiation of a crack that propagates rapidly along the loaded diameter. The solid curve of the force vs displacement graph displayed in figure 2.21.a corresponds to the force monitored during the test until the specimen fractures. The area under this curve encompasses not only the irretrievable energy consumed in the formation of the diametral crack, but also the recoverable elastic energy. In order to purge this recoverable contribution from the balance of energy, an additional test is needed. The specimen is split into two halves (see figure 2.20.b) and its response is evaluated under the same experimental conditions as in the previous test. The result of this additional experiment is the dashed curve also shown in figure 2.21.a. Finally, the energy $\mathcal{W}$ required to produce such a crack is grossly estimated as the shaded area enclosed by the solid and dashed lines.

As discussed in section 2.1.2, the fracture energy, denoted by $\mathcal{G}_f$, is a measure of the energy required for the formation of a unit of fracture surface. Thus, fracture energy values are obtained by simply dividing $\mathcal{W}$ by the area A_f of material affected by the crack (see figure 2.21.b). Experimental results for each relative density are shown in figure 2.22. An exponential equation seems to provide a good fit to these data:

$$\mathcal{G}_f^{(dct)}(\xi^h) = \frac{\eta_0}{\xi^h} A_{\mathcal{G}_f} e^{B_{\mathcal{G}_f}\xi^h}, \tag{2.5.93}$$

with $A_{\mathcal{G}_f} = 0.1487\ J/m^2$ and $B_{\mathcal{G}_f} = 9.5102$. [22].

[21] Observe that this path dependence is an inherent property of materials with different behavior in tension and compression. A classical pressure-independent Von Mises plasticity model, for instance, would not exhibit this path dependence, as it may be deduced from Eq.(2.5.92) by

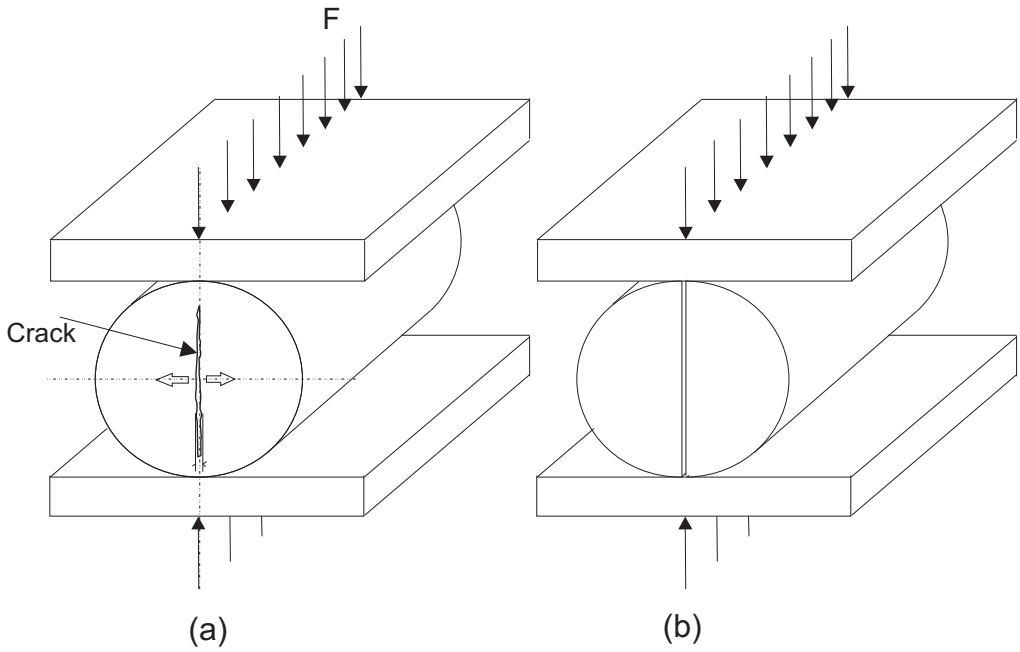

Figure 2.20 *Diametral compresison test. (a) The powder cylindrical specimen is subjected to two diametrically opposite forces. A crack develops along the loaded diameter. (b) The specimen is split into two halves along the loaded diameter.*

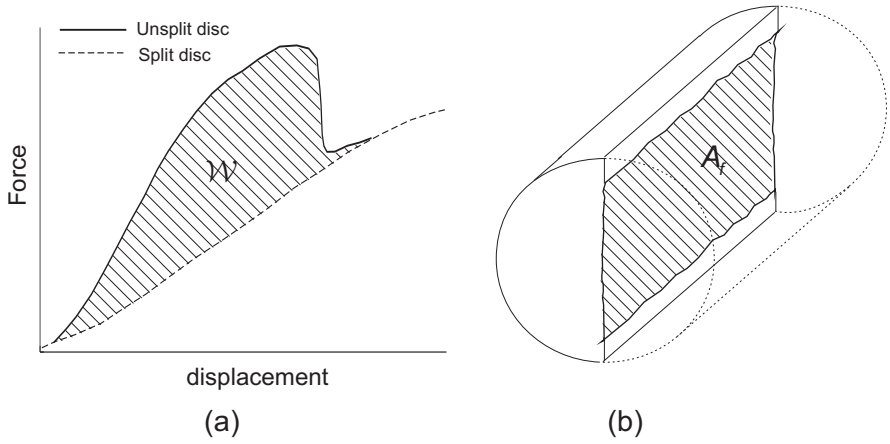

Figure 2.21 *(a) Typical force versus displacement graph for a diametral compression test. (b) Area of the specimen employed to compute the fracture energy.*

setting $\alpha = \gamma = 0$: $\mathrm{g_f} = \dfrac{c_0}{2H_0}\int_{c_0}^{0}\dfrac{2q^2}{cq}\,dc = \dfrac{-c_0^2}{H_0}$.

[22] It is important to remark that fracture energy values plotted in figure 2.22 are measures *per*

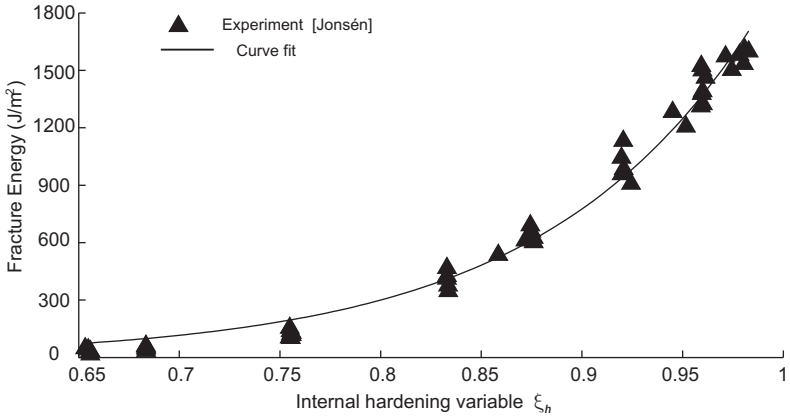

Figure 2.22 *Fracture Energy vs ξ^h. Fracture Energy is defined herein per unit current surface. Experimental values provided by Jonsén [50] (Distaloy AE powder specimens).*

The link between experimental data and the softening constitutive law is provided by the following balance of energy in the damaged volume Ω_f [75]:

$$\mathcal{W} = \mathcal{G}_f^{(dct)} A_f = \int_{\Omega_f} \mathsf{g}_\mathsf{f}(\mathbf{X}) dV. \tag{2.5.94}$$

Under the assumption that g_f is approximately uniform over Ω_f, and considering a localization bandwith l_f, the above expression takes the form

$$\mathcal{G}_f^{(dct)} = \mathsf{g}_\mathsf{f}(\mathbf{X}) l_f. \tag{2.5.95}$$

Inserting Eq.(2.5.92) in Eq.(2.5.95), we get

$$\mathcal{G}_f^{(dct)} = l_f \frac{c_0}{2H_0} \int_{c_0}^{0} \frac{2q^2 + \gamma\alpha cp}{cq}\, dc. \tag{2.5.96}$$

We mentioned in our introductory chapter (see section 2.1.2) that, with a view towards minimising the dependency to mesh refinement, the softening modulus is related to the localization bandwith[23] through the following expression

$$H_0 = l_f \hat{H}_0, \tag{2.5.97}$$

where $\hat{H}_0$ stands for the *intrinsic softening parameter* [76], defined as

$$\hat{H}_0 = \frac{c_0(\xi^h)}{2\mathcal{G}_f^{(dct)}} \int_{c_0}^{0} \frac{2q^2 + \gamma\alpha cp}{cq}\, dc. \tag{2.5.98}$$

unit current surface, which is the typical definition of fracture energy. However, in conformance with the rest of stress and energy quantities involved in the formulation of the constitutive equations, the fracture energy $\mathcal{G}_f^{(dct)}$ is defined on the reference configuration, i.e. it is an energy *per unit reference surface*, hence the factor $\frac{\eta_0}{\xi^h}$ in Eq.(2.5.93).

[23]The localization bandwith or *characteristic length* l_f is intimately tied to the size and orientation of the subsequent spatial discretization. See reference [74] for further details.

The superindex "*dct*" attached to the symbol $\mathcal{G}_f$ indicates that this quantity corresponds to the fracture energy measured in a diametral compression test. The intrinsic softening $\hat{H}_0$, on the other hand, is not accompanied by any superindex. This notational convention has been deliberately introduced to highlight one of our basic assumptions in this regard. Indeed, whereas fracture energy is clearly a quantity sensitive to the loading history followed during the experimental test, we shall consider that the intrinsic softening parameter does not depend on the loading history. In other words, *we regard the intrinsic softening parameter* $\hat{H}_0$ *as a state function*, i.e., a quantity that can be uniquely determined at any time by the point values of the state variables. In this case, according to Eq.(2.5.98) and Eq.(2.5.93), the softening parameter only depends on the internal hardening variable, that is $\hat{H}_0 = \hat{H}_0(\xi^h)$. The *intrinsic softening modulus* is then defined by analogy with Eq.(2.5.80) as:

$$\hat{H} = \hat{H}_0 \frac{c_0 + c_s}{c_0}, \tag{2.5.99}$$

is also a state function, but it further depends on the internal softening variable, $\hat{H} = \hat{H}(\xi^h, \xi^s)$. Note that neither the softening modulus H nor the softening parameter H_0 can be viewed as state functions.

To complete the calibration, it would be now pertinent to evaluate analytically the integral appearing in Eq.(2.5.98). To this end, one needs the analytical expression of the stress path traced during the de-cohesion process at points within the cracking band. For the case of a diametral compression test, the derivation of such expressions is far from being obvious, as it may surmised from the stress analysis (in the elastic range) carried out by Timoshenko [102].

To overcome this difficulty, it proves advantageous to exploit the fact that the diametral compression test is but an indirect test to measure the tensile strength of brittle or quasi-brittle materials (hence the alternative denomination of *indirect tension test* [107]), on which direct uniaxial tensile test are difficult to perform. The experimental configuration of the diametral compression test is such that the developing of the crack at the loaded diameter takes place under Mode I or opening mode conditions, which, in turn, are the same conditions encountered in a standard uniaxial tensile test. On this basis, a plausible assumption is to consider that the fracture energy measured in a uniaxial tensile test is approximately equal to that corresponding to the diametral compression test, i.e.:

$$\mathcal{G}_f^{(dct)} \approx \mathcal{G}_f^{(tt)}, \tag{2.5.100}$$

the superindex "*tt*" signifying tensile test. Under such assumption, the analytical evaluation of the integral in Eq.(2.5.98) becomes feasible, as we show in the following.

In a uniaxial tensile test, the ratio q/p at points belonging to the cracking band is approximately linear:

$$q \approx \hat{\mathsf{m}}\, p, \tag{2.5.101}$$

since necking is not very pronounced in quasi-brittle materials [41] and thus the uniaxial stress state prevails after bifurcation of the response. For a tensile test,

$\hat{\mathsf{m}} = \sqrt{6}$, as it is deduced from figure 2.18.a. Enforcing the yield condition in Eq.(2.5.101), we get an expression of q as a function of the cohesion c:

$$q = \frac{\hat{\mathsf{m}}}{\hat{\mathsf{m}} + \alpha}\, c = \tilde{\mathsf{m}} c. \tag{2.5.102}$$

Inserting the above equation into Eq.(2.5.98) and integrating, an expression for the intrinsic softening modulus $\hat{H}_0$ is finally achieved:

$$\hat{H}_0 = -\frac{c_0^2}{2\mathcal{G}_f^{(dct)}} \frac{2\tilde{\mathsf{m}}^2 - \gamma\tilde{\mathsf{m}} + \gamma}{\tilde{\mathsf{m}}}. \tag{2.5.103}$$

Inspection of the empirical laws (2.5.93) and (2.5.56) shows that both are exponential functions of the internal hardening variable. It follows from Eq.(2.5.103), thus, that the dependence of the intrinsic softening parameter on ξ^h exhibits also an exponential format:

$$|\hat{H}_0(\xi^h)| = \frac{\eta_0}{\xi^h} A_H e^{B_H \xi^h}, \tag{2.5.104}$$

where

$$A_H = \frac{2(\tilde{\mathsf{m}}^2 - \gamma\tilde{\mathsf{m}} + \gamma)}{3\tilde{\mathsf{m}}} \frac{A_{c_\mathrm{h}}^2}{A_{\mathcal{G}_f}}, \tag{2.5.105}$$

$$B_H = 2B_{c_\mathrm{h}} - B_{\mathcal{G}_f}. \tag{2.5.106}$$

In figure 2.23, relation (2.5.104) between the intrinsic softening parameter $|\hat{H}_0|$ and ξ^h is plotted. The graph shows that $\hat{H}_0$ is close to zero for the range of low densities. This observation confirms the hypothesis made in section 2.3, and represented by Eq.(2.3.3) , asserting that the softening mechanism is not active for low densities. Another interesting conclusion can be drawn from the values displayed in figure 2.23. The magnitude of $|\hat{H}_0|$ for $\xi^h \approx 0.95$ is approximately 1.0 MN/mm^3. Considering a typical width crack of, say, 0.1 mm, the resulting value of the softening parameter would be $|H_0| = 0.1 \cdot 1.0\, MN/mm^2 = 0.1 \cdot 10^6\, MPa$. On the other hand, the Young's Modulus corresponding to the same density range (see figure 2.17) is approximately$E^e \approx 150GPa = 0.15 \cdot 10^6 MPa$. This gives a ratio $E^e/H_0 \approx 1.5$, i.e., both moduli are of the same order of magnitude, which, in turn, implies that the order of magnitude of elastic and plastic strains are the same in deformation processes entailing only softening. This assertion is one of the basic assumptions made in section 2.2.1.

A noteworthy feature of the present approach is the hypothesis presented above by which the intrinsic softening parameter $\hat{H}_0$ is regarded as a state variable. The lack of experimental data concerning fracture energy in other fracture tests precludes the possibility of strictly corroborating this hypothesis. Nevertheless, it would be instructive to briefly examine and put on a quantitative basis the consequences of such proviso. For this purpose, consider a compression test characterized

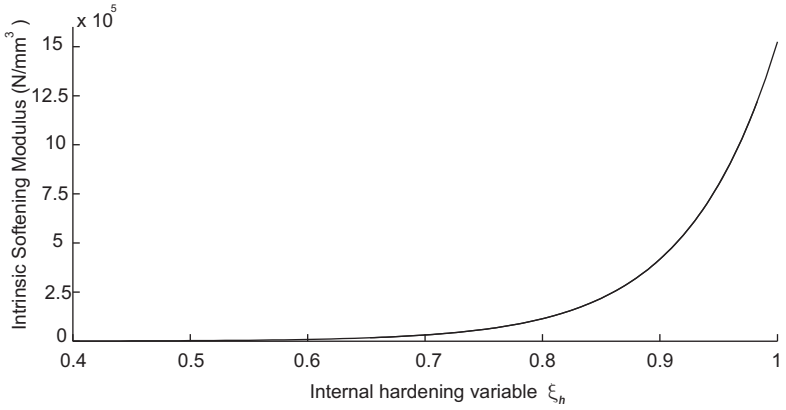

Figure 2.23 *Intrinsic softening parameter $\hat{H}_0$ vs internal hardening variable ξ^h.*

by a stress path during plastic loading given by $q = -\sqrt{6}p$ (see figure 2.14.b) [24]. For a typical value $\gamma = 0.01$ of the dilatational coefficient and a parameter of internal friction $\alpha = 2.29$, we get

$$\hat{H}_0 = -15.8\frac{c_0^2}{2\mathcal{G}_f^{(ct)}}. \tag{2.5.107}$$

where $\mathcal{G}_f^{(ct)}$ stands for the fracture energy associated to a uniaxial compression test. The same operations for a uniaxial tensile test yields

$$\hat{H}_0 = -0.52\frac{c_0^2}{2\mathcal{G}_f^{(tt)}}. \tag{2.5.108}$$

In view of Eq.(2.5.107) and Eq.(2.5.108), the fracture energy measured in a uniaxial compression test would be $15.8/0.52 \approx 30$ times greater that the linked to the one obtained in a uniaxial tensile test. For other granular media, such as concrete, this ratio gives approximately 100 [82].

[24] The ratio q/p is not linear in a compression test after bifurcation, since important shear stresses develop at the localization band [61] (fracture occurs under *shear mode* or mode II conditions (see figure 2.6)) and, consequently, the hypothesis of uniaxial stress state is no longer valid. However, the approximation adopted here $q/p = -\sqrt{6}$ (the same path traced during elastic loading) serves as a first approximation for estimating the fracture energy associated to this test.

Chapter 3

Integration of the constitutive equation

3.1 Preliminaries

The preceding chapter was devoted to describe mathematically the effects that a given deformation history has on the physical attributes of the powder at a point $\mathbf{X} \in \Omega_0$. The result was the formulation of a system of constitutive laws and evolution equations subjected to a set of unilateral constraints. For clarity, we summarize again these relations:

I. Deformation and strain history up to current time $t \in [t_0, t_f]$ (given):

$$\hat{t} \mapsto \mathbf{F}_{\hat{t}}(\mathbf{X}) = \mathbf{F}(\mathbf{X}, \hat{t}), \quad \text{where } \hat{t} \in [t_0, t], \tag{3.1.1}$$

$$\mathbf{e} = \frac{1}{2}\left(\mathbf{1} - \mathbf{F}^{-T} \cdot \mathbf{F}^{-1}\right). \tag{3.1.2}$$

II. Elastic strain-stress relationship

$$\boldsymbol{\tau} = \overbrace{\mathbf{F} \cdot \boldsymbol{S}_0 \cdot \mathbf{F}^T}^{\boldsymbol{\tau}_0} + \boldsymbol{c_e} : (\mathbf{e} - \mathbf{e}_p), \quad \text{where } \boldsymbol{S}_0 = \boldsymbol{S}(t_0), \tag{3.1.3}$$

$$\boldsymbol{c_e} = \kappa^e \mathbf{1} \otimes \mathbf{1} + 2\mu^e (\boldsymbol{I} - \frac{1}{3}\mathbf{1} \otimes \mathbf{1}), \tag{3.1.4}$$

with $\kappa^e = \kappa^e(\xi^h)$ and $\mu^e = \mu^e(\xi^h)$ given in Eqs. (2.4.2) and (2.5.60).

III. Elastic domain in Kirchhoff stress space

$$\mathbb{E}_{\boldsymbol{\tau}} = \left\{\boldsymbol{\tau} \mid \phi^\beta(\boldsymbol{\tau}, \xi^h, \xi^s) \leq 0, \text{ for all } \beta \in \{e, d, v\}\right\}, \text{ where} \tag{3.1.5}$$

$$\phi^e = \phi^1 = q^2 + s_2^2(\xi^h)p^2 - s_1^2(\xi^h)s_2^2(\xi^h), \tag{3.1.6}$$

$$\phi^d = \phi^2 = q + \alpha p - c(\xi^h, \xi^s), \tag{3.1.7}$$

$$\phi^v = \phi^3 = q - c_v(\xi^h), \tag{3.1.8}$$

with $p = \frac{1}{3}\mathrm{tr}\,\boldsymbol{\tau}$ and $q = \sqrt{dev\,\boldsymbol{\tau} : dev\,\boldsymbol{\tau}}$.

IV. Flow rule

$$\mathcal{L}_v \mathbf{e}_p = \mathbf{d}_p = \sum_{\beta=1}^{3} \dot{\lambda}^\beta \boldsymbol{m}^\beta, \quad \text{where} \tag{3.1.9}$$

$$\boldsymbol{m}^e = \boldsymbol{m}^1 = 2dev\,\boldsymbol{\tau} + \frac{2}{3} s_2^2(\xi^h) p\,\mathbf{1}, \tag{3.1.10}$$

$$\boldsymbol{m}^d = \boldsymbol{m}^2 = 2\,dev\,\boldsymbol{\tau} + \frac{1}{3}\gamma\, c(\xi^h, \xi^s)\,\alpha \mathbf{1}, \tag{3.1.11}$$

$$\boldsymbol{m}^v = \boldsymbol{m}^3 = 2\,dev\,\boldsymbol{\tau}. \tag{3.1.12}$$

V. Evolution of internal variables

$$\dot{\xi}^h = -\xi^h \dot{\lambda}^e 2 s_2^2(\xi^h) p, \tag{3.1.13}$$

$$\dot{\xi}^s = 2\dot{\lambda}^d q, \tag{3.1.14}$$

with initial values $\xi^h(t_0) = \eta_0$ and $\xi^s(t_0) = 0$.

VI. Softening and hardening laws (in rate form)

$$\dot{s}_1 = \frac{\partial s_{1\mathrm{h}}}{\partial \xi^h} \dot{\xi}^h, \tag{3.1.15}$$

$$\dot{s}_2 = \frac{\partial s_{2\mathrm{h}}}{\partial \xi^h} \dot{\xi}^h, \tag{3.1.16}$$

$$\dot{c} = \frac{\partial c_{\mathrm{h}}}{\partial \xi^h} \dot{\xi}^h + H \dot{\xi}^s, \tag{3.1.17}$$

$$\dot{c}_v = \frac{\partial c_{v\mathrm{h}}}{\partial \xi^h}, \tag{3.1.18}$$

where $s_{1\mathrm{h}} = s_{1\mathrm{h}}(\xi^h)$, $s_{2\mathrm{h}} = s_{2\mathrm{h}}(\xi^h)$, $c_{\mathrm{h}} = c_{\mathrm{h}}(\xi^h)$, $H = H(\xi^s)$ and $c_{v\mathrm{h}} = c_{v\mathrm{h}}(\xi^h)$ are given in Eqs. (2.5.53), (2.5.54), (2.5.56), (2.5.80) and Eq.(2.5.59), respectively.

VII. Karush-Kuhn-Tucker loading/unloading conditions and consistency condition

$$\dot{\lambda}^\beta \geq 0, \quad \phi^\beta(\boldsymbol{\tau}, \xi^h, \boldsymbol{\xi}^s) \leq 0, \tag{3.1.19}$$

$$\dot{\lambda}^\beta \phi^\beta(\boldsymbol{\tau}, \xi^h, \boldsymbol{\xi}^s) = 0, \qquad \text{(no sum on } \beta), \tag{3.1.20}$$

$$\dot{\lambda}^\beta \dot{\phi}^\beta(\boldsymbol{\tau}, \xi^h, \boldsymbol{\xi}^s) = 0, \qquad \text{(no sum on } \beta). \tag{3.1.21}$$

The underlying ODE structure of the governing equations listed above becomes apparent by expressing all the variables involved in the problem in terms of a set of *generalized stresses*, defined as $\boldsymbol{\Sigma} = (\boldsymbol{S}, \mathbf{r})$, where $\boldsymbol{S}$ is the second Piola-Kirchhoff stress tensor and $\mathbf{r}$ stands for the stress-like vector of internal variable with components:

$$\mathbf{r} = \begin{bmatrix} s_1 \\ c \end{bmatrix}, \tag{3.1.22}$$

which, in turn, is related with the vector of strain-like internal variables $[\xi^h, \xi^s]^T$ through the *generalized plastic moduli* $\boldsymbol{D}$, defined as

$$\boldsymbol{D} = \begin{bmatrix} \dfrac{\partial s_{1\mathrm{h}}}{\partial \xi^h} & 0 \\ \dfrac{\partial c_{\mathrm{h}}}{\partial \xi^h} & H \end{bmatrix}. \tag{3.1.23}$$

By performing *pull-back* transformations on the constitutive equations, and after some straightforward, albeit lengthy, manipulation, one gets the following generalized representation of the system of ordinary differential equations governing the local response of the powder at $\mathbf{X} \in \Omega_0$ [1]:

$$\dot{\boldsymbol{\Sigma}} = \boldsymbol{A}(\boldsymbol{\Sigma}, \dot{\mathbf{E}}) + \sum_{\beta=1}^{3} \dot{\lambda}^{\beta} \boldsymbol{\Xi}_{\beta}(\boldsymbol{\Sigma}). \tag{3.1.24}$$

This system is supplemented with the initial conditions $\boldsymbol{\Sigma}(t_0) = (\boldsymbol{S}_0, \mathbf{r}(\boldsymbol{\xi}_0))$. The components of the generalized stress tensor $\boldsymbol{\Sigma}$ and the plastic multipliers $\dot{\lambda}^{\beta}, (\beta = 1, 2, 3)$ are the dependent variables, whereas the rate of change of the Green-Lagrange strain tensor $\dot{\mathbf{E}}$ is the source term. The evolution of $\boldsymbol{\Sigma}$ is further restricted by the loading/unloading and consistency conditions, which in terms of $\boldsymbol{\Sigma}$ are written as

$$\dot{\lambda}^{\beta} \geq 0, \quad \phi^{\beta}(\boldsymbol{\Sigma}) \leq 0, \tag{3.1.25}$$

$$\dot{\lambda}^{\beta} \phi^{\beta}(\boldsymbol{\Sigma}) = 0, \qquad (\text{no sum on } \beta), \tag{3.1.26}$$

$$\dot{\lambda}^{\beta} \dot{\phi}^{\beta}(\boldsymbol{\Sigma}) = 0, \qquad (\text{no sum on } \beta). \tag{3.1.27}$$

The problem of integrating numerically the initial-value ODE equation represented by Eq.(3.1.24), in conjunction with conditions (3.1.25), (3.1.26) and (3.1.27), constitutes the *central problem of computational plasticity* [92]. The remainder of this chapter is focused on solving this problem and addressing the mathematical questions that arises in its treatment.

[1] The derivation of the expressions for $\boldsymbol{A} = \boldsymbol{A}(\boldsymbol{\Sigma}, \dot{\mathbf{E}})$ and $\boldsymbol{\Xi}_{\beta} = \boldsymbol{\Xi}_{\beta}(\boldsymbol{\Sigma})$ is not quoted herein. The interested reader is urged to consult Appendix A.2 for the details of such derivation.

3.1.1 Implicit Backward-Euler and IMPLEX integration schemes

As customarily, the continuous time domain $[t_0, t_f]$ of interest is discretized in non-overlapping intervals, $[t_0, t_f] = \bigcup_{n=1}^{N} [t_n, t_{n+1}]$. Then, the exact derivative in Eq.(3.1.24) is approximated by an algebraic finite difference. Finally, substitution of this approximation into the ODE equation leads to an algebraic finite difference equation [45]. One of the most employed methods in computational plasticity arises when the derivative at time t_{n+1} is approximated as

$$\left(\dot{\boldsymbol{\Sigma}}\right)_{n+1} \approx \frac{\boldsymbol{\Sigma}_{n+1} - \boldsymbol{\Sigma}_n}{\Delta t_{n+1}}. \tag{3.1.28}$$

The resulting finite difference scheme is known as the *implicit Backward Euler difference scheme*. The associated non-linear difference equation takes the form

$$\boldsymbol{\Sigma}_{n+1} - \boldsymbol{\Sigma}_n = \Delta t_{n+1} \boldsymbol{A}(\boldsymbol{\Sigma}_{n+1}, \dot{\mathbf{E}}_{n+1}) + \sum_{\beta \in \mathbb{J}^{act}} \Delta \lambda^{\beta}_{n+1} \, \boldsymbol{\Xi}_{\beta}(\boldsymbol{\Sigma}_{n+1}), \tag{3.1.29}$$

where $\Delta t_{n+1} = t_{n+1} - t_n$ and $\Delta \lambda^{\beta}_{n+1} = \Delta t_{n+1} \dot{\lambda}^{\beta}$ stand for the length of the time interval and the β-*th* discrete plastic multiplier, respectively. The discrete counterpart of the Karush-Kuhn-Tucker conditions (3.1.25), (3.1.26) and (3.1.27) read

$$\Delta \lambda^{\beta}_{n+1} \geq 0, \quad \phi^{\beta}(\boldsymbol{\Sigma}_{n+1}) \leq 0, \tag{3.1.30}$$

$$\Delta \lambda^{\beta}_{n+1} \phi^{\beta}(\boldsymbol{\Sigma}_{n+1}) = 0, \qquad (\text{no sum on } \beta). \tag{3.1.31}$$

The reason behind the popularity of such method is, on one hand, that it provides a suitable framework for the enforcement of the algebraic Karush-Kuhn-Tucker constraints, leading to the classical *return mapping algorithm* [92]. On the other hand, the implicit Backward Euler scheme turns out to be, in general, *unconditionally stable* [93]. Section 3.2 is devoted to discuss the salient features of such integration scheme when applied to our specific problem. One of the issue that will receive particular consideration is that of the uniqueness of solution. As a matter of fact, the task of ensuring the existence and uniqueness of solution will require to modify the evolution equations (3.1.13) and (3.1.14), although these modifications will be accommodated without significantly compromising the adequacy of the empirical correlations established in the previous chapter.

The source term in the ODE (3.1.24) is the rate of change of the Green-Lagrange strain tensor $\dot{\mathbf{E}}$. This fact is consistent with the strain-driven character of the constitutive model, whereby all variables can be expressed in terms of the deformation history through adequate functional relationships. Therefore, the deformation history is *presumed known* when solving the ODE (A.2.13). From the algorithmic point of view, this statement means that the *strain rate is prescribed* in the interval $[t_n, t_{n+1}]$ when solving the associated difference equation (3.1.29).

In practice, however, the function $\mathbf{F} = \mathbf{F}(t), t \in [t_0, t_F]$ is not available as such. Our aim is to obtain the mechanical response of the powder sub-system under

external loads (punch actions). To this end the weak form of the momentum equation is discretized via a Galerkin finite element projection[2]. Then, the numerical solution of the discrete system of equations, whose basic unknowns are the *nodal displacements*, is obtained by performing an incremental analysis accompanied by iterations so as to ensure convergence to equilibrium states. The strain increment $\boldsymbol{\Delta E} = \mathbf{E}_{n+1} - \mathbf{E}_n$ is calculated from the current displacement field, which is updated at the beginning of each iteration, and the previously converged configuration (at t_n) through adequate kinematic relationships.

If a standard Newton-Raphson procedure is employed for this iterative process, as is the case here, the spectral properties of the so-called *algorithmic tangent moduli* are a crucial issue for preserving the quadratic rate of asymptotic convergence that characterizes Newtown's method. It is widely known that if the positive definiteness of the the algorithmic tangent moduli cannot be guaranteed, the performance of the Newton-Raphson method may be seriously impaired, affecting eventually the ability of the considered algorithm to provide results at affordable computational costs. The algorithmic tangent moduli stemming from the implicit integration of an elasto-plastic model equipped with softening, as in our case, is a typical example in which the proviso of positive definiteness is not satisfied, a fact intimately tied with the character of unstable material model associated to this type of approach [6].

The need to circumvent this barrier to computability has prompted investigations of alternative means of integrating the constitutive model. The solution adopted herein is the one pioneered by *Oliver et al.* [79, 80], originally conceived for addressing the problem of robustness and stability arising in the numerical simulation of material failure within the framework of the Strong Discontinuity Approach. The algorithmic details concerning this integration scheme are given in section 3.3.

Oliver et al. coined the term *IMPLEX* (IMPLicit-EXplicit) to suggest that the proposed methodology shares some of the features of both implicit and explicit integration schemes. The essence of the method is to solve *explicitly* for some variables, in the sense that the values at the beginning of the increment are presumed known, and *implicitly* for other group of variables. In this aspect, the IMPLEX methodology parallels that followed in the so-called *semi-implicit* integration scheme, developed by Moran et al. [68, 5][3]. However, the primary motivation behind the semi-implicit strategy is to reduce the equation solving effort associated to the solution of the fully implicit scheme, whereas the IMPLEX method is basically intended to enhance the spectral properties of the algorithmic tangent moduli. Indeed, the remarkable stability exhibited by IMPLEX solutions [80] is attributed to the fact that the above mentioned group of explicit variables are *extrapolated values* of the same quantities *computed at previous time steps* by accomplishing a *fully implicit integration*. The distinguishing feature of the IMPLEX methodology is, hence, that it does entail the solution at each time increment of the non-linear

[2]So far, attention has been confined to the local response at a point $\mathbf{X} \in \Omega_0$, which, in fact, corresponds to a quadrature point of a typical finite element

[3]This integration procedure is characterized for being implicit in the incremental plastic strain, but explicit in the plastic flow direction and the hardening moduli

system of equations stemming from the implicit backward-Euler difference scheme.

Furthermore, with an appropriate choice of the *explicit variables*, the algorithmic tangent tensor adopts a very simplified format, to such an extent that if the terms due to non-linear kinematics are discarded, the resulting tangent tensor is *step-constant*. This means that if one disregards other sources of non-linearities rather than the material one, the structural tangent stiffness matrix would be constant and the convergence to equilibrium states could be achieved, theoretically, in only one iteration per time step, as it is shown in the original work of Oliver et al.[79]. A further implication of this statement is that, if during a computer run the convergence of the global Newton-Raphson iteration scheme is hindered by any reason, one should seek the causes that inhibit convergence in geometric singularities or in the roughness of the response associated to the contact with the punches (boundary conditions) rather than in material non-linearities.

Although the IMPLEX integration, as the fully implicit scheme, is first-order accurate [80], the global error associated to the IMPLEX scheme is comparatively larger for the same time step size. Hence, the IMPLEX method demands more time steps than the implicit procedure for obtaining the same accuracy in the results. Nevertheless, the consequences of this drawback are not too drastic, since, in practical loading situations, the step size is to be considerably reduced by the need to accurately resolve the abrupt nature of the contact response between the powder and the tooling.

Another characteristic of this integration scheme is that the yield condition is not enforced at time t_{n+1}, i.e, the updated stresses emanating from the IMPLEX integration *violates the consistency condition*. Note that this is a feature inherent to the explicit character of the proposed method. It should be remarked, however, that in contrast to standard explicit forward Euler procedures [27], the *accumulated error remains bounded* as the solution progresses[80]. Indeed, if one considers a process involving yielding in which the application of the external actions are reasonably smooth, the *explicit values*, obtained as extrapolations of implicitly integrated quantities at previous steps, would not differ substantially from those furnished by a fully implicit scheme at time t_{n+1}, and thus the stress state would remain very close to the boundary of the elastic domain. By contrast, in those circumstances in which the response is far from being smooth, as in the abrupt transition from compressive yielding to elastic conditions that accompanies the upper punch pressure release, the yield condition may be substantially violated. In order to overcome this adverse effect, Oliver et al.[80] have proposed an *adaptive time step* algorithm that keeps the error in these cases into appropriate bounds.

3.2 Implicit integration scheme

We consider a time discretization of the interval $[t_0, t_f] = \bigcup_{n=1}^{N} [t_n, t_{n+1}]$, and let $\{\xi_n^h, \xi_n^s, \mathbf{E}_n, \mathbf{E}_{p,n}\}$ be the *initial data* at t_n. We regard also the deformation gradient $\mathbf{F}_{n+1}$ at t_{n+1} as *given*. Our aim is to find the state variables at the end of the interval $[t_n, t_{n+1}]$ by applying a implicit backward Euler difference scheme to the constitutive evolution equations summarized at the beginning of this chapter.

We begin by the elastic constitutive relationship (3.1.3). Since this relation is not expressed in rate form, we can simply write its discrete counterpart as:

$$\boldsymbol{\tau}_{n+1} = \mathbf{F}_{n+1} \cdot \boldsymbol{S}_0 \cdot \mathbf{F}_{n+1}^T + \boldsymbol{c}_{\boldsymbol{e},n+1} : (\mathbf{e}_{n+1} - \mathbf{e}_{p,n+1}). \tag{3.2.1}$$

Observe that the notation $\boldsymbol{c}_{\boldsymbol{e},n+1}$ indicates that $\boldsymbol{c}_{\boldsymbol{e},n+1} = \boldsymbol{c}_{\boldsymbol{e}}(\xi_{n+1}^h)$. In order to satisfy the requirement of objectivity, the flow rule represented by *Eq.*(3.1.9) is transformed back to the reference configuration Ω_0 and then approximated as:

$$\mathbf{E}_{p,n+1} = \mathbf{E}_{p,n} + \sum_{\beta=1}^{3} \Delta\lambda_{n+1}^{\beta} \varphi^* \left(\boldsymbol{m}_{n+1}^{\beta} \right), \tag{3.2.2}$$

where $\Delta\lambda_{n+1}^{\beta}$ denotes the discrete plastic multiplier $\Delta\lambda_{n+1}^{\beta} = \Delta t_{n+1}\, \dot{\lambda}^{\beta}$, with $\Delta t_{n+1} = t_{n+1} - t_n$. The symbol $\varphi^*(\bullet)$ stands for the pull back operator[4] $\varphi_*(\bullet) = \mathbf{F}_{n+1}^{-T} \cdot (\bullet) \cdot \mathbf{F}_{n+1}^{-1}$. We revert again to the spatial description by obtaining the push forward, defined as $\varphi_*(\bullet) = \mathbf{F}_{n+1}^{-T} \cdot (\bullet) \cdot \mathbf{F}_{n+1}^{-1}$, of Eq.(3.2.2):

$$\begin{aligned} \varphi_*(\mathbf{E}_{p,n+1}) = \varphi_*(\mathbf{E}_{p,n}) + \sum_{\beta \in \mathbb{J}^{act}} \Delta\lambda_{n+1}^{\beta} \varphi_* \left(\varphi^* \left(\boldsymbol{m}_{n+1}^{\beta} \right) \right) \quad \Rightarrow \\ \mathbf{e}_{p,n+1} = \breve{\mathbf{e}}_{p,n} + \sum_{\beta \in \mathbb{J}^{act}} \Delta\lambda_{n+1}^{\beta} \boldsymbol{m}_{n+1}^{\beta}. \end{aligned} \tag{3.2.3}$$

Remark 3.2.1. The breve symbol in $\breve{\mathbf{e}}_{p,n}$ is attached to indicate that $\breve{\mathbf{e}}_{p,n}$ is a strain measure computed at time t_n but transformed to the current configuration Ω_{n+1} via a push forward operation:

$$\breve{\mathbf{e}}_{p,n} = \varphi_*(\mathbf{E}_{p,n}) = \mathbf{F}_{n+1}^{-T} \cdot \mathbf{E}_{p,n} \cdot \mathbf{F}_{n+1}^{-1}. \tag{3.2.4}$$

The above can be rephrased also, after simple algebra, in terms of the *incremental deformation gradient* $\boldsymbol{\Delta}\mathbf{F}_{n+1} = \mathbf{F}_{n+1} \cdot \mathbf{F}_n^{-1}$,

$$\breve{\mathbf{e}}_{p,n} = \mathbf{F}_{n+1}^{-T} \cdot \mathbf{E}_{p,n} \cdot \mathbf{F}_{n+1}^{-1} = \boldsymbol{\Delta}\mathbf{F}_{n+1}^{-T} \cdot \mathbf{e}_{p,n} \cdot \boldsymbol{\Delta}\mathbf{F}_{n+1}^{-1}, \tag{3.2.5}$$

or symbolically,

$$\breve{\mathbf{e}}_{p,n} = \varphi_*^{\Delta}(\mathbf{e}_{p,n}), \tag{3.2.6}$$

$\varphi_*^{\Delta}(\bullet)$ being the push-forward operation relating the incremental motion from configuration Ω_n to Ω_{n+1}. This notation will be used henceforth to denote any tensorial quantity computed at t_n but pushed forwardly to the current configuration Ω_{n+1}. In this way, for instance, $\breve{\boldsymbol{\tau}}_n = \varphi_*(\boldsymbol{S}_n) = \varphi_*^{\Delta}(\boldsymbol{\tau}_n)$. This notational convention will permit us to easily draw analogies with infinitesimal classical plasticity formulations, by simply setting $\breve{\mathbf{e}}_{p,n} \approx \mathbf{e}_{p,n}$, or $\breve{\boldsymbol{\tau}}_n \approx \boldsymbol{\tau}_n = \boldsymbol{\sigma}_n$.

[4]Push-forward and pull-back transformations depend on the covariant or contra-variant nature of their arguments. Strain measures are considered herein *covariant tensors*, whereas stress quantities are *contravariants*. For further details, see Appendix A, Eqs. (A.1.12) and (A.1.13)

The same approximation of the time derivative is carried out on the evolution equations (3.1.13) and (3.1.14), leading to the following difference equations:

$$\xi^h_{n+1} = \xi^h_n - 2\xi^h_{n+1}\Delta\lambda^e_{n+1} {s_{2,n+1}}^2 p_{n+1}, \tag{3.2.7}$$

$$\xi^s_{n+1} = \xi^s_n + 2\Delta\lambda^d_{n+1} q_{n+1}, \tag{3.2.8}$$

where $p_{n+1} = 1/3\mathrm{tr}\,\boldsymbol{\tau}_{n+1}$ and $q_{n+1} = \|dev\,\boldsymbol{\tau}_{n+1}\|$. The parameters governing the size and shape of the elliptical cap surface and the location of Von Mises yield surface can be obtained through functional evaluations, i.e. $s_{1,n+1} = s_1(\xi^h_{n+1})$, $s_{2,n+1} = s_2(\xi^h_{n+1})$ and $c_{v,n+1} = c_v(\xi^h_{n+1})$. On the other hand, the expression for the cohesion state variable can be drawn from the rate equation (3.1.17) as:

$$c_{n+1} = c_n + \left.\frac{\partial c_{\mathrm{h}}}{\partial \xi^h}\right|_{n+1} (\xi^h_{n+1} - \xi^h_n) + H_{n+1}(\xi^s_{n+1} - \xi^s_n). \tag{3.2.9}$$

Finally, the discrete counterpart of the Karush-Kuhn-Tucker loading/unloading conditions are given by

$$\Delta\lambda^\beta_{n+1} \geq 0, \quad \phi^\beta_{n+1} \leq 0, \quad (\beta = 1,2,3) \tag{3.2.10}$$

$$\Delta\lambda^\beta_{n+1}\phi^\beta_{n+1} = 0, \quad (\beta = 1,2,3) \qquad \text{(no sum on } \beta). \tag{3.2.11}$$

where

$$\phi^e_{n+1} = \phi^1_{n+1} = q^2_{n+1} + {s_{2,n+1}}^2 p^2_{n+1} - {s_{1,n+1}}^2 {s_{2,n+1}}^2, \tag{3.2.12}$$

$$\phi^d_{n+1} = \phi^2_{n+1} = q_{n+1} + \alpha\, p_{n+1} - c_{n+1}, \tag{3.2.13}$$

$$\phi^v_{n+1} = \phi^3_{n+1} = q_{n+1} - c_{v,n+1}. \tag{3.2.14}$$

A widely used procedure, which can be justified as a product formula based on an *elastic-plastic operator split* [92], to cast the loading-unloading conditions in a format readily amenable to computational implementation is to introduce the *trial elastic state*. This trial state arises from assuming elastic behavior throughout the time step $[t_n, t_{n+1}]$:

$$\mathbf{e}^{tr}_{p,n+1} = \breve{\mathbf{e}}_{p,n}, \tag{3.2.15}$$

$$\xi^{h,tr}_{n+1} = \xi^h_n, \tag{3.2.16}$$

$$\xi^{s,tr}_{n+1} = \xi^s_n. \tag{3.2.17}$$

$$\boldsymbol{\tau}^{tr}_{n+1} = \mathbf{F}_{n+1} \cdot \boldsymbol{S}_0 \cdot {\mathbf{F}}^T_{n+1} + \boldsymbol{c}_{\boldsymbol{e},n} : (\mathbf{e}_{n+1} - \breve{\mathbf{e}}_{p,n}). \tag{3.2.18}$$

If the convexity of the elastic domain holds[5], it can be shown [92] that if

$$\phi^{\beta,tr}_{n+1} = \phi^\beta(\boldsymbol{\tau}^{tr}_{n+1}, \xi^{h,tr}_{n+1}, \xi^{s,tr}_{n+1}) < 0, \quad \forall\,\beta = 1,2,3, \tag{3.2.19}$$

[5]By examination of figure 2.7 (section 2.5.2), and by straightforward geometric considerations, we can immediately conclude that the elastic domains displayed are convex in stress space. For a typical Distaloy AE, whose empirical correlations were detailed in section 2.5, this conclusion can be extended for the whole range of possible configurations of the three yield surfaces. For other materials, the fulfillment of the convexity condition must be inspected cautiously.

then the trial elastic state is inside the elastic domain and, therefore, the deformation is entirely elastic. In this case, the updated state corresponds to the above shown trial elastic state. By contrast, if one or more yield conditions are violated, i.e.

$$\phi_{n+1}^{\beta,tr} > 0, \quad \text{for any} \quad \beta = 1, 2, 3, \tag{3.2.20}$$

then the tentative assumption of elastic response is rejected, and the updated state is obtained by "returning" the trial state to the yield surface, in order to meet the corresponding consistency condition.

The computation of *elastic predictor step* does not entail any difficulty, since it involves only functional evaluations. The complexity lies thus in the *plastic corrector step*, which constitutes the thrust of the *return mapping algorithm*. A crucial issue in return mapping algorithms with multisurface yield conditions is the determination of the *set of active constrains* [92], defined as

$$\mathbb{J}_{n+1}^{act} = \left\{ \beta \in \{1, 2, 3\} \;\mid\; \Delta\lambda_{n+1}^{\beta} > 0 \right\}. \tag{3.2.21}$$

One salient feature of this set of active constrains is that $\mathbb{J}_{n+1}^{act} \subseteq \mathbb{J}_{n+1}^{act,tr}$, where $\mathbb{J}_{n+1}^{act,tr}$ is given by

$$\mathbb{J}_{n+1}^{act,tr} = \left\{ \beta \in \{1, 2, 3\} \;\mid\; \phi_{n+1}^{\beta,tr} > 0 \right\}. \tag{3.2.22}$$

This assertion means that if only one yield condition $\phi_{n+1}^{\alpha,tr}$ is violated, then $\Delta\lambda_{n+1}^{\alpha} > 0$, but if several yield conditions are active, then the condition $\phi_{n+1}^{\alpha,tr} > 0$ does not guarantee that $\Delta\lambda_{n+1}^{\alpha} > 0$ [92].

Inserting the discrete flow rule (3.2.2) in Eq.(3.2.1), we get

$$\begin{aligned} \boldsymbol{\tau}_{n+1} =& \mathbf{F}_{n+1} \cdot \boldsymbol{S}_0 \cdot \mathbf{F}_{n+1}^T + \boldsymbol{c}_{\boldsymbol{e},n+1} : (\mathbf{e}_{n+1} - \breve{\mathbf{e}}_{p,n}) \\ & - \sum_{\beta=1}^{3} \Delta\lambda_{n+1}^{\beta}\, \boldsymbol{c}_{\boldsymbol{e},n+1} : \boldsymbol{m}_{n+1}^{\beta}. \end{aligned} \tag{3.2.23}$$

Using the preceding relation and the definition (3.2.18) of *trial stress*, an easy manipulation produces the result

$$\boldsymbol{\tau}_{n+1} = \boldsymbol{\tau}_{n+1}^{tr} + \Delta\boldsymbol{c}_{\boldsymbol{e},n+1} : (\mathbf{e}_{n+1} - \breve{\mathbf{e}}_{p,n}) - \sum_{\beta=1}^{3} \Delta\lambda_{n+1}^{\beta}\, \boldsymbol{c}_{\boldsymbol{e},n+1} : \boldsymbol{m}_{n+1}^{\beta}. \tag{3.2.24}$$

The fourth-order tensor $\Delta\boldsymbol{c}_{\boldsymbol{e},n+1}$ in the above expression, defined as

$$\Delta\boldsymbol{c}_{\boldsymbol{e},n+1} = \boldsymbol{c}_{\boldsymbol{e}}(\xi_{n+1}^h) - \boldsymbol{c}_{\boldsymbol{e}}(\xi_n^h) = (\kappa_{n+1}^e - \kappa_n^e)\, \mathbf{1} \otimes \mathbf{1} + 2\,(\mu_{n+1}^e - \mu_n^e) \boldsymbol{I}_{\text{dev}}. \tag{3.2.25}$$

does not appear in classical plasticity formulation. This term reveals the coupling between elastic and plastic responses, i.e. the fact that the elastic moduli E^e increases as hardening progresses.

Remark 3.2.2. Expression (3.2.24) possesses a compelling geometric interpretation, illustrated in figure 3.1. The projection of the trial elastic stress $\boldsymbol{\tau}_{n+1}^{tr}$ in the *p-q*

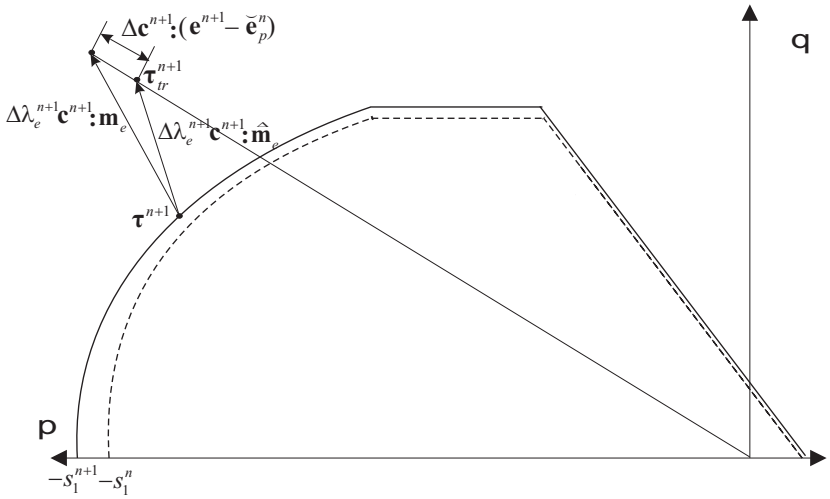

Figure 3.1 *Geometrical interpretation of the effect of coupling between elastic and plastic response.*

plane lies outside the elastic domain. Since only the elliptical yield surface is active, then $\Delta\lambda_{n+1}^e > 0$ and $\Delta\lambda_{n+1}^d = \Delta\lambda_{n+1}^v = 0$. The unusual feature here is that the *return direction is not determined by the vector* $\boldsymbol{c_e}_{,n+1} : \boldsymbol{m}_{n+1}^e$. Rather, the location of the trial stress is changed to $\boldsymbol{\tau}_{n+1}^{tr} + \Delta\boldsymbol{c_e}_{,n+1} : (\mathbf{e}_{n+1} - \breve{\mathbf{e}}_{p,n})$ before being projected back to the yield surface using the direction $\boldsymbol{c_e}_{,n+1} : \boldsymbol{m}_{n+1}^e$. Another remarkable feature is that, as the Poisson's ratio is regarded as a constant, the direction determined by $\Delta\boldsymbol{c_e}_{,n+1} : (\mathbf{e}_{n+1} - \breve{\mathbf{e}}_{p,n})$ is aligned with $\boldsymbol{c_e}_{,n+1} : (\mathbf{e}_{n+1} - \breve{\mathbf{e}}_{p,n})$.

Therefore, the effect of the coupling between plastic and elastic response is the *alteration of the projection direction.* In Appendix A.2, remark A.2.1, it is concluded that the *altered* plastic flow vector $\overset{\triangle}{\boldsymbol{m}}_e$, defined from the following expression

$$\Delta\lambda_{n+1}^{\mathbf{e}}\, \boldsymbol{c_e}_{,n+1} : \overset{\triangle}{\boldsymbol{m}}_{\mathbf{e}} = \Delta\lambda_{n+1}^{\mathbf{e}}\, \boldsymbol{c_e}_{,n+1} : \boldsymbol{m}_{n+1}^{\mathbf{e}} - \Delta\boldsymbol{c_e}_{,n+1} : (\mathbf{e}_{n+1} - \breve{\mathbf{e}}_{p,n}), \quad (3.2.26)$$

differs from the *associated* flow vector $\boldsymbol{m}_{n+1}^e$ by terms that are one order of magnitude larger than the elastic strains.

For convenience, we summarize in BOX 3.2 the resulting nonlinear coupled system for the unknown state variables at t_{n+1}.

3.2.1 Modification of the evolution equations

Our attention is concentrated now on the system of non-linear equations listed in BOX 3.2. The presence of the unilateral constrain, represented by the loading-unloading conditions, renders the task of solving this system of equations a challenging task. A widely employed strategy [92] for tackling such problem is to interpret

I. Trial elastic stress:

$$\boldsymbol{\tau}_{n+1}^{tr} = \mathbf{F}_{n+1} \cdot \boldsymbol{S}_0 \cdot \mathbf{F}_{n+1}^{T} + \boldsymbol{c}_{\boldsymbol{e},n} : (\mathbf{e}_{n+1} - \check{\mathbf{e}}_{p,n}).$$

II. Stress update:

$$\boldsymbol{\tau}_{n+1} = \boldsymbol{\tau}_{n+1}^{tr} + \Delta \boldsymbol{c}_{\boldsymbol{e},n+1} : (\mathbf{e}_{n+1} - \check{\mathbf{e}}_{p,n}) - \sum_{\beta=1}^{3} \Delta\lambda_{n+1}^{\beta}\, \boldsymbol{c}_{\boldsymbol{e},n+1} : \boldsymbol{m}_{n+1}^{\beta}.$$

III. Update of the internal variables:

$$\xi_{n+1}^{h} = \xi_{n}^{h} - 2\xi_{n+1}^{h}\Delta\lambda_{n+1}^{e} {s_{2,n+1}}^{2}\, p_{n+1},$$

$$\xi_{n+1}^{s} = \xi_{n}^{s} + 2\Delta\lambda_{n+1}^{d} q_{n+1},$$

IV. Hardening and softening laws:

$$s_{1,n+1} = s_{1\mathrm{h}}(\xi_{n+1}^{h}), \quad s_{2,n+1} = s_{2\mathrm{h}}(\xi_{n+1}^{h}), \quad c_{v,n+1} = c_{v\mathrm{h}}(\xi_{n+1}^{h}),$$

$$c_{n+1} = c_n + \left.\frac{\partial c_{\mathrm{h}}}{\partial \xi^h}\right|_{n+1} (\xi_{n+1}^{h} - \xi_{n}^{h}) + H_{n+1}(\xi_{n+1}^{s} - \xi_{n}^{s}), \quad \text{with}$$

$$H_{n+1} = \frac{c_{n+1}}{c_0(\xi_{n+1}^{h})} H_0(\xi_{n+1}^{h}).$$

$$\kappa_{n+1}^{e} = \kappa^{e}(\xi_{n+1}^{h}), \quad \mu_{n+1}^{e} = \mu^{e}(\xi_{n+1}^{h}).$$

V. Loading/unloading conditions:

$$\Delta\lambda_{n+1}^{\beta} \geq 0,\ \phi_{n+1}^{\beta} \leq 0,\ \ \Delta\lambda_{n+1}^{\beta}\phi_{n+1}^{\beta} = 0,\ \ (\beta = 1,2,3) \qquad \text{(no sum on } \beta),$$

Box 3.2.1 *Return mapping algorithm.*

the integration as the search for the optimality conditions of a convex minimization problem. The existence and uniqueness of solution of such problem can be thus asserted in a sound way, and techniques from mathematical programming theory can be used to devise efficient and robust algorithms [44].

However, for applying with confidence these convex mathematical theorems and programming procedures, one has to be sure that the integration problem represented in BOX 3.2 can take the form of the *minimization of a convex function on a convex set*. Departure from these convexity assumptions implies that the existence and uniqueness of solution cannot be guaranteed by means of fundamental theorems of convex analysis, and hence conventional mathematical programming techniques have to be employed cautiously.

In the context of rate-independent plasticity, the set on which the solution is to be searched is determined by the yield condition. Hence, one requirement is

the convexity of the elastic domain in the space of generalized stresses. The other standard prerequisite is that the diagonal *compliance* operator

$$\mathbb{G} = \begin{bmatrix} \boldsymbol{c_e}^{-1} & \mathbf{0} \\ \mathbf{0} & \boldsymbol{D}^{-1} \end{bmatrix}, \tag{3.2.27}$$

is to be positive definite, so as to ensure that it defines a metric, i.e. $\boldsymbol{\Sigma} : \mathbb{G} : \boldsymbol{\Sigma} \geq 0$ for all $\boldsymbol{\Sigma}$. Clearly, this is not the case, since the generalized hardening moduli $\boldsymbol{D}$ (see Eq.(3.1.23)) lacks positiveness when the softening mechanism is active ($H < 0$). Hence, we see that, again, the presence of softening affects adversely the algorithmic treatment of our model by means of standard procedures.

In view of these circumstances, we are compelled to find other means to both ensure the existence and uniqueness of solution and devise an algorithm to efficiently find this solution. As it may be surmised, this is not an obvious task, due to the tightly coupled character of the governing equations. The two main sources of difficulties are the coupling between elastic and hardening behavior, symboliced by the term $\Delta \boldsymbol{c_e}_{,n+1} : (\mathbf{e}_{n+1} - \breve{\mathbf{e}}_{p,n})$ in Eq.(3.2.24), and the coupling between hardening and softening, which takes place when the return mapping algorithm places the updated stresses on the intersection between the Drucker-Prager and the elliptical yield surfaces. The following two items explained how to alleviate these difficulties by modifying the evolution equation for the internal variables without eliminating important details of the response.

3.2.1.1 Internal hardening variable

One of the basic assumptions of the proposed model is that the magnitude of the elastic strains is negligible in comparison with the irrecoverable deformations. A consequence of such proviso (see section 2.5.1) is that, in the course of monotonic increasing compressive loading history, the *internal variable ξ^h can be practically identified with the relative density η*. In appendix B.2, the validity of this hypothesis is assessed by undertaking an analysis of the monotonic hydrostatic compression of a cylindrical specimen. The conclusion drawn from this analysis is that the ratio between the relative density and internal hardening variable is bounded by

$$\frac{\eta}{\xi^h} \leq \mathbf{e}^{\frac{s_1}{\kappa^e}}. \tag{3.2.28}$$

Hence, the validity of this assumption hinges on the ratio between the hydrostatic yield stress in compression s_1 and the elastic bulk modulus κ^e. The relation $|1 - e^{s_1/\kappa^e}|$ versus η is plotted in figure 3.2 using the empirical correlations derived for the Distaloy AE powder (see section 2.5.4, Eqs. (2.5.53) and (2.5.60)). It is clear from that figure that the difference between relative density and internal hardening variable is negligible ($\sim 10^{-3}$) for almost the whole range of densities. Therefore the experimentally *calibrated values of κ^e and s_1 for a typical Distaloy AE support the hypothesis that $\xi^h \approx \eta$* in monotonic increasing compressive loading history.

The only objection that can be raised against this hypothesis is when the *relative density approaches unity*. According to arguments set out in section 2.5.4, the

hydrostatic yield strength in compression asymptotes to infinity in this event, and since κ^e remains bounded, the hypothesis of $\xi^h \approx \eta$ would no longer hold. However, note that in this case neither the kinematics assumptions regarding the additive decomposition of $\mathbf{d}$ and $\mathbf{e}$ are valid, and, thus, the usefulness of the numerical prediction as a whole might be questionable. .

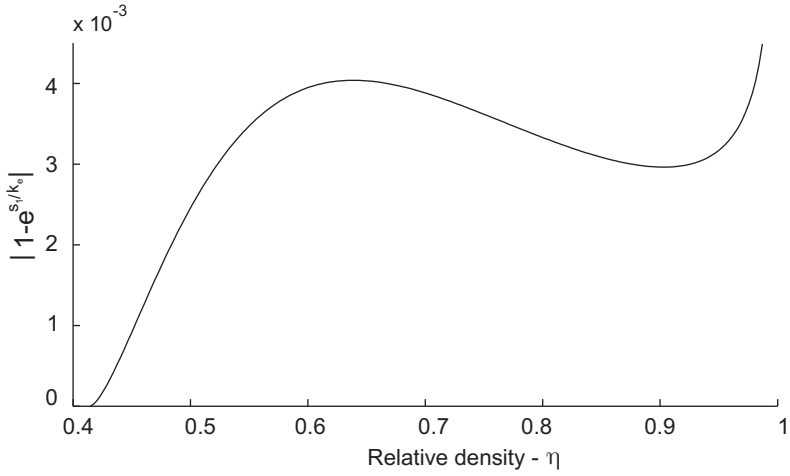

Figure 3.2 *Function $|1 - e^{s_1/\kappa^e}|$ vs η for a typical Distaloy AE powder.*

The following proposition demonstrates that the hypothesis of small elastic strains can be exploit further to derive an approximation of the discrete evolution equation (3.2.7) for the internal hardening variable.

Proposition 3.2.1. *Under the assumption of small elastic deformations, an approximation for the update of the internal hardening variable is given by*

$$\xi^h_{n+1} = \xi^h_n \mathcal{H}_J(\Delta\lambda^e_{n+1}(\eta_{n+1} - \eta_n), \frac{\eta_n}{\eta_{n+1}})\frac{\eta_{n+1}}{\eta_n}, \tag{3.2.29}$$

where $\mathcal{H}_J(\bullet)$ is the function defined by:

$$\mathcal{H}_J(x, y) = \begin{cases} 1, & x > 0, \\ y, & x \leq 0, \end{cases} \tag{3.2.30}$$

and $\eta_{n+1} = \dfrac{\eta_0}{\det \boldsymbol{F}_{n+1}}$ and $\eta_n = \dfrac{\eta_0}{\det \boldsymbol{F}_n}$ denote the relative densities at time t_{n+1} and t_n, respectively.

Proof.

The proof follows easily from the conservation of mass equation and the assumption of negligible elastic strains.

□

The foregoing result admits also an interpretation in the p-q plane. The following proposition is useful in this regard.

Proposition 3.2.2. *The trial stress defined in Eq.(3.2.18) can be alternatively expressed as:*

$$\boldsymbol{\tau}_{n+1}^{tr} = \overset{\diamond}{\boldsymbol{\tau}}_n + \Delta t_{n+1}\, \boldsymbol{c}_{\boldsymbol{e},n} : \boldsymbol{d}_{n+1}, \tag{3.2.31}$$

where $\overset{\diamond}{\boldsymbol{\tau}}_n$ *is defined through the following formula:*

$$\overset{\diamond}{\boldsymbol{\tau}}_n = \breve{\boldsymbol{\tau}}_n - (\breve{\boldsymbol{c}}_{\boldsymbol{e},n} - \boldsymbol{c}_{\boldsymbol{e},n}) : (\boldsymbol{e}_{n+1} - \breve{\boldsymbol{e}}_{p,n}), \tag{3.2.32}$$

where $\breve{\boldsymbol{\tau}}_n = \varphi_*^{\Delta}(\boldsymbol{\tau}_n)$ *and* $\breve{\boldsymbol{c}}_{\boldsymbol{e},n} = \varphi_*^{\Delta}(\boldsymbol{c}_{\boldsymbol{e},n})$.

Proof. First, the constitutive equation at time t_n is transformed to configuration Ω_{n+1} via the incremental push forward operator $\varphi_*^{\Delta}(\bullet)$[6], i.e.:

$$\varphi_*^{\Delta}(\boldsymbol{\tau}_n) = \varphi_*(\boldsymbol{S}_0) + \varphi_*^{\Delta}(\boldsymbol{c}_{\boldsymbol{e},n}) : \varphi_*^{\Delta}(\mathbf{e}_{n+1} - \mathbf{e}_n)\,. \tag{3.2.33}$$

This result is subtracted from Eq.(3.2.18), and upon rearrangement, we get

$$\begin{aligned}\boldsymbol{\tau}_{n+1}^{tr} &= \varphi_*^{\Delta}(\boldsymbol{\tau}_n) - (\varphi_*^{\Delta}(\boldsymbol{c}_{\boldsymbol{e},n}) - \boldsymbol{c}_{\boldsymbol{e},n}) : \varphi_*^{\Delta}(\mathbf{e}_n - \mathbf{e}_{p,n}) + \boldsymbol{c}_{\boldsymbol{e},n} : (\mathbf{e}_{n+1} - \varphi_*^{\Delta}(\mathbf{e}_n)) \\ &= \breve{\boldsymbol{\tau}}_n - (\breve{\boldsymbol{c}}_{\boldsymbol{e},n} - \boldsymbol{c}_{\boldsymbol{e},n}) : (\mathbf{e}_{n+1} - \breve{\mathbf{e}}_{p,n}) + \boldsymbol{c}_{\boldsymbol{e},n} : (\mathbf{e}_{n+1} - \varphi_*^{\Delta}(\mathbf{e}_n)).\end{aligned} \tag{3.2.34}$$

Using the properties of the push forward operator, the last term on the right-hand side of the above equation can be written as:

$$\boldsymbol{c}_{\boldsymbol{e},n} : (\mathbf{e}_{n+1} - \varphi_*^{\Delta}(\mathbf{e}_n)) = \boldsymbol{c}_{\boldsymbol{e},n} : \varphi_*(\mathbf{E}_{n+1} - \mathbf{E}_n)\,. \tag{3.2.35}$$

Finally, the discrete version of the rate of deformation tensor, which is given by

$$\mathbf{d}_{n+1} = \varphi_*\Big(\dot{\mathbf{E}}\Big) \approx \frac{1}{\Delta t_{n+1}} \varphi_*(\mathbf{E}_{n+1} - \mathbf{E}_n)\,, \tag{3.2.36}$$

is substituted into Eq.(3.2.34), yielding the desired result. □

This alternative format for the trial elastic stress is particularly appealing because it can be related to the modified evolution equation (3.2.29). Indeed, obtaining the volumetric part of Eq.(3.2.31):

$$p_{n+1}^{tr} = \breve{p}_n + \Delta t_{n+1}\, \kappa_n^e\, \mathrm{tr}\, \mathbf{d}_{n+1}. \tag{3.2.37}$$

Using the spatial version of the conservation of mass equation, the above equation can be expressed as

$$p_{n+1}^{tr} = \breve{p}_n + \kappa_n^e \log \frac{\eta_n}{\eta_{n+1}}. \tag{3.2.38}$$

In virtue of the preceding equation, it turns out that a compressive deformation ($\eta_{n+1} > \eta_n$) is characterized by a component of $\boldsymbol{\tau}_{n+1}^{tr} - \overset{\diamond}{\boldsymbol{\tau}}_n$ along the p-axis of the vector *negative*, i.e.

$$p_{n+1}^{tr} \geq \breve{p}_n \quad \Rightarrow \quad \eta_n \geq \eta_{n+1}. \tag{3.2.39}$$

[6]The push forward of the double the contraction between a fourth-order tensor and second-order tensor is equal to the double contraction of the push forward of both tensors, i.e. $\varphi_*(\boldsymbol{c}_{\boldsymbol{e}} : \mathbf{e}) = \varphi_*(\boldsymbol{c}_{\boldsymbol{e}}) : \varphi_*(\mathbf{e})$.

It proves expedient to use this result for interpreting graphically the evolution equation (3.2.29). In figure 3.3, several plausible trial stress states are plotted (labelled from A to F). Only in the situation[7] A the internal hardening variable evolves, since the elliptical yield surface is clearly active ($\Delta\lambda^e_{n+1} > 0$), and the deformation is compressive $p^{tr}_{n+1} < \breve{p}_n$. In the situation encountered in B, note that $\Delta\lambda^e_{n+1} > 0$, but $p^{tr}_{n+1} > \breve{p}_n$, hence $\xi^h_{n+1} = \xi^h_n$. The other scenarios, C, D and E, represent also states in which the internal variable remains in its converged value ξ^h_n.

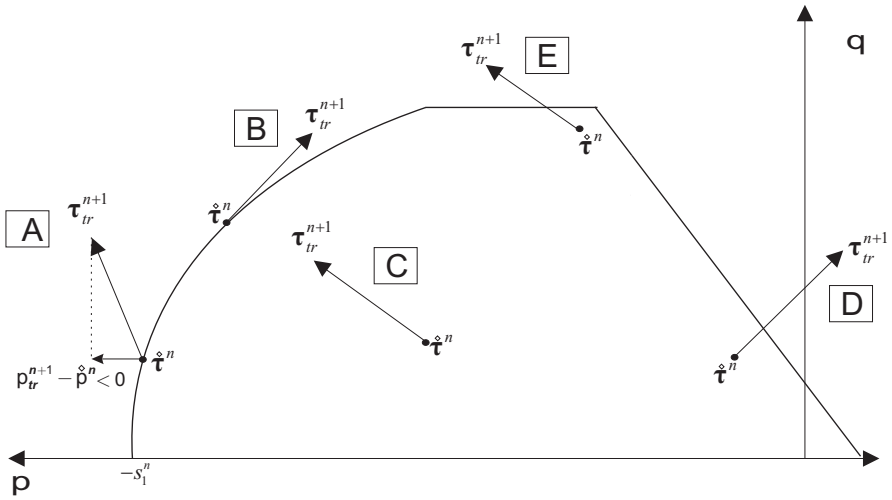

Figure 3.3 *Different scenarios for the evolution of the internal hardening variable. Only in situation labelled as A, the internal hardening evolves, i.e.* $\xi^h_{n+1} > \xi^h_n$.

3.2.1.2 Internal softening variable

The experimental correlations set forth in sections 2.5.4 and 2.5.5 were obtained by monitoring the evolution of the corresponding yield stress, say the cohesion c, as one of the internal variables increases, say ξ^h, and whilst the other (ξ^s) is held fixed. Thus, the hardening response is calibrated assuming that no degradation of mechanical strength -softening- occurs during the experiment, and vice versa, *softening mechanism is calibrated presuming that* ξ^h *does not evolve.*

The hardening behavior is linked to yielding on the elliptical cap surface through the plastic multiplier $\dot{\lambda}^e$, and strain softening is associated to yielding on the Drucker-Prager surface through $\dot{\lambda}^d$. In accordance to Koiter's rule, when the updated stress lies on the intersection $\partial\mathbb{E}^{d,e}_{\boldsymbol{\tau}}$ between both yield surfaces, the consistency parameters $\dot{\lambda}^d$ and $\dot{\lambda}^e$ are nonzero and, therefore, the *hardening and softening*

[7] For illustration purposes, $\overset{\diamond}{\boldsymbol{\tau}}_n$ in situation A have been considered *consistent* with the yield condition, i.e $\phi^e(\overset{\diamond}{\boldsymbol{\tau}}_n, \xi^h_n) = 0$. However, observe that this condition is not necessarily satisfied, since $\overset{\diamond}{\boldsymbol{\tau}}_n \neq \boldsymbol{\tau}_n$ (only in small strains $\overset{\diamond}{\boldsymbol{\tau}}_n = \boldsymbol{\tau}_n$ holds).

mechanism act concurrently. From the physical standpoint, this implies that hardening and softening counteract each other, that is, the strain hardening produced by densification is partially counterbalanced by the softening mechanism. Which of these effects dominates the response eventually cannot be known a priori.

From an algorithmic point of view, this simultaneous occurrence of both hardening and softening may cause problems of convergence during the iterations of the return mapping algorithm. It is the author's experience that under such circumstances the iterates move on and off the active constraints and cause the algorithm to zigzag, placing in each iteration the solution on a different location without converging to any value.

Besides, in a fully implicit integration scheme, inconsistencies during the local integration of the constitutive equations at any point of the body generally manifest themselves in other stages of the computational cycle, affecting, for instance, the convergence of the global iterations. By contrast, in our algorithmic treatment, the internal forces at t_{n+1} are computed using stresses stemming from the *IMPLEX* integration scheme, and the updated values arising from the implicit integration are used only, via extrapolation, in subsequent time steps. Consequently, *the convergence of the global iteration scheme may mask the lack of convergence of the local iterative procedure* associated to the implicit integration, giving a false sense of security by suggesting that everything is correct, while in fact the computed results may be utterly misleading.

These computational drawbacks motivate the following simplification of the discrete evolution equation (3.2.8) for the internal softening variable:

$$\xi^s_{n+1} = \xi^s_n + \big(1 - \mathcal{H}(\Delta\lambda^e_{n+1})\big)\big(1 - \mathcal{H}(\Delta\lambda^v_{n+1})\big)\, 2\,\Delta\lambda^d_{n+1} q_{n+1}. \tag{3.2.40}$$

where $\mathcal{H}(\bullet)$ stands for the Heaviside function. This modification implies that the occurrence of strain softening is precluded when the updated stress lies on either $\partial\mathbb{E}^{d,e}_{\boldsymbol{\tau}}$ or $\partial\mathbb{E}^{d,v}_{\boldsymbol{\tau}}$, i.e., the interception points of the Drucker-Prager surface with the cap surface and with the Von-Mises surface, respectively. It is emphasized again that, according to the arguments given in the beginning paragraph, there are no empirical laws accounting for the simultaneous occurrence of hardening and softening an, thus, this modification does not actually compromise the correctness of the hardening and softening laws derived in sections 2.5.4 and 2.5.5.

3.2.2 Return mapping algorithm using a fractional-step based method.

In this section, the procedure to solve the return-mapping equations is described. The distinguishing feature of this procedure is the *iterative process adopted to "return" the trial stress to the yield surface*, which is not a standard Newton-Raphson scheme or variants thereof. The algorithmic procedure is summarized in BOX 3.2.2.

The proposed methodology can be viewed as a natural extension of the two-step algorithm derived from the elastic-plastic operator split, in the sense that it consists in the *repetitive application of a predictor-corrector procedure*. In each iteration, the *predictor* state arises from *freezing the internal variables* and solving the resulting

1. Compute trial elastic stress

$$\boldsymbol{\tau}_{n+1}^{tr} = \mathbf{F}_{n+1} \cdot \boldsymbol{S}_0 \cdot \mathbf{F}_{n+1}^T + \boldsymbol{c}_{\boldsymbol{e},n} : (\mathbf{e}_{n+1} - \check{\mathbf{e}}_{p,n}), \tag{3.2.41}$$

$$\mathbb{J}_{n+1}^{act,tr} = \Big\{ \beta \in \{e,d,v\} \;\mid\; \phi_{n+1}^{\beta,tr} > 0 \Big\}. \tag{3.2.42}$$

IF $\mathbb{J}_{n+1}^{act,tr} = \emptyset$ THEN
  Set $(\bullet)_{n+1} = (\bullet)_{n+1}^{tr}$ EXIT
ELSE
  k =1, $\mathbb{J}^{act,(1)} = \mathbb{J}_{n+1}^{act,tr}$, $\boldsymbol{\xi}^{(0)} = [\xi_n^h, \xi_n^s]$,
ENDIF

2. *Predictor step* of the FSM return mapping algorithm. Obtain $\boldsymbol{\tau}^{(k)}$ and $\Delta\lambda^{\beta,(k)}$, $\beta \in \mathbb{J}^{act,(k)}$ solving*

$$\boldsymbol{\tau}^{(k)} = \boldsymbol{\tau}_{n+1}^{tr} + \Delta \boldsymbol{c}_{\boldsymbol{e}}^{(k-1)} : (\mathbf{e}_{n+1} - \check{\mathbf{e}}_{p,n}) - \sum_{\beta \in \mathbb{J}^{act,(k)}} \Delta\lambda^{\beta,(k)}\, \boldsymbol{c}_{\boldsymbol{e}}^{(k-1)} : \boldsymbol{m}^{\beta,(k)}, \tag{3.2.43}$$

$$\phi^{\beta}(\boldsymbol{\tau}^{(k)}, \boldsymbol{\xi}^{(k-1)}) = 0, \; \forall \beta \in \mathbb{J}^{act,(k)}, \tag{3.2.44}$$

where

$$\boldsymbol{c}_{\boldsymbol{e}}^{(k-1)} = \boldsymbol{c}_{\boldsymbol{e}}(\boldsymbol{\xi}^{(k-1)}), \; \boldsymbol{m}^{\beta,(k)} = \boldsymbol{m}^{\beta}(\boldsymbol{\tau}^{(k)}, \boldsymbol{\xi}^{(k-1)}). \tag{3.2.45}$$

(*If $\mathbb{J}^{act,(k)}$ contains more than two indices, this system has to be solved for each pair of indices).

IF $\Delta\lambda^{\beta,(k)} < 0$, for any $\beta \in \mathbb{J}^{act,(k)}$
  Reset $\mathbb{J}^{act,(k)} = \Big\{ \beta \in \{e,v,d\} \;\mid\; \Delta\lambda^{\beta,(k)} > 0 \Big\}$.
  Goto to step 2.
ENDIF

3. *Corrector step* . Update of the internal variables.

$$\xi^{h,(k)} = \xi_n^h\, \mathcal{H}_J(\Delta\lambda^{e,(k)}(\eta_{n+1} - \eta_n), \frac{\eta_n}{\eta_{n+1}}) \frac{\eta_{n+1}}{\eta_n}, \tag{3.2.46}$$

$$\xi^{s,(k)} = \xi_n^s + \big(1 - \mathcal{H}(\Delta\lambda^{e,(k)})\big)\big(1 - \mathcal{H}(\Delta\lambda^{v,(k)})\big)\, 2\, \Delta\lambda^{d}(\boldsymbol{\tau}^{(k)}, \boldsymbol{\xi}^{(k)})\, q^{(k)}. \tag{3.2.47}$$

4. Check convergence
IF $|\phi^{\beta}(\boldsymbol{\tau}^{(k)}, \boldsymbol{\xi}^{(k)})| < TOL_1, \; \forall\, \beta \in \mathbb{J}^{act,(k)}$ AND $\|\boldsymbol{\xi}^{(k)} - \boldsymbol{\xi}^{(k-1)}\| < TOL_2$
  Set $(\bullet)_{n+1} = (\bullet)_k$ EXIT
ELSE
  Set $k \leftarrow k+1$. Goto step 2.
ENDIF

Box 3.2.2 *Basic steps of FMS return mapping algorithm.*

return-mapping problem (Eqs. (3.2.43) and (3.2.44) in BOX 3.2.2). The *corrector* step consists in *updating* the internal variables (Eqs. (3.2.46) and (3.2.47)) using the stress state computed in the predictor stage . The cycle is repeated until a convergence criterion is met. Note that this procedure can be also regarded as a *fractional step method*[111], extensively applied in fluid mechanics [8], since it is based on the *decoupling of the evolution equations for the the plastic strains and the internal variables*. For this reason, we shall henceforth use the shorthand denotation *FSM* method for designating the proposed procedure.

In accordance with the proposal put forward by Simo[92], the *set of active constraints* $\mathbb{J}^{act}$ is updated *during the iterative process*, specifically at the end of the predictor stage (see BOX 3.2.2). If it turns out that any of the presumed active constrains is negative, then the predictor-corrector scheme is halted and the first step is performed again with the new set of active constrains, obtained from dropping the corresponding indices from $\mathbb{J}^{act,(k)}$. One of the most attractive feature of the FSM method lies precisely on the simplicity in the determination of this set. Such simplicity can be attributed mainly to the particular functional forms of both the yield condition and the plastic flow vector. Indeed, note that the yield condition is constructed by a quadratic function (the elliptical cap yield surface $\partial\mathbb{E}^e_{\boldsymbol{\tau}}$) and two affine functions (the Drucker-Prager yield surface $\partial\mathbb{E}^d_{\boldsymbol{\tau}}$ and the Von Mises yield surface $\partial\mathbb{E}^e_{\boldsymbol{\tau}}$). Then, it follows that the intersection between those curves ($\partial\mathbb{E}^{e,d}_{\boldsymbol{\tau}}, \partial\mathbb{E}^{e,v}_{\boldsymbol{\tau}}, \partial\mathbb{E}^{d,v}_{\boldsymbol{\tau}}$) can be obtained straightforwardly in *closed form*. Moreover, inspection of (3.1.10), (3.1.11) and (3.1.12) reveals that the plastic flow vector on each surface can be viewed as an *affine transformation* of the Kirchhoff stress tensor, namely

$$\boldsymbol{m}^{\beta} = 2\, dev\, \boldsymbol{\tau} + (u^{\beta}\, p + v^{\beta})\mathbf{1}, \tag{3.2.48}$$

where the coefficients u^{β} and v^{β} for each surface are given by

$$u^{\mathbf{e}} = \frac{2}{3}s_2^2, \quad u^d = u^v = 0, \tag{3.2.49}$$

$$v^e = v^v = 0, \quad v^d = \frac{1}{3}\gamma\, c\, \alpha. \tag{3.2.50}$$

To explain why the proposed formats of both the yield condition and the plastic flow vectors allow considerable simplification on the update of the set $\mathbb{J}^{act,(k)}$, let us consider, for instance, that $\mathbb{J}^{act,(k)} = \{d, v\}$, i.e. the Drucker-Prager and the Von Mises yield surfaces are active at iteration k. The enforcement of the plastic consistency conditions $\phi^{d,(k)} = 0$ and $\phi^{v,(k)} = 0$ places the value of the stress[8] $\boldsymbol{\tau}^{(k)}$ at the interception point $\partial\mathbb{E}^{d,v}_{\boldsymbol{\tau}}$, which, as pointed out above, can be computed in closed form. Equation (3.2.43) (see BOX 3.2.2) for the particular case in which $\mathbb{J}^{act,(k)} = \{d, v\}$ takes the form:

$$\boldsymbol{\tau}^{(k)} = \boldsymbol{\tau}^{tr}_{n+1} - \sum_{\beta\in\{d,v\}} \Delta\lambda^{\beta,(k)}\, \boldsymbol{c}_{\boldsymbol{e}}^{(k-1)} : \boldsymbol{m}^{\beta,(k)}. \tag{3.2.51}$$

[8]For notational simplicity, we omit the index $n+1$ to those variables that are updated during the iterative process, i.e. $\boldsymbol{\tau}^{(k)} = \boldsymbol{\tau}^{n+1,(k)}$

Projection of the above equation onto the p-q plane yields the following scalar equations

$$p^{tr}_{n+1} - p^{(k)} = \sum_{\beta\in\{d,v\}} \Delta\lambda^{\beta,(k)} \big(3\kappa^{e,(k-1)}(u^{\beta,(k-1)}\, p^{(k)} + v^{\beta,(k-1)})\big), \tag{3.2.52}$$

$$q^{tr}_{n+1} - q^{(k)} = \sum_{\beta\in\{d,v\}} \Delta\lambda^{\beta,(k)} (4\mu^{e,(k-1)}\, q^{(k)}). \tag{3.2.53}$$

The only unknowns in the above equations are the plastic multipliers $\Delta\lambda^{d,(k)}$ and $\Delta\lambda^{v,(k)}$. Thus, Eqs. (3.2.52) and (3.2.53) constitute a *linear* system of two equations with two unknowns, that can also be easily solved in *closed form*. To disclose whether the two constraints are active, one has to check if both $\Delta\lambda^{d,(k)}$ and $\Delta\lambda^{v,(k)}$ are positive. If not, the index associated to the negative plastic multiplier is discarded from the set of active constraints, and the iteration is restarted.

The question of uniqueness of solution of the predictor stage is easily resolved, in view of the *convexity of the elastic domain in stress space*. Furthermore, we shall see later that this solution can be also obtained in *closed form*, regardless onto which yield surface the trial stress is projected. This reduction of the equation solving effort is another motivation for favoring the FSM method over other conventional procedures.

However, the issue of existence of uniqueness of solution of the global algorithm deserves more consideration, since it is not apparent which conditions guarantee such desirable feature. To make matters as concrete as possible, we shall ascertain these conditions separately for each representative set of active constraints.

***CASE I*: Elliptical yield surface**

Consider a trial stress state such that $\mathbb{J}^{act,tr}_{n+1} = \{e\}$. The *predictor stage* at the first iteration ($k = 1$) involves the solution of the following system of equations:

$$p^{(k)} = \frac{p^{(k-1)}_{up}}{1 + 2\,\kappa^{e,(k-1)}\,\Delta\lambda^{e,(k)} {s_2^{(k-1)}}^2}, \tag{3.2.54}$$

$$q^{(k)} = \frac{q^{(k-1)}_{up}}{1 + 4\,\mu^{e,(k-1)}\,\Delta\lambda^{e,(k)}}, \tag{3.2.55}$$

$$\phi^{e,(k)} = {q^{(k)}}^2 + {s_2^{(k-1)}}^2\, {p^{(k)}}^2 - (s_1^{(k-1)} s_2^{(k-1)})^2 = 0, \tag{3.2.56}$$

where, for this first iteration, $p^{(k-1)}_{up} = p^{(0)}_{up} = p^{tr}_{n+1}$ and $q^{(k-1)}_{up} = q^{(0)}_{up} = q^{tr}_{n+1}$, and $(\bullet)^{(k-1)} = (\bullet)^n$. Thus, the only unknown quantities in the above are $p^{(k)}$, $q^{(k)}$ and $\Delta\lambda^{e,(k)}$. Once the values of $p^{(k)}$ y $q^{(k)}$ have been obtained, the stress tensor can be calculated as

$$\boldsymbol{\tau}^{(k)} = p^{(k)}\,\mathbf{1} + \frac{q^{(k)}}{q^{tr}_{n+1}}\, dev\, \boldsymbol{\tau}^{tr}_{n+1}. \tag{3.2.57}$$

Notice that the flow on the elliptical yield surface is associative. Thus, according to the geometric interpretation suggested by *Simo* [92], solving the above system

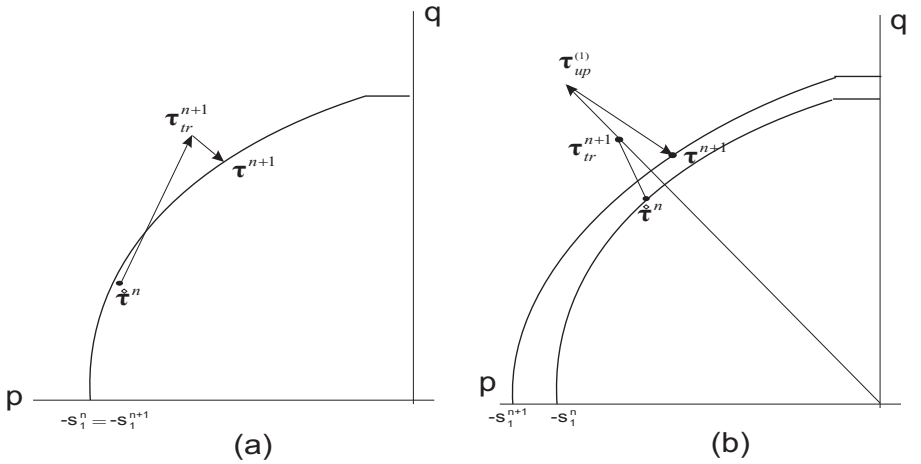

Figure 3.4 *FSM scheme when only the elliptical yield surface is active. (a) No densification occurs . (b) Densification takes place.*

amounts to find the *closest point projection* of the trial stress onto the elliptical yield surface in the metric defined by $\boldsymbol{c}_{\boldsymbol{e}}^{(k-1)}$. This case has been studied extensively and powerful general methods have been established for their solution. Furthermore, this elliptical model falls within the class of general *quadratic models of classical plasticity*[9]. The *existence and uniqueness* of the solution are guaranteed in this case by virtue of the convexity of the yield condition. Furthermore, this unique solution can be computed by solving a *quartic equation* [92]. In particular, after some algebra, Eqs. (3.2.54), (3.2.55) and (3.2.56) can be reduced to the following quartic polynomial in $q^{(k)}$:

$$a_4\, q^4 + a_3\, q^3 + a_2\, q^2 + a_1\, q + a_0 = 0, \tag{3.2.58}$$

where the coefficients $a_i, i = 1 \ldots 4$ are given by

$$a_4 = {b_2}^2, \quad a_3 = 2\, b_1\, s_2^2\, q_{up}\, b_2, \quad a_2 = s_2^2\big((q_{up}\, s_2\, b_1)^2 + {p_{up}}^2 - s_1^2 {b_2}^2\big), \tag{3.2.59}$$

$$a_1 = -2\, s_2^2 (s_1\, s_2)^2\, b_1\, q_{up} b_2, \quad a_0 = -(s_1\, s_2^3\, b_1\, q_{up})^2, \tag{3.2.60}$$

and

$$b_2 = (1 - b_1\, s_2^2), \quad b_1 = \frac{\kappa^e}{2\,\mu^e}. \tag{3.2.61}$$

The unique positive root of Eq.(3.2.58) in the interval $[0, s_1\, s_2]$ can be determined in *closed form* by a modified version of a classical solution procedure for quartic equations[92].

The update of ξ^h, see Eq.(3.2.46), the so-called *corrector stage*, is solely governed by the change of relative density (which is prescribed during the iterations) and

[9]Note that during the predictor stage of the FSM method, the internal variables do not evolve, hence we can say that this step represents a problem of *perfect plasticity*.

the nonzero character of $\Delta\lambda^{e,(k)}$. Hence, the value of $\boldsymbol{\tau}^{(k)}$ is not actually needed for computing $\xi^{h,(k)}$. To improve the performance of the algorithm (see BOX 3.2.2), it proves convenient thus to check before undertaking the predictor stage if $\eta_{n+1} > \eta_n$. Such being the case, the predictor step for $k = 1$ can be *skipped* and one can directly update the internal variable as $\xi^{h,(1)} = \xi^h_n\, \eta_{n+1}/\eta_n$. Then, the predictor step is accomplished by solving equations Eqs. (3.2.45),(3.2.46) and (3.2.47), with $p^{(k-1)}_{up}$ and $q^{(k-1)}_{up}$ defined in this case as

$$p^{(k-1)}_{up} = p^{tr}_{n+1} + \Delta\kappa^{e,(k-1)}\, \mathrm{tr}\,(\mathbf{e}_{n+1} - \breve{\mathbf{e}}_{p,n}), \tag{3.2.62}$$

$$q^{(k-1)}_{up} = \|dev\, \boldsymbol{\tau}^{tr}_{n+1} + 2\,\Delta\mu^{e,(k-1)}\, dev\,(\mathbf{e}_{n+1} - \breve{\mathbf{e}}_{p,n})\|. \tag{3.2.63}$$

Once obtained $(p^{(k)}, q^{(k)})$, the stress is updated as

$$\boldsymbol{\tau}^{(k)} = p^{(k)}\,\mathbf{1} + \frac{q^{(k)}}{q^{(k-1)}_{up}}\left(dev\, \boldsymbol{\tau}^{tr}_{n+1} + 2\,\Delta\mu^{e,(k-1)}\, dev\,(\mathbf{e}_{n+1} - \breve{\mathbf{e}}_{p,n})\right). \tag{3.2.64}$$

In summary, when only the elliptical yield surface is active, convergence of the iterative predictor-corrector scheme is actually achieved only in *one effective iteration*. If no densification occurs ($\eta_{n+1} \leq \eta_n$), then $\xi^h_{n+1} = \xi^h_n$ and the updated stress is computed projecting the trial stress $\boldsymbol{\tau}^{tr}_{n+1}$ onto the elliptical surface, which, in turn, involves the solution of a quartic equation. If densification takes place ($\eta_{n+1} > \eta_n$), the internal hardening variable is updated and the stress $\boldsymbol{\tau}_{n+1}$ is obtained as the projection of a *modified* trial state onto the elliptical yield surface defined by ξ^h_{n+1}. This procedure is outlined in BOX (3.2.2) and illustrated in figure 3.4.

***CASE II*: Elliptical and Drucker-Prager/Von Mises yield surface**

Consider now a situation in which $\mathbb{J}^{act,(1)} = \{e, d\}$ (see figure 3.5.a). This means that the trial state lies within the *cone* defined by the vectors $\boldsymbol{c}^{(0)}_{\boldsymbol{e}} : \boldsymbol{m}^{e,(1)}$ and $\boldsymbol{c}^{(0)}_{\boldsymbol{e}} : \boldsymbol{m}^{d,(1)}$ emanating from $\boldsymbol{\tau}^{(1)}$. The stress state $\boldsymbol{\tau}^{(1)}$ is simply obtained as the intersection point between the Drucker-Prager line and the elliptical cap. The expression for this intersection point is given by:

$$p_{e,d} = \frac{2\,c\,\alpha - 2\,s_2\,\sqrt{(\alpha^2 + s_2^2)s_1^2 - c^2}}{2\,(\alpha^2 + s_2^2)}, \tag{3.2.66}$$

$$q_{e,d} = c - \alpha\, p_{e,d}. \tag{3.2.67}$$

Remark 3.2.3. A crucial observation concerning the existence of solution is that the expression under the radical in Eq.(3.2.66) must be positive. In figure 3.5.b, this term is plotted against the internal hardening variable for the Distaloy AE calibrated in the previous chapter. From this plot it can be concluded that this condition is satisfied for the considered material, a fact that could be expected[10] as

[10]Care is to be exercised to ensure that this proviso is satisfied in the range of low densities, since curve fitting may lead to inconsistencies in this respect.

1. Initializations

$$k = 1, \quad \xi^{h,(0)} = \xi^h_n, \quad \xi^s_{n+1} = \xi^s_n,$$

2. Predictor stage

$$\boldsymbol{\tau}^{(k-1)}_{up} = \boldsymbol{\tau}^{tr}_{n+1} + \Delta \boldsymbol{c}^{(k-1)}_{\mathbf{e}} : (\mathbf{e}_{n+1} - \breve{\mathbf{e}}_{p,n}). \tag{3.2.65}$$

IF $\eta_{n+1} > \eta_n$
Goto step 3
ELSE
Compute $\boldsymbol{\tau}^{(k)}$ as the projection of $\boldsymbol{\tau}^{(k-1)}_{up}$ onto the yield surface defined by $\xi^{h,(k-1)}$ ($\sim$ solve the *quartic equation* (3.2.58))
ENDIF

3. *Corrector step*

$$\xi^{h,(k)} = \xi^h_n \mathcal{H}_J(\eta_{n+1} - \eta, \frac{\eta_n}{\eta_{n+1}}) \frac{\eta_{n+1}}{\eta_n}.$$

4. Check convergence

IF $|\phi^{\mathbf{e}}(\boldsymbol{\tau}^{(k)}, \xi^{h,(k)})| < TOL_1$, AND $\|\xi^{h,(k)} - \xi^{h,(k-1)}\| < TOL_2$
Set $(\bullet)_{n+1} = (\bullet)_k$ EXIT
ELSE
Set $k \leftarrow k + 1$. Goto step 2.
ENDIF

Box 3.2.3 *FSM method when only the elliptical yield surface is active ($\mathbb{J}^{act,tr}_{n+1} = \{e\}$). Since the update of the internal hardening variable (step 3) does not depend on the stress state computed in step 2, the predictor stage has to be accomplished only once, i.e. only one effective iteration is required for achieving convergence.*

the hydrostatic yield strength in compression s_1 is much larger than the cohesion c ($s_1 \gg c$). Furthermore, it follows from Eq.(3.2.66) that

$$p < 0 \iff s_1^2(s_2^2 + \alpha^2) > c^2\,(1 - 4\,\alpha^2). \tag{3.2.68}$$

Since $\alpha \sim 2 > 0.25$, Eq.(3.2.68) reveals that the intersection point $\partial\mathbb{E}^{e,d}_{\boldsymbol{\tau}}$ lies for all ξ^h in the *second quadrant* of the $p - q$ plane ($p < 0$). This observation further substantiates the correctness of one of our basic hypothesis made in the previous chapter (see Eq.(2.5.26)).

Since, in virtue of Eq.(3.2.40), the internal softening variable is unaffected when $\Delta\lambda^e > 0$, then the corrector stage of the FSM scheme *only involves the update of* ξ^h, in a manner analogous to the procedure described in the previous case ($\mathbb{J}^{act} = \{e\}$). The only difference may arise in the update of the set of active constraints. In

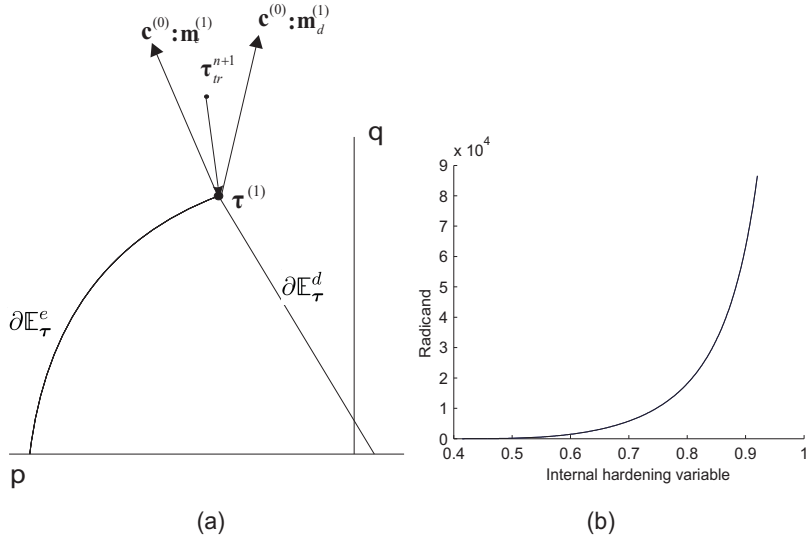

Figure 3.5 *(a) Case in which the Drucker-Prager and elliptical yield surfaces are active in the first iteration of the FSM scheme. (b) Radicand of expression (3.2.66) versus the internal hardening variable. This graph has been obtained using the calibrated curves for the Distaloy AE presented in the previous chapter. The positiveness of these values ensures that the intersection $\partial\mathbb{E}_{\boldsymbol{\tau}}^{d,e}$ exists for all ξ^h.*

iteration $k = 2$, this set may remain unaltered ($\mathbb{J}^{act,(2)} = \{e, d\}$) or change to either $\mathbb{J}^{act,(2)} = \{e\}$ or $\mathbb{J}^{act,(2)} = \{d\}$.

If $\eta_{n+1} > \eta_n$, the former scenario $\mathbb{J}^{act,(2)} = \{e, d\}$ would require only to compute again the intersection between the updated yield surfaces (see figure 3.6.a). Thus, convergence would be achieved in only *two iterations* of the FSM scheme. The situation $\mathbb{J}^{act,(2)} = \{e\}$ is depicted in figure 3.6.b. The *modified* trial stress $\boldsymbol{\tau}_{up}^{(1)}$ (see Eq.(3.2.65) in BOX 3.2.2) is placed *outside* the cone defined by $\boldsymbol{c}_{\boldsymbol{e}}^{(1)} : \boldsymbol{m}^{e,(2)}$ and $\boldsymbol{c}_{\boldsymbol{e}}^{(1)} : \boldsymbol{m}^{d,(2)}$, and, hence, the plastic multiplier $\Delta\lambda^{d,(2)}$ would result negative. In this case the updated stress would be computed by projecting $\boldsymbol{\tau}_{up}^{(1)}$ back to elliptical cap (solving the quartic equation (3.2.58)). Therefore, a total of *three predictor-corrector iterations* would be necessary to converge.

It is worth noting that the other situation $\mathbb{J}^{act,(2)} = \{d\}$ is not *feasible*, that is, if the elliptical yield surface is active in the first iteration of the FSM procedure, it remains necessarily active also in the second iteration. To show this, consider, for simplicity, an unstressed configuration $\boldsymbol{S}_0 = \boldsymbol{0}$. The statement $\Delta\lambda^{e,(2)} > 0$ is tantamount to requiring that the modified trial stress $\boldsymbol{\tau}_{up}^{(1)}$ lies in the region above the straight line, in the $p - q$ plane, emanating from $\boldsymbol{\tau}^{(2)}$ and with direction $\boldsymbol{c}_{\boldsymbol{e}}^{(1)} : \boldsymbol{m}^{d,(2)}$ (see figure 3.5.b). To avoid a clash with the superscripts for the iterations, we simply denote the projections of $\boldsymbol{\tau}^{(2)}$, $\boldsymbol{\tau}_{up}^{(1)}$ and $\boldsymbol{\tau}_{n+1}^{tr}$ onto the $p - q$ plane by (p_n, q_n), (p_u, q_u) and (p_t, q_t), respectively. Hence the condition we have

to ascertain can be write as

$$q_u \geq q_n + a\,(p_n - p_u), \tag{3.2.69}$$

wherein a denotes the slope of the line $a = \kappa^e \gamma c \alpha / (2\mu^e q_u) > 0$. From expressions (3.2.62) and (3.2.63), it follows that

$$p_t = \kappa_n^e \mathrm{tr}\,\mathbf{e}_{n+1} - \breve{\mathbf{e}}_{p,n}, \qquad p_u = \kappa_{n+1}^e \mathrm{tr}\,\mathbf{e}_{n+1} - \breve{\mathbf{e}}_{p,n}, \tag{3.2.70}$$

$$q_t = 2\,\mu_n^e \|dev\mathbf{e}_{n+1} - \breve{\mathbf{e}}_{p,n}\|, \qquad q_u = \mu_{n+1}^e \|dev\,\mathbf{e}_{n+1} - \breve{\mathbf{e}}_{p,n}\|, \tag{3.2.71}$$

and, thus,

$$q_t = \frac{E_n^e}{E_{n+1}^e} q_u = b\,q_u, \qquad p_t = \frac{E_n^e}{E_{n+1}^e} p_u = b\,p_u, \tag{3.2.72}$$

for the Poisson's ratio is constant and so the quotient $\kappa_n^e / \kappa_{n+1}^e$ is directly $E_n^e / E_{n+1}^e = b > 0$. By substituting Eq.(3.2.72) into inequality (3.2.69), and upon rearrangement, we are led to

$$\big(q_t - \big(q_n + a\,(p_t - p_n)\big)\big) + b\,(q_t + a\,p_t) \geq 0. \tag{3.2.73}$$

Since $\Delta\lambda^{e,(1)} > 0$, the following inequality holds

$$q_t - \big(q_n + a\,(p_t - p_n)\big) \geq 0, \tag{3.2.74}$$

and hence the first term on the right-hand side of (3.2.73) is always non-negative. To prove that the other term is also non-negative, consider the limit case in which $q_t = q_n + a\,(p_n - p_t)$. In this instance, inequality (3.2.73) takes the form

$$b\,(q_n - a\,p_n) \geq 0. \tag{3.2.75}$$

For the above inequality to hold for all $a, b > 0$, it is sufficient that $p_n < 0$, i.e., the intersection $\partial\mathbb{E}_{\boldsymbol{\tau}}^{d,e}$ must lie in the second-quadrant of the $p-q$ plane. This condition is always satisfied, as stated in Eq.(3.2.68).

In conclusion, *the solution of the return-mapping algorithm when the Drucker-Prager yield surface and the elliptical yield surface are involved is unique, and can be obtained only in two or three iterations of the FSM predictor-corrector scheme.* This conclusion can be also extended to cover the case in which the elliptical and the Von Mises yield surfaces may be active, by simply noting that the yield condition represented by the Von-Mises surface is a degenerate case ($\alpha = \gamma = 0$) of the Drucker-Prager yield condition.

***CASE III*: Drucker-Prager and Von Mises yield surface**

Consider a stress state such that $\mathbb{J}^{act,(1)} = \{d, v\}$. Computing the updated stress state in this case is trivial, since it does not require any further labor other than determining the intersection between both the Drucker-Prager surface and the Von-Mises surface:

$$q_{d,v} = c_v(\xi_n^h), \tag{3.2.76}$$

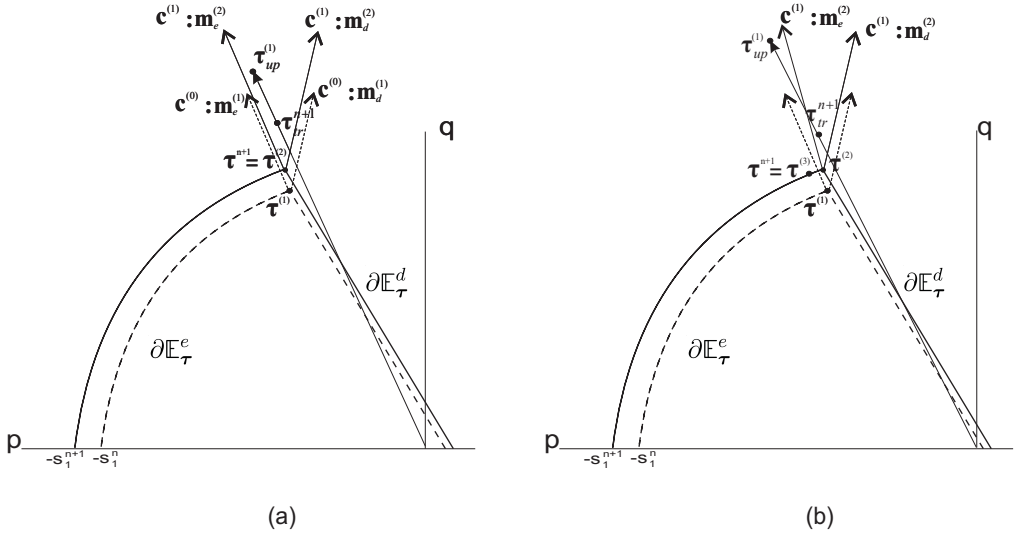

Figure 3.6 *(a) Case in which the Drucker-Prager and elliptical yield surfaces are active in the second iteration. (b) Case in which only the elliptical yield surface is active after performing the predictor step of the second iteration.*

$$p_{d,v} = (c(\xi_n^h) - q_{d,v})/\alpha, \tag{3.2.77}$$

where $(p_{d,v}, q_{d,v})$ denotes the intersection between both surfaces. Recall that this aspect of simplicity stems from the modification of the evolution equation for the internal softening variable proposed in subsection 3.2.1.2.

CASE IV: Drucker-Prager yield surface

The remaining situation is that in which only the Drucker-Prager yield surface is active, that is, $\mathbb{J}_{n+1}^{act,tr} = \mathbb{J}^{act,(k)} = \{d\}$, for all $k = 1, 2 \ldots$ The evolution equations Eq.(3.2.46) and Eq.(3.2.47) suggest that the internal hardening variable remains in its converged value, $\xi_{n+1}^h = \xi_n^h$, whereas the softening variable evolves according to:

$$\xi_{n+1}^s = \xi_n^s + 2\,\Delta\lambda_{n+1}^d\, q_{n+1}. \tag{3.2.78}$$

The above equation clearly shows that the update of ξ^s depends on the *current stress* through its deviatoric part q_{n+1}. Therefore, the return mapping algorithm cannot be handled *exactly* in a finite number of iterations, in contrast to the situations encountered in cases I, II and III. Our concern here is to check if the sequence defined by the predictor-corrector FSM scheme is *convergent* to an unique solution, and to analyze the conditions under which such convergence, if any, can be guaranteed.

The equations for the *predictor stage* are obtained by projecting Eq.(3.2.43) (see BOX 3.2.2) onto the $p - q$ plane:

$$p^{(k)} = p_{n+1}^{tr} - \Delta\lambda^{d,(k)}\,\kappa_n^e\,\gamma\,\alpha c^{(k-1)}, \tag{3.2.79}$$

$$q^{(k)} = \frac{q^{tr}_{n+1}}{1 + 4\,\mu^e_n\,\Delta\lambda^{d,(k)}}, \tag{3.2.80}$$

$$\phi^{d,(k)} = q^{(k)} + \alpha\, p^{(k)} - c^{(k-1)} = 0. \tag{3.2.81}$$

After some algebra, the above system of equations can be reduced to the following *quadratic polynomial* in $q^{(k)}$:

$$\Gamma(q^{(k)}) = {q^{(k)}}^2 + \big(\alpha\, p^{tr}_{n+1} + c^{(k-1)}(\chi - 1)\big) q^{(k)} - \chi\, c^{(k-1)} q^{tr}_{n+1} = 0, \tag{3.2.82}$$

where

$$\chi = \alpha^2 \gamma\, \frac{\kappa^e}{4\,\mu^e}. \tag{3.2.83}$$

As $\Delta\lambda^{d,(k)} \geq 0$, it follows from Eq.(3.2.80) that $q^{(k)} \in [0, q^{tr}_{n+1}]$. Evaluating Eq.(3.2.82) at $q^{(k)} = 0$ yields

$$\Gamma(0) = -\chi\, c^{(k-1)} q^{tr}_{n+1}, \tag{3.2.84}$$

All the variables appearing in the above are positive, hence $\Gamma(0) \leq 0$ for all $c^{(k-1)} \geq 0$. Similarly, at $q^{(k)} = q^{tr}_{n+1}$ we have

$$\Gamma(q^{tr}_{n+1}) = q^{tr}_{n+1}\,(q^{tr}_{n+1} + \alpha\, p^{tr}_{n+1} - c^{(k-1)}) \geq q^{tr}_{n+1}\,(\overbrace{q^{tr}_{n+1} + \alpha\, p^{tr}_{n+1} - c_n}^{\phi^{d,tr}_{n+1}}) > 0, \tag{3.2.85}$$

since $c^{(k-1)} \leq c_n$ and $\phi^{d,tr}_{n+1} > 0$. Therefore, from the intermediate value theorem we deduce that the quadratic equation Eq.(3.2.82) have only one root in the interval $[0, q^{tr}_{n+1}]$, and, consequently, the *solution* $\boldsymbol{\tau}^{(k)}$ *to the system of equations of the predictor step is unique.*

The update of the internal softening variable that characterize the *corrector step* can be directly inferred from Eq.(3.2.78):

$$\xi^{s,(k)} = \xi^s_n + 2\,\Delta\lambda^d(\xi^{s,(k)}, \boldsymbol{\tau}^{(k)})\, q^{(k)}. \tag{3.2.86}$$

It is important to observe that $\Delta\lambda^d(\xi^{s,(k)}, \boldsymbol{\tau}^{(k)}) \neq \Delta\lambda^{d,(k)}$, that is, the plastic multiplier $\Delta\lambda^{d,(k)}$ arising from the solution of the predictor step is not used for updating the internal variable. The only information from the predictor step employed to *correct* the internal variables is the stress state $\boldsymbol{\tau}^{(k)}$. With this in mind, $\Delta\lambda^d(\xi^{s,(k)}, \boldsymbol{\tau}^{(k)})$ is obtained from Eq.(3.2.80) and then substituted in Eq.(3.2.78), leading to

$$\xi^{s,(k)} = \xi^s_n + \frac{q^{tr}_{n+1} - q^{(k)}}{2\,\mu^e_n}. \tag{3.2.87}$$

The predictor equation (3.2.82) depends on $\xi^{s,(k-1)}$ through the cohesion $c^{(k-1)}$. It is expedient, thus, to invoke the constitutive law (3.2.9) and recast Eq.(3.2.87) also in terms of $c^{(k)}$:

$$c^{(k)} = c_n + H^{(k)}(\xi^{s,(k)} - \xi^s_n) = c_n + \frac{H^{(k)}}{2\,\mu^e_n}(q^{tr}_{n+1} - q^{(k)}). \tag{3.2.88}$$

Recall (see Eq.(2.5.80) in section 2.5.5) that the expression for the exponential softening modulus $H^{(k)}$ is given by:

$$H^{(k)} = H_0(\xi_n^h)\frac{c^{(k)}}{c_0(\xi_n^h)} = H_0^n\frac{c^{(k)}}{c_{\mathrm{h}}^n}. \tag{3.2.89}$$

Finally, Eq.(3.2.89) is inserted into Eq.(3.2.88). Upon rearrangement, one obtains the following expression for the *update of cohesion*:

$$\Theta_{cr} = c^{(k)} = \frac{c_n}{1 - \dfrac{\hat{H}_0^n}{c_{\mathrm{h}}^n}(q_{n+1}^{tr} - q^{(k)})} = \frac{c_n}{1 + \dfrac{|\hat{H}_0^n|}{c_{\mathrm{h}}^n}(q_{n+1}^{tr} - q^{(k)})}, \tag{3.2.90}$$

with $\hat{H}_0^n$ defined as a dimensionless softening parameter:

$$\hat{H}_0^n = \frac{H_0^n}{2\mu_n^e}. \tag{3.2.91}$$

3.2.2.1 Convergence analysis

Equation (3.2.82), corresponding to the predictor stage, can be conveniently rephrased as:

$$\Theta_{pd} = c^{(k-1)} = \frac{q^{(k)}(q^{(k)} + \alpha p_{n+1}^{tr})}{\dfrac{1}{2}\chi(q_{n+1}^{tr} - q^{(k)}) + q^{(k)}}. \tag{3.2.92}$$

Note that, according to the above equation,

$$\Theta_{pd} = c^{(k-1)} \geq 0 \;\Leftrightarrow\; q \geq q_{min} = \max(0, -\alpha\, p_{n+1}^{tr}). \tag{3.2.93}$$

Hence the solution q_{n+1} necessarily lies in the interval $[q_{min}, q_{n+1}^{tr}]$. Likewise, since $q_{n+1} \in [q_{min}, q_{n+1}^{tr}]$, it follows immediately from Eq.(3.2.90) that $c^{(k)} \in [c_{min}, c_n]$, where

$$c_{min} = \frac{c_n}{1 + \dfrac{|\hat{H}_0^n|}{c_{\mathrm{h}}^n}(q_{n+1}^{tr} - q_{min})}. \tag{3.2.94}$$

Inspection of Eq.(3.2.90) and Eq.(3.2.92) indicates that the problem can be posed in the alternative form of *finding the limit of the sequence* $\{q^{(k)}\}$ defined by the *recursion formula*:

$$\Theta_{pd}(q^{(k+1)}) = \Theta_{cr}(q^{(k)}), \tag{3.2.95}$$

that is,

$$\frac{q^{(k+1)}(q^{(k+1)} + \alpha p_{n+1}^{tr})}{\dfrac{1}{2}\chi(q_{n+1}^{tr} - q^{(k+1)}) + q^{(k+1)}} = \frac{c_n}{1 + \dfrac{|\hat{H}_0^n|}{c_{\mathrm{h}}^n}(q_{n+1}^{tr} - q^{(k)})}, \tag{3.2.96}$$

with $q^{(0)} = q_{n+1}^{tr}$.

Sufficient conditions for convergence

Our concern now is to analyze the properties of this sequence. The next result establishes *sufficient conditions* for convergence[11].

Proposition 3.2.3. *Let* $\{q^{(k)}\}$ *be the sequence defined by the recursion formula*

$$\Theta_{pd}(q^{(k+1)}) = \Theta_{cr}(q^{(k)}), \quad q^{(0)} = q^{tr}_{n+1}.$$

Assume that:

I) $\Theta_{pd}(q)$ *and* $\Theta_{cr}(q)$ *are continuously differentiable in* $[q_{min}, q^{tr}_{n+1}]$.

II) $\Theta_{pd}(q)$ *and* $\Theta_{cr}(q)$ *are monotonically increasing functions, i.e* $\dot{\Theta}_{pd}(q) \geq 0$ *and* $\Theta_{cr}(q) \geq 0$, $\forall q \in [q_{min}, q^{tr}_{n+1}]$.

III) $\Theta_{pd}(q^{tr}_{n+1}) \geq \Theta_{cr}(q^{tr}_{n+1})$ *and* $\Theta_{pd}(q_{min}) \leq \Theta_{cr}(q_{min})$.

IV) There exists an unique solution q^* *in the interval* $[q_{min}, q^{tr}_{n+1}]$ *to the equation* $\Theta_{pd} = \Theta_{cr}$.

Then, the sequence $\{q^{(k)}\}$ *converges to* q^*.

Proof. The proof is carried out by showing that $\{q^{(k)}\}$ is a bounded monotonic (decreasing) sequence. In virtue of assumption I, we can expand $\Theta_{pd}(q^{(k+1)})$ and $\Theta_{pd}(q^{(k+1)})$ in Taylor series about $q^{(k)}$:

$$\Theta_{pd}(q^{(k+1)}) = \Theta_{pd}(q^{(k)}) + \dot{\Theta}_{pd}(\eta_p)(q^{(k+1)} - q^{(k)}), \quad \eta_p \in [q^{(k+1)}, q^{(k)}], \quad (3.2.97)$$

$$\Theta_{cr}(q^{(k+1)}) = \Theta_{cr}(q^{(k)}) + \dot{\Theta}_{cr}(\eta_c)(q^{(k+1)} - q^{(k)}), \quad \eta_c \in [q^{(k+1)}, q^{(k)}]. \quad (3.2.98)$$

Employing the recursion formula, we may write the above equations as

$$\Theta_{cr}(q^{(k)}) - \Theta_{pd}(q^{(k)}) = \dot{\Theta}_{pd}(\eta_p)(q^{(k+1)} - q^{(k)}), \quad \eta_p \in [q^{(k+1)}, q^{(k)}], \quad (3.2.99)$$

$$\Theta_{cr}(q^{(k+1)}) - \Theta_{pd}(q^{(k+1)}) = \dot{\Theta}_{cr}(\eta_c)(q^{(k+1)} - q^{(k)}), \quad \eta_c \in [q^{(k+1)}, q^{(k)}]. \quad (3.2.100)$$

The monotonic character of $\{q^{(k)}\}$, i.e. $q^{(k+1)} \leq q^{(k)}$ for all $k = 0, 1, 2 \ldots$ is proved by induction on k. The result holds trivially for $k = 0$, $q^{(1)} \leq q^{(0)}$, as can be deduced from assumptions II and III and by evaluating Eq.(3.2.99):

$$\begin{aligned} &\Theta_{cr}(q^{(0)}) - \Theta_{pd}(q^{(0)}) = \dot{\Theta}_{pd}(\eta_p)(q^{(1)} - q^{(0)}) \Rightarrow \\ &\Theta_{cr}(q^{tr}_{n+1}) - \Theta_{pd}(q^{tr}_{n+1}) \leq 0, \quad \dot{\Theta}_{pd}(\eta_p) \geq 0 \ \Rightarrow q^{(1)} \leq q^{(0)}. \end{aligned} \quad (3.2.101)$$

Therefore, assume now that the result is also true for some $k = i$, that is, $q^{(i)} \leq q^{(i-1)}$. Combining *Eq.*(3.2.99) and *Eq.*(3.2.100) we get

$$q^{(i+1)} - q^{(i)} = \frac{\dot{\Theta}_{cr}(\eta_c)}{\dot{\Theta}_{pd}(\eta_p)}(q^{(i)} - q^{(i-1)}). \quad (3.2.102)$$

[11] These conditions only applies when *softening* is involved.

Since both $\dot{\Theta}_{cr}$ and $\dot{\Theta}_{pd}$ are nonnegative for all $q \in [q_{min}, q^{tr}_{n+1}]$ (assumption II), it follows immediately that $q^{(i+1)} - q^{(i)} \leq 0$.

To complete the proof, we shall show that $q^{(k)} \in [q_{min}, q^{tr}_{n+1}]$ for all k, i.e. the sequence is *bounded*, and hence convergent. To this end, we shall argue by contradiction. Suppose that there exists $k > 0$ such that $q^{(k)} \in [q_{min}, q^*]$. From Eq.(3.2.99), the following property can be deduced:

$$\Theta_{cr}(q^{(k)}) \leq \Theta_{pd}(q^{(k)}), \tag{3.2.103}$$

for all k. Since from assumption III $\Theta_{pd}(q_{min}) - \Theta_{cr}(q_{min}) \leq 0$, we know by the intermediate value problem that $\Theta_{pd} - \Theta_{cr}$ has a zero in $[q_{min}, q^{(k)}]$, a fact that contradicts assumption IV, hence $q^{(k)} \in [q_{min}, q^{tr}_{n+1}]$ for all k. Furthermore, since the sequence is decreasing, it follows immediately that q^* is its *limit*, as asserted.

□

We are now confronted with the task of ascertaining whether the particular functional forms of Θ_{cr} and Θ_{pd} (see Eqs. (3.2.92) and (3.2.90), respectively) satisfy the *sufficient conditions* listed in the foregoing result. In regards to the condition of continuity and differentiability, notice that both Θ_{pd} and Θ_{cr} are *rational functions* of q:

$$\Theta_{pd} = \frac{N_{pd}(q)}{D_{pd}(q)}, \quad \Theta_{cr} = \frac{N_{cr}}{D_{cr}(q)}. \tag{3.2.104}$$

Since $D_{cr}(q) \neq 0$ for all $q \in [q_{min}, q^{tr}_{n+1}]$, $\Theta_{cr}(q)$ is *continuously differentiable* on the interval $[q_{min}, q^{tr}_{n+1}]$. For $q^{tr}_{n+1} = 0$, the predictor function Θ_{pd} has a singularity at $q = 0$, i.e. $D_{pd}(0) = 0$. However, as it may inferred from Eqs. (3.2.82) and (3.2.88), in this case the solution to the return mapping algorithm is *trivial*, since the internal variable does not evolve and the trial stress is simply "returned" to the Drucker-Prager apex, i.e.:

$$q^{tr}_{n+1} = 0 \implies q_{n+1} = 0, \quad c_{n+1} = c_n, \quad p_{n+1} = \frac{c_n}{\alpha}. \tag{3.2.105}$$

Thus, in order to ensure also the continuity and differentiability of Θ_{pd}, the particular case $q^{tr}_{n+1} = 0$ will be excluded from the analysis.

Condition II states that $\dot{\Theta}_{cr}(q) \geq 0$ and $\dot{\Theta}_{pd}(q) \geq 0$. The verification for Θ_{cr} is straightforward:

$$\dot{\Theta}_{cr}(q) = \frac{c_n \, |\hat{H}^n_0|}{c^n_{\mathrm{h}} \big(1 + \dfrac{|\hat{H}^n_0|}{c^n_{\mathrm{h}}} (q^{tr}_{n+1} - q^{(k)})\big)^2} \geq 0, \quad \forall q. \tag{3.2.106}$$

To study the sign of the derivative of Θ_{pd}, we can write

$$\Theta_{pd}(q) = \frac{q}{\dfrac{1}{2}\chi(q^{tr}_{n+1} - q) + q} \, (q + \alpha \, p^{tr}_{n+1}) = F(q) \, (q + \alpha \, p^{tr}_{n+1}), \tag{3.2.107}$$

where $F(q) \in [0,1]$ for $q \in [q_{min}, q^{tr}_{n+1}]$. Using the product rule, we get

$$\dot{\Theta}_{pd}(q) = \dot{F}\,(\overbrace{q + \alpha\, p^{tr}_{n+1}}^{>0}) + F. \tag{3.2.108}$$

Since $\chi \geq 0$, the derivative of F:

$$\dot{F} = \frac{1}{2}\frac{\chi\, q^{tr}_{n+1}}{\big(\frac{1}{2}\chi(q^{tr}_{n+1} - q) + q\big)^2}, \tag{3.2.109}$$

is also positive for all q. Hence, it follows from Eq.(3.2.108) that $\dot{\Theta}_{pd}(q) \geq 0$ for all $q \in [q_{min}, q^{tr}_{n+1}]$.

The condition III at the extremes of the interval is also satisfied:

$$\Theta_{pd}(q^{tr}_{n+1}) - \Theta_{cr}(q^{tr}_{n+1}) = q^{tr}_{n+1} + \alpha\, p^{tr}_{n+1} - c_n = \phi^{d,tr}_{n+1} > 0 \tag{3.2.110}$$

$$\Theta_{pd}(q_{min}) - \Theta_{cr}(q_{min}) = 0 - \frac{c_n}{1 + \dfrac{|\hat{H}^n_0|}{c^n_{\mathrm{h}}}(q^{tr}_{n+1} - q_{min})} \leq 0. \tag{3.2.111}$$

Finally, we prove in the following that the function $\Theta(q) = \Theta_{pd}(q) - \Theta_{cr}(q)$ has an *unique zero* in the interval $[q_{min}, q^{tr}_{n+1}]$ (condition IV). In turn, this result provides the assurance that there exists[12] an *unique solution to the return mapping algorithm* when $\mathbb{J}^{act,tr}_{n+1} = \{d\}$.

Proposition 3.2.4. *The function defined as $\Theta(q) = \Theta_{pd}(q) - \Theta_{cr}(q)$, with Θ_{pd} and Θ_{pd} given in Eq.(3.2.90) and Eq.(3.2.92), respectively, has an unique zero in the interval $[q_{min}, q^{tr}_{n+1}]$.*

Proof. Multiplying $\Theta = 0$ by the denominators of Θ_{pd} and Θ_{cr} (which are non-vanishing $\forall\, q \in [q_{min}, q^{tr}_{n+1}]$), a *cubic polynomial* $R(q) = \sum_{i=0}^{3} r_i\, q^i = 0$ is obtained. After elementary manipulations, the coefficients (r_i, $i = 0 \ldots 3$) are found to be given by:

$$r_3 = -\frac{|\hat{H}^n_0|}{c^n_{\mathrm{h}}}, \quad r_2 = (1 + \frac{|\hat{H}^n_0|}{c^n_{\mathrm{h}}}(q^{tr}_{n+1} - \alpha\, p^{tr}_{n+1})), \tag{3.2.112}$$

$$r_0 = -\frac{1}{2}c_n q^{tr}_{n+1}\chi, \quad r_1 = r_2 - c_n(1 - \frac{1}{2}\chi). \tag{3.2.113}$$

[12] In proposition 3.2.4 it is shown that the norm of the updated deviatoric stress tensor can be obtained by finding the root of a cubic equation in $[q_{min}, q^{tr}_{n+1}]$. Hence, the return mapping problem when $\mathbb{J}^{act,tr}_{n+1} = \{d\}$ can be viewed also as a root finding problem. This root may be obtained by other numerical means, such as the closed-form expressions based on Cardano's method [87], or variants thereof, and not necessarily by the proposed method. Nonetheless, for completeness, the convergence properties of the sequence defined by the FSM algorithm is discussed herein.

Evaluation of the polynomial R at the extremes of the interval yields

$$R(q_{min}) = -c_n \, (\overbrace{\frac{1}{2}\chi(q^{tr}_{n+1} - q_{min}) + q_{min}}^{>0}) \leq 0, \tag{3.2.114}$$

$$R(q^{tr}_{n+1}) = q^{tr}_{n+1}(q^{tr}_{n+1} + \alpha\, p^{tr}_{n+1}) - c_n = q^{tr}_{n+1}\, \phi^{d,tr}_{n+1} \geq 0. \tag{3.2.115}$$

Thus, since $R(q_{min})$ and $R(q^{tr}_{n+1})$ have opposite signs, we know by the intermediate value theorem that there exist n roots of R in $[q_{min}, q^{tr}_{n+1}]$, with $n = 1$ or $n = 3$. The signs of r_0 and r_3 indicate that $R(0) < 0$ and $R(-\infty) > 0$. Therefore, following the same logic as above, $R = 0$ have m negative roots, with $m = 1$ or $m = 3$. If we suppose that $n = 3$, then the total number of zeros would be $n + m = 4$ or $n + m = 6$, which cannot be true, since the polynomial is cubic. Hence, R has only one root in $[q_{min}, q^{tr}_{n+1}]$, and, consequently, Θ possesses an unique zero in $[q_{min}, q^{tr}_{n+1}]$, as asserted. □

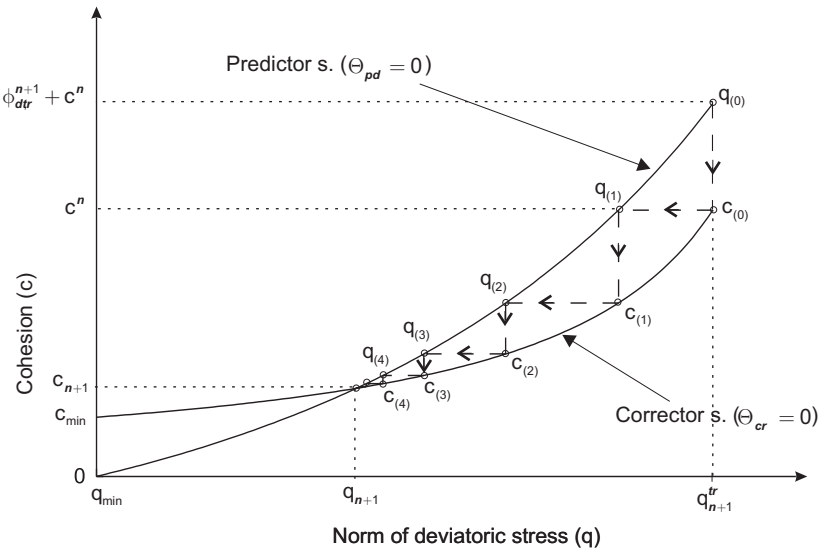

Figure 3.7 *Linearly convergent FSM sequence.*

Therefore, we conclude that the functional forms of Θ_{cr} and Θ_{pd}, given in Eq.(3.2.90) and Eq.(3.2.92), respectively, *fulfill the sufficient conditions* for the sequence defined by the recursion formula (3.2.95) to converge. As a corollary, we can say that *the FSM algorithm for the case* $\mathbb{J}^{act,tr}_{n+1} = \{d\}$ *converges to the solution of the return mapping algorithm regardless of the location of the trial stress* $(p^{tr}_{n+1}, q^{tr}_{n+1})$ *and the value of the material parameters* χ, α and $\hat{H}^n_0$. It is worth noting that no restriction is placed on the *amount of allowable softening*, symbolized by $\hat{H}^n_0$, which is one of the drawbacks that plague elastic-plastic models equipped with softening [92].

Rate of convergence

To assess the computational efficiency of the FSM algorithm, it is of paramount interest to study its *rate of convergence*. The following result address this question.

Proposition 3.2.5. *Let $\{q^{(k)}\}$ be the convergent sequence defined by the recursion formula $\Theta_{pd}(q^{(k+1)}) = \Theta_{cr}(q^{(k)})$. Let q^* denote the limit of this sequence and consider an interval $[q^*, \beta] \subset [q^*, q^{tr}_{n+1}]$ such that*

$$\frac{\dot{\Theta}_{pd}(\eta)}{\dot{\Theta}_{cr}(\eta)} < 1, \tag{3.2.116}$$

for all $\eta \in [q^*, \beta]$. Let N be a positive integer such that $q^{(N)} \leq \beta$. Then, the error, denoted as $e = q - q^*$, decreases for all $k \geq N$, being the rate of this decrease linear.

Proof. Expressing $\Theta_{pd}(q^{(k+1)})$ and $\Theta_{cr}(q^{(k)})$ in Taylor series about q^* and truncating after the first order term yields:

$$\Theta_{pd}(q^{(k+1)}) = \Theta_{pd}(q^*) + \dot{\Theta}_{pd}(\eta_p)(\overbrace{q^{(k+1)} - q^{(q^*)}}^{e^{(k+1)}}), \quad \eta_p \in [q^*, q^{(k+1)}], \tag{3.2.117}$$

and

$$\Theta_{cr}(q^{(k)}) = \Theta_{cr}(q^*) + \dot{\Theta}_{cr}(\eta_c)(\overbrace{q^{(k+1)} - q^{(k)}}^{e^{(k)}}), \quad \eta_c \in [q^*, q^{(k)}], \tag{3.2.118}$$

respectively. Subtracting Eq.(3.2.118) from Eq.(3.2.117) gives:

$$\begin{aligned} \Theta_{pd}(q^{(k+1)}) - \Theta_{cr}(q^{(k)}) = &\big(\Theta_{pd}(q^*) - \Theta_{cr}(q^*)\big) \\ &+ \dot{\Theta}_{pd}(\eta_p)\, e_{(k+1)} - \dot{\Theta}_{cr}(\eta_c)\, e_{(k)}. \end{aligned} \tag{3.2.119}$$

Since $\Theta_{pd}(q^*) = \Theta_{cr}(q^*)$ and $\Theta_{pd}(q^{(k+1)}) = \Theta_{cr}(q^{(k)})$, after solving for $e_{(k+1)}$ we get

$$e_{(k+1)} = \frac{\dot{\Theta}_{cr}(\eta_c)}{\dot{\Theta}_{pd}(\eta_p)} e_{(k)}. \tag{3.2.120}$$

For $k > N$, $q^{(k)}, q^{(k-1)} \in [q^*, \beta]$. Then, the error *decreases* by a factor $\dot{\Theta}_{cr}(\eta_p)/\dot{\Theta}_{pd}(\eta_c)$, $\eta_p \in [q^*, q^{(k+1)}]$, $\eta_c \in [q^*, q^{(k)}]$. Eq.(3.2.120) further shows that $e_{(k+1)}$ depends *linearly* on $e_{(k)}$. □

Thus, the above proposition shows that the *rate of convergence is linear* in a neighborhood of the solution in which $\dot{\Theta}_{cr} > \dot{\Theta}_{pd}$. It is straightforward to prove, by contradiction, that this condition of greater slope of the predictor curve in some $[q^*, \beta]$, $\beta \in [0, q^{tr}_{n+1} - q^*]$ always holds. Suppose that $\dot{\Theta}_{cr}(q^*) < \dot{\Theta}_{pd}(q^*)$. The continuity assumption implies that for some $\epsilon > 0$ $\Theta_{pd}(q^* + \epsilon) < \Theta_{cr}(q^* + \epsilon)$, which is a contradiction, since $\Theta_{pd}(q) \geq \Theta_{cr}(q)$ for all $q \in [q^*, q^{tr}_{n+1}]$.

The so-called *asymptotic convergence factor* [87] $\dot{\Theta}_{cr}/\dot{\Theta}_{pd}$ can be estimated grossly using the mean value theorem:

$$\begin{aligned}\frac{\Theta_{cr}}{\Theta_{pd}} &= \frac{\Theta_{cr}(q_{n+1}^{tr}) - \Theta_{cr}(q_{min})}{\Theta_{pd}(q_{n+1}^{tr}) - \Theta_{pd}(q_{min})} \\ &= \frac{|\hat{H}_0^n|/c_{\mathrm{h}}^n(q_{n+1}^{tr} - q_{min})}{1 + |\hat{H}_0^n|/c_{\mathrm{h}}^n(q_{n+1}^{tr} - q_{min})} \frac{1}{\dfrac{\phi_{n+1}^{d,tr}}{c_n} + 1}.\end{aligned} \tag{3.2.121}$$

This estimation reveals that the asymptotic convergence factor is inversely proportional to the yield equation evaluated at the trial stress $\phi_{n+1}^{d,tr}$. Hence the FSM algorithm *converges more rapidly with trial stresses located far from the yield surface* ($\phi_{n+1}^{d,tr} \gg c_n$), since in this case $\dot{\Theta}_{cr}/\dot{\Theta}_{pd}$ approaches zero.

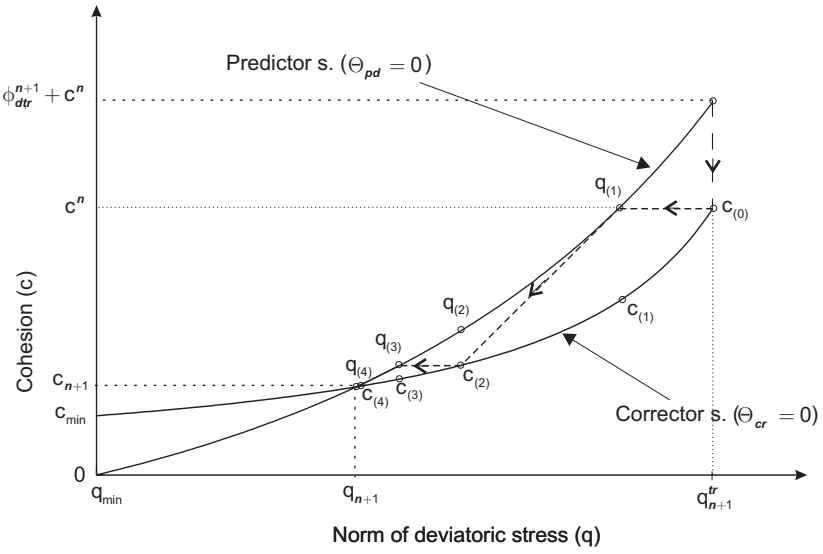

Figure 3.8 *Quadratically convergent FSM sequence.*

The conclusion that can be drawn from the preceding discussion is that *the FSM algorithm offers a remarkable aspect of robustness*, *inasmuch as it converges to the solution regardless of the values of the material properties*, and furthermore, *its convergence is even faster when the trial stress is placed far from the yield surface.* Nevertheless, it is natural to inquire at this point whether other schemes, viewed also in the light of the predictor-corrector methodology, might exhibit higher rates of convergence. To assist in the answering of this question, it proves helpful to, first, illustrate graphically the performance of the standard FSM method. In figure 3.7 the predictor and corrector equations $\Theta_{pd} = 0$ and $\Theta_{cr} = 0$ are represented in the $c - q$ plane. The predictor step consists in finding the intersection between the horizontal lines (c constant) and the predictor curve $\Theta_{pd} = 0$. The *corrector step*,

on the other hand, involves solving the intersection of the corrector graph $\Theta_{cr} = 0$ and the vertical lines (q constant).

The plot in figure 3.8 clearly identifies the strategy to follow in arriving at a FSM algorithm with a higher rate of convergence. The predictor stage would remain unaltered (projection onto the yield surface with c constant), whereas the corrector step would be modified and accomplished by finding the intersection between the curve $\Theta_{cr} = 0$ and the straight line tangent to $\Theta_{pd} = 0$ at $q^{(k-1)}$. The corresponding sequence is defined by the recursion formulae:

$$\Theta_{pd}(q^{(2k-1)}) = \Theta_{cr}(q^{(2k-2)}), \tag{3.2.122}$$

$$\Theta_{cr}(q^{(2k)}) = \Theta_{pd}(q^{(2k-1)}) + \dot{\Theta}_{pd}(q^{(2k-1)})(q^{(2k)} - q^{(2k-1)}), \tag{3.2.123}$$

with $k = 1, 2 \ldots$ and $q^{(0)}$. The analysis of the convergence of this sequence is undertaken in a similar manner to that presented in proposition 3.2.5.[13] We simply quote the final result (for $k \to \infty$):

$$e_{(2k-1)} = \frac{\dot{\Theta}_{cr}(q^*)}{\dot{\Theta}_{pd}(q^*)} e_{(2k-2)}, \tag{3.2.124}$$

$$e_{(2k)} = \frac{1}{2} \frac{\ddot{\Theta}_{cr}(q^*)}{\dot{\Theta}_{pd}(q^*) - \dot{\Theta}_{cr}(q^*)} e^2_{(2k-1)}. \tag{3.2.125}$$

Combining Eqs. (3.2.124) and (3.2.125), we get

$$e_{(2k)} = \frac{1}{2} \frac{\ddot{\Theta}_{cr}(q^*)}{\dot{\Theta}_{pd}(q^*) - \dot{\Theta}_{cr}(q^*)} \left(\frac{\dot{\Theta}_{cr}(q^*)}{\dot{\Theta}_{pd}(q^*)} \right)^2 e^2_{(2k-2)}. \tag{3.2.126}$$

The above equation reveals that the rate of convergence of this modified FSM algorithm is *quadratic*. However, in return for its enhanced convergence, a *necessary condition* for the sequence defined by Eqs. (3.2.124) and (3.2.125) to be monotonic decreasing is that $\ddot{\Theta}_{pd} > 0$ in a neighborhood of the solution, i.e., the predictor function must be *convex*. To check if this condition is satisfied, Eq.(3.2.108) is differentiated with respect to q, yielding

$$\ddot{\Theta}_{pd} = 2\dot{F} + \ddot{F}(q + \alpha\, p^{tr}_{n+1}). \tag{3.2.127}$$

After some manipulation, $\ddot{F}$ can be expressed as

$$\ddot{F} = \frac{-2\,(1 - 1/2\,\chi)}{q(1 - 1/2\,\chi) + 1/2\chi q^{tr}_{n+1}} \dot{F}. \tag{3.2.128}$$

Substitution of the above into Eq.(3.2.127) leads to

$$\ddot{\Theta}_{pd} = 2\dot{F}\big(1 - \frac{-\,(1 - 1/2\,\chi)}{q(1 - 1/2\,\chi) + 1/2\chi q^{tr}_{n+1}} (q + \alpha\, p^{tr}_{n+1})\big). \tag{3.2.129}$$

[13] The only difference lies in that, in Eq.(3.2.123), $\Theta_{pd}(q^{(2k-1)})$ is expanded in a Taylor series around q^* *up to the second order term.*

So the predictor function is convex whenever the following inequality is satisfied:

$$1 > \frac{(1 - 1/2\,\chi)}{q(1 - 1/2\,\chi) + 1/2\chi q^{tr}_{n+1}}(q + \alpha\, p^{tr}_{n+1}), \tag{3.2.130}$$

which, upon rearranging, gives

$$\frac{1}{2}\chi(q^{tr}_{n+1} + \alpha\, p^{tr}_{n+1}) - \alpha\, p^{tr}_{n+1} > 0. \tag{3.2.131}$$

It follows from the preceding equation that the *convexity condition cannot be guaranteed* for any admissible values of the trial stress and the material parameter χ. Only for $p^{tr}_{n+1} < 0$ the above inequality holds regardless of the value of χ.

In conclusion, we have seen that, by simply modifying the equation for the update of cohesion in the corrector step, it is plausible to devise a quadratically convergent method preserving the predictor-corrector character. This modification, in turn, involves the linearization of the predictor function, and as a consequence, the *convexity* of this function appears as an additional requirement for convergence. However, inequality (3.2.131) clearly shows that this condition cannot be ensured for all conceivable trial stress states. Therefore, in the interest of robustness, this appealing quadratically convergent FSM scheme is abandoned in favor of the original linearly converging one.

3.3 IMPLEX integration scheme

The arguments in support of the implicit-explicit (IMPLEX) integration scheme were already put forward in subsection 3.1.1. Here we simply choose those variables to be treated explicitly and derive the stress update and the algorithmic tangent modulus arising from this choice. The reader is referred to the work of *Oliver et al.* [79, 80] for further details on the structure of this integration scheme.

By definition, the internal variables are monotonically increasing functions of time, i.e. $\dot{\boldsymbol{\xi}} \geq 0$. For this reason, they are logical candidates to be treated explicitly, since its evolution can be predicted more accurately than other variables exhibiting non-monotonic behavior. The following analysis pursues, thus, to develop an expression for *explicitly updating* the set of internal variable at t_{n+1} using values obtained in previous time steps by an implicit integration procedure.

To this end, consider first the Taylor expansion of the *exact* solution, denoted by an overbar on the symbol for the internal hardening, to the governing differential equation at t_{n-1} around t_n:

$$\bar{\boldsymbol{\xi}}_{n-1} = \bar{\boldsymbol{\xi}}_n + \left.\frac{\partial \boldsymbol{\xi}}{\partial t}\right|_{\bar{\boldsymbol{\xi}}_n} (t_{n-1} - t_n) + \mathcal{O}(\Delta^2 t_n), \tag{3.3.1}$$

or alternatively,

$$\bar{\boldsymbol{\xi}}_n = \bar{\boldsymbol{\xi}}_{n-1} + \left.\frac{\partial \boldsymbol{\xi}}{\partial t}\right|_{\bar{\boldsymbol{\xi}}_n} \Delta t_n + \mathcal{O}(\Delta^2 t_n), \tag{3.3.2}$$

where

$$\left.\frac{\partial \boldsymbol{\xi}}{\partial t}\right|_{\bar{\boldsymbol{\xi}}_n} = \dot{\boldsymbol{\xi}}(\bar{\boldsymbol{\xi}}_n, \bar{\boldsymbol{\tau}}_n). \tag{3.3.3}$$

Next, the Taylor expansion is carried out again around t_n, but evaluated at t_{n+1}, yielding

$$\bar{\boldsymbol{\xi}}_{n+1} = \bar{\boldsymbol{\xi}}_n + \left.\frac{\partial \boldsymbol{\xi}}{\partial t}\right|_{\bar{\boldsymbol{\xi}}_n} \Delta t_{n+1} + \mathcal{O}(\Delta^2 t_{n+1}). \tag{3.3.4}$$

If the remainder term $\mathcal{O}(\Delta^2 t_{n+1})$ is truncated in the above equation, then the resulting expression would correspond to a standard *explicit finite difference equation*. The application of the above explicit difference equation for marching the solution forward from one time level to the next time level presents the inconvenience that, since the yield condition is not enforced at t_{n+1}, the error would accumulate and the yield condition may be substantially violated, leading to updated stress prohibitively far from the yield surface. In order to avoid that this drift from the yield surface grows unboundedly, *Oliver et al.*[79, 80] propose to approximate the derivative in Eq.(3.3.4) using the derivative appearing in expression Eq.(3.3.2). Therefore, truncating the term $\mathcal{O}(\Delta^2 t_n)$ in Eq.(3.3.2), one gets

$$\boldsymbol{\xi}_n = \boldsymbol{\xi}_{n-1} + \left.\frac{\partial \boldsymbol{\xi}}{\partial t}\right|_{\boldsymbol{\xi}_n} \Delta t_n, \qquad \mathcal{O}(\Delta^2 t_n). \tag{3.3.5}$$

The above constitutes an *implicit finite difference* equation, in the sense that the internal variable at t_n, ξ_n^h, is obtained by an expression that uses a derivative evaluated also at t_n. Hence $\boldsymbol{\xi}_{n-1}$ and $\boldsymbol{\xi}_n$ can be regarded as the values of the internal variables obtained at times t_{n-1} and t_n, respectively, by solving the return mapping algorithm outlined in the previous section. From Eq.(3.3.5), we can deduce that

$$\left.\frac{\partial \boldsymbol{\xi}}{\partial t}\right|_{\boldsymbol{\xi}_n} = \frac{\boldsymbol{\xi}_n - \boldsymbol{\xi}_{n-1}}{\Delta t_n}, \qquad \mathcal{O}(\Delta t_n). \tag{3.3.6}$$

Finally, inserting the above approximation into Eq.(3.3.4), and truncating the remainder term, yields

$$\tilde{\boldsymbol{\xi}}_{n+1} = \boldsymbol{\xi}_n + (\boldsymbol{\xi}_n - \boldsymbol{\xi}_{n-1})\frac{\Delta t_{n+1}}{\Delta t_n}, \qquad \mathcal{O}(\Delta t_{n+1}\Delta t_n). \tag{3.3.7}$$

This expression represents the *update of the internal variables* at t_{n+1} in terms of *implicit values* computed at t_n and t_{n-1}. The distinction between approximated quantities stemming from the IMPLEX integration and from the pure implicit integration schemes is made by attaching a tilde symbol over the IMPLEX variables.

Note that the IMPLEX algorithm is a *multistep* method, since two points (t_n and t_{n-1}) are used to advance the solution in time to point t_{n+1}. The order of the *extrapolation* represented by Eq.(3.3.7) can be increased by simply using a higher-order approximation for the derivative at t_n. However, accuracy assessments carried out by Oliver et al. [80] show that the benefits arising from this practice are quite subtle and do not outweight the concomitant increase of computational storage requirements.

The set of state variables defining the size and shape of the yield surfaces can be obtained at time t_{n+1} from the corresponding hardening/softening laws, using the vector of internal variables derived in Eq.(3.3.7) as argument, that is:

$$\tilde{s}_{1,n+1} = s_{1\mathrm{h}}(\tilde{\xi}^h_{n+1}), \quad \tilde{s}_{2,n+1} = s_{2\mathrm{h}}(\tilde{\xi}^h_{n+1}), \quad \tilde{c}_{v,n+1} = c_{v\mathrm{h}}(\tilde{\xi}^h_{n+1}), \tag{3.3.8}$$

$$\tilde{c}_{n+1} = c_n + \left.\frac{\partial c_{\mathrm{h}}}{\partial \xi^h}\right|_{n+1} (\tilde{\xi}^h_{n+1} - \xi^h_n) + \tilde{H}_{n+1}(\tilde{\xi}^s_{n+1} - \xi^s_n), \tag{3.3.9}$$

where

$$\tilde{H}_{n+1} = \frac{\tilde{c}_{n+1}}{c_0(\tilde{\xi}^h_{n+1})} H_0(\tilde{\xi}^h_{n+1}). \tag{3.3.10}$$

In regards to the plastic multipliers, the update suggested by *Oliver et al.* is also adopted:

$$\Delta\tilde{\lambda}^{\beta}_{n+1} = \Delta\lambda^{\beta}_n \frac{\Delta t_{n+1}}{\Delta t_n}, \quad \beta = e, d, v, \tag{3.3.11}$$

i.e., the IMPLEX discrete plastic multiplier $\Delta\tilde{\lambda}^{\beta}_{n+1}$ at t_{n+1} is directly computed by multiplying the corresponding implicit discrete plastic multiplier at t_n by the quotient $\Delta t_{n+1}/\Delta t_n$. It should be mentioned, however, that the derivation of this update does not display the same mathematical rigor as the one presented in Eq.(3.3.7) for the internal variables. This can be explained as follows. The IMPLEX scheme was originally conceived for integrating numerically elastic-plastic constitutive models with *associated flow* rules and a *single internal variable* [79]. Under such conditions, and by properly defining the flow rule, the rate of change of the internal variable can be identified with the continuum plastic multiplier, i.e., $\dot{\xi} = \dot{\lambda}$. In this instance, one can legitimately obtain the update as $\Delta\tilde{\lambda}_{n+1} = \Delta\lambda_n \Delta t_{n+1}/\Delta t_n$, since $\Delta\lambda = \Delta\xi$. In our case, by contrast, we have three plastic multipliers and two independent internal variables whose evolution equations also involve stress measures, and thus, such identity cannot be established, hence the *ad-hoc* character of the proposed update (3.3.11).

Notice that the extrapolation of the plastic multipliers does not entails allocating additional storage for implicit values at t_{n-1}. Expression (3.3.11) also reveals that the elastic or inelastic nature of the response predicted by the IMPLEX integration scheme at t_{n+1} is dictated by the response computed *implicitly* at t_n. This may give rise to numerical overshoots and oscillations in the transition from elastic to plastic conditions and vice versa. Schemes for adaptively controlling the length of the time step, also covered by the work of Oliver et al.[80], prove advantageous in diminishing the deleterious effects on the quality of the computed response of such shortcomings.

Our developments in this section have been focused thus far on those variables ($\boldsymbol{\xi}$ and $\Delta\lambda^{\beta}$) whose updates can be handled *explicitly*. Attention is confined now to compute the Kirchhoff stress tensor at t_{n+1}. Since the concept of extrapolation is not applied for such computation (stresses are treated *implicitly*), the methodology for deriving this update equation parallels that followed for devising Eq.(3.2.24) in

the implicit case. Thus, we can directly write

$$\tilde{\boldsymbol{\tau}}_{n+1} = \boldsymbol{\tau}^{tr}_{n+1} + \Delta\tilde{\boldsymbol{c}}_{\boldsymbol{e},n+1} : (\mathbf{e}_{n+1} - \breve{\mathbf{e}}_{p,n}) - \sum_{\beta=1}^{3} \Delta\tilde{\lambda}^{\beta}_{n+1}\, \tilde{\boldsymbol{c}}_{\boldsymbol{e},n+1} : \tilde{\boldsymbol{m}}^{\beta}_{n+1}, \tag{3.3.12}$$

where we have simply replaced the implicit quantities in Eq.(3.2.24) by IMPLEX quantities (with tilde). The fourth-order tensors $\Delta\tilde{\boldsymbol{c}}_{\boldsymbol{e},n+1}$ and $\tilde{\boldsymbol{c}}_{\boldsymbol{e},n+1}$ are evaluated as

$$\Delta\tilde{\boldsymbol{c}}_{\boldsymbol{e},n+1} = \boldsymbol{c}_{\boldsymbol{e}}(\tilde{\xi}^{h}_{n+1}) - \boldsymbol{c}_{\boldsymbol{e}}(\xi^{h}_{n}), \qquad \tilde{\boldsymbol{c}}_{\boldsymbol{e},n+1} = \boldsymbol{c}_{\boldsymbol{e}}(\tilde{\xi}^{h}_{n+1}), \tag{3.3.13}$$

whereas the plastic flow vector is given by

$$\tilde{\boldsymbol{m}}^{\beta}_{n+1} = \boldsymbol{m}^{\beta}(\tilde{\xi}^{h}_{n+1}, \tilde{\boldsymbol{\tau}}_{n+1}). \tag{3.3.14}$$

In general, obtaining $\tilde{\boldsymbol{\tau}}_{n+1}$ from Eq.(3.3.12) requires solving a non-linear tensor equation. However, as alluded to earlier (see Eq.(3.2.48)), in our case, the plastic flow vector on each surface is an *affine transformation* of the Kirchhoff stress tensor, i.e.,

$$\tilde{\boldsymbol{m}}^{\beta}_{n+1} = \tilde{\boldsymbol{A}}^{\beta}_{n+1} : \tilde{\boldsymbol{\tau}}_{n+1} + \tilde{\boldsymbol{B}}^{\beta}_{n+1} \tag{3.3.15}$$

where the fourth-order and second-order tensors $\tilde{\boldsymbol{A}}^{\beta}_{n+1}$ and $\tilde{\boldsymbol{B}}^{\beta}_{n+1}$ are defined as

$$\tilde{\boldsymbol{A}}^{\beta}_{n+1} = 2\,\boldsymbol{I}_{\mathrm{dev}} + \frac{1}{3}\tilde{u}^{\beta}_{n+1}\,\mathbf{1}\otimes\mathbf{1}, \tag{3.3.16}$$

$$\tilde{\boldsymbol{B}}^{\beta}_{n+1} = \tilde{v}^{\beta}_{n+1}\,\mathbf{1}, \tag{3.3.17}$$

respectively, with the yield surface dependent parameters $\tilde{u}^{\beta}_{n+1}$ and $\tilde{v}^{\beta}_{n+1}$, $\beta = e, d, v$, given by (see Eqs. (3.2.49) and (3.2.50)):

$$\tilde{u}^{e}_{n+1} = \frac{2}{3}(\tilde{s}_{2,n+1})^2, \quad \tilde{u}^{d}_{n+1} = \tilde{u}^{v}_{n+1} = 0, \tag{3.3.18}$$

$$\tilde{v}^{e}_{n+1} = \tilde{v}^{v}_{n+1} = 0, \quad \tilde{v}^{d}_{n+1} = \frac{1}{3}\gamma\,\tilde{c}_{n+1}\,\alpha. \tag{3.3.19}$$

Substituting Eq.(3.3.15) into Eq.(3.3.12) and solving for $\tilde{\boldsymbol{\tau}}_{n+1}$ yields

$$\begin{aligned}\tilde{\boldsymbol{\tau}}_{n+1} = \tilde{\boldsymbol{R}}^{-1}_{n+1} \,:\, \big(&\boldsymbol{\tau}^{tr}_{n+1} + \Delta\tilde{\boldsymbol{c}}_{\boldsymbol{e},n+1} : (\mathbf{e}_{n+1} - \breve{\mathbf{e}}_{p,n}) - \\ &\tilde{\boldsymbol{c}}_{\boldsymbol{e},n+1} \,:\, \sum_{\beta=1}^{3} \Delta\tilde{\lambda}^{\beta}_{n+1}\, \tilde{\boldsymbol{B}}^{\beta}_{n+1}\big),\end{aligned} \tag{3.3.20}$$

where

$$\tilde{\boldsymbol{R}}_{n+1} = \boldsymbol{I} + \tilde{\boldsymbol{c}}_{\boldsymbol{e},n+1} : \sum_{\beta=1}^{3} \Delta\tilde{\lambda}^{\beta}_{n+1} \tilde{\boldsymbol{A}}^{\beta}_{n+1}. \tag{3.3.21}$$

Equation Eq.(3.3.20) constitutes a *closed-form* formula for the Kirchhoff *stress update* at t_{n+1}. This update admits the following deviatoric-hydrostatic decomposition:

$$\tilde{\boldsymbol{\tau}}_{n+1} = dev\,\tilde{\boldsymbol{\tau}}_{n+1} + \tilde{p}_{n+1}\,\mathbf{1}, \tag{3.3.22}$$

where

$$dev\,\tilde{\boldsymbol{\tau}}_{n+1} = \frac{dev\,\boldsymbol{\tau}^{tr}_{n+1} + 2\,\Delta\tilde{\mu}^{e}_{n+1}\,dev\,(\mathbf{e}_{n+1} - \breve{\mathbf{e}}_{p,n})}{1 + 4\,\tilde{\mu}^{e}_{n+1}\sum_{\beta=1}^{3}\Delta\tilde{\lambda}^{\beta}_{n+1}} \tag{3.3.23}$$

$$\tilde{p}_{n+1} = \frac{p^{tr}_{n+1} + \Delta\tilde{\kappa}^{e}_{n+1}\,\mathrm{tr}\,(\mathbf{e}_{n+1} - \breve{\mathbf{e}}_{p,n}) + 3\,\tilde{\kappa}^{e}_{n+1}\sum_{\beta=1}^{3}\Delta\tilde{\lambda}^{\beta}_{n+1}\tilde{v}^{\beta}_{n+1}}{1 - \tilde{\kappa}^{e}_{n+1}\sum_{\beta=1}^{3}\Delta\tilde{\lambda}^{\beta}_{n+1}\tilde{u}^{\beta}_{n+1}}. \tag{3.3.24}$$

3.3.1 Algorithmic elastoplastic tangent moduli

Our emphasis so far has been entirely *local*, i.e., attention has been confined to determine the local stress state at time t_{n+1}, given a prescribed deformation state and a set of initial data. However, the ultimate goal in the numerical simulation of the powder sub-system is to solve an *initial boundary problem* for the displacement field. The numerical solution of this problem relies on the spatial discretization, via a Galerkin finite element projection, of the weak form of the momentum equation. Due to the non-linear character of the problem, a time-discretization of this variational form is also necessary, and the response is finally obtained by solving a *sequence of linearized problems*.

The theory underlying the spatial and time discretization, as well as the linearization of the resulting weak formulation are not addressed in this work. The reader is referred to the vast literature on the subject [5, 113, 88] for further details. Here we limit ourselves to provide an expression for the *algorithmic tangent moduli*, which is a key step in the above mentioned linearization of the weak formulation.

The algorithmic tangent moduli is obtained merely by applying the *directional derivative* relative to a strain increment to the update formulas of the integration algorithm [92]. In connection with this, we recall that the stress values furnished by the IMPLEX integration scheme *determine the internal forces appearing in the weak formulation* of the problem. Hence we shall focus on the algorithmic tangent operator *consistent* with this integration scheme.

In using the *algorithmic tangent moduli* on the computation of the response, one is tacitly assuming that the linearization is carried out after the stress-update algorithm is introduced [5]. Therefore, consider the term corresponding to the *internal forces* of the total lagrangian weak form statement at time t_{n+1}:

$$G^{int}_{\boldsymbol{\varphi}_{n+1}}(\tilde{\boldsymbol{S}}_{n+1}, \boldsymbol{\eta}_0) = \int_{\Omega_0} \mathbf{F}_{n+1}\cdot\tilde{\boldsymbol{S}}_{n+1}\cdot\mathrm{Grad}\,\boldsymbol{\eta}_0\,d\Omega. \tag{3.3.25}$$

We shall not dwell on formal considerations concerning the above expression, sufficient be it to say that $\mathrm{Grad}\,\boldsymbol{\eta}_0$ symbolizes the *material* gradient operator, defined in cartesian coordinates as

$$(\mathrm{Grad}\,\boldsymbol{\eta}_0)_{aA} = \frac{\partial\boldsymbol{\eta}_{0\,a}}{\partial X^{A}}. \tag{3.3.26}$$

acting on the material *test function* $\boldsymbol{\eta}_0$, which, in turn, belongs to a proper space of functions. The Second Piola-Kirchhoff stress tensor $\tilde{\boldsymbol{S}}_{n+1}$ is the material counterpart of the spatial Kirchhoff stress tensor obtained by the IMPLEX stress-update

formula (3.3.20). Linearization about the current configuration Ω_{n+1} involves obtaining the *directional derivative* of Eq.(3.3.25) in the direction of an incremental displacement $\Delta \boldsymbol{U}$, that is,

$$D_{\Delta \boldsymbol{U}}\, G^{int}_{\boldsymbol{\varphi}_{n+1}}(\tilde{\boldsymbol{S}}_{n+1}, \boldsymbol{\eta}_0) = \int_{\Omega_0} D_{\Delta \boldsymbol{U}}\, \mathbf{F}_{n+1} \cdot \tilde{\boldsymbol{S}}_{n+1} \cdot \operatorname{Grad} \boldsymbol{\eta}_0 \, d\Omega + \int_{\Omega_0} \mathbf{F}_{n+1} \cdot D_{\Delta \boldsymbol{U}}\, \tilde{\boldsymbol{S}}_{n+1} \cdot \operatorname{Grad} \boldsymbol{\eta}_0 \, d\Omega. \tag{3.3.27}$$

We restrict our attention to the second term on the right-hand side of the above equation, which after the finite element projection, gives rise to the so-called *material stiffness matrix*. From the definition of directional derivative, and by using the chain rule, we get

$$\begin{aligned} D_{\Delta \boldsymbol{U}}\, \tilde{\boldsymbol{S}}_{n+1} &= \left. \frac{d}{d\epsilon} \right|_{\epsilon=0} \big(\tilde{\boldsymbol{S}}_{n+1}(\boldsymbol{\varphi}_{n+1} + \epsilon\, \Delta \boldsymbol{U}) \big) \\ &= \tilde{\boldsymbol{C}}_{\boldsymbol{ep},n+1} : \left. \frac{d}{d\epsilon} \right|_{\epsilon=0} \big(\mathbf{E}_{n+1}(\boldsymbol{\varphi}_{n+1} + \epsilon\, \Delta \boldsymbol{U}) \big), \end{aligned} \tag{3.3.28}$$

where the components of the *material algorithmic tangent moduli* $\tilde{\boldsymbol{C}}_{\boldsymbol{ep},n+1}$ are given by

$$(\tilde{\boldsymbol{C}}_{\boldsymbol{ep},n+1})^{ABCD} = \frac{(\tilde{\boldsymbol{S}}_{n+1})^{AB}}{(\mathbf{E}_{n+1})_{CD}}. \tag{3.3.29}$$

Thus, $\tilde{\boldsymbol{C}}_{\boldsymbol{ep},n+1}$ can be derived by finding the operator satisfying

$$\frac{\partial \tilde{\boldsymbol{S}}_{n+1}}{\partial t_{n+1}} = \tilde{\boldsymbol{C}}_{\boldsymbol{ep},n+1} : \frac{\partial \mathbf{E}_{n+1}}{\partial t_{n+1}}. \tag{3.3.30}$$

However, since the stress-update formula (3.3.20) is cast in terms of spatial quantities, it is convenient to obtain first the *spatial algorithmic tangent moduli* $\tilde{\boldsymbol{c}}_{\boldsymbol{ep},n+1}$, and then transforming this tensor into the reference configuration via a pull-back operation.

The spatial algorithmic tangent moduli $\tilde{\boldsymbol{c}}_{\boldsymbol{ep},n+1}$ is defined by the spatial counterpart of Eq.(3.3.30):

$$\mathcal{L}_v \tilde{\boldsymbol{\tau}}_{n+1} = \tilde{\boldsymbol{c}}_{\boldsymbol{ep},n+1} : \mathcal{L}_v \mathbf{e}_{n+1} = \tilde{\boldsymbol{c}}_{\boldsymbol{ep},n+1} : \mathbf{d}_{n+1}, \tag{3.3.31}$$

wherein the Lie derivative $\mathcal{L}_v(\bullet)$ is used to preserve objectivity. An expression for $\tilde{\boldsymbol{c}}_{\boldsymbol{ep},n+1}$ is obtained by applying the Lie operator to the stress-update formula Eq.(3.3.20). The simplicity, in comparison to an standard implicit integration scheme, afforded by the use of the IMPLEX stress-update scheme is manifested by the fact that the *derivative of the plastic multipliers and the internal variables vanishes*, in virtue of the extrapolated character of these variables, that is, $\Delta \tilde{\lambda}^{\beta}_{n+1}$ and $\tilde{\boldsymbol{\xi}}_{n+1}$ *do not depend on the deformation state at* t_{n+1}. However, even with this simplification, it takes tedious algebra to derive a closed-form expression for

$\tilde{\boldsymbol{c}}_{\boldsymbol{ep},n+1}$. This derivation is hence relegated to Appendix (A.4), and we simply record here the final expression, which takes the following form:

$$\tilde{\boldsymbol{c}}_{\boldsymbol{ep},n+1} = \tilde{\boldsymbol{R}}_{n+1}^{-1} : \Big(\tilde{\mathbf{a}}_{\mathbf{e},n+1}(\tilde{\mathbf{e}}_{e,n+1}) + \tilde{\boldsymbol{c}}_{\boldsymbol{e},n+1} : \Big(\boldsymbol{I} - \sum_{\beta=1}^{3} \Delta\tilde{\lambda}_{n+1}^{\beta} \tilde{\boldsymbol{z}}_{n+1}^{\beta}(\tilde{\boldsymbol{\tau}}_{n+1}) \Big) \Big). \tag{3.3.32}$$

The isotropic fourth order tensor $\tilde{\boldsymbol{R}}_{n+1}$ was introduced when deriving the closed form expression for the stress-update (see Eq.(3.3.21)). On the other hand, the tensor $\tilde{\mathbf{a}}_{\mathbf{e},n+1}(\tilde{\mathbf{e}}_{e,n+1})$ is given by the following formula

$$\tilde{\mathbf{a}}_{\mathbf{e},n+1}(\tilde{\mathbf{e}}_{e,n+1}) = -2 \Big(\big(\tilde{\kappa}_{n+1}^{e} - \frac{2}{3} \tilde{\mu}_{n+1}^{e} \big) \big(\mathbf{1} \otimes \tilde{\mathbf{e}}_{e,n+1} + \operatorname{tr} \tilde{\mathbf{e}}_{e,n+1} \boldsymbol{I} \big) + 2\, \tilde{\mu}_{n+1}^{e}\, \boldsymbol{\mathcal{I}}_s(\tilde{\mathbf{e}}_{e,n+1}) \Big), \tag{3.3.33}$$

where $\tilde{\mathbf{e}}_{e,n+1}$ is the elastic strain tensor computed as

$$\tilde{\mathbf{e}}_{e,n+1} = \mathbf{e}_{n+1} - \big(\breve{\mathbf{e}}_{p,n} + \sum_{\beta=1}^{3} \Delta\tilde{\lambda}_{n+1}^{\beta} \tilde{\boldsymbol{m}}_{n+1}^{\beta} \big). \tag{3.3.34}$$

and the operator $\boldsymbol{\mathcal{I}}_s(\bullet)$ has the following component form:

$$(\boldsymbol{\mathcal{I}}_s(\bullet))^{abef} = \frac{1}{2} \big((\bullet)^{af} \delta^{be} + (\bullet)^{bf} \delta^{ae} \big). \tag{3.3.35}$$

The expression for $\tilde{\boldsymbol{z}}_{n+1}^{\beta}(\tilde{\boldsymbol{\tau}}_{n+1})$ is given by

$$\tilde{\boldsymbol{z}}_{n+1}^{\beta}(\tilde{\boldsymbol{\tau}}_{n+1}) = \tilde{\mathbf{a}}_{\tau,n+1}(\tilde{u}_{n+1}^{\beta}, \tilde{\boldsymbol{\tau}}_{n+1}) + 2\, \tilde{v}_{n+1}^{\beta} \boldsymbol{I}, \tag{3.3.36}$$

where the yield surface dependent parameters $\tilde{u}_{n+1}^{\beta}$ and $\tilde{v}_{n+1}^{\beta}$ were defined in Eqs. (3.3.18) and (3.3.19), respectively. The structure of tensor $\tilde{\mathbf{a}}_{\tau,n+1}$ is rather similar to that of $\tilde{\mathbf{a}}_{\mathbf{e},n+1}$:

$$\tilde{\mathbf{a}}_{\tau,n+1}(\tilde{u}_{n+1}^{\beta}, \tilde{\boldsymbol{\tau}}_{n+1}) = 2 \Big(\frac{1}{3} \big(\tilde{u}_{n+1}^{\beta} - 2 \big) \big(\mathbf{1} \otimes \tilde{\boldsymbol{\tau}}_{n+1} + \operatorname{tr} \tilde{\boldsymbol{\tau}}_{n+1} \boldsymbol{I} \big) + 4\, \boldsymbol{\mathcal{I}}_s(\tilde{\boldsymbol{\tau}}_{n+1}) \Big). \tag{3.3.37}$$

Remark 3.3.1. The fourth order tensors $\tilde{\mathbf{a}}_{\mathbf{e},n+1}(\tilde{\mathbf{e}}_{e,n+1})$ and $\tilde{\boldsymbol{z}}_{n+1}^{\beta}(\tilde{\boldsymbol{\tau}}_{n+1})$ arise from applying the Lie derivative to the *metric tensor*, which is involved in the definition of both the elasticity tensor and the plastic flow vectors. Thus, if these terms are discarded from Eq.(3.3.32), one obtains the algorithmic tangent operator for the IMPLEX integration scheme corresponding to a *small strain formulation*, since in this kinematical approach the distinction between reference and current configurations are negligible for the purposes of computing stress and strain. The resulting expression reads

$$\tilde{\boldsymbol{c}}_{\boldsymbol{ep},n+1}\big|_{\|\mathbf{e}\| \ll 1} = \tilde{\boldsymbol{R}}_{n+1}^{-1} : \tilde{\boldsymbol{c}}_{\boldsymbol{e},n+1}. \tag{3.3.38}$$

Expanding this equation using Eq.(3.3.21) gives

$$\tilde{\boldsymbol{c}}_{\boldsymbol{ep},n+1}\big|_{\|\mathbf{e}\| \ll 1} = \tilde{\kappa}_{n+1}^{imx}\, \mathbf{1} \otimes \mathbf{1} + 2\, \tilde{\mu}_{n+1}^{imx}\, \boldsymbol{I}_{\mathrm{dev}}, \tag{3.3.39}$$

where

$$\tilde{\kappa}^{imx}_{n+1} = \frac{\tilde{\kappa}^{e}_{n+1}}{1 + 3\,\tilde{\kappa}^{e}_{n+1} \sum_{\beta=1}^{3} \Delta\tilde{\lambda}^{\beta}_{n+1} \tilde{u}^{\beta}_{n+1}} = \frac{\tilde{\kappa}^{e}_{n+1}}{1 + 2\,\tilde{\kappa}^{e}_{n+1} \Delta\tilde{\lambda}^{e}_{n+1} (\tilde{s}_{2,n+1})^2} \tag{3.3.40}$$

$$\tilde{\mu}^{imx}_{n+1} = \frac{\tilde{\mu}^{e}_{n+1}}{1 + 4\,\tilde{\mu}^{e}_{n+1} \sum_{\beta=1}^{3} \Delta\tilde{\lambda}^{\beta}_{n+1}} \tag{3.3.41}$$

Inspection of Eq.(3.3.39) indicates that, in the small strain setting, the algorithmic tangent operator emanating from the IMPLEX integration scheme is an *isotropic tensor* of rank 4, characterized by two parameters, which, in analogy to the notation for the elastic bulk and shear modulus, are denoted by $\tilde{\kappa}^{imx}_{n+1}$ and $\tilde{\mu}^{imx}_{n+1}$. Furthermore, since $\Delta\tilde{\lambda}^{\beta}_{n+1} \geq 0$, it follows from Eqs. (3.3.40) and Eq.(3.3.41) that

$$\tilde{\kappa}^{imx}_{n+1} \leq \tilde{\kappa}^{e}_{n+1}, \tag{3.3.42}$$

$$\tilde{\mu}^{imx}_{n+1} \leq \tilde{\mu}^{e}_{n+1}, \tag{3.3.43}$$

where the inequality or equality holds accordingly as the material is deforming plastically or elastically, respectively.

As alluded to in section 3.1.1, the development of the implicit-explicit integration scheme was prompted by the need to enhance the spectral properties of the algorithmic elastoplastic moduli, whose positive definiteness cannot be guaranteed when using an standard implicit integration scheme, mainly due to the presence of strain softening. Since, according to Eqs. (3.3.40) and Eq.(3.3.41), $\tilde{\kappa}^{imx}_{n+1} > 0$ and $\tilde{\mu}^{imx}_{n+1} > 0$, it follows then that the algorithmic elastoplastic moduli shown in Eq.(3.3.39) is *positive-definite*. Another remarkable property of this small strain algorithmic operator is that it does not depend on the deformation state at t_{n+1}, hence it turns out to be *step-constant*.

One can conclude from the foregoing remark that the positive-definiteness of the algorithmic elastoplastic moduli is guaranteed in those situations in which a small strain kinematics is sufficient to yield a realistic description of the deformation state. As pointed out in section 2.2.1, the ejection stage, which, in turn, is the part of the compaction cycle in which the compacted powder is more liable to develop cracks, falls within this type of situations, since the magnitude of plastic and elastic strains are relatively small, and, besides, the motion of the compact through the die cavity during ejection involves no solid rigid rotations. Therefore, we can assert that, in contrast to the situation that one would encounter if a standard implicit integration scheme is employed, *the numerical performace of the algorithm is not impaired*[14] *by the presence of strain softening*, at least in the computation of the response corresponding to the ejection stage.

[14] This is, of course, insofar as material non-linearities are concerned. The numerical performance may be seriously affected by the characteristics of the contact problem, specially the stick-slip behavior when Coulomb friction models are used.

To further improve the confidence in the numerical performace of this integration scheme, the spectral properties of the (large strains) algorithmic elastoplastic tensor shown in Eq.(3.3.32) should be also examined. As it may be surmised, a rigorous analysis concerning the positive-definite character of $\tilde{\boldsymbol{c}}_{\boldsymbol{ep},n+1}$ in a general situation, i.e., for any $\tilde{\mathbf{e}}_{e,n+1}$ and $\tilde{\boldsymbol{\tau}}_{n+1}$ entails substantial difficulties. An easier route is to determine the order of magnitude of the tensors $\tilde{\mathbf{a}}_{\mathbf{e},n+1}$ and $\tilde{\boldsymbol{z}}^{\beta}_{n+1}$, and see if their influence in the value of $\tilde{\boldsymbol{c}}_{\boldsymbol{ep},n+1}$ is significant.

Consider first a situation in which the response predicted by the integration scheme is entirely elastic. In this case, the spatial elastoplastic tensor adopts the form:

$$\tilde{\boldsymbol{c}}_{\boldsymbol{ep},n+1}|_{\Delta\lambda^{\beta}=0} = \tilde{\boldsymbol{c}}_{\boldsymbol{e},n+1} + \tilde{\mathbf{a}}_{\mathbf{e},n+1}(\tilde{\mathbf{e}}_{e,n+1}). \tag{3.3.44}$$

According to expression (3.3.33), the order of magnitude of $\tilde{\mathbf{a}}_{\mathbf{e},n+1}$ is $\|\tilde{\mathbf{a}}_{\mathbf{e},n+1}\| \sim \tilde{E}^{e}_{n+1}\,\|\tilde{\mathbf{e}}_{e,n+1}\|$, whereas $\|\tilde{\boldsymbol{c}}_{\boldsymbol{e},n+1}\| \sim \tilde{E}^{e}_{n+1}$. Hence,

$$\frac{\tilde{\boldsymbol{c}}_{\boldsymbol{e},n+1}}{\tilde{\mathbf{a}}_{\mathbf{e},n+1}} \sim \|\tilde{\mathbf{e}}_{e,n+1}\|. \tag{3.3.45}$$

By hypothesis, the extent of elastic strains is significantly less than unity ($\|\tilde{\mathbf{e}}_{e,n+1}\| \sim 10^{-3}$, in accordance with data plotted in figure 3.2). We see thus that the *contribution of* $\mathbf{a}_{\mathbf{e}}$ *in the computation of* $\tilde{\boldsymbol{c}}_{\boldsymbol{ep},n+1}$ *is not significant*[15].

On the other hand, in the course of plastic deformation, the term involving $\tilde{\boldsymbol{z}}^{\beta}_{n+1}$, that is,

$$\sum_{\beta=1}^{3} \Delta\tilde{\lambda}^{\beta}_{n+1}\tilde{\boldsymbol{z}}^{\beta}_{n+1}(\tilde{\boldsymbol{\tau}}_{n+1}), \tag{3.3.46}$$

comes also into play. In this case, however, the task of disclosing whether the influence of this contribution is relatively important or not is by no means trivial, due mainly to the variability of the plastic multipliers $\Delta\tilde{\lambda}^{\beta}_{n+1}$. We proceed first by estimating the order of magnitude of $\tilde{\boldsymbol{z}}^{\beta}_{n+1}(\tilde{\boldsymbol{\tau}}_{n+1})$. According to Eq.(3.3.36), we have

$$\|\tilde{\boldsymbol{z}}^{\beta}_{n+1}\| \sim max(\|\tilde{\mathbf{a}}_{\tau,n+1}\|, \|\tilde{v}^{\beta}_{n+1}\|). \tag{3.3.47}$$

Using Eq.(3.3.37), we get

$$\|\tilde{\mathbf{a}}_{\tau,n+1}(\tilde{\boldsymbol{\tau}}_{n+1})\| \sim \|\tilde{u}^{\beta}_{n+1}\|\|\tilde{\boldsymbol{\tau}}_{n+1}\| \sim \|\|\tilde{\boldsymbol{\tau}}_{n+1}\|\|, \tag{3.3.48}$$

since $\|\tilde{u}^{v}_{n+1}\| = \|\tilde{u}^{d}_{n+1}\| = 0$ and $s_2 \sim 1$ (see figure 2.12), and, hence, $\|\tilde{u}^{e}_{n+1}\| \sim (\tilde{s}_{2,n+1})^2 \sim 1$. Besides, taking into account Eq.(3.3.19):

$$\tilde{v}^{\beta}_{n+1} \sim \begin{cases} 0, & if \quad \Delta\tilde{\lambda}^{d}_{n+1} = 0, \\ \alpha\,\gamma\,\tilde{c}_{n+1}, & if \quad \Delta\tilde{\lambda}^{d}_{n+1} > 0. \end{cases} \tag{3.3.49}$$

[15]Incidentally, if one discards the term $\mathbf{a}_{\mathbf{e}}$ from the definition of $\tilde{\boldsymbol{c}}_{\boldsymbol{ep},n+1}$, then a *hypoelastic* constitutive equation would be recovered, $\mathcal{L}_v\boldsymbol{\tau} = \boldsymbol{c}_{\boldsymbol{e}} : \mathcal{L}_v\mathbf{e}_e$

According to the empirical correlations set forth in the previous chapter, $\alpha \sim 2$, and γ is chosen close to zero, say $\gamma \sim 10^{-2}$, hence

$$\tilde{v}^{\beta}_{n+1} \sim \begin{cases} 0, & if \quad \Delta\tilde{\lambda}^{d}_{n+1} = 0, \\ 10^{-2}\,\tilde{c}_{n+1}, & if \quad \Delta\tilde{\lambda}^{d}_{n+1} > 0. \end{cases} \tag{3.3.50}$$

Using estimations (3.3.48) and (3.3.50) in (3.3.47), we finally obtain

$$\|\tilde{\boldsymbol{z}}^{\beta}_{n+1}\| \sim \begin{cases} \|\tilde{\boldsymbol{\tau}}_{n+1}\|, & if \quad \Delta\tilde{\lambda}^{d}_{n+1} = 0, \\ max(\|\tilde{\boldsymbol{\tau}}_{n+1}\|, 10^{-2}\,\tilde{c}_{n+1}), & if \quad \Delta\tilde{\lambda}^{d}_{n+1} > 0. \end{cases} \tag{3.3.51}$$

We concentrate our attention now in an estimation for the the plastic multipliers. The following expression for $\Delta\tilde{\lambda}^{\beta}_{n+1}$ can be deduced from Eq.(3.3.11):

$$\Delta\tilde{\lambda}^{\beta}_{n+1} = \Delta\lambda^{\beta}_{n}\frac{\Delta t_{n+1}}{\Delta t_n} = \frac{\Delta t_{n+1}}{\Delta t_n}\frac{q^{tr}_n - q_n}{4\,\mu^{e}_n\,q_n}, \quad \beta = e, d, v. \tag{3.3.52}$$

The above expression becomes indeterminate when $q_n \to 0$, that is, when the updated stress state at a given t_n is either at the intersection of the elliptical yield surface cap with the $p-$axis, or at the Drucker-Prager yield surface apex. We address first the case in which this singularity does not occur. Assuming that the time discretization is sufficiently regular and fine so as to ensure that $\Delta t_n \sim \Delta t_{n+1}$ and $\|\boldsymbol{\tau}_n\| \sim \|\tilde{\boldsymbol{\tau}}_{n+1}\|$, we obtain

$$\Delta\tilde{\lambda}^{\beta}_{n+1} \sim \frac{\|\boldsymbol{\tau}^{tr}_{n+1} - \tilde{\boldsymbol{\tau}}_{n+1}\|}{\|\tilde{\boldsymbol{\tau}}_{n+1}\|\tilde{E}^{e}_{n+1}}, \quad \beta = e, d, v. \tag{3.3.53}$$

Therefore, from (3.3.53) and (3.3.51), it follows that, in a situation in which the updated stress does not lie in the vicinity of neither the Drucker-Prager yield surface apex nor the intersection of the cap surface with the $p-$axis, the order of magnitude of the term shown in Eq.(3.3.46) can be estimated as

$$\|\sum_{\beta=1}^{3}\Delta\tilde{\lambda}^{\beta}_{n+1}\tilde{\boldsymbol{z}}^{\beta}_{n+1}\| \sim \begin{cases} \dfrac{\|\boldsymbol{\tau}^{tr}_{n+1} - \tilde{\boldsymbol{\tau}}_{n+1}\|}{\tilde{E}^{e}_{n+1}}, & if \quad \Delta\tilde{\lambda}^{d}_{n+1} = 0, \\ max(\dfrac{\|\boldsymbol{\tau}^{tr}_{n+1} - \tilde{\boldsymbol{\tau}}_{n+1}\|}{\tilde{E}^{e}_{n+1}}, \dfrac{10^{-2}\,\tilde{c}_{n+1}}{\tilde{E}^{e}_{n+1}}), & if \quad \Delta\tilde{\lambda}^{d}_{n+1} > 0. \end{cases} \tag{3.3.54}$$

The above estimation indicates that, using a time discretization so that $\|\boldsymbol{\tau}^{tr}_{n+1} - \tilde{\boldsymbol{\tau}}_{n+1}\| \ll \tilde{E}^{e}_{n+1}$ suffices to ensure that the term represented by (3.3.46) is *negligible in comparison with unity*, and thus, it can be disregarded when analyzing the spectral properties of the algorithmic elastoplastic tensor $\tilde{\boldsymbol{c}}_{\boldsymbol{e},n+1}$. Roughly speaking, the time discretization of the interval of interest should avoid that the trial stress lies "too far" from the yield surface [16]. It would be enough to guarantee that the

[16] As a matter of fact, this restriction of the size of the time steps arises also from accuracy requirements of the return mapping algorithm.

distance between the trial stress and the yield surfaces remains of the same order (or lesser) than the magnitude of the stresses, that is, $\|\boldsymbol{\tau}_{n+1}^{tr} - \tilde{\boldsymbol{\tau}}_{n+1}\| \sim \|\tilde{\boldsymbol{\tau}}_{n+1}\|$, since in this case

$$\|\sum_{\beta=1}^{3} \Delta\tilde{\lambda}_{n+1}^{\beta} \tilde{\boldsymbol{z}}_{n+1}^{\beta}\| \sim \frac{\|\boldsymbol{\tau}_{n+1}^{tr} - \tilde{\boldsymbol{\tau}}_{n+1}\|}{\tilde{E}_{n+1}^{e}} \sim \frac{\|\tilde{\boldsymbol{\tau}}_{n+1}\|}{\tilde{E}_{n+1}^{e}} \sim \|\tilde{\mathbf{e}}_{e,n+1}\|, \tag{3.3.55}$$

i.e., it would result of the same order as the elastic strains.

The indeterminacy arising in Eq.(3.3.52) when the stress state is at the intersection between the cap yield surface and the $p-$axis ($p_n = -s_{1,n}$) can be resolved by using the volumetric counterpart of Eq.(3.3.52), which in the case of the elliptical cap surface can be deduced from Eq.(3.2.54), and reads:

$$\Delta\tilde{\lambda}_{n+1}^{e} = \frac{\Delta t_{n+1}}{\Delta t_n} \frac{p_n^{tr} - p_n}{p_n \, 2\,\kappa_n^e (s_{2,n})^2} = \frac{\Delta t_{n+1}}{\Delta t_n} \frac{p_n^{tr} - s_{1,n}}{s_{1,n} \, 2\,\kappa_n^e (s_{2,n})^2}. \tag{3.3.56}$$

Note that, according to the experimental correlations outlined in the previous chapter, $s_1 > 0$ [17] and $s_2 > 0$. Thus, the value of the plastic multiplier $\Delta\tilde{\lambda}_{n+1}^{e}$ remains bounded and, following the same logic that led to (3.3.53), it can be concluded that the validity of the estimation (3.3.55) also holds in this particular case.

We deal now with the situation in which the stress state is placed at the apex of the Drucker-Prager yield surface. In this case, the plastic multiplier can be alternatively obtained from Eq.(3.2.79):

$$\Delta\tilde{\lambda}_{n+1}^{d} = \frac{\Delta t_{n+1}}{\Delta t_n} \frac{p_n^{tr} - p_n}{\kappa_n^e \, \alpha \, \gamma c_n}. \tag{3.3.57}$$

The above expression indicates that $\Delta\tilde{\lambda}_{n+1}^{d}$ grows unboundedly as the deterioration of cohesion progresses, that is, $\Delta\tilde{\lambda}_{n+1}^{d} \to \infty$ as $c_n \to 0$. On the other hand, the fact that $c_n \to 0$ implies that $\tilde{c}_{n+1} \to 0$. Hence, in this limit case, it follows from (3.3.51) that

$$\|\tilde{\boldsymbol{z}}_{n+1}^{d}\|\big|_{c\to 0} \sim \|\tilde{\boldsymbol{\tau}}_{n+1}\| \to 0. \tag{3.3.58}$$

Consequently, the order of magnitude of the term represented by Eq.(3.3.46) cannot be determined *a priori*, since $\Delta\tilde{\lambda}_{n+1}^{d}\|\tilde{\boldsymbol{z}}_{n+1}^{d}\|\Big|_{c\to 0} \sim 0 \cdot \infty$, that is, an indeterminacy arises. If it turns out that $\Delta\tilde{\lambda}_{n+1}^{d}\|\tilde{\boldsymbol{z}}_{n+1}^{d}\| \sim 1$ (or greater), the resulting *algorithmic elastoplastic moduli lose its positive-definite character*, as it may deduced from Eq.(3.3.32), and, eventually, this may lead to a deterioration of the numerical performance of the algorithm.

The solution adopted herein to overcome this potential source of difficulties is to set a *lower limit, greater than zero, for the cohesion*. In this way, the plastic multiplier remains bounded and the indeterminacy in (3.3.57) is eliminated. This

[17] As a consequence of the curve fitting process, values of s_1 close to zero may appear at low densities. However, it is highly recommended, in the interest of numerical robustness, to modify the curve fit in this cases and set a lower limit for the hydrostatic yield strength s_1, say $s_1 > 10^{-4} MPa$.

solution has proved useful in circumventing the aforementioned potential problems. However, the physical implications of such *ad-hoc* solution has not been properly evaluated, and this aspect of the analysis of the spectral properties of $\tilde{\boldsymbol{c}}_{\boldsymbol{ep},n+1}$ should be subject of debate in future developments on this topic.

In conclusion, the unconditional positive definiteness exhibited by the *small strain* algorithmic elastoplastic tensor, see Eq.(3.3.39), is inherited by the *large strain* algorithmic elastoplastic tensor $\tilde{\boldsymbol{c}}_{\boldsymbol{e},n+1}$, provided that the size of the time steps is small enough to keep the trial stress close to the yield surface. Furthermore, a lower limit for the cohesion has to be set in order to avoid potential singularities when the deformation process entails updated stresses at the apex of the Drucker-Prager yield surface.

Chapter 4

Numerical assessment

4.1 Introduction

The objective of this chapter is to assess the formulation and numerical implementation of the model presented in the preceding chapters. To this end, we consider two representative examples, namely, a *Brazilian or diametral compression test* and the *pressing and ejection of a thin cylindrical part.*

Quantitative and qualitative assessment

A *quantitative assessment* of the mechanism of crack formation requires to *monitor the crack during its development* and to *evaluate the effects of the developing crack in some measure of forces.* During die compaction processes, the powder specimen is encapsulated in the die cavity and, consequently, any attempt to observe "in situ" how the crack is formed is, to date, unfeasible [99]. Therefore, the quantitative assessment of this facet of the model must be carried out by recourse to common *fracture tests*, in which previously compacted parts are subjected to controlled loads. In particular, the *Brazilian or diametral compression test* is employed here. Numerical results will be compared with the experimental response on Distaloy AE powder specimens reported in the work of *Jonsén et al* [50], which includes, among other experimental data, a pictorial description of the development of the crack at different stages of the test. The simulation of the diametral compression serves also to analyze the implications of using either a displacement-based finite element formulation or a mixed formulation with displacements and pressures as basic variables.

The simulation of the *pressing and ejection of a thin cylindrical part* seeks to highlight the utility of the numerical model in reinforcing the physical understanding of how well-known crack typologies are developed. The experimental data to validate this test have been obtained from the extensive crack database collected by *Zenger et al.* [112]. As opposed to the diametral compression test, this simulation provides only a *qualitative assessment* of the model, as far as prediction of cracks is concerned.

Before launching into details of the numerical validation, it is convenient to provide an abridged overview of some aspects of the numerical implementation which, albeit not addressed in depth in this work, are crucial for acquiring a proper grasp of the ensuing computed results.

4.1.1 Overview of the modeling setting

Characterization of the tooling sub-system

The tooling sub-system is regarded as a set of isotropic continuum bodies that interact with each other and with the powder sub-system. It is assumed that during operation the tools undergo small deformations in comparison with their dimensions, and that plastic flow and other inelastic events do not take place. Consequently, a small strain elastic constitutive model is sufficient to yield a realistic description of the behavior of the tooling sub-system, with the material of each tool characterized by its corresponding Young's modulus and Poisson's ratio.

Finite element formulation

The standard *displacement-based discretization* is employed in all the simulations shown here. Nevertheless, with a view towards assessing the adequacy of this standard formulation, an alternative finite element approximation based on a mixed variational formulation, with displacements and pressure as basic variables, has also been tested in the simulation of the diametral compression test. For details on the implementation procedure of the standard formulation, the reader is referred to the classical finite element literature [5, 113, 24, 27]. The methodology for implementing the mixed formulation, including the corresponding stabilization, parallels that followed in Cervera et Agelet [1, 18] for J2-flow theory plasticity model[1], with continuous linear interpolation for both displacements and pressure fields.

The formulation has been specialized to address plane strain and axisymmetric problems[2]. Although the derivation of a general three-dimensional formulation is conceptually straightforward, the associated increase in computational cost compelled us to disregard three-dimensional simulations in this work.

A word concerning axisymmetric conditions is in order here. Considering the simulation of the uniaxial compaction process as an axisymmetric problem requires axial symmetry in both geometry and loading. The vast majority of manufactured parts are not, in strict sense, solids of revolution, since the presence of features such

[1] Galerkin mixed elements with continuous linear interpolation for both fields are subject to *pressure instability*[6]. In the small strain case, the structure of the stabilization method adopted by Cervera et Agelet [1, 18], which, incidentally, is based on the *sub-grid scale concept* [23], is readily tailored to the weak form containing our multi-surface constitutive model. However, extension to large strains is fraught with serious difficulties that undermine considerably the robustness of the global algorithm. This fact has to be kept in mind when debating the merits and drawbacks of using standard or mixed formulations.

[2] No *practical* applications of powder compaction occurs under plane stress conditions. When needed, the plane stress constraint can be imposed (exactly in the elastic range and *approximately* in the plastic one) by an appropriate conversion of the elastic constants[5].

as through and blind holes disrupts the axial symmetry. Nevertheless, in most cases these features do not alter significantly neither density nor stress fields, and one can analyze the process studying a characteristic cross section in which the influence of such geometric alterations is negligible. Another implication of regarding the problem as axisymmetric is that the development of a crack is assumed to exhibit also axial symmetry. Experience shows us that this fact is at odds with reality, since the propagation of cracks is inherently a three-dimensional phenomenon. Indeed, if, after cutting a compacted part into pieces, one detects a crack-like defect on a particular cross-section, it is hardly expected to observe the same defect on every cross sections. In this regard, however, it should be remarked again that the accurate representation of the actual propagation of the crack is not the primary goal in this work, but merely to detect its initiation. Therefore, the hypothesis of axial symmetry seems a reasonable simplification for an initial exploratory analysis.

Remeshing strategy. Element technology

A Lagrangian viewpoint is adopted for describing the motion of the mesh. Rather than *adaptive remeshing* [54] or similar techniques, the procedure followed here to avoid the detrimental effect of progressive mesh distortion is based on the so-called Particle Finite Element Method (PFEM). The distinguishing feature of this method, which was originally conceived for solving incompressible flows with free-surfaces [47] and later on extended to solid mechanics problems [77], is that, roughly speaking, the set of nodes (material points) defining the finite element mesh is the same throughout the deformation; only the connectivity matrix is modified. As a consequence, the mapping of history dependent variables from the "old mesh" to the "new mesh" is trivial for the case of nodal properties, such as the velocity. For the case of variables defined at the quadrature points, such as the stress and the density fields, a standart least-square smoothing is used to obtain nodal values and eventually transfer the information to the new mesh. In order to avoid spurious numerical diffusion, it proves advantageous in this respect to accomplish the smoothing process *incrementally*, in the sense that the smoothing operator is applied to the incremental change in the corresponding field rather than to the total values [77]. Another salient feature of the PFEM strategy is its ability to recognize free boundary surfaces. This a key issue in the simulation of the powder fill and powder transfer operations, in which the powder can easily flow. However, we shall not delve into such details since the study of these manufacturing stages is not contemplated in this work.

The PFEM imposes a limitation concerning element technology. Indeed, an essential requirement in using such method is that the finite elements are to be *three-nodes triangular elements* (linear). The acclaimed inaccuracies that may emerge in the response when using linear triangular elements are discussed in section 4.2.2.

The formulation of the the weak form has been carried out using an updated Lagrangian strategy, in which the reference configuration is taken as the placement of the body at the previous converged step[77].

During the simulation of the pressure release and ejection stages, the finite elements are not severely distorted, since, as discussed in section 2.2, the magnitude of both elastic and plastic strain is not significant (small strain regime). In the in-

terest of computational efficiency, it is convenient to split the problem and consider separately the simulation of the pressing stage and the post-pressing stages, since it seems devoid of meaning to apply any mesh update procedure in the computation of these post-pressing stages. This can be automatically accomplished with the aid of some restart utility that takes the set of historic variables recorded at the end of the computation of the pressing phase as the initial conditions for simulating the subsequent ejection stage.

Regularization of the softening law

In section 2.5.5, see Eq.(2.5.97), the localization bandwidth l_f appeared as a link between the continuum softening modulus H_0 and the intrinsic softening modulus $\hat{H}_0$. In order to alleviate the detrimental effect of mesh sensitivity, i.e., lack of convergence under mesh refinements, which is inherent to constitutive models equipped with softening, it was pointed out that the localization bandwidth at each quadrature point should depend on the size and orientation of the corresponding element. Here we simply set $l_f = \sqrt{A_e}$, where A_e is the area of the corresponding triangular element, that is, the localization bandwidth depends only on the element size. More elaborate theories [74] have been put forward to also acknowledge the orientation of the crack within the element. However, such sophistication is only warranted when the concern is to reproduce the exact details of crack propagation, which is not our case.

Time discretization

The choice of an adequate partition of the time interval of interest is, in general, a matter of experience. An uniform discretization is not advisable from a computational efficiency point of view, being preferable to devise some heuristic or adaptive schemes. During the pressing stage, the major restriction on the size of the time step arises from accuracy considerations of the IMPLEX integration scheme. As alluded to in section 3.3, one can use the adaptive time stepping scheme proposed by Oliver et al.[79] to keep the error adequately bounded. Alternatively, a heuristic that proves effective is to select the length of the time increment according to the compressibility curve of the material (pressure vs density), so that the size of the time step is reduced as the slope of the compressibility curve becomes more pronounced. On the other hand, elastic conditions prevail presumably throughtout the post-pressing stages. Hence, the choice of the size of the time step in this case is dictated mainly by considerations of the powder-tooling contact response. Special care is to be exercised at those points in the fabrication cycle in which the nature of the input data is abrupt, as in the transition from pressure release to the stripping of the compact from the die.

Contact algorithm

Concerning the computation of the interaction powder-tooling, contact conditions in the normal direction are imposed as a pure geometrical constraint. Two different strategies are used to treat numerically such constraint, namely, the penalty method and the augmented Lagrangian strategy. The implication of considering one or other method are examined in section 4.3. In order to account for the fact

that the powder becomes stiffer as densification progresses, a density dependent penalty parameter is employed when using the penalty strategy. On the other hand, the constitutive behavior in the tangent direction is characterized by the corresponding friction coefficient, which may be distinct for each member of the tooling set. This friction coefficient depends upon density and sliding velocity at the interface. The contact detection algorithm is based on the construction of an interface mesh by which the interacting portions of two contacting bodies are readily identified. Penetration of one body into another is, in turn, characterized by a certain strain measure defined at each element of this interface mesh (see Ref. [77] for more details).

4.2 Diametral compression test

A brief description of this test was outlined in section 2.5.5. As pointed there, the experimental data for checking the validity of the computed results have been obtained from the work of Jonsén et al. [50, 49]. This experimental work includes a detailed pictorial description of the crack development [50], as well as relevant quantities concerning the characterization of fracture, such as tensile strength and fracture energy, for several densities (ranging from 4.90 g/cm^3 to 7.35 g/cm^3). The numerical simulations presented here correspond to an specimen of final average density $\rho = 7.21\, g/cm^3$. Load data corresponding to this density level are given in [49].

Note that the diametral compression test was also employed in section 2.5.5 for calibrating the softening law. At first glance, it appears that, in using this test for also assessing the model, we are violating a well-known precept of numerical modeling according to which the experimental results used for calibrating a model should not be also employed for its validation. However, the observance of this rule is only strictly necessary when the distribution of stress and stain is practically uniform and therefore the connection between overall strain and stress measures is direct, as in the characterization of the hardening response. Indeed, in this case one has to simply record average density values (strain measure) and pressure values (stress measure) during a closed die compaction test and, then, the exact form of the constitutive relationship is obtained by fitting these data. By contrast, the derivation of the softening law is not direct, due to the localization of strains associated with strain softening. The only available experimental data is the fracture energy, and, consequently, a host of assumptions is implied in relating the decrease of cohesion in the zone affected by the cracking process (stress measure) and the accumulated inelastic shear deformation (strain measure). Thus, the use of the same test for validating the model can be viewed as a legitimate means of assessing the correctness of such assumptions.

A schematic description of the experimental setup is shown in figure 4.1. Force is applied over two diametrically opposite arcs of angular width $2\alpha_B = 14°$. The fixture tools are modeled as elastic bodies, with Young's modulus $E_{tool} = 2.1\, 10^5\, MPa$ and Poisson's coefficient $\gamma = 0.3$. The specimen is compacted by single-action pressing of an iron based Distaloy AE powder. The apparent density of the powder is

3.10 g/cm^3, and the full green density 7.48 g/cm^3. An uniform density distribution is assumed, as the only information provided in this regard is the final average density ($\rho_0 = 7.21 g/cm^3$) of the compacted specimen. The final dimensions are $D = 25mm$ and $t = 5mm$, where D denotes the diameter and t the height of the cylindrical specimen. According to [31], these dimensions ($t/D = 0.2$) ensure that the proviso plane stress can be employed to analyze the stress state during the experiment. For simulating the experiment, a vertical displacement of 0.2 mm is prescribed upon the top face of the upper fixture tool.

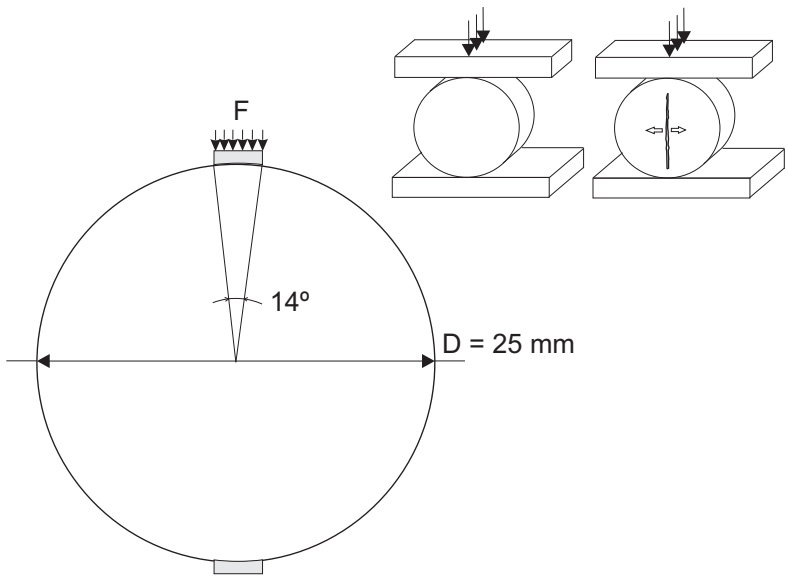

Figure 4.1 *Diametral compression test*

As regards to material properties, the yielding mechanism is characterized by an initial cohesion $c = 29.9MPa$ and an internal friction parameter $\alpha = 2.2$. These values follow from the curve-fitting equations derived in chapter 2 (see Eqs. 2.5.56 and 2.5.58) by simply setting the internal hardening parameter to $\xi^h \approx \eta = 7.21/7.48 = 0.96$.

A remark concerning calibration of material parameters, however, is in order here. The material parameters appearing in the hardening law relating cohesion and relative density, represented by Eq.(2.5.56), see section 2.5.4, were calibrated using data collected from fracture tests carried out by Coube [25] on Distaloy AE powder specimen. However, the composition of the mixture employed by Coube is slightly different from that used by Jonsén et al. The subtle difference lies in the additives, specifically, in the lubricant. The mixture in Coube's experiments incorporates 1% Hoechst microwax, whereas Jonsén's diametral compression tests were conducted using Distaloy AE powder with 0.6% Kenolube. We shall assume in this respect that the use of different lubricants does not affect significantly the mechanical properties of the green compact. This assumption is made in the absence of

experimental data concerning cohesion of Distaloy AE with 0.6% Kenolube. Nevertheless, we must note carefully that presuming that the cohesion (green strength) of a green compact part is not influenced by the type of lubricant and the addition level is quite objectionable, as it is shown in the work of Degnan et al. [29], and, therefore, this hypothesis should be adequately contrasted in future developments.

As mentioned in previous chapters, the characterization of the elastic response is a somewhat controversial issue. Two empirical relations were presented in section 2.5.4 for the Young's modulus as a function of relative density (internal hardening variable) (see Eqs. 2.5.60 and 2.5.61). Evaluation of the former, the one advocated by Pavier [83], at $\xi^h = 0.96$ yields $E^e = 168444.0\, MPa$, whereas the linear relation proposed by Coube [25], on the basis of measurements of the velocity of sound on an unstressed specimen Eq.(2.5.61), gives $E^e = 21127.0\, MPa$. The consequences of using one or the other relation will be properly assessed later. Other relevant material parameters are the Poisson's coefficient ($\nu^e = 0.29$) and the intrinsic softening modulus, which can be obtained from the graph shown in figure 2.23, giving $\hat{H}_0 = 9.0 \cdot 10^5\, MPa/mm$. The dilatancy factor γ is set to 0.01.

4.2.1 Results

4.2.1.1 Numerical aspects

Prior to compare the experimental results with the calculated response, it is expedient to carry out a preliminary convergence analysis, under refinement of the discretized time and spatial domains, and to investigate the implications of employing either standard displacement-based or mixed displacement-pressure formulations. The experimental data that will serve as the basis for the quantitative assessment of the problem is the graph of applied load F versus deflection v in the vertical direction. Thus, it seems appropriate to perform these analysis by examining $F - v$ plots. The vertical deflection v corresponds to the displacement prescribed upon the nodes located at the top face of the fixture tool, whereas the applied load F is obtained as the sum of the forces at these nodes.

Using the mesh layout displayed in figure 4.2, in which the higher mesh density in the vertical central band is dictated by foresight of the fact that the dominant crack will be located along the loaded diameter, and setting $E^e = 21127.0\, MPa$, a study varying the number of time steps[3] is undertaken. Figure 4.3 shows the result of such study. The plot of applied load versus deflection takes essentially the same form in all the studied cases, the only substantial difference being the post-peak behavior. The branch OA corresponds to linear elasticity. After point A, a slight decrease in slope occurs. This subtle change of stiffness indicates crack initiation at the center of the disc. The development of the central dominant crack progresses until the maximum force is reached (point B in case $N = 800$). The magnitude of the maximum force estimated using N = 50 steps differs from that

[3] In order to facilitate the comparison, equally space intervals have been used. However, we should note that considerable gain in computational efficiency can be achieved by means of an adaptive time stepping scheme, as the one proposed by Oliver et al. [79]. For instance, due to the implicit contribution of the IMPLEX integration algorithm, the elastic response OA could be obtained in a single step.

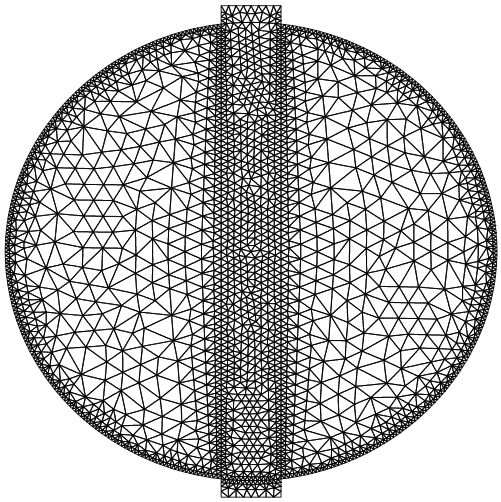

Figure 4.2 *Mesh layout*

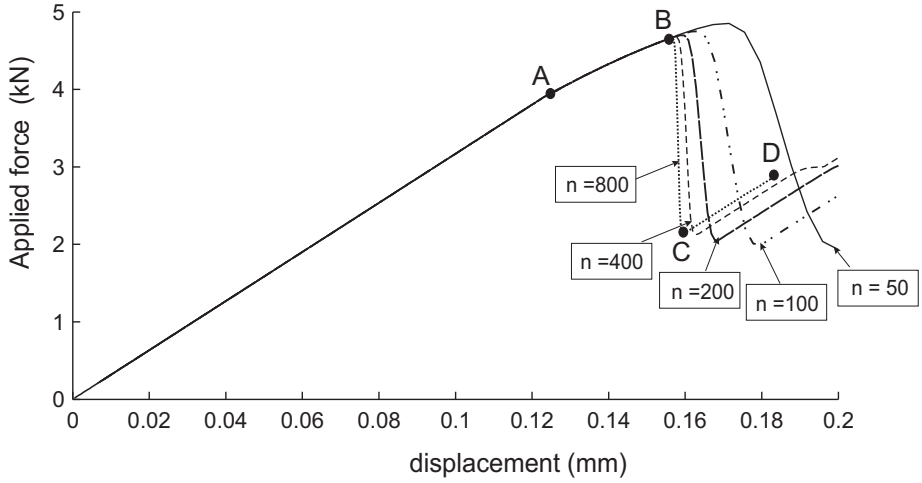

Figure 4.3 *Applied load versus deflection. Results for several number of time steps.*

calculated with N = 800 by only 4.3 %. Following the attainment of the peak-load, the central fiber suddenly ceases to contribute to the rigidity in the vertical direction, and the computed force drops rapidly (point C). The abruptness of this decay is accentuated as the time step size is reduced. The post-peak ascending branch (CD) corresponds, approximately, to the response of a specimen spli into two halves. As it is apparent that further increase in the number of step will not significantly improve the accuracy, the prediction using N=800 steps will be considered as reliable, and therefore, this discretization of the time domain will be

employed throughout the subsequent simulations. It has to be mentioned that, in computing the five cases presented, only one equilibrium iteration at each time step was required to achieve convergence.

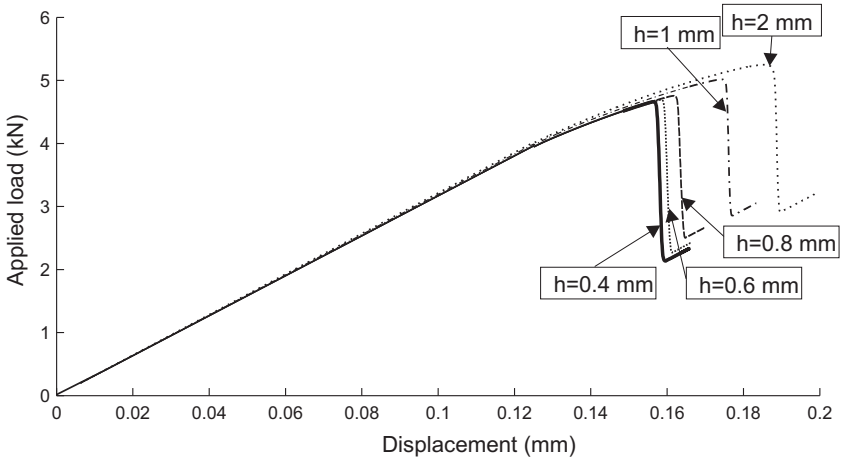

Figure 4.4 *Applied load against deflection. Result for several meshes, characterized by the size h of their elements.*

Our concern now is to examine the sensitivity of the numerical results to subsequent mesh refinement. Five different meshes characterized by the size of their elements h are used[4]. Computed results are shown in figure 4.4. As far as the magnitude of the peak value of the load is concerned, the sequence of graphs displayed in figure 4.4 exhibits clear convergence with refinement of the mesh. The peak value predicted by using the mesh labelled as $h = 0.4mm$ is only a 0.6 % lower than the one obtained with the coarser mesh $h = 0.6mm$. On the other hand, the magnitude of the "residual force" - the force calculated at the onset of the post-peak ascending branch - ranges between 2.85 kN and 2.91 kN, although without a clear monotonic convergence tendency. In view of these circumstances, it seems that going to finer discretizations will not improve significantly the accuracy. Hence, the mesh labelled as $h = 0.4mm$, which corresponds to the one displayed previously in figure 4.2, will be taken as the finite element mesh for the simulations shown in the sequel.

The force versus displacement curves obtained by using two different finite element procedures, namely, a *standard displacement-based formulation and a mixed displacement-pressure approximation*, are depicted in figure 4.5. Inspection of this diagram indicates that the use of one or another formulation is inconsequential, as the two curves are practically indistinguishable.

[4]The mesh layouts used in this study are patterned after the non-uniform mesh depicted in figure 4.2. The typical size h corresponds hence to the size of the elements in the central region that will eventually contain the dominant crack. Care is to be exercised in selecting the mesh size in the region where the load is applied to the specimen, since excessively coarse meshes may not represent adequately the stress concentration, leading to a mechanism of failure different from that of cracking along the loaded diameter.

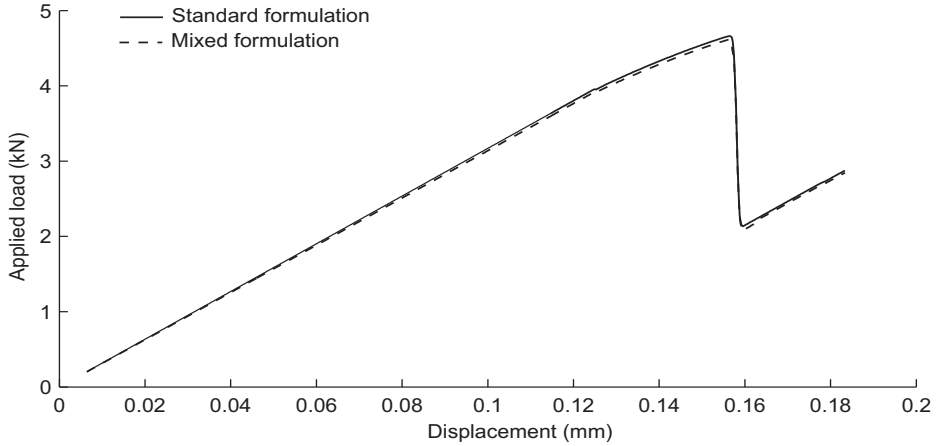

Figure 4.5 *Applied load against deflection. Comparison between results computed using a standard displacement-based formulation and a mixed displacement-pressure formulation.*

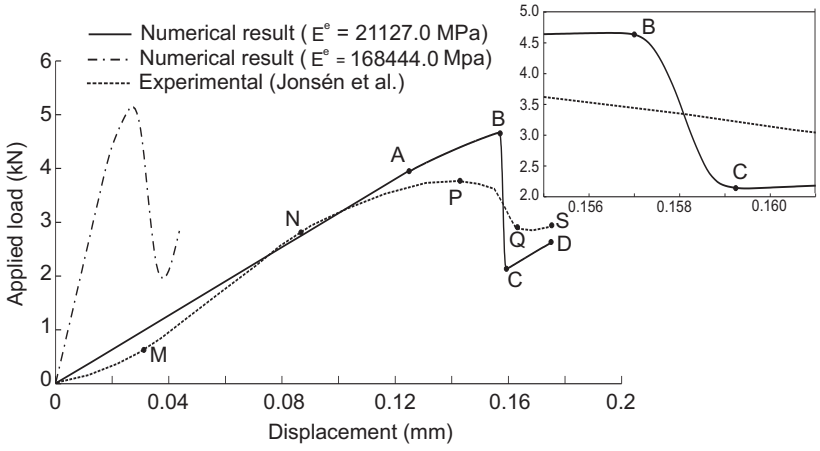

Figure 4.6 *Applied load versus deflection. Comparison of computed results using different elastic properties with experimental data collected by Jonsén et al. [49]. The post-peak descending branch B-C is shown in magnified form.*

4.2.1.2 Computed versus experimental results

Quantitative results

We are now in the position to compare the computed response (using N = 800 steps , typical mesh size $h = 0.4\,mm$ and standard displacement-based formulation) with the experimental results. The plots of the computed force versus vertical deflection for two distinct Young's modulus $E^e = 168444.0\,MPa$ and $E^e = 21127.0\,MPa$, in conjunction with the corresponding experimental curve, pro-

vided by Jonsén et al. [49], are depicted in figure 4.6. This diagram clearly shows that the Young's modulus estimation $E^e = 168444.0\,MPa$, obtained from triaxial measurements [83], is utterly inadequate for characterizing the elastic response of the green compact under the conditions of this diametral compression test, being more appropriate the estimation $E^e = 21127.0\,MPa$, derived from ultrasound tests [25]. Nonetheless, even in this case, significant differences with experimental data are observed. Indeed, the slope of the numerical $F - v$ graph remains constant until point A. By contrast, the plot of the experimental force versus deflection traces initially a non-linear path OM. Then, it becomes linear up to the point N, at which, according to Jonsén et al. [49], the elastic nature of the graph ceases due to the initiation of the central crack. The progressive decrease in slope observed experimentally (path NP) during crack growth is more pronounced that the decrease in slope predicted by the model (path AB), which is practically unnoticeable. As a consequence, the computed peak load (point B) exceeds notably (20 %) the maximum force measured experimentally (point P). Discrepancies in the post-peak behavior are also noteworthy. In the experiment, a relatively gradual decay of load is recorded (path PQ), whereas this decay occurs precipitously (path BC) in the simulated response, resulting a residual force underestimated by approximately 30 %. The enlarged view of path BC, shown in the upper-right part of figure 4.6, reveals that the transition from B to C, albeit quite abrupt, is not instantaneous, that is, several time steps are required in its computation[5].

Qualitative results

Figure 4.7.a contains images recorded experimentally by Jonsén et al [50] during the loading process. The leftmost picture corresponds to the initiation of the crack at the center of the disc (point N in the $F - v$ curve shown in figure 4.6). The central image shows the state of the crack at the point of maximum load (point P in figure 4.6). Finally, the rightmost picture displays the aspect of the crack at the end of the loading process (point S in figure 4.6). Aside from the central "dominant" crack, secondary cracks are distinguishable around the contact zones.

Cracks impair strength. Thus, a natural way of representing such defects is by plotting *contours of cohesion* (green strength), in which crack locations are identified as those areas affected by a *local decrease of cohesion*. The corresponding sequence (initiation of the central crack, maximum load and end of the test) of computed contour plots of cohesion is shown in figure 4.7.b. In the leftmost plot, the local decay of cohesion observed in the center of the disc indicates the initiation of the crack. In the central contour plot (maximum load), we can see that this loss of cohesion propagates to the periphery of the disc along the loaded diameter. Close to the center of the disc, this propagation occurs along a single path. Near the loading surface, however, the de-cohesion path seems to bifurcate into two branches. Such bifurcation (or "crack branching") is not detected in the experiment. Inspection of the rightmost plot (end of the test), indicates that, eventually, loss of cohesion has been more intense along one of these branches. The resulting "dominant" path,

[5] An instantaneous drop would correspond to a *perfectly brittle response*. A force versus displacement graph that exhibits such feature warns of trouble with potential *snap-back behavior*[27].

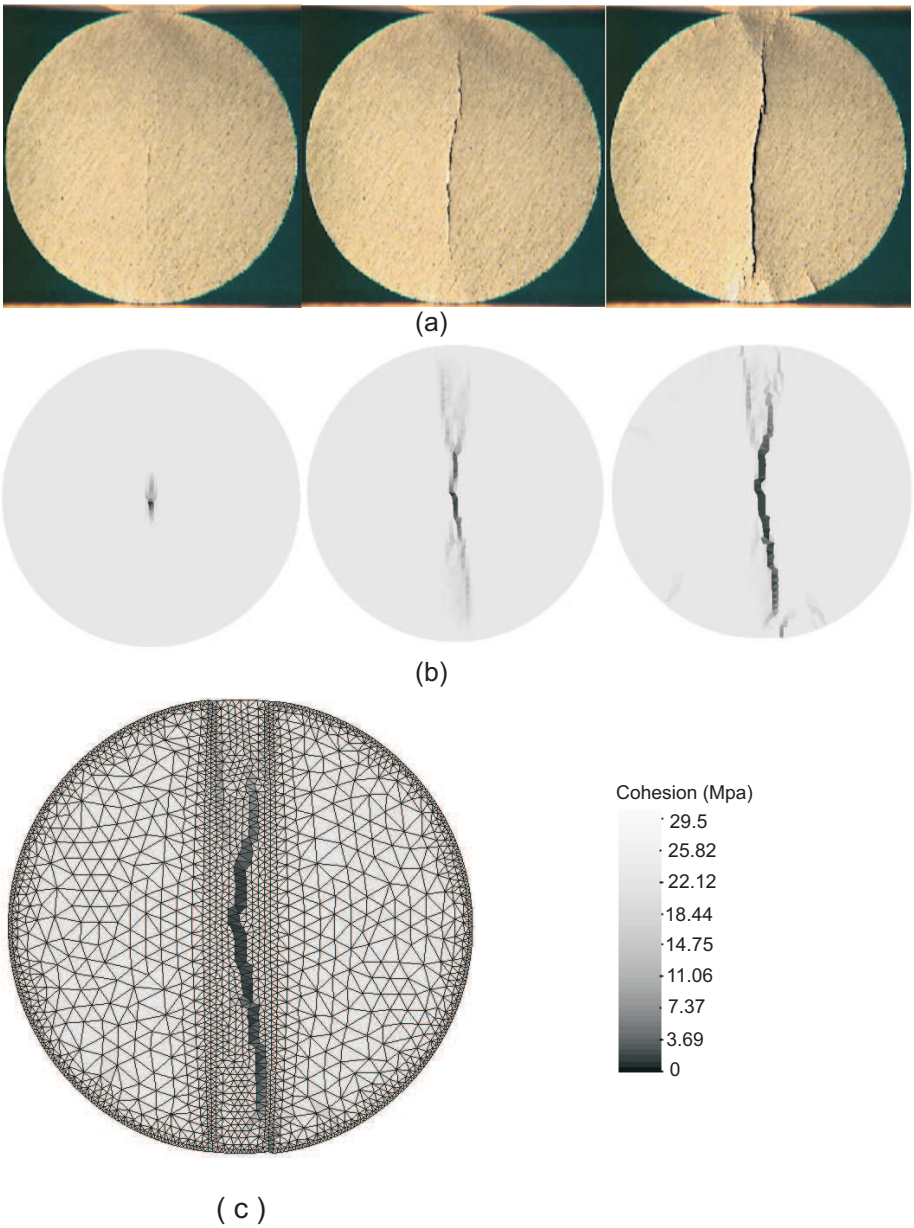

Figure 4.7 *(a) Images recorded experimentally by Jonsén et al [50]: initiation of the crack, point of maximum load, and end of the loading process. (b) Contour plots of computed cohesion corresponding to such stages. (c) Contour plot of computed cohesion at the end of the loading process, showing the spatial grid used in the computation.*

which spans approximately 80% of the length of the diameter, displays a distinctly

crack-like appearance, and bears close similarity with the crack observed in the corresponding photograph. Note that other regions with relatively low cohesion, located mainly around the contact zones, are discernable in the final contour plot. The aspect of these patterns of low cohesion are in remarkable agreement with the abovementioned secondary cracks detected experimentally.

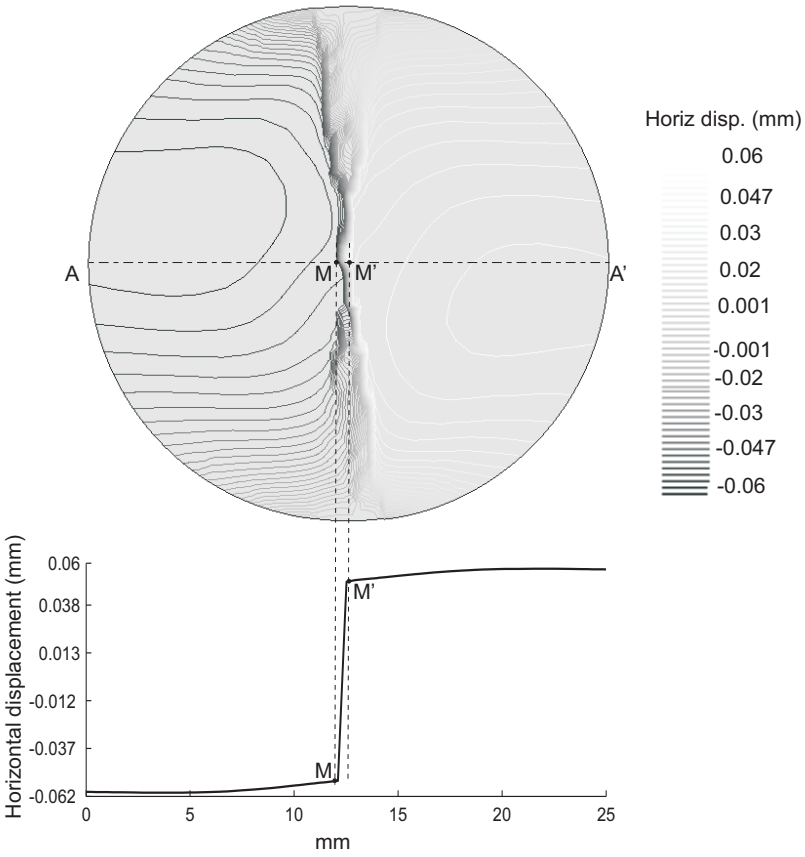

Figure 4.8 *Horizontal displacement contour lines. The graph shows the horizontal displacement measured along the horizontal diameter* $AA\hat{A}\,'$.

In figure 4.7.c, the final cohesion contour is plotted in conjunction with the finite element mesh used for the computation. This plot allows us to distinguish the band of elements along which loss of strength is *localized*. A result that also assists in visualizing this *localization phenomenon* is the plot of horizontal displacement contour lines, displayed in figure 4.8. Close spacing of lines relates to steep slopes and wide spacing to gentle inclines. Hence, the intense concentration of lines presented along the loaded diameter is indicative of an abrupt change in the horizontal displacement, as it is shown in the accompanying graph of figure 4.8.

4.2.2 Discussion and concussions

The numerical results shown in figure 4.3 serve as a convincing proof that the solution provided by the IMPLEX integration algorithm *converges as the length of the time step is reduced*. In addition, we pointed out that only *one iteration per step*, for the five cases presented, was required to achieve convergence to equilibrium states, a fact that highlights the *robustness* of the IMPLEX integration scheme. Not least among its merits is the ability to compute the post-peak response (curve BCD in figure 4.3). A pure implicit integration scheme, without further enhancements such as cumbersome *continuation methods* [71, 27], would probably fail in simulating the post-peak behavior, since the tangent stiffness matrix derived from this integration scheme ceases to be positive definite at this point.

The sequence of force versus displacement diagrams presented in figure 4.4 indicates that the energy[6] dissipated during the loading process apparently converges as the mesh is refined. As mentioned in section 2.1.2.1, lack of convergence upon refinement of the finite mesh is one of the flaws that plagues the numerical treatment of models exhibiting strain-softening behavior. Hence, the proposed regularization of the softening law proves useful, at least in this example, in alleviating this problem. We should note that this assessment only furnishes information regarding the dependency of the results on the size of the elements. A complete assessment should also acknowledge the directional dependence on mesh topology [4]. The smeared crack model presented in this work is very elementary in this respect and does not contain any enhancement to deal with such issue . The predictions made by our model will be thus inevitably affected by this mesh-induced directional bias. However, knowing with detail the exact orientation of the potentially developing cracks is not the goal of our analysis, thus such modeling deficiency is relatively inconsequential.

It is widely known that, in many applications such as metal plasticity, the use of linear triangular elements in conjunction with displacement-based finite element formulation, suffers a detrimental overstiff phenomenon known as "volumetric locking" [9]. With a view towards assessing the efficiency, in our context, of the standard formulation in comparison with alternative formulations not theoretically prone to volumetric locking, a mixed finite element approximation with displacements and pressure as basic variables has been tested. Results presented in figure 4.5 were aimed at comparing the calculated force versus displacement response under these two approaches. According to this diagram, no appreciable differences are found in using mixed or standard formulation. This "unexpected" similarity may be explained as follows. The developing of the crack (see figure 4.7) along the loaded diameter takes place under mode I or opening mode conditions, which, incidentally, are the same conditions that characterizes fracture in a pure tensile test. This implies that the the stress state at a representative plastically deforming element traces a path which lies approximately within the first quadrant of the p-q plane

[6] Recall (see figure 2.21) that the energy dissipated can be estimated in terms of the area enclosed by the force displacement graphs of unsplitted and splitted tests.

(tensile regime). As illustrated in figure 2.9 (chapter 2), in this stress regime, the plastic flow involves a *dilatational component*, due to the use of a parabolic plastic potential function, and this volumetric component, in turn, becomes dominant as the stress state approaches the vertex of the Drucker-Prager failure line. Hence, the material represented by our plasticity model in this range of stresses is not *plastically incompressible*. The absence of this kinematical constraint may thus explain why both formulations yield identical responses[7].

According to the preceding discussion, thus, the simulation of cracks which develops under *mode I* is not affected by volumetric locking, even when using standard displacement based formulation. Experimental observations indicate that, during the manufacturing process, the vast majority of cracks usually grows under this opening mode [99]. Consequently, in view of these facts, and considering, in regards to the mixed approach, the increase of computational effort and the previously mentioned questionable reliability of the stabilization procedure, it seems reasonable to favor the standard displacement based formulation over the mixed approach. Certainly, volumetric locking may emerge in other situations. At high densities, for instance, the material flows at constant volume when yielding on the von Mises yield surface, i.e., it becomes plastically incompressible. However, as mentioned in chapter 2, the validity of the constitutive relationships might be questionable as a whole, since the basic hypothesis of small elastic strain is violated. Hence, further sophistication is not warranted.

As regards the results shown in figure 4.6, the large difference observed between the responses obtained by using different elastic parameters conveys the relevance of choosing an adequate estimation for the Young's Modulus. In this case, the computed $F-v$ graph corresponding to the the Young's modulus estimation $E^e = 21127.0\,MPa$, derived from ultrasound tests conducted by Coube [25], is in closer agreement with the experimental data. This fact is in conformity with the argument set out in section 2.5.4 when dealing with the calibration of the elastic parameters, according to which, Coube's empirical relationship (Eq.(2.5.61)) is more appropriate in circumstances of low degree of confinement. However, even in this case, significant discrepancies between predicted and experimental curves are detected.

The different elastic behavior exhibited by the computed response and the experimental data, linear and non-linear[8], respectively, highlights, again, concern with the characterization of the elastic response, which should receive more careful consideration in future improvements of the model. On the other hand, the different trends observed in the inelastic branches up to the peak load -the computed response has a steeper slope (see figure 4.6, paths AB)- may be attributable to several

[7] Another apparently plausible explanation is that, in plane stress problems, the thickness of the element can change to accommodate incompressible materials, and hence volumetric locking will not occur[5]. However, as alluded to earlier, this reasoning is not valid, as the plane stress proviso is imposed here in an approximated manner, which follows from a plane strain formulation by an appropriate conversion of elastic constants.

[8] The non-linear behavior at the beginning of the curve may be alternatively attributed to initial seating and settling errors during experiments, and not necessarily to non-linear material behavior.

factors. A plausible explanation is that the stress conditions along the localization band may be not adequately represented by the *approximated* plane stress formulation. This hypothesis should be corroborated in future developments by undertaking a three-dimensional analysis. The model overpredicts the maximum force in approximately 20 %, and the displacement at which this peak value is reached in 11 %., amounts which are within a reasonable range of accuracy, considering the significant uncertainty (10-15%) attached to the experimental determination of tensile properties in green compacts[9].

The post-peak portion of the curve corresponds to the unstable growth of the central dominant crack. The computed force experiments a drastic decrease, as opposed to the relatively mild decay observed experimentally. The computed residual force is underestimated in approximately 30%. As a result, the energy dissipated during the process is overestimated. The main contributor to this discrepancy[10] may be found in the elementary character of our crack modeling approach. Indeed, as mentioned earlier, our model does not permit a precise tracking of the developing cracks. As a consequence, the propagating localization band could tend to follow certain preferred directions dictated by the mesh, and, eventually it may travel along bifurcated paths, giving rise to spurious "crack branching", as the one observed in the contour plot of cohesion displayed in figure 4.7.b (central picture). An immediate implication of such spurious branching is that the extent of the region affected by loss of cohesion increases, resulting in a overestimation of the dissipated energy.

We reiterate that the quality of the obtained results must be judged in the light of the aim and purpose of our investigation. The model has undoubtedly proved to be efficient in *detecting the formation* of the experimentally observed macroscopic crack. In addition, as seen in figure 4.7, the de-cohesion pattern predicted by the model is in remarkable agreement with the experimental images of the crack development. Admittedly, the results can be improved. However, as it may be inferred from the preceding discussion, if one wishes to bring the computed solution into closer agreement with experimental evidence, aside from possible refinements of the hypothesis involved in the calibration of the fracture energy, it would be necessary to abandon the elementary smeared crack approach in favor of more sophisticated, and complex, continuum-based methods [75].

[9]The material parameter that has more influence in the location of the peak load is the cohesion variable (c). Note that the experimental values for cohesion shown in chapter 2 are *derived data* [14], in the sense that they are obtained from *raw data* (tensile and compression strength, for instance) through an interpretation process full of assumptions. Thus, in addition to the error involved in obtaining the *raw data*, one has to acknowledge the uncertainty associated to such assumptions.

[10]The post-peak portion of the curve is also highly sensitive to test conditions [61]. Hence, the relevant features of the experimental environment (total stiffness of the testing frame, for instance) should be also acknowledged if the response is to be accurately predicted.

4.3 Pressing and ejection of a thin cylindrical part

A cylindrical part made of an iron based Distaloy AE powder, with apparent density $\rho_{app} = \rho_0 = 3.04\, g/cm^3$ and theoretical density $\rho_{th} = 7.33\, g/cm^3$ is pressed until reaching a final density $\rho = 7.18 g/cm^3$. The punches and the die are considered elastic materials characterized by a Young's modulus $E_{tool} = 210000 MPa$ and a Poisson's ratio $\nu_{tool} = 0.3$. Their dimensions are displayed in figure 4.9.

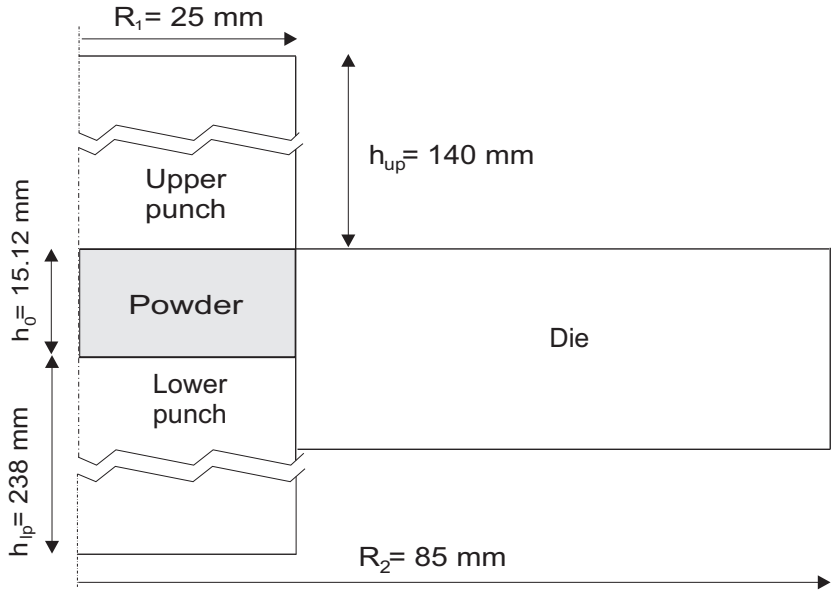

Figure 4.9 *Dimensions of punches and initial die cavity.*

The motion of the upper and lower punches is controlled by prescribing vertical displacements on its top and bottom surfaces, respectively. During pressing, the upper punch moves downward with constant velocity $10\, mm/s$ while the lower punch and the die remain stationary. Release of axial pressure takes place at a rate $20\, mm/s$ by gradually lifting the upper punch. During ejection from the die, the lower punch pushes the compact upward at a constant rate $40\, mm/s$.

This example focuses on the formation of cracks due exclusively to *elastic expansion of the compact upon exiting the die*. Contribution of friction effects to the occurrence of cracks will be therefore ignored by setting the friction coefficient to a low constant value [11] $\mu = 0.01$. Furthermore, these circumstances of negligible friction will allow us to draw approximated analytical expressions for estimating the stress state during axial unloading. In order not to disrupt the continuity of the presentation, these derivations are relegated to appendix B.3.

Material parameters are obtained from the calibration presented in chapter 2.

[11] Assuming an ideally frictionless process is not advisable since, upon total removal of the upper punch, ill-conditioning may arise due to the absence of restrictions on the vertical direction.

We recall that two alternative empirical relationships for the Young's modulus as a function of relative density were quoted. Here we shall adopt the one advocated by Pavier [83], see Eq.(2.5.60), since it yields substantially larger values that Coube's estimation [26] (see Eq.(2.5.60)) and, therefore, the effects of elastic expansion are accentuated.

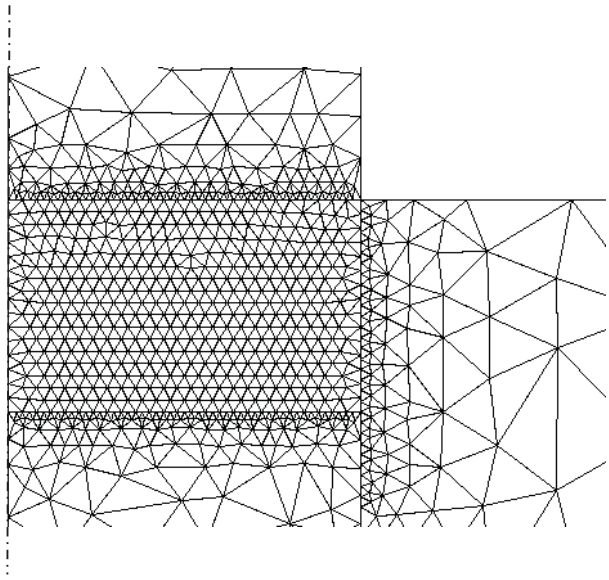

Figure 4.10 *Initial mesh layout.*

The initial finite element mesh is shown in figure 4.10. The average size of the elements of the powder body is $l_e = 1mm$, whereas the size of the elements at the boundaries of punches and die in contact with the powder is, approximately, $0.5mm$. In general, a practice that proves advantageous in ensuring a successful performance of the contact-detection algorithm is to select the element size at the boundaries of the tooling bodies equal or smaller than the element size used at the boundary of the powder body. Tooling elements can be graded from small-size at the boundaries in contact with the powder to become coarser with increasing distance from these surfaces.

4.3.1 Results and discussion

4.3.1.1 Study of convergence with refinement of time discretization

In the example of the Brazilian test, see section 4.2.1.1, the issue of convergence under refinement of the time discretization was examined in a problem involving softening behavior. The goal now is to explore this issue in situations in which hardening behavior dominates the response, i.e., during pressing of the powder within the die.

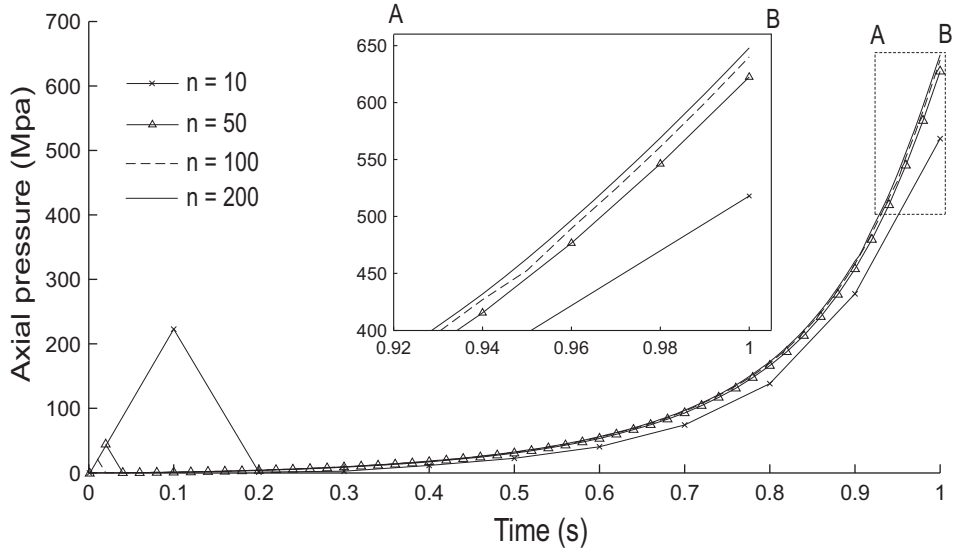

Figure 4.11 *Average axial pressure during pressing versus time. Results for several number of time steps (uniformly spaced). The final portion of the curves is shown in magnified form.*

Figure 4.11 shows axial pressure versus time graphs computed using different number of (constant) time steps. The sequence of graphs is clearly convergent. The simulation with N = 200 steps can be taken as the "correct" solution, as it is apparent that going to smaller time step sizes will not improve significantly the accuracy of the predictions. Inspection of the initial portion of the curves, however, reveals an anomalous behavior. At the very first increment, the solution calculated for the four cases presented "overshoots". The magnitude of the deviation decreases as the time step is reduced, being practically imperceptible for N = 200 steps. This overshooting is not connected with any type of instability, since the computed response returns to the presumably correct course at the second step. For instance, for N = 50 steps, the axial stress computed at the first increment is largely overestimated (40 MPa, in contrast to the 0.1 MPa predicted with N = 200 steps). Despite this initial substantial error, the drift from the correct curve in subsequent increments remains bounded, being the magnitude of the maximum pressure (compaction pressure) only 3.5 % below the pressure computed with N = 200 steps.

The origin of this non-physical overshooting behavior is to be sought in the numerical integration of the constitutive equation, more precisely, in the intricacies of the *IMPLEX* integration scheme. As explained in section 3.1.1, the essence of this integration procedure is to obtain the stresses and other state variables at a given time step in terms of variables computed at the previous time step by accomplishing an implicit integration. At the very first increment, obviously, no information is available to carry out the extrapolation. The integration algorithm resolves this

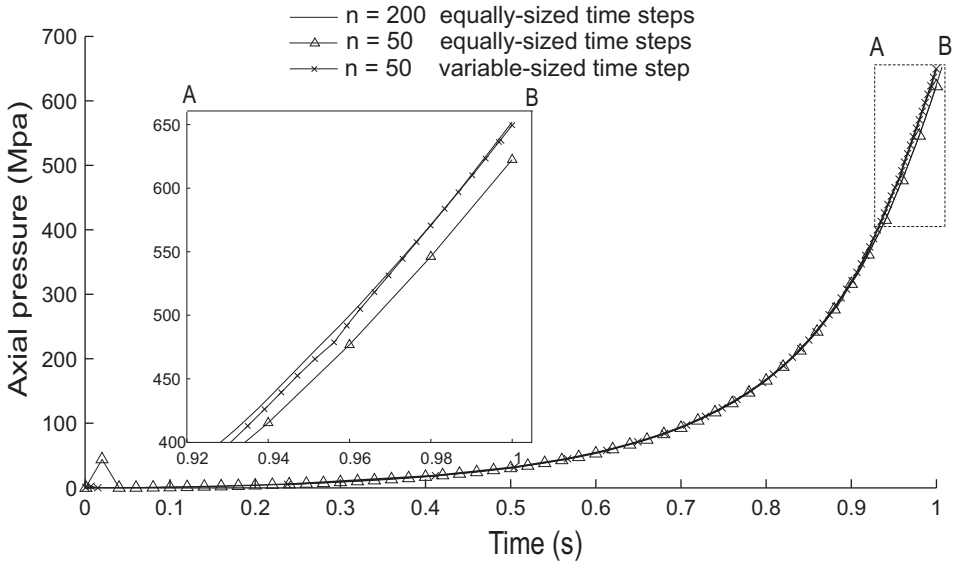

Figure 4.12 *Average axial pressure during pressing versus time. Results for several number of time steps (constant and variable time steps). The final portion of the curves is shown in magnified form.*

inconsistency by further assuming that the *plastic multipliers* are initially zero. Such assumption, in turn, amounts to presume that the body *behaves elastically* at the first step. This explains why, for the four cases, axial stresses at the first increment lie along a straight line (see figure 4.11).

It follows then that the natural way to counteract this overshooting problem is to reduce the time step size[12]. However, dimishing uniformly the step size over the whole time domain is not an efficient practice. It is preferable a "smart" distribution of the time step lenght that permits the reduction of the integration error at reduced computational cost. To reinforce this view, in figure 4.12, the response obtained using 50 and 200 equally-sized spaced time intervals is compared with the solution computed with 50 *variable-sized time steps*. The size distribution for the non-uniform discretization is shown in figure 4.13.b. The relatively small size of the two first intervals is dictated by the need to overcome the overshooting problem. The size of the subsequent time steps is directly connected with the compressibility of the material. As the slope of the pressure versus density curve becomes more pronounced, the length of the time step is progressively reduced, so that the *incremental changes in stress remains approximately constant*. Inspection of figure 4.12 indicates that a similar level of accuracy is obtained by using either

[12]Alternative ad-hoc procedures can be put forward to alleviate this problem. For instance, a plausible option is to obtain the response at the initial step by performing a classical pure implicit integration. This procedure is quite effective provided the exact implicit algorithmic tangent moduli is available. Such not being the case, convergence failure may occur and, therefore, the solution may be "worse than the disease".

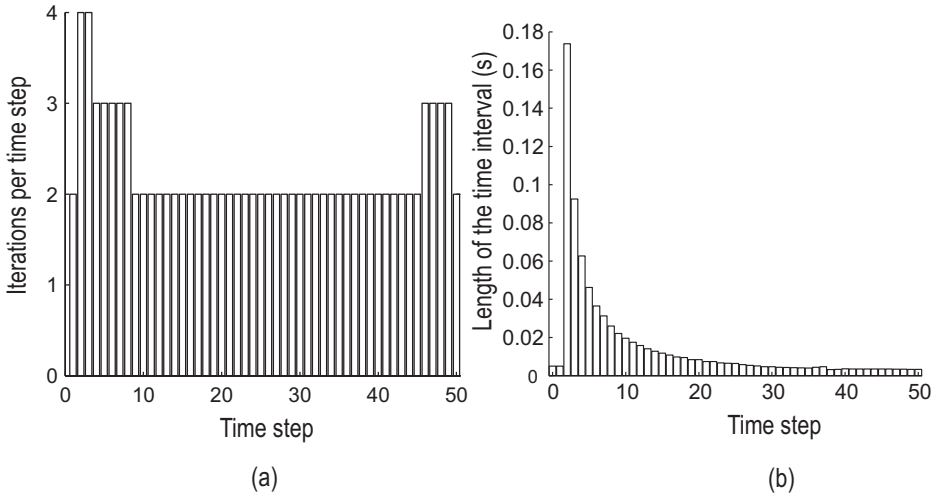

Figure 4.13 *(a) Number of iterations (global scheme) against time step number and (b) length of the time interval versus time step number. Both results correspond to the case N = 50 (variable) steps shown in figure 4.12*

200 steps uniformly spaced or 50 steps with sizes non-uniformly distributed. The use of this "smart" step size distribution has reduced thus the computational effort by a factor 200/50 = 4. Finally, figure 4.13.b. displays the number of global equilibrium iterations required to achieve convergence at each increment for the case N = 50 variable time steps. The number of iterations ranges between 2 and 4, resulting in a total number of computational cycles (number of increments times number of iterations) of 113.

4.3.1.2 Assessment of the contact algorithm

Figure 4.14 displays the average axial and radial pressure versus time on the compact during pressing and axial unloading computed with two different contact algorithms, namely, the *contact penalty method* and the *augmented Lagrangian technique*[13]. The *penalty factor*, denoted here as K_p, is made proportional to the Young's modulus[14] of the material, that is, $K_p = a\,E^e$. Two values of the proportionality factor a has been tested.

The initial shallow portion of the curves is not shown, since the three solutions are practically identical. The ascending and descending branches correspond to

[13]The augmented Lagrangian method is applied together with a *double loop Uszawa type algorithm*.The inner loop refers to the iterations for solving the weak form whilst the lagrange multiplier is held constant. The *outer loop* serves for updating the lagrange multiplier [110].

[14]As mentioned at the outset of this chapter, the contact detection algorithm used here is based on the construction of an *powder-tooling interface mesh*[77]. This, in turn, allows us to define the penalty parameter locally at each element of the interface mesh. Here it is made proportional to the Young's modulus of the powder elements adjoining the nodes that define the corresponding interface element.

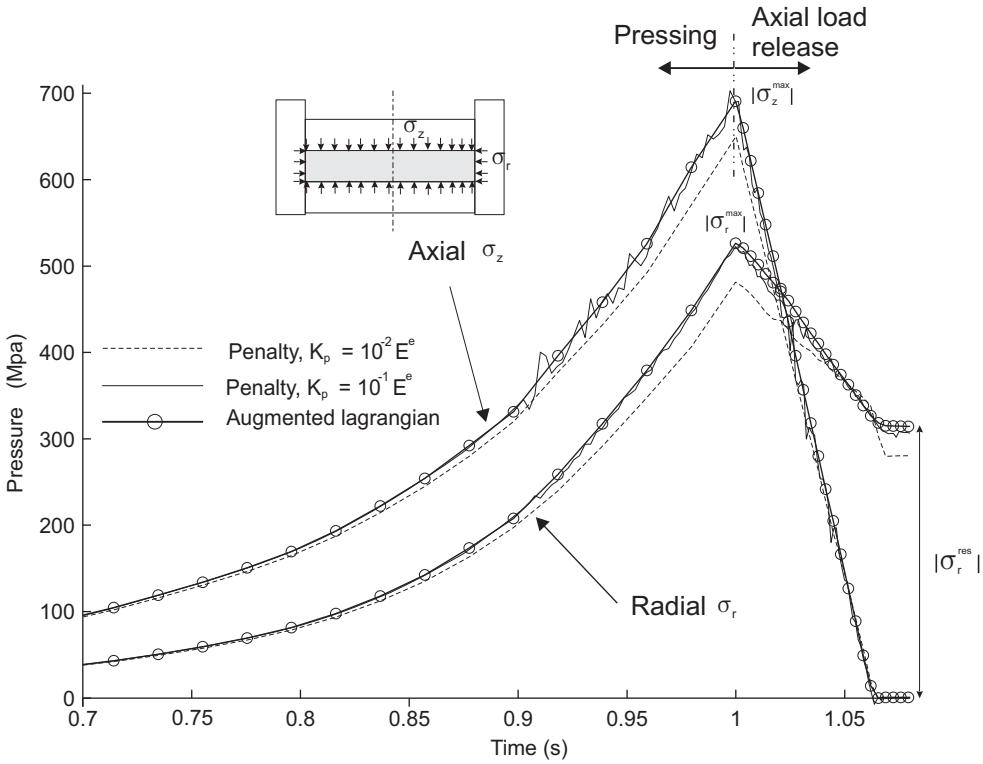

Figure 4.14 *Average axial and radial pressure versus time (during pressing and axial load release stages). Comparison between results computed by using two different contact algorithms, namely, a contact penalty strategy, for two different penalty parameters K_p (which are proportional to Young's modulus E^e of the compacting powder), and an augmented lagrangian technique.*

pressing and axial unloading, respectively. The penalty method with the larger parameter ($a = 10^{-1}$) and the augmented lagrangian technique are undistinguishable up to $t = 0.92\,s$ for both axial and radial pressures. Thereafter, the penalty solution with larger parameter ($a = 10^{-1}$) oscillates about the smooth solution obtained with the augmented lagrangian method. The oscillations are more intense in the axial response. The response calculated with the low penalty factor ($a = 10^{-2}$) exhibits a progressive drift from the other two solutions. The magnitude of this deviation at the end of pressing is approximately 10 % for both axial and radial pressures, whereas the radial pressure upon total axial unloading, denoted by σ_r^{res}, is underestimated by almost 12 %.

The solution obtained by using the augmented Lagrangian strategy can be considered as the more accurate, and therefore reliable, solution, since the constraint of impenetrability is more rigorously enforced that in the penalty case, at the expense

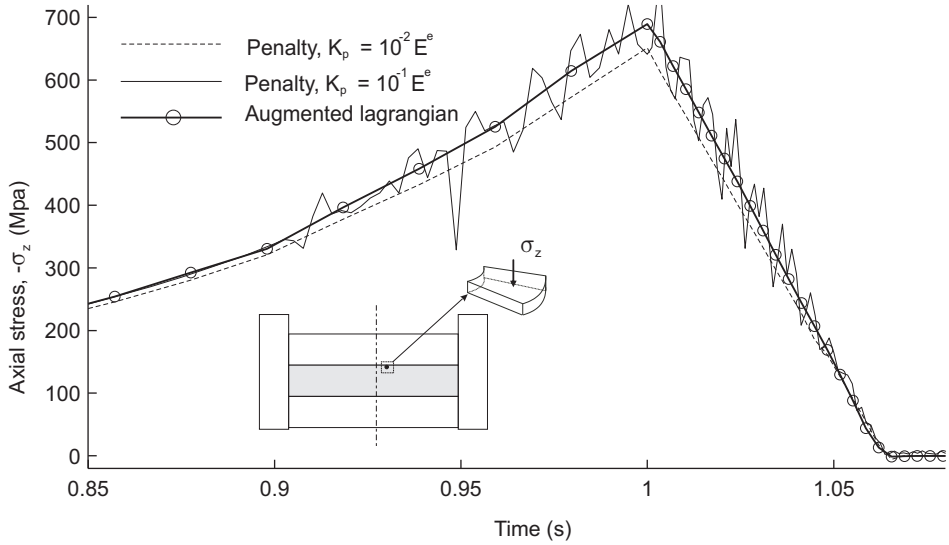

Figure 4.15 *Axial stress, at a node located on the top surface of the compact, versus time (pressing and axial load release stages). Comparison of the performance of penalty and augmented lagrangian contact techniques.*

of a substantial increase of computational cost [15]. The gradual deviation of the penalty solution with the low parameter ($a = 10^{-2}$) is due precisely to a poor enforcement of the non-penetration constraint. On the other hand, the non-physical oscillatory behavior exhibited by the penalty response with the large parameter $a = 10^{-1}$ can be plausibly attributed to an *ill-conditioning* of the problem due to an excessive large penalty factor. The magnitude of such oscillations becomes more evident by plotting, instead of average pressure, the axial stress at a node belonging to the upper boundary surface (see figure 4.15).

If the scope of the analysis were to merely examine average density and stresses after compaction in relatively large domains, the effect of these oscillations would be not too deleterious. Indeed, during the analysis of the pressing stage, this oscillatory behavior manifests itself in uneven density and stress distributions along the boundary of the powder body. Due to the stable character of hardening behavior, these uneven patterns tend to dissapear as we move far from the boundary, and as a consequence, final average quantities are not seriously affected. By contrast, the consequences of inaccurately resolving the contact response are more dramatic when the main concern is the analysis of cracks. The reason behind this is the sensitiveness, of both physical and computational nature, exhibited by the green compact during the post-pressing operations. If the oscillations of the computed

[15] For the outer loop, the number of iterations is between 4 and 20, on average 8, depending on the difficulty in determining the correct status (active or inactive) of the interface elements. This implies that the computational cost rises more than 8 times in comparison with the more simplistic contact penalty approach.

forces are sufficiently severe, the stress state at a boundary element may result seriously perturbed, with the consequent drop of mechanical strength (cohesion). Due to the unstable nature of softening materials, this perturbation may propage inwards, leading to the formation of "spurious" numerical cracks, which can be quite misleading and eventually lead to incorrect design decisions.

In view of the importance of obtaining an *oscillation-free contact response*, the augmented Lagrangean contact strategy appears to be more appropriate. The solution with the small penalty parameter $a = 10^{-2}$ is also ostensibly smooth and regular, and, in addition, the maximum deviation in predicting final forces is approximately 12%, which, although certainly not a negligible error, can be considered within acceptable engineering accuracy. However, we should keep in mind that the choice of this particular penalty factor is based on heuristics rather than in any physical argument. Although it gives an oscillation-free response in this example, it is uncertain whether it will behave satisfactorily in other cases. Therefore, in the interest of robustness and reliability of the computed solution, it is preferable to adopt the more expensive augmented Lagrangian strategy for computing, at least, the contact response during the phases of axial pressure release and ejection from the die.

Analytical estimation of the lateral pressure upon axial unloading

The *residual radial pressure*, denoted as σ_r^{res}, is the pressure exerted by the die upon total release of the applied axial load (see figure 4.14). This pressure and the roughness of the die wall will determine the magnitude of the frictional forces that will have to be overcome for ejecting the part. According to the radial pressure versus time graph shown in figure 4.14, the residual lateral pressure, for the augmented Lagrangean case , yields $|\sigma_r^{res}| \approx 320\,MPa$. Considering that the maximum radial pressure is $|(|\sigma_r^{max}) \approx 517\,MPa$, this implies a reduction in lateral pressure of 38% upon axial unloading.

In appendix B.3, the stress state during axial load release is studied analytically by presuming elastic conditions and a homogeneous deformation state. According to Eq.(B.3.9) in this appendix, such drop in lateral pressure can be expressed as a function of the compaction pressure $|\sigma_z^{max}|$:

$$|\Delta\sigma_r| = M_{ul}|\sigma_z^{max}|, \tag{4.3.1}$$

where M_{ul} is a parameter that includes the effects of the die geometry and the elasticity of the powder and the die:

$$M_{ul} = \frac{\nu^e}{(1-\nu^e) + \dfrac{E^e}{K_{tool}}}. \tag{4.3.2}$$

The Young's Modulus of the powder E^e can be obtained by evaluating expression Eq.(2.5.60) (section 2.5.4) at $\xi^h \approx \eta = 7.18/7.33 = 0.98$, yielding $E^e = 196068\,MPa$. The constant K_{tool} represents the stiffness of the die in the radial direction (see figure B.3 in appendix B.3). For the given geometry $K_{tool} = 470600\,MPa$. Substituting these quantities in Eq.(4.3.2), we have $M_{ul} = 0.28$.

Thus, taking into account that $|\sigma_z^{max}| \approx 685\,MPa$, the drop in lateral pressure estimated analytically gives 37%, only 1% less than the decrease calculated with the finite element solution.

4.3.1.3 Assessment of the crack prediction methodology

We consider first the case corresponding to an ejection with total removal of the upper punch followed by an upward movement of the lower punch. Figure 4.16.a contains a sequence of three contour plots of cohesion during this ejection process. In the leftmost plot, the compact is still confined within the die cavity. It follows from the uniformity exhibited by the cohesion distribution that the green strength has not been altered and remains at the same value attained at the end of the pressing stage. In the central plot, almost one half of the compact has already emerged from the die. To make more distinguishable changes in cohesion, this plot is displayed in magnified form in figure 4.16.b with a narrower grayscale. A de-cohesion pattern, in the form of darker "spots", is observed along the emerged portion of lateral surface. This mechanical damage is apparently superficial, since only the outer layer of elements is appreciably affected by loss of cohesion.

The rightmost plot of figure 4.16.a is the cohesion contour map at a point where 85% of the upper portion of the part is clear of the die. An enlarged view of such plot is displayed in 4.16.c. In addition to the above mentioned lateral de-cohesion pattern, which has progressed along the perimeter, decrease in cohesion is detected at the upper half portion of the part. The degradation is more intense along the upper layer of elements. Near the axis, the resulting decay is estimated in 95% of the value of cohesion attained at the end of the pressing stage. As we move downward, the intensity of the degradation diminishes gradually and becomes more diffuse.

Figure 4.16.d shows schematic descriptions of two type of crack patterns observed experimentally in *Class I parts*[16]. These sample crack layouts have been obtained from the almost exhaustive crack database elaborated by Zenger et al [112], and are accompanied by a code that facilitates the identification of plausible causes of the formation of these cracks. The agreement with experimental evidences, therefore, becomes qualitatively apparent by comparing the computed contour plots with these schematic descriptions. The mechanical deterioration observed on the lateral surface appears due to the absence of a smooth taper to allow some degree of radial relaxation. The other typology of failure, the one detected on the top surface, is almost ubiquitous in the ejection of Class I parts, and is caused by bending stresses. As illustrated in figure 4.17.a, radial pressure acts only on the portion of the outer surface still restrained by the die. The line of action of the resultant radial force passes through a point P located at a distance e below the center of gravity C. A bending moment is therefore induced because of the eccentricity of the resultant force, and consequently, tensile stresses are set up at

[16] A commonly used classification system groups the P/M manufactured parts according to their complexity, features, number of levels and the tooling system used to make the part. "Class I" parts, the simplest ones, are one level thin (height less than 6.35 mm) parts, pressed in only one direction and with little density variation. Thus, the compacted cylinder shown in this example falls into this category[112].

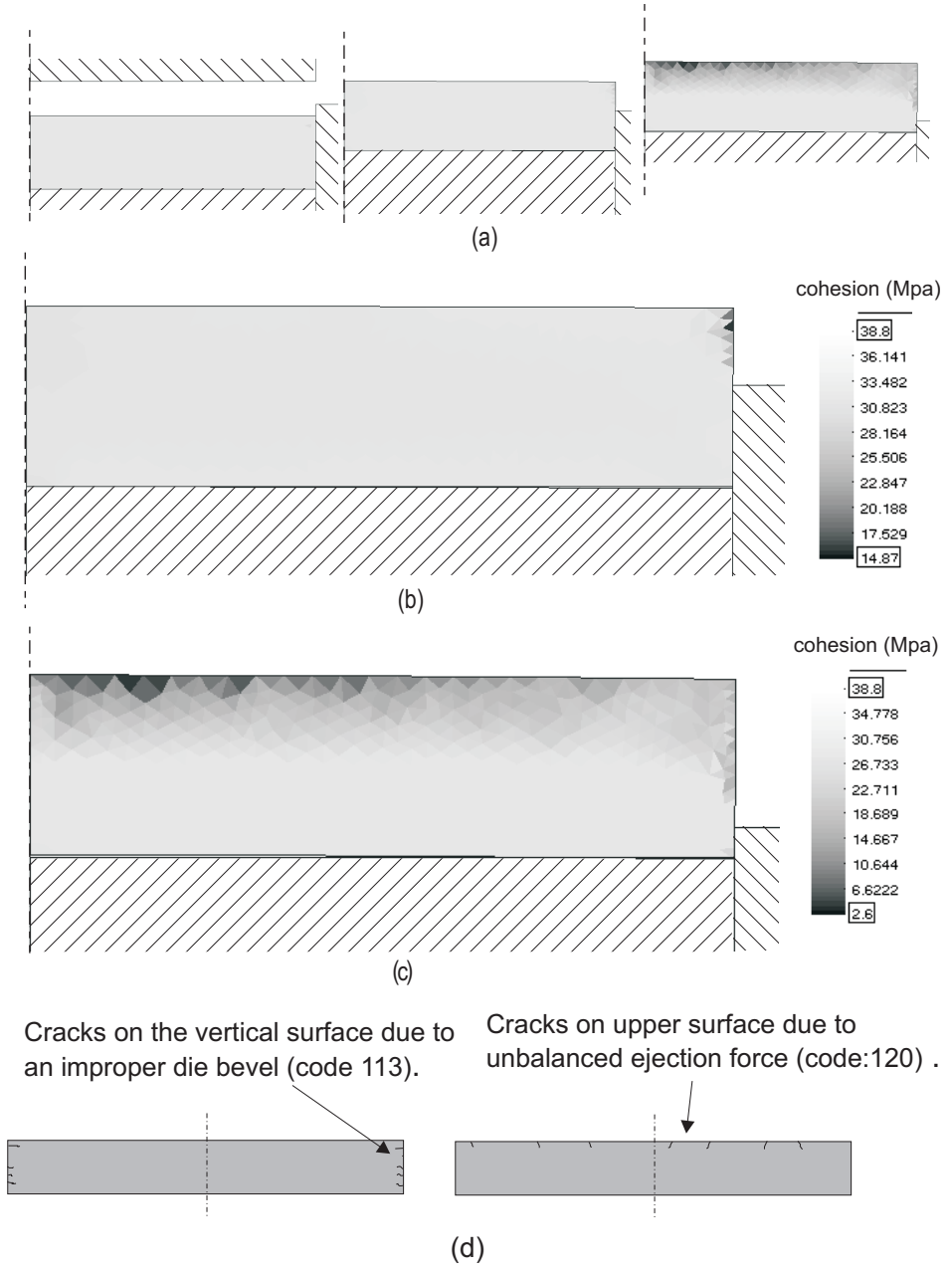

Figure 4.16 *(a) Contour plots of computed cohesion during emergence of the compact from the die. The central and rightmost plots are displayed in magnified form in (b) and (c), respectively. (d) Qualitative description of cracks observed in thin parts reported in the database of common cracks collected by Zenger et al. [112]*

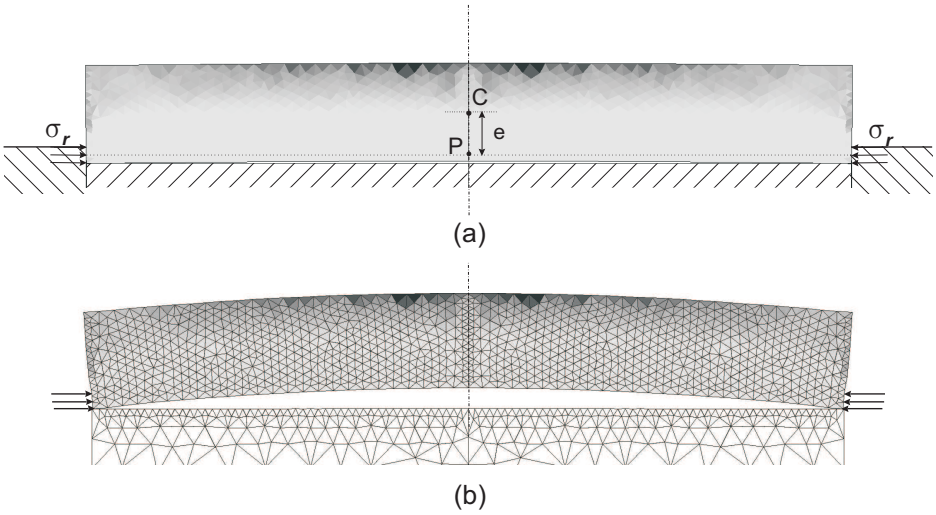

Figure 4.17 *(a) Eccentricity of the the resultant of lateral stresses causes bending of the part. (b) Deflected shape showing the finite element mesh in the simulated part (displacements scaled up 10 times).*

the upper horizontal fibers. The magnitude of these flexural stresses varies directly as the bending moment and inversely as the moment of inertia with respect the circumferential direction. This fact explains why thin parts are prone to this type of failure. The bending deformation mode becomes more evident by scaling up the displacements (see figure 4.17.b).

The non-homogeneity of the computed cohesion distribution indicates that the mechanisms of strain softening have been certainly activated. Elements of the lateral and upper surface at which the cohesion is markedly lower may be loosely interpreted as locations of *macroscopic cracks*. However, the de-cohesion patterns shown above do not exhibit, admittedly, a distinctly crack-like appearance, if compared, for example, with the results depicted in figure 4.7, section 4.2, when discussing the simulation of the Brazilian test. Several hypothesis can be put forward to explain this apparently "poor" representation. Foremost of them is that the finite mesh employed in the calculations (see figure 4.17.b) may be too coarse for adequately capturing localization of plastic strains. In support of this hypothesis, we should point out that the defects on the lateral surface have been described experimentally as "very shallow" surface cracks (*lamination cracks*) [112].

In order to further inquire about this conjecture, an analysis with a finer mesh has been carried out. The alternative mesh is shown in figure 4.18.a. The typical element size has been set to approximately 0.15 mm, which results in almost 10000 elements only for the body powder, in contrast with the 1000 elements of the mesh displayed in figure 4.17.b. The aim is not to examine the compaction process in its entirety, but merely to evaluate the ability of the model in replicating the flexural cracks appearing on the horizontal top surface. For simplicity, thus, the effect of

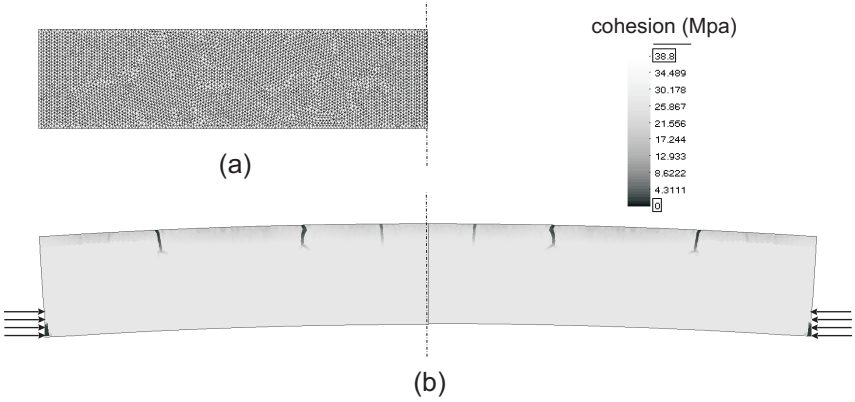

Figure 4.18 *Dieless case (a) Overly refined mesh (b) Contour plot of cohesion with displacements scaled up 10 times.*

the die has been replaced by prescribed lateral pressure ($200MPa$) acting on the lower fourth of the part. The corresponding contour plot of computed cohesion is shown in figure 4.18.b. Loss of cohesion is more accentuated along three (on each half) easily discernable vertical paths emanating from the top surface of the part, which, in turn, implies that localization of plastic strain has indeed taken place.

The hypothesis advanced previously seems thus to be sustained. A finer mesh ensures a more "pleasing" and realistic aspect. However, it should be stressed again that the ultimate goal of the results provided by the numerical model is to ascertain whether a given fabrication route will lead to defective parts or not. The model should have the capability of predicting the formation of macroscopic cracks, but without the need of giving an accurate description. From the contour plots of cohesion obtained with the coarser mesh shown in figure 4.17.b, one can conceivably conclude that, in this case, the ejection schedule with total axial unloading will lead invariably to defective parts due to tensile stresses induced by bending. The exact dimensions of these bending cracks and their exact distribution over the upper surface are of little concern. Consequently, going to unduly fine meshes, as the one displayed in figure 4.18.a, is inefficient from a practical point of view. Too many refinements in engineering solutions pertain to secondary errors; they increase the complexity, but do not improve the solution [14].

Analysis of the process in the mean-deviatoric stress plane

In order to disclose in full the nature of the phenomenological events (hardening, softening and elastic behavior) that takes place during the process, it proves instructive to plot in the mean-deviatoric stress plane[17] the stress history at a representative point together with the respective sequence of surfaces defining the

[17]The constitutive equations developed in chapter 2 were cast in terms of Kirchhoff stress measures. However, the engineering sense of stress is more clearly conveyed by using Cauchy or true stresses. Hence the mean (or hydrostatic) stress is defined in this case as $p^* = 1/3\,\mathrm{tr}\,\boldsymbol{\sigma}$, and the deviatoric stress measure as $q^* = \sqrt{3/2\,dev\,\boldsymbol{\sigma} : dev\,\boldsymbol{\sigma}}$

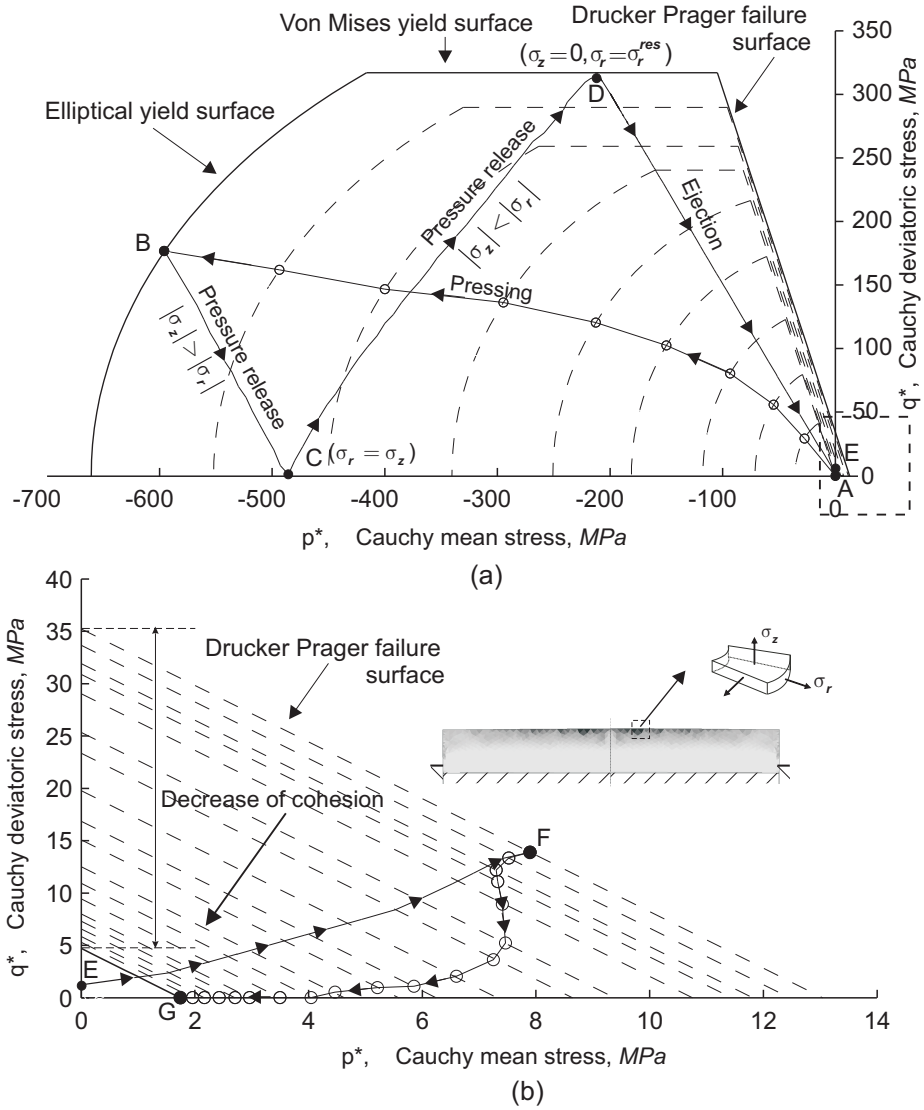

Figure 4.19 *Stress trajectory in the mean-deviatoric stress plane of a point located on the top face of the part. (a) Pressing (path AB), release of axial load (path BCD) and ejection (up to the onset of bending, path DE). (b) Enlarged view of the first quadrant. Path EF represents elastic loading due to tensile bending stresses. Path FG indicates decrease of cohesion (green strength) due to strain softening.*

yield condition.

Figure 4.19.a represents the stress evolution at a node located close to the upper face of the part. During the pressing stage, the stress state traces the path AB. The monotonically increasing character of this loading history ensures that the

powder is always at yielding during this phase. The strength of the material thus raises progressively. This hardening behavior is indicated by the expanding yield surfaces (dashed lines). The yield surfaces drawn with a solid line represents the yield condition at the end of the pressing stage. Within the region enclosed by these yield surfaces, the behavior of the material is presumed to be elastic.

During axial unloading, the stress state follows a piecewise approximated linear path BCD. The yield condition is not affected during this phase, since the entire trajectory lies within the elastic region and, thus, mechanical properties are not altered. By definition, the deviatoric stress measure q^* must remain positive. Thereby, the descending tendency of the stress trajectory breaks down at point C, at which the trajectory is "reflected". The slopes (in absolute value) of the descending and ascending branches are consequently identical. An analytical estimation for this slope is developed in appendix B.3, Eq.(B.3.10). Point C corresponds to a hydrostatic stress state and it marks[18] the transition to stress states in which the radial pressure is dominant ($\sigma_r > \sigma_z$). At point D, the axial pressure exerted by the upper punch is totally released.

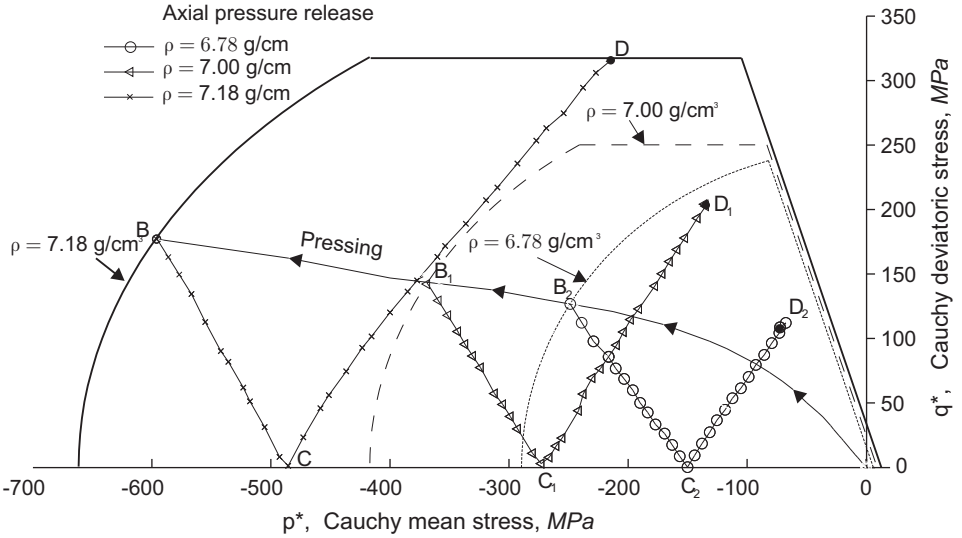

Figure 4.20 *Stress trajectory in the mean-deviatoric stress plane. Pressing and axial pressure release for three different densities.*

The removal of the upper punch is followed by the upward movement of the lower punch for ejecting the part out of the die. As the part moves toward the die exit, the radial stress at the analyzed material point diminishes gradually. This elastic unloading process is represented by the descending path DE in figure 4.19.a. When the analyzed point starts emerging from the die, the magnitude of the stress

[18]Due to the deliberately low value of the friction coefficient, shear stresses are negligible and radial stresses are approximately constant along the radial direction. Hence radial and hoop stresses are identical, and the deviatoric stress measure can be expressed simply as $q^* = |\sigma_z - \sigma_r|$. Hence, $q^* = 0$ implies $\sigma_z = \sigma_r$. See appendix B.3 for further details.

at this node practically vanishes, and the stress state remains thus close to the origin (point E). Ejection progresses and, when half of the part is out of the die, the eccentricity of the lateral force begins to produce the aforementioned bending deformation (see figure 4.17.b). As a consequence, the upper portion of the part is stretched, hence put into tension. This bending deformation causes the stress state to move within the elastic tensile region (first quadrant of the mean-deviatoric stress plane), which is shown in magnified form in figure 4.19.b, until eventually reaching the Drucker-Prager failure line at point F. Yielding on this failure surface induces a decrease of cohesion (softening) of approximately 85%, from 35 MPa to 5 MPa, and consequently, the Drucker-Prager failure line shifts toward the origin. This is illustrated graphically by the sequence of parallel dashed lines. During this continued yielding, the stress stress traces the path FG.

Observe that, upon total axial unloading, the stress state lies practically on the Von Mises yield surface (point D in figure 4.19.a). We pointed out in section 2.5.5 that this yield surface can be also conceivably viewed as a failure envelope associated with compressive and triaxial failure mechanisms. Therefore, the closeness of point D to this threshold gives clear indication that a final density of 7.18 g/cm^3 (98 % of the theoretical density) is unduly high and some type of failure, such as radial crushing, may be thereby imminent. This fact would have escaped notice by merely examining the computed distribution of the Von Mises yield strength c_v, since, as mentioned in section 2.5.5, the magnitude of this variable results unaffected when yielding takes place on the Von Mises yield surface[19].

In order to further clarify the influence of the final density on the stress state upon axial pressure release, two additional analysis with lower compaction densities have been run. The results are given in figure 4.20. From this diagram, one can immediately conclude that moderate target densities imply more favorable circumstances, since points D_1 and D_2 are relatively far from the critical Von Mises threshold[20]. Incidentally, observe that the slopes of the axial unloading paths are practically identical for the three cases. This observation is in conformity with the insensitiveness, analytically inferred in appendix B.3 (see figure B.5), of the value of the slope to changes in the magnitude of the Young's modulus.

4.3.1.4 Hold down ejection

The key factor to prevent cracking caused by bending of the part is to maintain a certain level of axial load during ejection [112]. The upper punch must accompany the lower punch in its upward motion, "sandwiching" the part until it is completely out of the die cavity and thus avoiding the tendency to bend. The modeling of the *hold down* pressure is accomplished here by simply controlling the displacement of the top surface of the upper punch, which is gradually lifted until reduction of the axial load to the desired level. Due to the negligible character of friction forces, this procedure ensures the constancy of the upper punch pressure during ejection,

[19]The unavailability of adequate experimental data in this stress regime compelled us to disregard the incorporation of softening for this state variable

[20]For density $\rho = 6.78 g/cm^3$, the Von Mises yield surface "reduces" to a point: the intersection of the other two yield surfaces (see figure 2.16 in section 2.5.4).

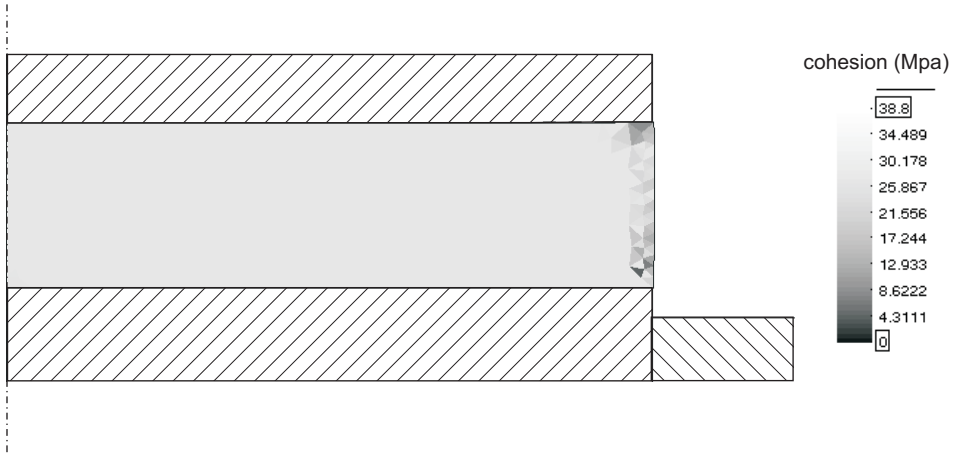

Figure 4.21 *Ejection with a hold down pressure of 13% of the compaction pressure. Contour plots of computed cohesion at the end of the process.*

as it can be checked in the axial pressure versus time graph shown in figure 4.22.a (path *be*).

Figure 4.21 shows the contour plot of cohesion at the end of the ejection phase for a case with a hold down pressure of 13% of the compaction pressure. Evidences of mechanical degradation are detected only along the lateral surface. It is clear therefore, that, as expected, the hold down ejection method has proven useful in eliminating the de-cohesion pattern on the upper portion of the part.

This procedure admits a compelling interpretation in the mean-deviatoric stress plane. In figure 4.22.b, the stress evolution during axial unloading and ejection at the same material point analyzed previously (see figure 4.19), is drawn for several hold down pressures. The ejection branches HJ and BG correspond to total axial unloading and 13 % hold down pressure, respectively. In essence, the effect of keeping a certain level of axial load is reflected in the mean-deviatoric stress space as a translation of the unloading branch HJ, which shifts towards the compression side to BG, so that the final stress state moves far from the tensile region (first quadrant), thus avoiding the formation of tensile cracks. Needless to say, the larger the hold down pressure, the further the final stress will be from the tensile region (points E and F) and, consequently, the likelihood of tensile-type failure will decrease. However, large hold down pressures may promote other mechanism of failure, such as crushing, and, furthermore, due to the concomitant increase of radial pressure, the deterioration of the lateral surface will be invariably aggravated.

4.3.1.5 Die exit geometry: Estimation of a proper taper angle

The graph shown in figure 4.23 represents the trajectory, in the $r - z$ plane, of the peripherical upper corner node P. Radial displacements are measured with respect to the undeformed configuration, whereas changes in vertical position are referred to the top face of the die. The part gradually expands as it moves toward

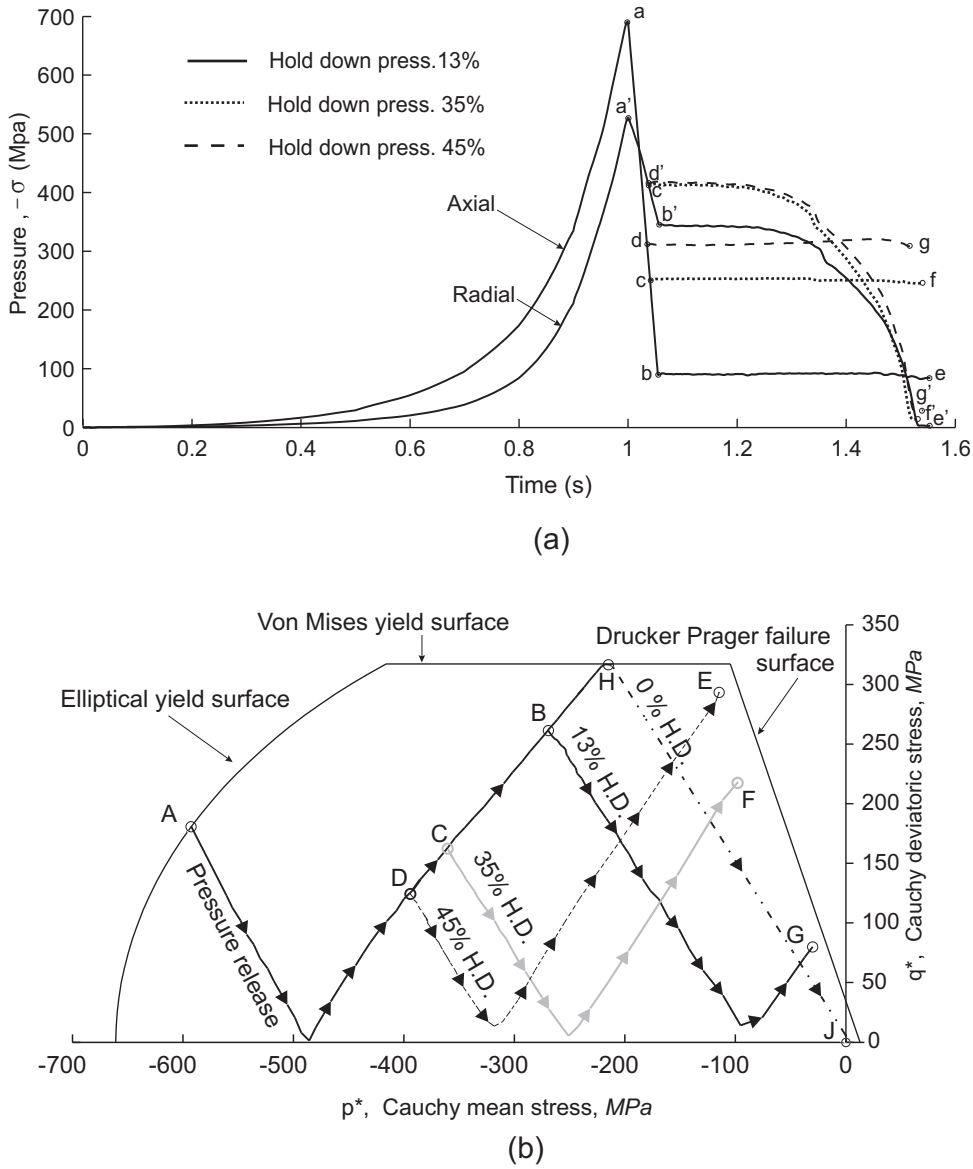

Figure 4.22 *(a) Average axial and radial pressure during compaction for ejection schemes with different hold down pressures. (b) Stress trajectories in the mean-deviatoric stress plane corresponding to these ejection schedules.*

the die exit. The extent of this radial expansion becomes more pronounced after emergence from the die (point *b*). The path *bc* is approximately straight, a fact that suggests the elastic nature of radial relaxation. The linear approximation to this path subtends an angle of 0.47 ° with the vertical axis. Expansion ceases when

the node P is located approximately 3 *mm* above the top face of the die.

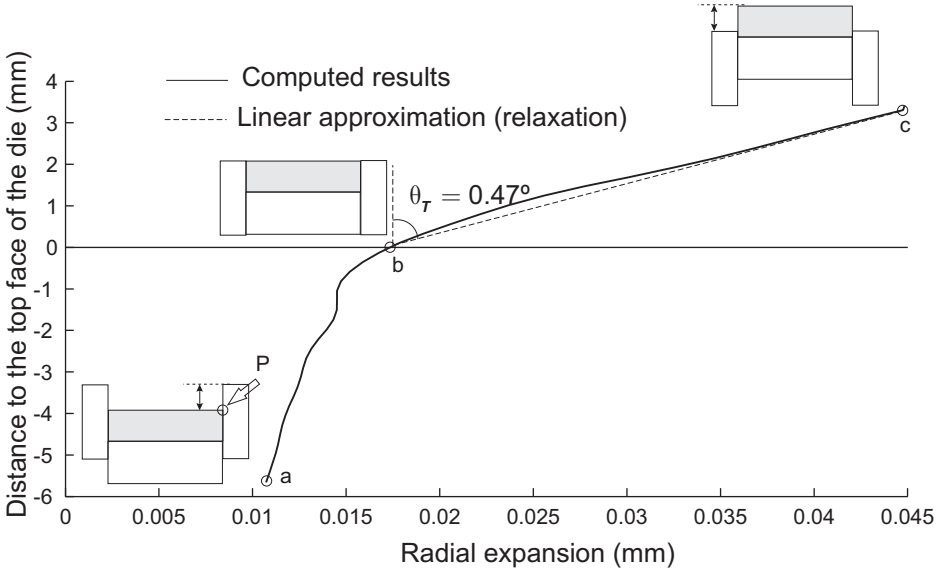

Figure 4.23 *Axial versus radial displacement of a peripherical upper corner point P. Path bc corresponds to the trajectory traced by P as the emerged portion of the compact expands elastically.*

As mentioned earlier, the loss of computed cohesion observed along the vertical surface of the cylinder (see figure 4.16.b) can be interpreted as the formation of superficial cracks (lamination) due to the stress concentration derived from the shaft corner at the die exit. To minimize this deleterious effect, the die exit has to be provided with a slight taper, so as to control radial expansion. The usefulness of the information presented in figure 4.23 is therefore evident. The taper can be patterned after the computer displacement profile contained in this figure (path *bc*). Accoding to this profile, the tapered die exit would have to be at least 3 mm height and with a lead-in angle of 0.47 °.

4.3.2 Conclusions

The simulation of the pressing and ejection of a cylindrical part seeks to highlight the utility of the proposed model in reinforcing the physical understanding of how well-known crack typologies, namely, bending and lateral *lamination* cracks, are developed. In addition, this simple example typifies perfectly the process of compaction, since it touches upon all the relevant issues: pressing, axial unloading, ejection, radial spring-back, development of cracks, etc. Therefore, the distinct phenomenological facets of powder behavior can be grasped easily by analyzing the stress state throughout the process. This task is further facilitated by the approximated analytical closed-form solutions derived in B. In-depth study of one simple

case is always of great assistance in anticipating and interpreting results for more complex examples.

The de-cohesion patterns observed in the contour plots shown in figure 4.16.a demonstrates the ability of the model to *detect evidence of macroscopic defects*. The format in which the results are displayed is certainly advantageous from a practical point of view, as it dispenses with the need for either jointly interpreting several stress contours, or scrutinizing density distributions to find "suspiciously" intense gradients.

As pointed out at the outset of this chapter, a rigorous quantitative validation of the model, as far as formation of crack is concerned, is somewhat elusive. The assessment of the calculated results in this example is thus largely *qualitative*. For instance, comparison of the contour plots of computed cohesion shown in 4.17.b and 4.21 reveals that maintaining a certain level of axial pressure during ejection assists in avoiding flexural cracks. This numerical prediction concurs with well-known experimental and industrial findings. Therefore, the numerical model proves useful in *qualitatively evaluating the influence, in the formation of cracks, of variations in the input data* (material parameters, tooling kinematics, etc.).

The qualitative nature of the numerical predictions restricts somewhat the spectrum of practical questions that can be conceivably answered by our approach. It is important to be aware of such limitations and guard against unrealistically high expectations. We mentioned that the graph of the trajectory of an upper peripherical point during ejection, shown in figure 4.23, suggests somewhat the dimensions of the taper at the die exit. However, it cannot be expected that the information contained in such graph provides the *exact* taper lead-in angle that ensures a lamination-free part. To account for the uncertainty associated the calibration of the material parameters and the unavoidable modeling errors, one has to perform several runs with different input data so as to assess the effect of such variations and to obtain a more reliable impresion of the "true" answer. Computer simulations are there to support engineering judgement, not to supplant it.

The study of convergence with time discretization has shown that, in computing the pressing stage, the use of variable time steps is essential for avoiding needlessly small increments and, therefore, exploiting to the maximum the computational advantages offered by the IMPLEX integration scheme. Adequate time step distributions can be obtained by using either adaptive time stepping schemes, of the type described in Ref. [79], or from elaborated heuristics taking into account the inherent non-linearity of the material. By contrast, in computing the post-pressing operations, the use of variable time steps only improves marginally the computational efficiency, since in this case the non-linearity of the problem is due largely to the roughness of the contact response rather than to material behavior.

Although the theoretical aspects of the contact problem have not been a topic of discussion in this work, the relevance of the interaction between the compacted part and the tooling in the formation of post-pressing cracks has rendered necessary a brief assessment of the accuracy of two alternative contact algorithms, namely, the penalty method and the augmented Lagrangian strategy. The conclusion reached from this evaluation is that the *augmented lagrangian strategy is more appropriate for simulating the post-pressing operations*. The reason for the rejection of the less

computational costly penalty method is the oscillatory pattern exhibited by the computed boundary stresses, which may affect seriously the quality of the results. The main drawback of the augmented Lagrangian strategy is the dramatic increase of computational cost - up to 8 times- in comparison with the penalty approach. Work in progress is precisely aimed at reducing the computational cost associated to the modeling of the contact response [78, 40].

Even with this more accurate contact algorithm, an inappropriate time or spatial discretization, or any other modeling error may provoke the appearance of "spurious" numerical cracks, mainly at the boundary surfaces. The natural inclination upon casual inspection of contour plots is to accept as "true" these de-cohesion patterns, especially when they appear in appealing and pleasing crack-like shapes. The risk of misinterpretation is therefore high. For this reason, it is strongly recommended to check whether the observed loss of cohesion is physically plausible or, by contrast, it is caused by numerical inaccuracies. This can be conveniently accomplished by tracking, in the mean-deviatoric stress plane, the stress history at a representative point of the affected area. If no anomalous oscillations are detected, then the result, in principle, can be trusted. When the stress state is plotted sequentially together with the corresponding yield surfaces, this procedure has the added benefit of providing a great deal of insight into the phenomenological behavior of the material since, depending on the location of the stress state in relation with the yield surfaces, one can ascertain at each step whether the powder at the analyzed point is deforming elastically or elastoplastically with either softening or hardening trends.

Chapter 5

Modeling guidelines for industrial applications: compaction of a multilevel part

The aim of this chapter is to evaluate the capabilities of the numerical model developed in previous chapters as a tool for assisting in the design and analysis of PM uniaxial die compaction processes, including both pressing and ejection stages. For this purpose, a detailed case study of the compaction of an axially symmetric multilevel adapter in an advanced CNC press machine is performed, focusing exclusively on the truly engineering aspect, thus leaving aside mathematical and numerical formalities. Such carefully analyzed case will also serve to provide some modeling guidelines, sketch frequent difficulties, as the unavailability of some input data, and reveal relevant technical details that, although probably trivial for powder metallurgy technologists, may escape notice by researchers, especially if they possess a deficient background knowledge of advanced CNC press machines.

The geometry and dimensions of the part are displayed in figure 5.1. A salient attribute is its relatively low height. The finished lengths of the thinner and thicker levels of the part are 2.7 mm and 5.32 mm, respectively. This means that a small error of, say, 0.2 mm, which is in the order of the value of the maximum final elastic deflection of the longest punch, in describing the position of one of the tooling members may induce an unacceptable discrepancy in the predicted density of about 0.4 g/cm^3, and it needs no further arguments that the success in predicting numerically the formation of cracks during the ejection phase relies considerably on the quality of the density and stress distribution computed in simulating the pressing stage. Furthermore, an accurate prediction of tooling deflection is essential for capturing the formation of cracks in the post-pressing operations. These circumstances explain the prominence given to the accurate characterization of the

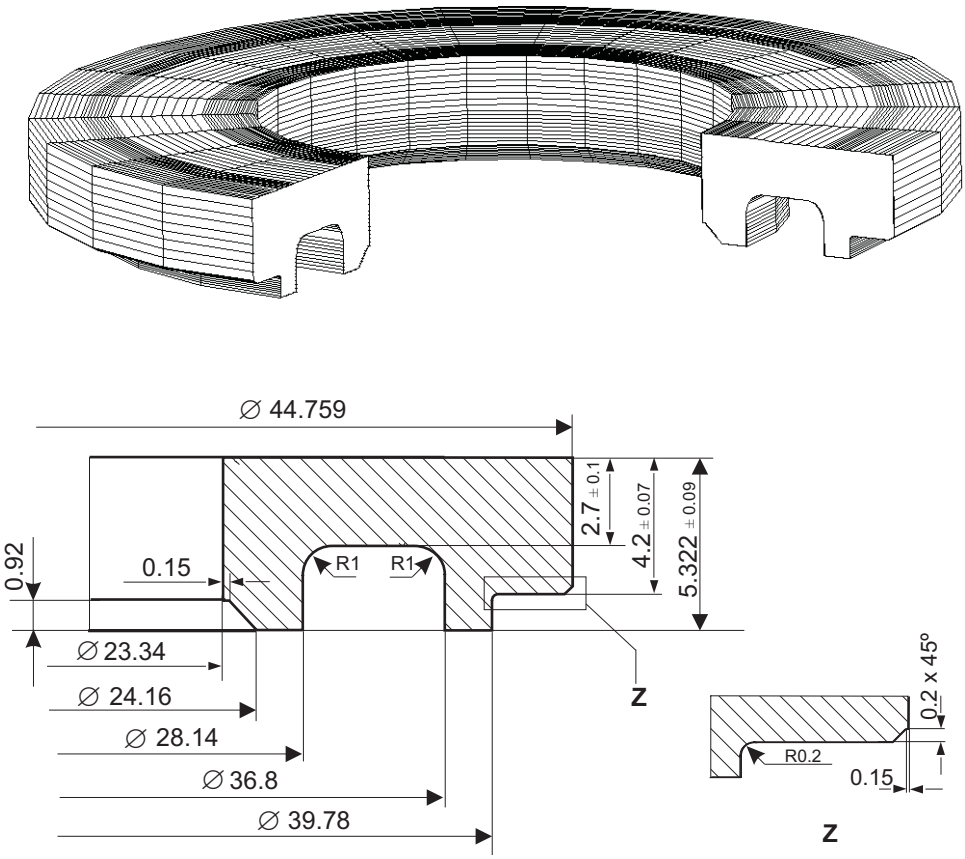

Figure 5.1 *Geometry of the part (dimensions in mm). The axisymmetric geometry is revolved 270 ° for ease of visualization.*

tool set and the external loads acting on it in the first part of this chapter (sections 5.1 and 5.2). An aspect that receives careful consideration is the description of possible deviations from "nominal" or design values of tooling motions. The effect, in terms of final density distribution, of including such deviations is conveniently assessed in section 5.3.2.

In dealing with the pressing of complex multilevel parts, it is natural to raise the question of how to approach the ideal tooling motion that leads to uniform density throughtout the compact. This question is also addressed in this chapter (section 5.3.3), but only in an exploratory sense, with a view towards stimulating the pursue of this line of enquiry in the future, rather than establishing a procedure of widespread applicability.

It should be anticipated that the part was not finally manufactured according to the geometry shown in 5.1, which corresponds to the initial customer's specification. Unsurmountable difficulties were encountered in ejecting the part safely from the

die, and this circumstance dictated a slight modification -inconsequential to the performance of the finished component- in the original geometry. This modification turned out to be effective and the part was successfully manufactured according to the revised design. The goal in section 5.4 is, by means of numerical simulations of several ejection sequences, to explain the reasons behind the difficulties in ejecting the original part and understand the connection between such difficulties and the suggested geometry modification.

5.1 Modeling of the compacting tool set

The forces transmitted to the compacting powder during the pressing operation, as well as the release of such forces during the ejection stage, should be represented as accurate as possible in order to obtain reliable results. Ideally, the entire press machine should be modeled, including punches, core rod, die, press fittings, punch platens and even the mechanical and hydraulic drives. However, the geometrical and physical characterization of all these press members would require a daunting labor and a dramatic increase in computational effort. In this work, thus, we shall consider only those elements directly involved in forming the part, namely, the upper punch and lower punches, the die and the core rod, the so-called *tool set*[67], which, incidentally, constitutes the *tooling sub-system*, according to the systemic conception presented in the introductory chapter.

Punch platens, punch holders and punch adapters are excluded from our model on the basis of their larger rigidity, in comparison with punches, and therefore the negligible character of their elastic deflections. An assumption intimately connected with this simplification is that the vertical displacement prescribed at punch faces in contact with clamp rings is taken directly as the corresponding platen motion. As it will emerge later, some deviations may be occasionally detected from this assumed behavior. In this event, the deviation can be incorporated as a perturbation of the externally applied load.

In figure 5.2.a, we show the schematic of the multi-platen press machine employed in manufacturing the part. The accompanying drawing, figure 5.2.b, represents the tooling assembly included in the modeling. The tool set comprises an upper punch (UP), four lower punches (LIP, LMP, LOP-I and LOP-II), a die and a core rod. Observe that the lower outer punch labelled as LOP-II is mounted on the die table. Such an arrangement can be considered as a stepped die or "shelf" die configuration [35].

The dimensions of the core rod, die and punches are shown in figure 5.3. A crucial issue in modeling the tool set is to account for the actual length and the different diameters sections of punches, so as to predict with the maximum level of accuracy elastic deflections. Features such as blend fillets to reduce stress concentrations at change of section are washed out, as the main concern is the study of the powder behavior. Factors related to the tool set that are also ignored in our modeling are, among others, the magnitude of the clearances between moving tools, the wear resistance of tools and busting and buckling phenomena. Such range of details is important in its own right and should be studied separately.

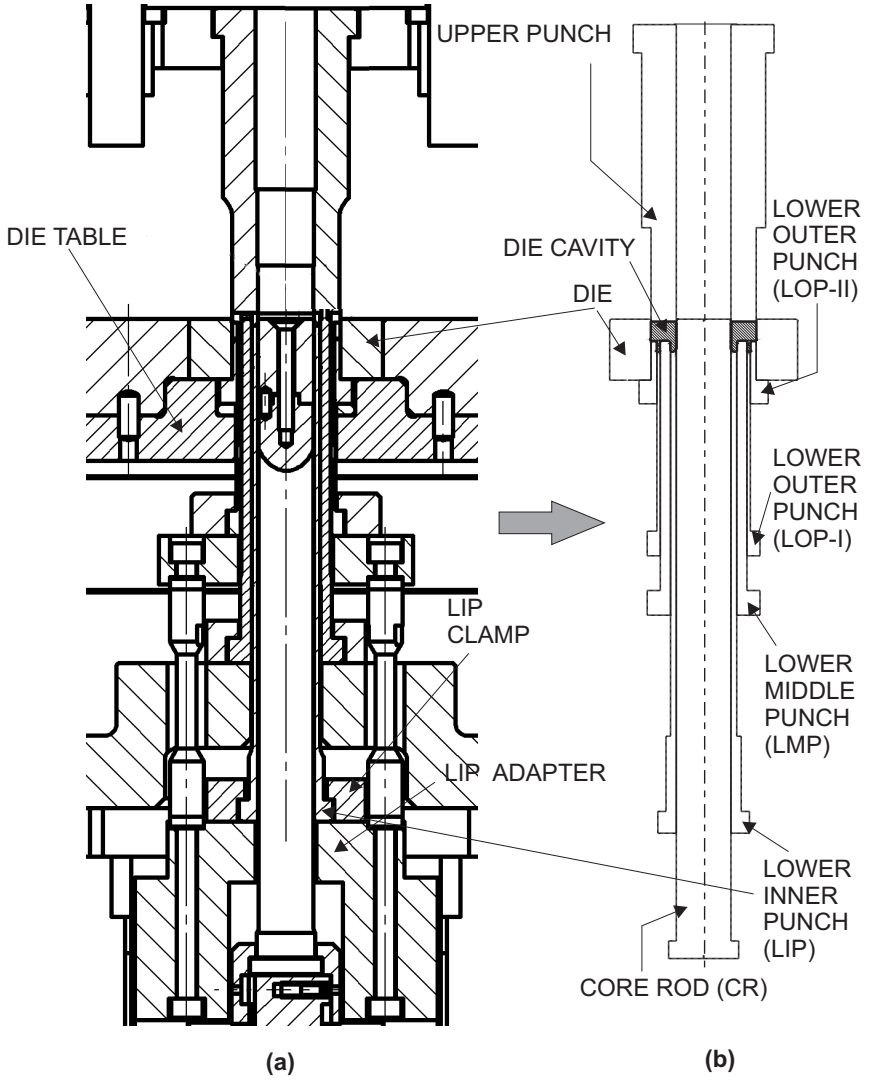

Figure 5.2 *(a) Cross sectional view of the compacting press. (b) Geometric model of the tooling items included in the simulation.*

5.2 External actions

The effect of mechanical and hydraulic drives is replaced by *prescribed conditions* on the portion of punch surface in contact with the clamp rings that fasten mechanically the punches to their corresponding adapters (see figure 5.2). These actions represent mathematically the *boundary conditions* of the governing differential equations, and can be specified as *displacement or traction conditions* depending on the circumstances and the type of press used for compacting the part.

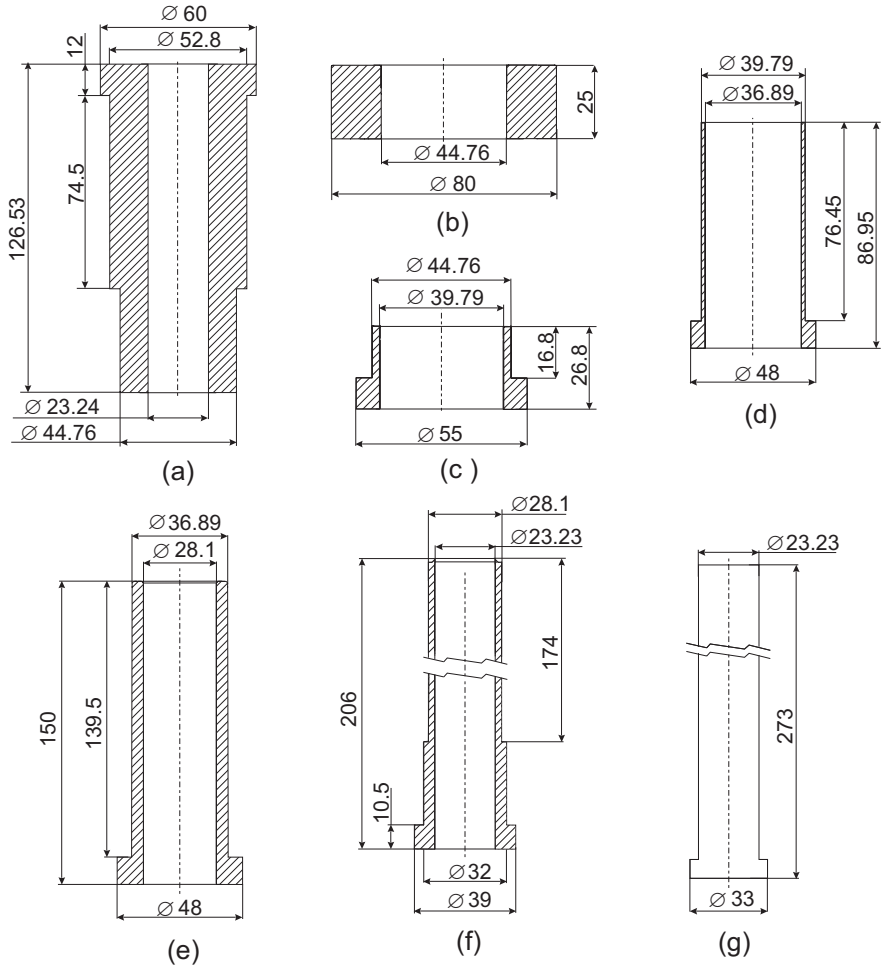

Figure 5.3 *Tooling dimensions (mm). (a) Upper punch (b) Die (c) Lower outer punch-II (d) Lower outer punch-I (e) Lower middle punch (f) Lower inner punch (g) Core rod.*

The action of mechanical drives is usually modeled as prescribed displacement conditions, whereas the effect of hydraulic drives is more adequately represented by imposing traction (pressure) conditions on the corresponding tool. Occasionally, in simulating the same compacting process, prescribed conditions can switch from traction type to displacement type, or viceversa. For instance, standard hydraulic presses are programmed to apply a fixed pressure, which, from a modeling viewpoint, amounts to impose a traction (pressure) condition on the corresponding punch. However, the press may incorporate a mechanical stop to limit the downward ram movement and therefore control the finished length of the corresponding level. When such mechanical stop comes into action, fixed pressure condition should be replaced by a zero incremental displacement constraint.

In advanced CNC press machines, the movement of punch platens is more accurately controlled and synchronized than in standard presses. This fact renders CNC presses more amenable to be modeled than standard ones. Computer numerical controlled press machines can be programmed to execute a wide variety of motions, with different displacement and/or pressure profiles. In the following, we shall concentrate on the description of the CNC press machine employed to compact the studied part.

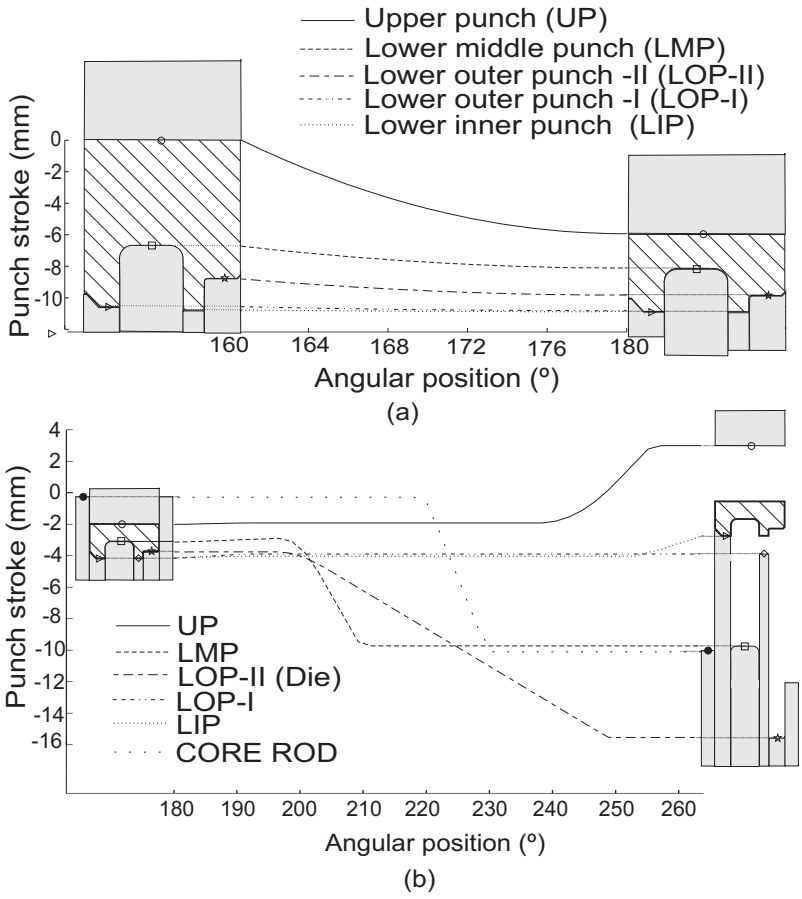

Figure 5.4 *Typical tooling motions. (a) Pressing sequence (b) Ejection sequence.*

The multiplaten press used for compacting the part incorporates a combination of mechanically and hydraulically driven systems. The final compacting stroke is provided by the force of an electric motor. A connecting rod converts the rotary motion of the main shaft into the reciprocating motion of the upper ram. Consequently, the displacement of the upper ram during the pressing portion of the cycle exhibits a *sinusoidal profile*, given by the expression:

$$u_{up} = \left(1 - \sqrt{1 - \left(\frac{l_c}{l_r} sin\varphi_0\right)^2}\right) l_r + (1 + cos\varphi_0) l_c, \tag{5.2.1}$$

where l_c and l_r stand for the lengths of the crank and the connecting rod, respectively, and u_{up} is the *pressing stroke*, i.e., the distance travelled by the upper ram from the onset of pressing (φ_0) - the position at which the bottom surface of the upper punch enters the die and comes into contact with the powder- to the extreme lowest position of the cycle, the so-called *bottom dead center*, located at $\varphi = 180°$. The rotary motion occurs at constant angular velocity, hence the motion can be legitimately parameterized in terms of the angular position φ, as displayed in figure 5.4.

During the pressing stage, all elements of the tooling system move downward. The lower punches labelled in figure 5.2.b as LIP, LMP and LOP-I are mounted on separate platens, whereas the lower outer punch identified as LOP-II is attached to the die platen. The core rod support is also a movable member, and they all are operated by hydraulic cylinders placed on the stationary member of the press.

One of the major advantages of using advanced CNC press machines is the flexibility in reproducing any physically realizable motion. The hydraulic drives controlling the motion of the lower rams are, in fact, *closed-loop motion control systems*. In our case, the velocity of the lower rams during pressing is kept proportional to the velocity of the upper ram, hence their motions also exhibit a sinusoidal profile, as can be readily appreciated in figure 5.4.a. The angular position and velocity of the rotating shaft is monitored at any time during the cycle by a rotary encoder. This information is sent to a motion controller, which causes the hydraulic devices to speed up or slow down to correct the velocity of the punch motion so as to keep the proportionality. The following equation expresses such condition:

$$v_p = f_p \cdot v_{up}, \tag{5.2.2}$$

v_{up} is the linear velocity of the upper ram and v_p is the downward velocity of any of the lower rams. Furthermore, the condition of vanishing velocity at the bottom dead center, $v_{up}(\varphi = 180°) = 0$, enables us to write directly

$$u_p = f_p \cdot u_{up}, \tag{5.2.3}$$

i.e., given an upper ram pressing stroke u_{up}, the desired stroke for the lower punches can be adjusted by changing the constant f_p. The proportionality parameters f_p, henceforth referred to as *motion scale factors*, must be less than one in order to ensure that pressing takes place, and they constitute one of the basic *operating parameters* of the CNC press machine, that is, parameters that can be easily modified by the CNC operator by interacting with the CNC display screen.

In figure 5.4.b, we show the withdrawal type tooling kinematics used in removing the analyzed part from the die cavity. It can be readily seen that tool displacements are *linear* functions of the angular position, except in the blend regions between paths with different slopes. Observe also that the movement of the

upper punch is not governed by the sinusoidal relation (5.2.1). This is because the upper punch is not connected directly to the rotary main shaft. A hydraulically controlled mechanism, inserted between the upper punch and the upper ram, allows independent movements so that, for instance, the upper punch can still apply a certain downward load on the compact after reaching the bottom dead center, the so-called *counter pressure* or *top-punch hold-down pressure*. In summary, in designing and modeling the ejection operation, one specifies the prescribed motion of each movable tool as a piecewise linear function. In the case in which the upper punch is to maintain a certain level of axial pressure, by contrast, one should impose fixed pressure conditions rather than prescribed displacement.

5.2.1 Theoretical and true prescribed conditions

The tooling displacement diagrams described in the preceding discussion and illustrated in figure 5.4 are the motions that, theoretically, the mechanical and hydraulic drives impart to the corresponding rams or platens. Quite frequently, in modeling the compaction process, the displacements prescribed at punch faces in contact with clamp rings are taken directly as such theoretical platen motions, a tendency also observed in the design of PM parts. Furthermore, these displacement curves are very often simplified to facilitate their handling, eliminating some apparently irrelevant details. The resulting data are commonly termed as "theoretical" or "nominal" displacement profiles.

However, departures from this assumed behavior invariably exist. The exact displacements of the supported portions of punches, core rod and die seldom coincide with the theoretical displacement profiles. In analyzing an already manufactured part, the "true" motion curves might be at the disposal of the analyst, provided that the CNC press has displacemet transducers located sufficiently close to the punch clamps, and in addition, the CNC data acquisition system was set up to store digitally displacement data so as to enable subsequent handling and analysis. In such circumstances, one should employ the recorded data directly as input data for the numerical simulation, especially if the scope of the analysis is to simply reproduce the conditions under which the part was produced.

In other situations, however, as when attacking the design problem or when testing numerically alternative pressing schedules, true displacement curves are not available. In such cases, the analyst is faced with the task of having to *antipate or predict* potential deviations from nominal tooling motions. Of invaluable help for this purpose is to examine and rationalize the discrepancies between "theoretical" and "true" motions detected either in compacting parts requiring similar compaction tonnage - in the case of design analysis - or in producing the same part but under different pressing and ejection schedules. Not every deviation observed between "true" and "theoretical" curves is susceptible to theoretical predictions. We shall distinguish therefore between *predictable deviations* and *unpredictable deviations*.

- *Predictable deviations*: This group includes those deviations that can be estimated with a certain degree of accuracy. The analyst should have some

grasp of the press machine performance in order to ascertain the origin of such discrepancies. An comprehensive listing of all realizable predictable deviations is not possible, since they depend largely on the nature of the CNC press machine employed in manufacturing the part. We summarize the most relevant predictable deviations encountered in our analysis.

(a) *Deviations due to a poor characterization of the tooling subsystem.* The fact that only punches, core rod and die are included in the model introduces an unavoidable error. Excluded press members, such as punch holders, punch adapters and platens also deflect under high pressures. However, the major contribution to this modeling error can be attributed to the existence of adjustable mechanisms inserted between a punch and its corresponding platen. In the analyzed press machine, for instance, the force exerted by the hydraulic drives on the lower rams is transmitted to the lower punches through a practically rigid assembly of mechanically fastened elements . Hence, little deviation is expected. By contrast, the hydraulically controlled mechanism inserted between the upper punch and the upper ram, alluded to earlier, contributes considerably to the discrepancy between theoretical and true upper punch motion because of the inevitably looseness (play) of the parts involved in such mechanism. To calibrate such error in full load operation, one has to first measure the deviation in idle conditions, i.e., by compressing an empty die, and then consider that, approximately, the error increases linearly with increasing compacting pressure.

(b) *Deviations due to overloading of lower rams.* In CNC presses in which the stroke of lower punches is displacement-controlled during pressing, one cannot ignore the limited capacity of the hydraulic devices that governs their motions to sustain any applied force. If the programmed press kinematics induces a unduly high density, and consequently a high force, the servosystem controller may be pushed out of its regular operating conditions and the lower ram will simply descends maintaining the level of pressure approximately constant, and thus not obeying the scheduled motion. Such deviation can be included in the simulation by simply shifting the condition of prescribed displacement to prescribed traction on the affected lower punch when the corresponding force threshold is exceed. Later on, the impact of overlooking such limited capacity will be assessed in terms of density distribution.

(c) *Deviations due to interpolation of punch motions.* As can be checked in figure 5.5, the actual position of the corresponding platens is slightly altered in the blended portions of the displacement diagrams. These deviations may be of the order of magnitude of the elastic deflection of the longer punches, hence their effect should be included when studying the ejection process. Furthermore, tooling displacement diagrams exhibiting sharp corners are physically unacceptable, since they imply instantaneous change of velocity and therefore infinite accelerations. In practice, velocity is ramped up or down gradually so as to avoid these unrealistic accelerations (see figure 5.5). These details are normally ignored in designing - and also very frequently in modeling - the compaction process, mainly due to obvious simplicity rea-

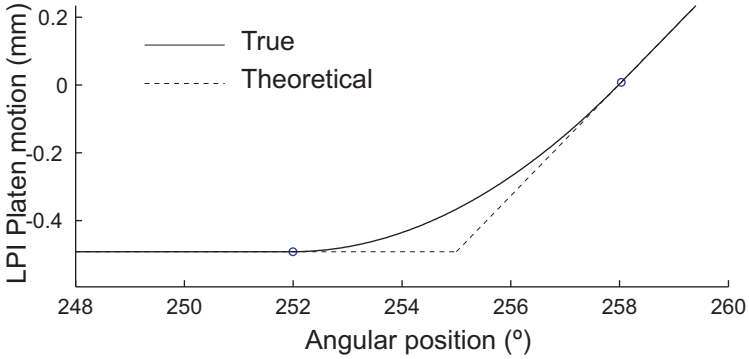

Figure 5.5 *Theoretical and true motion of the lower inner punch platen at the end of the ejection stage.*

sons. However, from the numerical standpoint, one cannot underestimate the benefits arising from using the actual smooth displacement profiles instead of the sharp ones. In general, computability is affected adversely by rough input data [6]. This is evident in the case of dynamic analysis. More subtle, although equally important, is its implications in the numerical integration of the constitutive equation. As pointed in section 3.3, the degree of accuracy of the *IMPLEX* integration scheme hinges to some extent on the input data smoothness. All the numerical simulations shown in the sequel employ interpolated punch trajectories, with peaks rounded using cubic (spline) blends.

- *Unpredictable deviations.* This group embodies those deviations that display a distinctly random pattern and, thus, cannot be predicted on the basis of a deterministic analysis. The impact of the individual and combined effect of such deviations can be only evaluated by statistical analysis.

It should be remarked that the borderline between predictable and unpredictable deviations depends largely on the beholder and the degree of knowledge on the press machine. As experience accumulates, initially presumed unpredictable discrepancies can be converted into predictable ones. Conversely, presumably foreseeable deviations turning into uncontrolled perturbations may indicate misfunction of any of the press machine elements or poor maintenace conditions.

5.3 Simulation of the pressing stage

5.3.1 Estimation of the starting conditions

In modeling the pressing stage of an already manufactured part, one should have at one's disposal not only an accurate description of the tooling motion, but also reliable data concerning the *starting conditions* of the process. Such starting conditions include the *fill position* of the lower punches, for calculating the fill height corresponding to each thickness level, and the *powder fill density distribution.* In

realistic circumstances, however, the direct determination of such starting conditions may be plagued by some difficulties. The CNC data acquisition system usually monitors only absolute position of punch platens. Knowing with sufficient accuracy, say $\pm 0.1\,mm$, the position of the bottom face of lower punches would require thus careful measurements of the length of the assembly of press members connecting lower rams and punches. This may be somewhat difficult to achieve if, for instance, the die set has been removed and disassembled for repairing when tackling the computer analysis.

In view of such circumstances, we shall outline in the ensuing discussion the procedure followed here to confront the unavailability of reliable information concerning the aforementioned starting conditions. Incidentally, observe that the unavailability of such data creates an scenario very similar to that encountered in the analysis of a *trial design*, in which one has to *guess* appropriate initial die cavity dimensions consistent with the finished lengths of each of the levels within the compacted part. Thus, the procedure described in the sequel is merely an *inverse analysis*, typically used in PM designing. The peculiarity that renders, in our case, this inverse analysis worthy of special consideration arises from the combination of two facts: tool motions are non-linear functions of the angular position (time), and punch elastic deflections have to be included in the calculation of the die cavity dimensions.

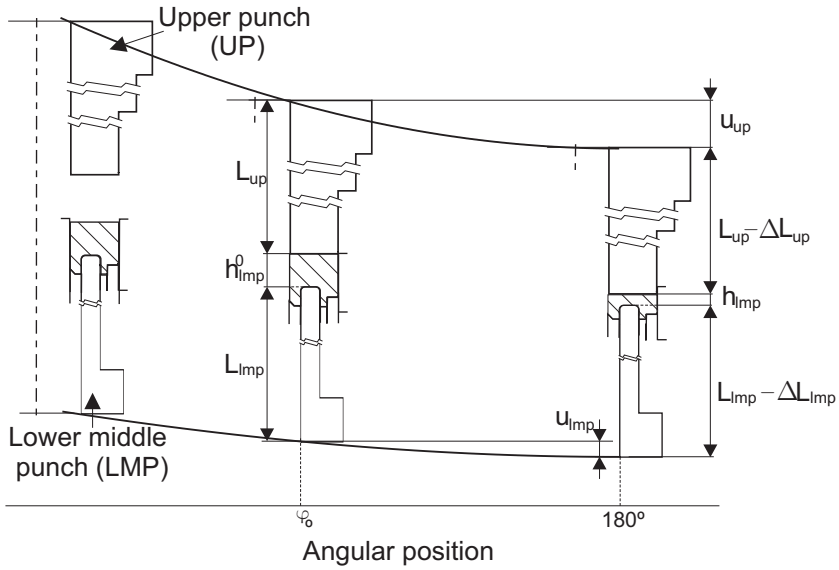

Figure 5.6 *Pressing sequence, indicating motion of the upper punch and the lower middle punch. The angle φ_0 denotes the point in the cycle at which the upper punch enters the die cavity. The pressing stroke ends at $\varphi = 180°$, which corresponds to the bottom dead center.*

The fundamental relation between the prescribed displacement on a given punch and the height of the level formed by this punch is illustrated in figure 5.6 for the

particular case of the lower middle punch (LMP). This relation can be expressed analytically as

$$h^0_{lpm} - h_{lpm} = u_{up}(\varphi_0) - u_{lpm}(\varphi_0) - (\Delta L_{up} + \Delta L_{lpm}). \tag{5.3.1}$$

The meaning[1] of each term of the above equation is also clarified in figure 5.6. The quantity h_{lpm} is the length, measured at the end of the pressing stage ($\varphi = 180°$), of the level formed by the lower middle punch . This length is approximately the length measured upon ejection from the die, except for a small correction due to *spring-back*. The depth of fill or *fill height* corresponding to the thickness level formed by the LMP is denoted by h^0_{lpm}, and it is defined as the distance from the working end of the upper punch to the working end of the lower middle punch when pressing commences[2] ($\varphi = \varphi_0$). The displacements prescribed at the top and bottom surfaces of upper and lower middle punch are symbolized by u_{up} and u_{lpm}, respectively. As already discussed, the shape of the displacement profiles are, theoretically, sinusoidal (see Eqs. 5.2.1 and 5.2.3), although they may be eventually affected by some deviations. Finally, the terms ΔL_{up} and ΔL_{lpm} stand for the total elastic deflections in the axial direction experienced by the upper punch and the lower middle punch, respectively.

Similar equations to Eq.(5.3.1) can be derived for the other three thickness levels:

$$h^0_{lpi} - h_{lpi} = u_{up}(\varphi_0) - u_{lpi}(\varphi_0) - (\Delta L_{up} + \Delta L_{lpi}). \tag{5.3.2}$$

$$h^0_{lpo'} - h_{lpo'} = u_{up}(\varphi_0) - u_{lpo'}(\varphi_0) - (\Delta L_{up} + \Delta L_{lpo'}). \tag{5.3.3}$$

$$h^0_{lpo''} - h_{lpo''} = u_{up}(\varphi_0) - u_{lpo''}(\varphi_0) - (\Delta L_{up} + \Delta L_{lpo''}). \tag{5.3.4}$$

Expressions 5.3.1 to 5.3.4 form a system of four equations - one equation for each lower punch, with ten unknowns: the fill heights corresponding to each level (4 unknowns), the elastic deflections of punches (5 unknowns), and the angular position at which the upper punch comes into contact with the powder (1 unknown), denoted as φ_0. The elastic deflections $\Delta L_\bullet$ can be estimated either on the basis of available data for similar parts, or by means of the uniaxial approximation:

$$\Delta L_\bullet = \frac{\sigma_z(\rho_f)}{E_{tool}} \sum_{k=1}^{n_r} \frac{R_1^2 - R_i^2}{R_k^2 - R_i^2} L_\bullet. \tag{5.3.5}$$

The above equation follows from assuming that an uniaxial stress state prevails throughtout the tubular punch. The constant E_{tool} is the Young's Modulus characterizing the tooling material whereas R_i stands for the inner radius of the corresponding tubular punch and R_k ($k = 1, 2, \ldots$) denotes the outer radii of each cross section of the punch, sorted by increasing magnitude. The magnitude of the pressure $\sigma_z(\rho_f)$ acting on the punch face can be estimated from the compressibility curve[3] as the axial pressure corresponding to the final density ρ_f of the compact.

[1] The prefix "*lpm*" identifies the lower punch that forms the corresponding level of thickness

[2] We further assume that the time at which the lower punches are established in their filling positions and the time at which the upper punch comes into contact with the powder coincide.

[3] The analytical expression for this curve can be derived by combining material curves s_1 and s_2, see Eq.(B.3.11) in appendix B.

Substituting these estimations for the elastic deflection of punches in equations 5.3.1 to 5.3.4 leads to a system of four equations with five unknowns, namely the 4 fill heights and the initial angular position. The closure for this system, as may be surmised, is provided by the conservation of mass equation:

$$\rho_0 V_0(h^0_{lpi}, h^0_{lpm}, h^0_{lpo'}, h^0_{lpo''}) = \rho_f V_f(h_{lpi}, h_{lpm}, h_{lpo'}, h_{lpo''}). \tag{5.3.6}$$

wherein ρ_0 and ρ_f are the initial and final density, respectively, V_0 stands for the volume occupied by the powder at the onset of pressing and V_f denotes the volume of the finished part. Note that, in writting Eq.(5.3.6), the hypothesis of uniform powder fill density[4] distribution has been tacitly invoked. This hypothesis is adopted in the absence of further information in this respect. If more accurate data concerning this distribution were available, the left-hand side member of Eq.(5.3.6) would have to be replaced by the corresponding integral expression.

To obtain the solution of the resulting system of equations, the values of the unknown quantities $h^0_\bullet$ have to expressed as a function of $h_\bullet$ and $u_\bullet(\varphi_0)$. Upon substitution of $h^0_\bullet$ in Eq.(5.3.6), the system is reduced to a single equation in the unknown φ_0. Due to its non-linear character, this equation is not amenable to analytical solution and, consequently, recourse to approximate algorithms, as the bisection method, is to be made. Once the angular position φ_0 has been obtained, the dimensions of the initial cavity $h^0_\bullet$ can be retrieved from equations 5.3.1 to 5.3.4.

With these estimated starting conditions at our disposal, we have all the basic ingredients to construct the geometric model, impose boundary conditions and, finally, undertake the finite element analysis of the pressing stage. Nevertheless, it is by no means guaranteed that the final lengths computed in this preliminary FEM analysis will correspond to the desired design values $h_\bullet$. The closeness of the computed values to $h_\bullet$ relies on the quality of the deflection estimations. A poor estimation of $\Delta L_\bullet$ will invariably lead to incorrect final dimensions. In our case, the relatively small thickness of the part (2.7 mm in its thinner lever) aggravates the situation, since such inaccuracies in estimating $\Delta L_\bullet$ will translate in innacurate density predictions.

A strategy that proves efficient in successively improving the quality of these estimations is to use the punch deflections computed in the FEM analysis as the estimations for a subsequent reverse analysis. This iterative strategy is schematically described in the flowchart displayed in figure 5.7. Iterations are halted when the difference between computed finished lengths and design values $h_\bullet$ are within prescribed tolerances. In our case, such tolerances are taken as the dimensional tolerances contained in the customer's specification (see figure 5.1). A more in-depth appreciation of this procedure will be gained through the analysis presented in the following.

[4]The initial density ρ_0 is taken in this cases as the apparent density of the powder.

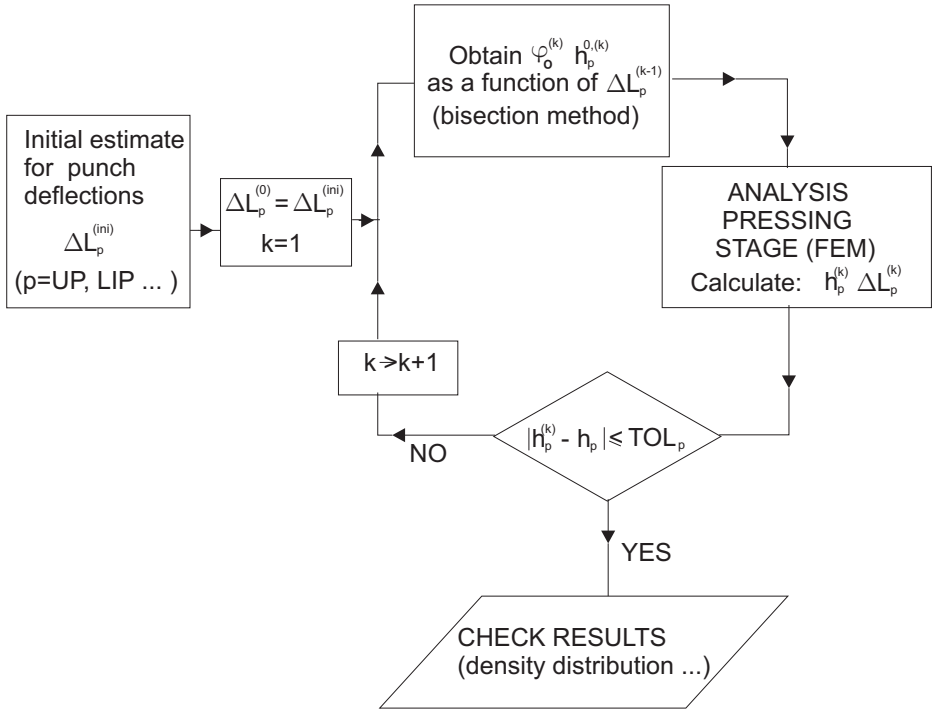

Figure 5.7 *Flowchart indicating the computational cycle used for estimating the initial die cavity dimensions.*

5.3.2 Assessment of the effect of an innacurate description of tooling motions

In this section, the computed results of final density distributions produced by using *theoretical displacement curves* as prescribed conditions on tools, on the one hand, and prescribed conditions closer to *true tooling motions*, on the other hand, will be examined and compared so as to assess the impact of overlooking some of the deviations summarized in section 5.2.1.

The powder employed in making the part is a Distaloy AE iron based powder with apparent density $\rho_{app} = 3.25\, g/cm^3$. Material parameters can be obtained thus from the empirical adjustment presented in chapter 2. Fill density, which is assumed uniform throughtout the die cavity, is taken as the apparent density. Friction between the powder mass and the faces of the tools-die walls and core rod is modeled via a friction Coulomb law, with coefficient $\mu = 0.12$. The elastic behavior of the tooling is characterized by a Young's Modulus $E_{tool} = 210\, GPa$ and a Poisson's ratio $\nu_{tool} = 0.3$.

The axial symmetry of the part is exploited and the study is concentrated on a characteristic radial section so that the FEM analysis can be accomplished in two

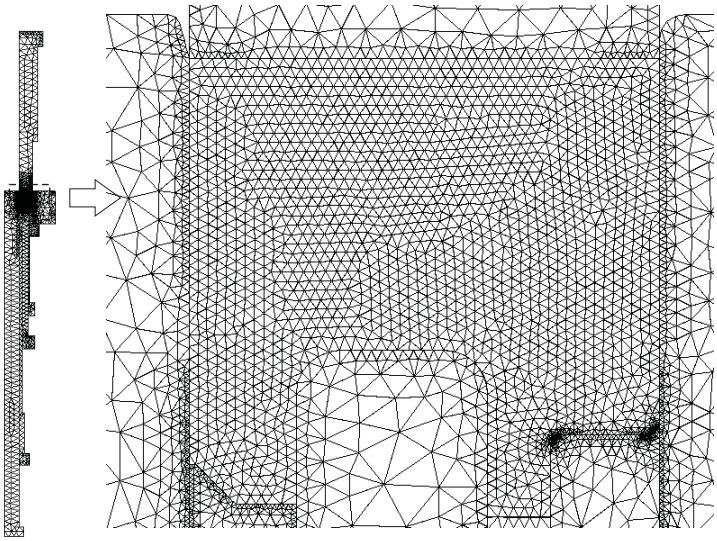

Figure 5.8 *Initial mesh layout.*

dimensions. The initial finite element mesh is shown in figure[5] 5.8. The average size of the elements of the powder body is $l_e = 0.25mm$, whereas the size of the elements at the boundaries of punches and die in contact with the powder is, approximately, $0.15mm$, although features on the bottom faces of the part, as over the lower outer punch-II, demands smaller elements ($\approx 0.05mm$) at these locations. Observe that tooling elements are graded from small-size at the boundaries in contact with the powder to coarser with increasing distance from these surfaces. A glance at figure 5.8 also allows us to appreciate the startling contrast between the volume occupied by the powder die cavity and the volume occupied by the tooling set.

Results using theoretical punch displacements

The *theoretical or nominal* displacement profile for the upper punch reciprocating motion can be obtained from Eq.(5.2.1). The values of the lengths of the crankshaft and the connecting rod appearing in such equation are $l_c = 90\,mm$ and $l_r = 580\,mm$, respectively. On the other hand, the theoretical motions of lower punches, core rod and die are fully determined by the *motion scale factors* shown in table 5.1. The motion scale factor of the lower outer punch $LOP - II$ and the die are identical, as they are mounted in the same platen. On the other hand, it follows from the motion scale factors of LIP and LOP-I that those punches are held practically stationary during the pressing stage.

The information tabulated in Table 5.2 serves to illustrate the previously men-

[5]The working end of the upper punch is not flush with the top surface of the die when the upper punch comes into contact with the powder, as one may expect (see figure 5.8). Nevertheless, this modification, which has been motivated by simplicity reasons in preprocessing the geometry, has no influence in the computed results.

	UP	LIP	LMP	LOP-I	LOP-II/DIE	CORE ROD
f	1	0.043	0.234	0.019	0.26	0.233

Table 5.1 *Motion scale factors*

			UP	LIP	LMP	LOP-I	LOP-II
TOLERANCE in h			-	0.09	0.10	0.09	0.07
k = 0	ΔL(Uniaxial est.)		0.307	0.352	0.245	0.130	0.036
k = 1	$\varphi_0 = 160.2$	$\Delta L^{(k)}$	0.175	0.298	0.123	0.153	0.0241
		$h^{(k)} - h$	-	**-0.162**	-0.080	-0.080	-0.068
k = 2	$\varphi_0 = 160.9$	$\Delta L^{(k)}$	0.195	0.197	0.167	0.0928	0.0204
		$h^{(k)} - h$	-	-0.070	0.055	-0.049	0.003

Table 5.2 *Iterative procedure for calculating the initial die cavity dimensions. Theoretical tooling motion case.*

tioned procedure for the calculation of the initial die cavity dimensions. The starting values of the elastic deflections ΔL are obtained from the uniaxial estimation (5.3.5). The iterative sequence is halted when the discrepancis between the computed finished length $h^{(k)}$ and the design value h (see figure 5.1) is within prescribed tolerances. In the first iteration, the convergence tolerance for the lower inner punch is not met, due to a too high initial estimation of its deflection. An additional computer run was hence required to achieve consistent starting conditions.

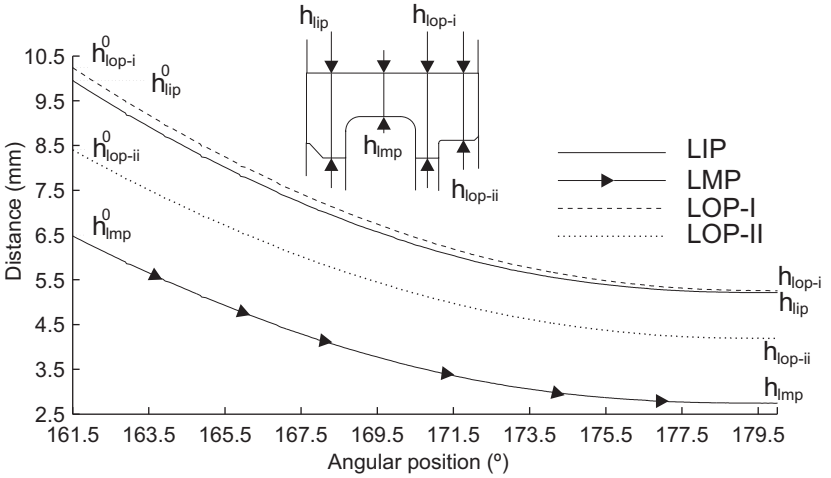

Figure 5.9 *Distance between working ends of upper punch and lower punches as a function of the angular position during the pressing cycle. Theoretical tooling motion case.*

In figure 5.9, we show the evolution of the lengths of each thickness level as a function of the angular position. As expected, these curves mimic the sinusoidal

pattern of the reciprocating motion of the upper ram. The contour plot of the density computed - by the finite element method - at the end of the pressing stage is displayed in figure 5.10. The level formed by the lower middle punch exhibits the highest density, whereas the region with the lowest density is located above the lower inner punch. To enable direct comparison with experimentally measure densities, the part is divided into five volumes. The averaged density over those volumes is shown also in figure 5.10. Experimental and computed results are presented in table 5.3. It is apparent that numerical results barely resemble the experimental density measures. Discrepancies between numerical and experimental data are especially unacceptable in region labelled as five, just over the lower inner punch.

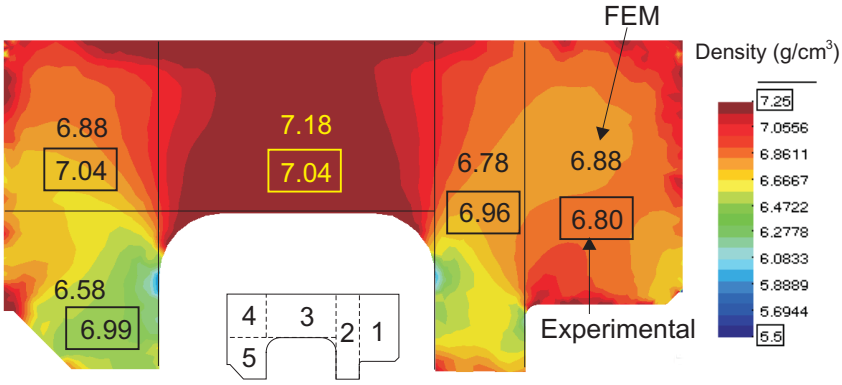

Figure 5.10 *Contour plot of density computed at the end of the pressing stage. Theoretical tooling motion case.*

Zone	1	2	3	4	5	Overall
$\rho_{num}\,(g/cm^3)$	6.88	6.78	7.18	6.88	6.58	6.91
$\rho_{exp}\,(g/cm^3)$	6.80	6.96	7.04	7.04	6.99	6.94
$\rho_{num} - \rho_{exp}\,(g/cm^3)$	0.08	-0.18	0.14	-0.16	-0.41	-0.03

Table 5.3 *Comparison between computed densities using theoretical tooling motion (ρ_{num}) and experimentally measured values(ρ_{exp}) .*

.

Results using "true" punch displacements

We carry out now the simulation of the pressing stage using prescribed condition on tools closer to the tool motions monitored by the CNC computer during the compression. The discrepancies between the theoretically predicted and true motions of LIP, LOP-I, die and core rod are insignificant and the prescribed displacements are therefore the same as in the previous case. By contrast, substantial errors are detected in the description of the upper punch and lower middle punch motions. Figure 5.11 shows the theoretical and "true" positions of the top face of

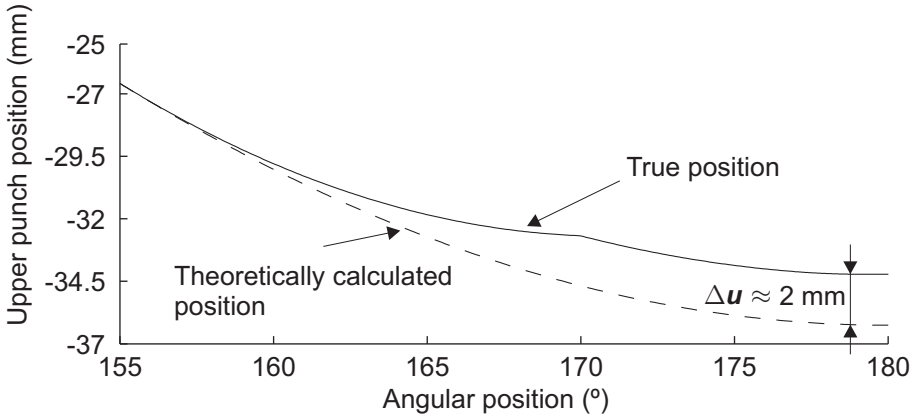

Figure 5.11 *Position of the upper punch ram. Theoretically calculated value (dashed line) and value monitored and recorded by the CNC data acquisition system (solid line).*

the upper punch during the pressing portion of the cycle. The position recorded by the CNC data acquisition system exhibits a gradual deviation from the theoretically calculated reciprocating motion of the main shaft. At the bottom dead center, the amplitude of this deviation can be estimated at approximately 2 mm. This deviation is ascribed to the looseness of the parts comprising the hydraulically operated mechanism, alluded to in section 5.2.1, that controls the force exerted by the upper punch during ejection, and which is located between the upper punch and the upper ram.

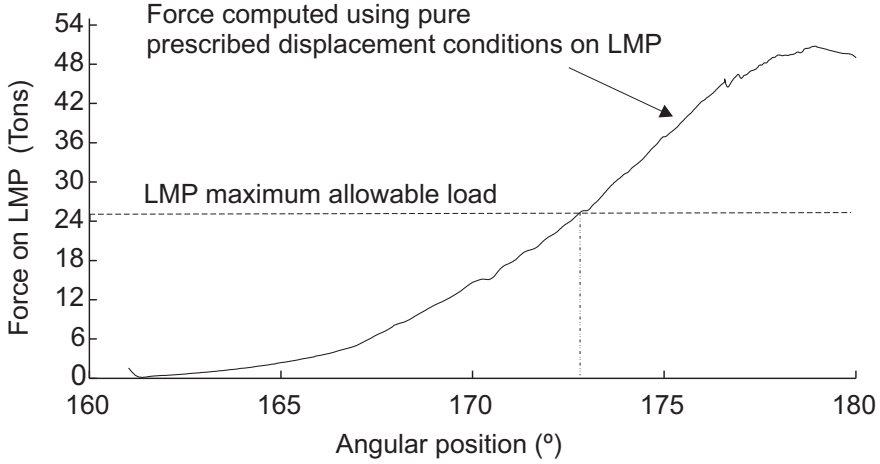

Figure 5.12 *Force on the lower inner punch computed using pure prescribed displacement condition on the lower middle punch. The horizontal dashed line indicates the threshold below which the hydraulic device controlling the LMP platen operates correctly.*

In discussing the classification of what we have termed "predictable deviations"

(see section 5.2.1), we pointed out that the hydraulic drives operating the lower rams execute the scheduled motion only if the resulting force on each punch is below a certain threshold. In the case of the lower middle punch, the corresponding hydraulic servosystem operates under regular conditions below 25 Tons. Figure 5.12 shows the FEM computed evolution of the force exerted by the compacting powder on the lower middle punch using theoretical tooling kinematics, in which the stroke of the lower punches is assumed to be displacement-controlled during the entire pressing stage. The information displayed in figure 5.12, however, makes apparent the inadequacy of such assumption. The computed force at the end of the end of pressing operation exceeds the maximum allowable force by a factor of almost two. This unduly high force on the LMP is intimately connected with the overdensification observed in the region over the lower middle punch (see figure 5.10). According to the suggestion given in section 5.10, the prescribed condition on the lower middle punch must be modified to accommodate this limited capacity of the hydraulic device. For forces below 25 Tons, displacements given by the expression $u_{lmp} = f_{lmp} \cdot u_{up}$ will be imposed on the bottom surface of the punch. When the force rises slightly above 25 Tons, the displacement condition will be replaced by a pressure-type condition so as to ensure that the lower middle punch moves downward maintaining the force in 25 Tons.

			UP	LIP	LMP	LOP-I	LOP-II
TOLERANCE in h			-	0.09	0.10	0.09	0.07
k = 0	ΔL(Previous simul.)		0.175	0.298	0.123	0.153	0.0241
k = 1	$\varphi_0 = 156.7°$	$\Delta L^{(k)}$	0.182	0.325	0.136	0.196	0.016
		$h^{(k)} - h$	-	-0.0043	-0.057	0.0125	-0.034

Table 5.4 *Iterative procedure for calculating the initial die cavity dimensions. "True" tooling motion case.*

	LIP	LMP	LOP-I	LOP-II
$h^0_\bullet$ comp. using nominal displacement	10.22	6.70	10.52	8.63
$h^0_\bullet$ comp. using true displacement	10.87	6.47	11.23	8.20
Difference (%)	5.97	-3.54	6.37	-5.35

Table 5.5 *Fill heights (mm) corresponding to each thickness level. Theoretical and "true" tooling motion cases.*

The simulation of the pressing stage is carried out again with these new boundary conditions on both upper punch and lower middle punch, First, we determine the starting conditions by means of the strategy illustrated in the flowchart contained in figure 5.7. The information concerning such procedure is set forth in table 5.4. In the first iteration, the differences between calculated lengths of each thickness levels and the design values are between the prescribed tolerances, hence, in this case, guesswork is limited to a single computer run[6]. In table 5.5, we sum-

[6]The initial estimation of punch deflections employed in this case has been obtained from the

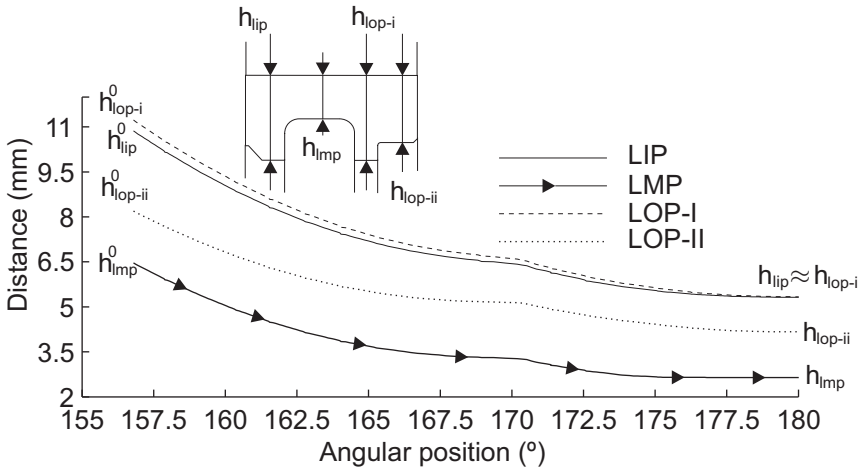

Figure 5.13 *Distance between working ends of upper punch and the lower punches as a function of the angular position during the pressing cycle. "True" tooling motion case.*

marize the fill heights corresponding to each thickness level calculated on the basis of theoretical and "true" prescribed conditions. According to such data, including the aforementioned deviations in the UP and LMP motions implies changes on the die cavity dimensions of, on the average, 5 %. The variation during pressing of the lengths of the levels formed by each lower punch is depicted in figure 5.13. The effect of the alluded to earlier deficient transmission of motion between the connecting rod and the upper punch is apparent, as the curves do not display the characteristic sinusoidal shape observed in the prescribed displacement case.

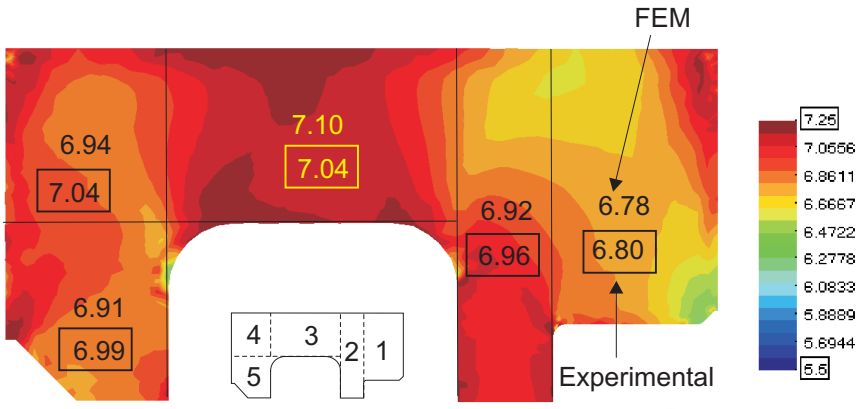

Figure 5.14 *Contour plot of density computed at the end of the pressing stage. "True" tooling motion case.*

first iteration in computing the starting conditions of the theoretical motion case (see table 5.2).

Density contours at the end of compression are shown in 5.14, accompanied by computed averaged density within the analyzed subdomains. These averaged values are compared with experimental measures in both figure 5.14 and table 5.6. Clearly, numerically predicted densities obtained with the model using "true" tooling motions correspond more closely with empirically measured densities than in the theoretical tooling motion case (see figure 5.10). Furthermore, the agreement can be deemed satisfactory, as differences are within 0.1 g/cm^3. This comparison yields convincing proof of the importance of having *an accurate description of the pressing motion* at one's disposal if one wishes to bring computed results into quantitative agreement with experimental data, especially if the analyzed part is relatively thin.

Zone	1	2	3	4	5	Overall
$\rho_{num}\,(g/cm^3)$	6.78	6.92	7.10	6.94	6.91	6.93
$\rho_{exp}\,(g/cm^3)$	6.80	6.96	7.04	7.04	6.99	6.94
$\rho_{num} - \rho_{exp}\,(g/cm^3)$	-0.02	-0.04	0.06	-0.10	-0.08	-0.01

Table 5.6 *Comparison between computed densities using "true" tooling motion (ρ_{num}) and experimentally measured values(ρ_{exp}) .*

5.3.3 Optimization of the pressing sequence

Inspection of the contour plot contained in figure 5.14 reveals that the density field obtained with the tooling motion analyzed in the previous section exhibits a considerable degree of non-uniformity. For instance, the averaged density in the powder column formed by the lower outer punch LOP-II is 0.24 g/cm^3 below the averaged density in the column formed by the lower middle punch. In view of this considerable lack of uniformity, it is natural to inquire whether other tooling motions might have led to more uniform density fields, and how these sequences of motion can be obtained. This raises the issue of *optimization of the pressing sequence*, i.e., how to approach the "ideal" tooling motion that leads to an uniform density field throughout the compact.

In essence, the strategy followed here to obtain the optimum pressing sequence is the determination of the tooling motion that ensures a near *constant compression ratio*[7] in each thickness level of the part. This method is, certainly, but the common manner in which the dimensions of the fill cavity are calculated in the design stage [100]. However, rather than address the question in this conventional manner[8], we couch our discussion in the broader context of *optimization problems*, so as to

[7]The compression ratio is defined as the ratio of the height of the loose powder to that of the green compact (for each thickness level).

[8]An added difficulty here is that, on the one hand, tool motions are non-linear functions of the angular position - due to the reciprocating nature of the upper punch motion and the inclusion of the previously outlined *predictable deviations* -, and in the other hand, punch deflections have to be taken into consideration. It can be shown that, under such conditions, the system of nonlinear equations that arises from imposing the condition of constant compression ratio may have no solution.

regard the problem from the most general standpoint and, eventually, encourage further advances in this line of development.

Objective function

A crucial step in the formulation of any optimization problem is the definition of the function that has to be minimized, the so-called *objective function*. In our case, this objective function has to measure the degree of non-uniformity of density distribution. If we divide the part into n nonoverlapping volumes, an indication of the degree of deviation from a state of uniform density is provided by the euclidean norm of the differences between the average density ρ_i calculated in each volume and the overall density ρ_f:

$$e_{dens} = \sqrt{\sum_{i=1}^{n} (\rho_i - \rho_f)^2}. \tag{5.3.7}$$

The manner in which the part is divided into volumes has a significant influence on the nature of the solution. Different divisions may lead to distinctly different optimal pressing routes. Besides, the complexity in obtaining the solution increases with increasing number of subdivisions. A limiting case is to choose the partition provided by the own finite element mesh. However, the density in the volume associated to a typical finite element is too small to be measured in practice. With a view towards eventual experimental validation, thus, it proves more convenient to select easily measurable volumes.

As mentioned above, the aim is to devise a tooling kinematics that approaches a constant compression ratio in each thickness level of the compact. This consideration leads naturally to the part division sketched in figure 5.15. The compact is divided by cylindrical surfaces parallel to the pressing direction, resulting in four "column" subdomains, one for each lower punch. The objective function (5.3.7) for

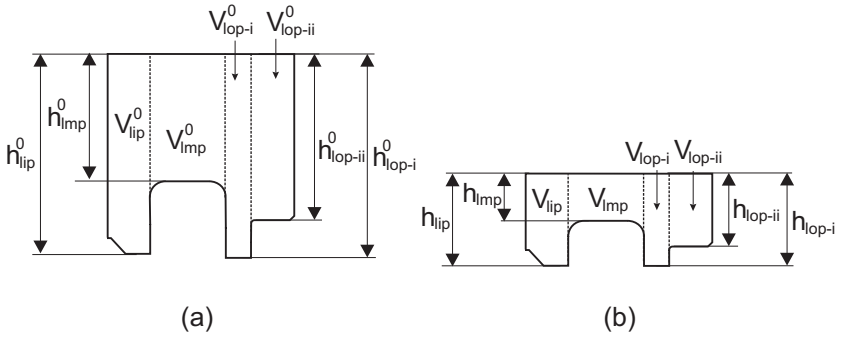

Figure 5.15 *Division of the part in columns. (a) Initial columns (b) Final columns.*

this case reads:

$$e_{dens} = \sqrt{(\rho_{lip} - \rho_f)^2 + (\rho_{lmp} - \rho_f)^2 + (\rho_{lop'} - \rho_f)^2 + (\rho_{lop''} - \rho_f)^2}. \tag{5.3.8}$$

Note that the optimization problem associated to this objective function only quantifies density gradients between the columns formed by each lower punch. Variation of density along the pressing direction owing to wall friction is, consequently, completely ignored. For parts of relatively low height, as the one analyzed here, in which friction effects do not play a relevant role in determining density distribution, this division in columns proves adequate. On the contrary, for parts of considerable height, in which density changes promoted by wall friction become dominant, this partition may fail in providing useful information and the part should be subjected to additional horizontal subdivision.

In evaluating the objective function (5.3.8), the overall density ρ_f can be calculated from simple mass conservation considerations. The determination of the average density in each column requires more elaborate computations: first one has to obtain the fill heights consistent with the given tooling motion the finished lengths of the part - following the procedure outlined in section 5.3.1 - and then to launch the finite element analysis so as to finally determine these average densities.

Variables or parameters of the problem

The following step in the formulation of our optimization problem is to define the so-called *design variables* or *parameters*. All controllable factors, related with the press kinematics, whose variation affects to some extent the final density distribution can be included in this group. The logical candidates for being considered as the *design variables* of our optimization problem are the set of *motion scale factors*, as they entirely characterize the tooling motion. In order to reduce the number of variables, one of the lower punches that forms the lowest face of the part, the LOP-I, is assumed to remain stationary, that is, $f_{lop'} = 0$. The motion scale factor associated to the core rod is also excluded from the variables or parameters of the problem, as it induces only density gradients in the pressing direction, which are practically inconsequential to the value of the objective function. We are left thus with a total of *three variables*, namely, the motion scale factors of the LIP, LMP and LOP-II, or expressed symbolically $\mathbf{f} = [f_{lip}, f_{lmp}, f_{lop'}]$. The problem can be mathematically posed as the *determination of the motion scale factors* $\mathbf{f}$ *that minimizes the objective function* (5.3.8). This problem falls under the general rubric of *nonlinear constrained optimization problems*. The *constrained* character refers to the fact that the value of the motion scale factors must lie in the interval $[0, 1]$. A zero value amounts to keep fixed the corresponding lower punch during the entire pressing stage, whereas a motion scale factor equal to one means that the lower punch moves downward at the same velocity as the upper punch and, thus, no effective pressing takes place. The problem is *nonlinear* because of the nonlinear character of the relation between the objective function and the variables.

Solution of the optimization problem. Simplified "column" model.

This *nonlinear constrained optimization problem* can be attacked, as done for instance in Ref. [57], by recourse to the standard optimization techniques described in the related literature [71, 85, 19]. However, the discussion of the formalism involved in such techniques, as well as their adaptation to the problem of optimization of the pressing sequence, are huge and complex topics in their own right, and

falls thereby beyond the scope of this work. Here, we limit ourselves to provide a reliable *approximation* to this solution. This approximation may be eventually used as the *starting point*[9] for solving the problem by the aforementioned elaborate optimization algorithms.

To determine this *approximation* of the minimizer of the original functional objective (5.3.8), we introduce an alternative model for replicating the powder behavior. The essence of this model is intimately connected with the division in column subdomains shown previously in figure 5.15. Each powder column is treated as a separate component, in the spirit of the *"column model"* described in reference [103]. This means that transfer of mass between columns is neglected. Densification on each domain can be studied thus by simply applying the conservation of mass equation:

$$\rho_{lp}^{col} = \rho^0 \frac{V_{lp}^0(h_{lp}^0)}{V_{lp}(h_{lp})}, \tag{5.3.9}$$

where ρ_{lp}^{col} denotes the column average density at the end of compression, ρ^0 is the fill density (assumed uniform), and $V_{lp}^0(h_{lp}^0)$ and $V_{lp}(h_{lp})$ the initial and final volumes, respectively, of the column corresponding to the lower punch labelled as "lp". Now we define, in analogy with (5.3.8), the following objective function:

$$e_{dens}^{col} = \sqrt{(\rho_{lip}^{col} - \rho_f)^2 + (\rho_{lmp}^{col} - \rho_f)^2 + (\rho_{lop'}^{col} - \rho_f)^2 + (\rho_{lop''}^{col} - \rho_f)^2}. \tag{5.3.10}$$

This "column model" is indeed a very *crude approximation to reality*, and, in general, the values of density predicted by the elementary estimation (5.3.9) would differ substantially from the values computed by the more sophisticated and realistic finite element model. In situations in which overdensification in one column takes place at the expense of deficient consolidation in the adjoining regions, the discrepancies would be particularly drastic. In circumstances, on the contrary, in which transfer of mass between columns is not pronounced, the two estimations would be more in agreement. Accordingly, the *minimum difference* between both predictions would be detected in the case in which *redistribution of mass between columns is, on the average, minimum.* It follows from this physically plausible reasoning that the minimizer of the objective function (5.3.10) associated to the elementary column model can be regarded as an *approximation* of the minimizer of the objective function associated to the finite element model. The quality of this approximation must be eventually assessed by undertaking a finite element analysis.

The advantage of this strategy relies on the fact that the solution of the optimization problem linked to the column model is comparatively easy to obtain. The number of variables is only three, and the evaluation of the objective function is, computationally speaking, inexpensive. Consequently, evaluation of the function

[9]Standard optimization techniques are based in iterative schemes. The number of iterations to achieve convergence relies mainly on the closeness of the starting point to the solution. In view of the high computational cost associated to each evaluation of the objective function, the process may become prohibitively expensive if the choice of starting point is not adequate.

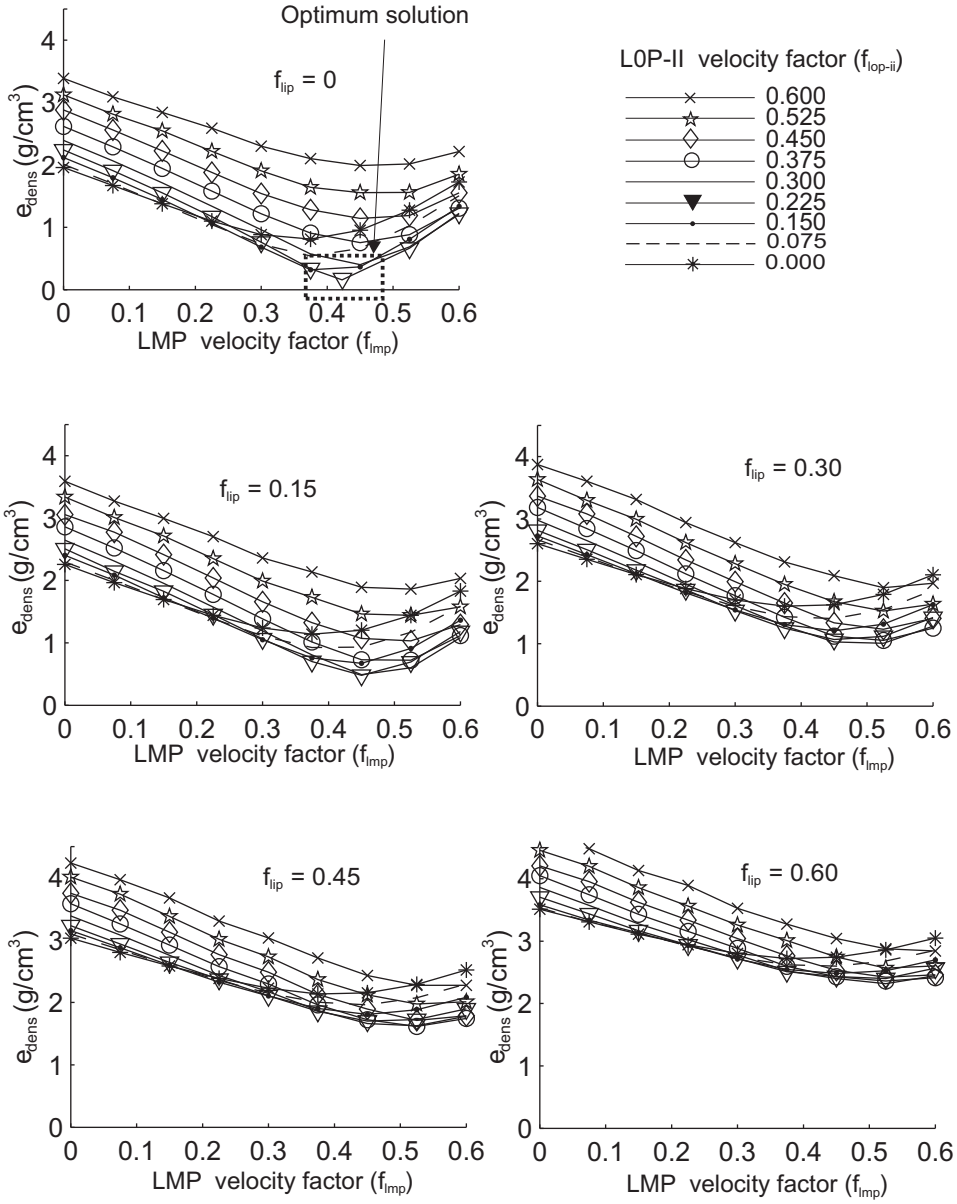

Figure 5.16 *Objective function e_{dens} as a function of motion scale factors. The lower outer punch (I) is held stationary in all cases, i.e., $f_{lop'} = 0$, whereas the motion scale factors of the other lower punchers are varied from 0 to 0.6.*

at a sufficient number of points so as cover the entire range of these variables (the *feasible region* [71]) is computationally affordable. The minimum can be directly obtained as the lowest value of the vector resulting from such evaluations. We

should remark, however, that this straightforward, although certainly not very elegant, way of finding the solution may be not feasible in other cases, because of either the unaffordable computational cost associated with the evaluation of the objective function or the large number of variables. In those cases, recourse to standard optimization algorithms should be made.

Further insight into the nature of the solution is gained if these points are represented graphically. Figure 5.16 shows five diagrams. Each of these diagrams is a parametric plot, with the LOP-II motion scale factor $f_{lop''}$ as parameter, of the objective function e^{col}_{dens} versus the LMP motion scale factor f_{lmp}, holding fixed f_{lip}.

It is readily apparent from these graphs that holding stationary the lower inner punch ($f_{lip} = 0$) represents the most favorable situation. This concurs with one's intuitive expectation, as the finished length of the levels formed by the LIP and the LOP-I are identical, $h_{lip} = h_{lop'}$. The global minimum is to be sought then in the diagram displayed on the top left corner of figure 5.16. Visual inspection of this plot indicates that the global minimum is approximately located at $f_{lmp} = 0.415$ and $f_{lop''} = 0.225$.

	UP	LIP	LMP	LOP-I	LOP-II/DIE
f	1	0.000	0.225	0.000	0.415

Table 5.7 *Set of motion scale factors that minimizes the objective function associated to the elementary column model.*

FEM Validation

The combination of motion scale factors[10] that minimizes the objective function associated to the elementary column model is summarized again for convenience in table 5.7. According to the physical arguments put forward previously, these motion scale factors should lead to a "near" uniform density distribution. To confirm this hypothesis, one *must* perform a finite element analysis, since the column model is too simplistic as to accept its results at face value. Thus, only a *FEM analysis* can *provide the assurance* that the presumably near-optimum motion scale factors, listed in table 5.7, define indeed tooling displacements that lead to more uniform density distribution.

As usual, to carry out the finite element analysis, we obtain first the fill cavity dimensions consistent with such tooling motion. The iterative procedure is illustrated in table 5.8. In figure 5.17, the computed evolution of the length of the levels formed by each lower punch is displayed. Observe that the curves exhibit a very subtle inflexion point around $\varphi = 170°$, a fact that reflects that the deviation due to plays in the hydraulic mechanism controlling the position of the upper punch has been included in constructing the punch displacement profiles.

The average densities in each column subdomain at the end of compression obtained by the elementary column estimation and by finite element calculations

[10]The motion scale factor associated to this tool has been set to the one corresponding to the DIE/LOP-II.

			UP	LIP	LMP	LOP-I	LOP-II
TOLERANCE in h			-	0.09	0.10	0.09	0.07
k = 0	ΔL(Previous simul.)		0.257	0.249	0.219	0.107	0.0288
k = 1	$\varphi_0 = 157.5°$	$\Delta L^{(k)}$	0.209	0.324	0.134	0.183	0.0232
		$h^{(k)} - h$	-	-0.012	**-0.152**	-0.039	**-0.075**
k = 2	$\varphi_0 = 157.7°$	$\Delta L^{(k)}$	0.187	0.312	0.115	0.181	0.0211
		$h^{(k)} - h$	-	-0.074	-0.062	-0.090	-0.046

Table 5.8 *Iterative procedure for calculating the initial die cavity dimensions. Optimized tooling motion case.*

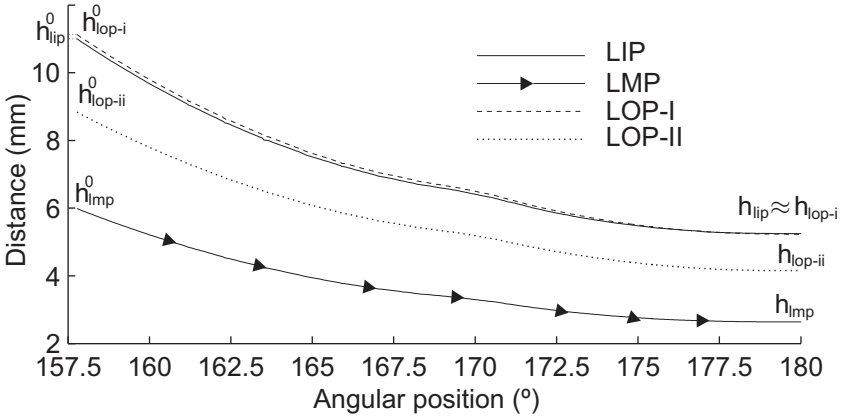

Figure 5.17 *Distance between working end of upper punch and lower punches as a function of the angular position during the pressing stage. Optimized tooling motion case.*

COLUMN	LIP	LMP	LOP-I	LOP-II	Overall
Column model	6.98	7.02	6.91	6.90	6.96
FEM model	6.95	7.04	6.98	6.97	6.98
$\rho_{col} - \rho_{fem}\ (g/cm^3)$	0.03	-0.02	-0.06	-0.08	-0.02

Table 5.9 *Averaged densities ((g/cm^3)) obtained by the elementary column estimations and by the finite element calculations.*

.

are compared in table 5.9. Discrepancies between both set of values are within 0.08 g/cm^3. Such satisfactory agreement substantiates the hypothesis of the closeness between the minimizers of the original FEM optimization problem and the one associated to the column model. Certainly, further improvements in uniformity of the density distribution might be achieved. The density over the lower middle punch, for instance, (see figure 5.18), is still 0.09 g/cm^3 higher than the average density above the lower middle punch. As already pointed out, the determination of motion scale factors leading to further improvements would require a local search,

by standard optimization techniques, in the vicinity of the values tabulated in table 5.9.

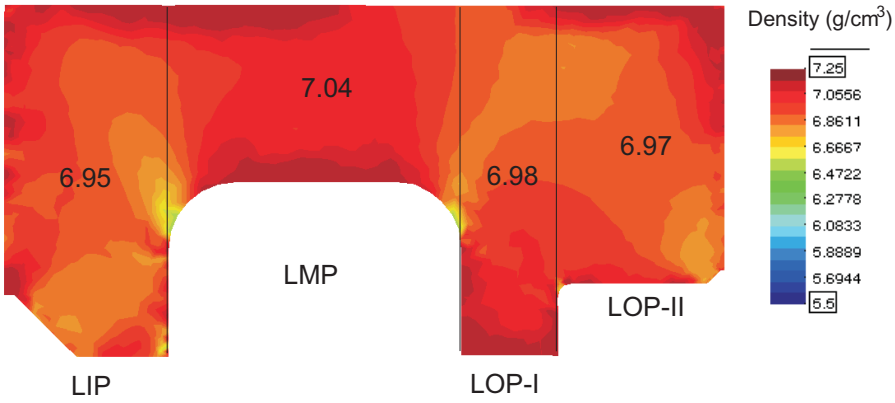

Figure 5.18 *Contour plot of computed density at the end of compression. Optimized tooling motion case.*

So far, the discussion has been limited to the improvement in uniformity of the *final* density field. One would expect that motion scale factors leading to uniform density distribution will also contribute to uniform density fields at any other point during the pressing operation. In figure 5.19, the variation, with angular position, of averaged densities in each subdomain is shown for the optimized tooling motion case and for the tooling motion characterized in the previous section (with "true" displacement profiles). Comparison of these diagrams clearly confirms this expectation. The five paths in each case emanates from the same point, which corresponds to the fill density ($\rho_0 = 3.25$), and deviates gradually from one another as pressing progresses. However these deviations are considerably more pronounced in the non-optimized case (figure 5.19.a). Especially intense is the magnitude of the drift exhibited by the averaged density in the region above the lower middle punch (zone 3).

A quite relevant result is the magnitude of the forces induced on the punches during compression. The FEM computed evolution of these forces is depicted in figure 5.20. Observe that the punch on the lower middle punch remains below 25 Tons, which means that the hydraulic drive controlling this punch remains, according to the finite element calculations, within the controlled-displacement regime.

For a rigorous assessment of the proposed methodology, the numerically predicted improvement in density should be experimentally corroborated. Unfortunately, owing to unavailability of the press machine, it was not possible to manufacture the part according to the pressing route determined by the proposed procedure. This experimental validation, as well as the extension of the methodology to other part geometries in which friction effects are to be accounted for, are left to future work.

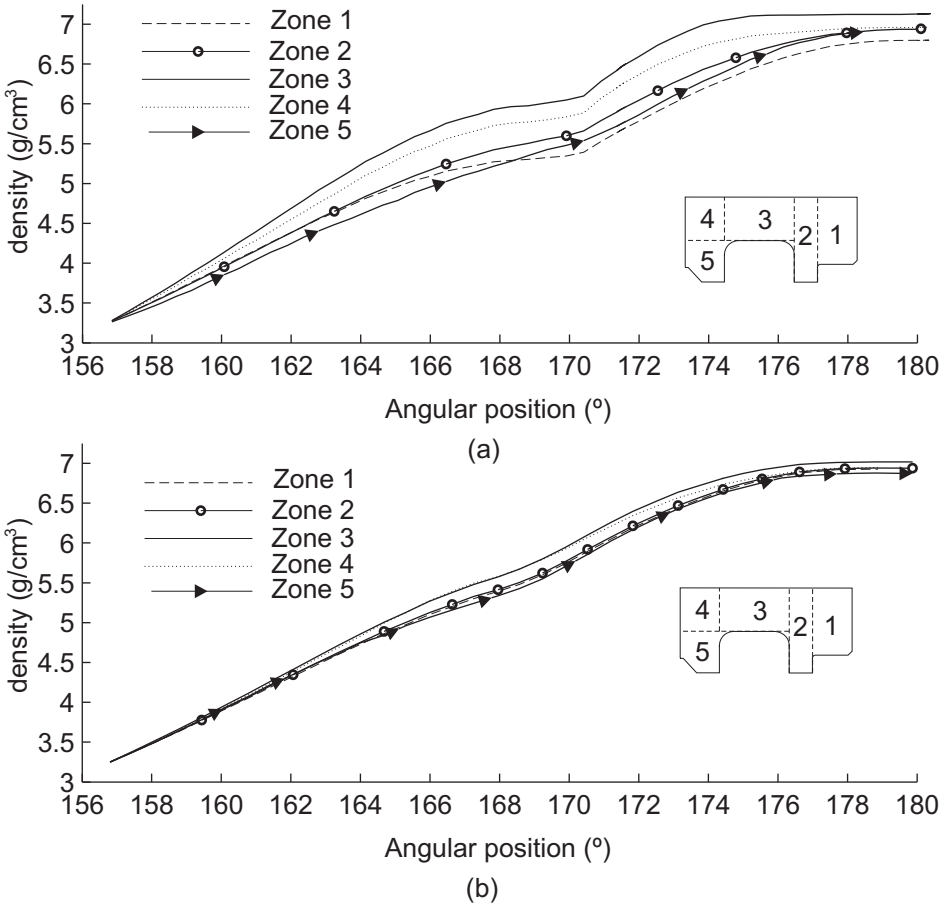

Figure 5.19 *Evolution of averaged density in each volume. (a) Non-optimized tooling motion (b) Optimized tooling motion.*

5.4 Ejection

Attention is confined now to the simulation of the *ejection stage*. This stage covers approximately the portion of compaction cycle ranging from 180° to 265°, and can be further subdivided into three distinctly different phases. This division is illustrated schematically in figure 5.21. The first phase corresponds to partial *pressure release*. The upper punch moves slightly upward so as to reduce radial forces and facilitate the subsequent withdrawal of the die. This phase covers only a small portion of the entire ejection operation, from[11] 180° to 190°.

In the second phase, from 190° to approximately 240°, the die moves downward

[11] Considering that the production rate is approximately 660 pieces per hour, the time required to carry out a complete cycle can be estimated by $t_{cycle} = 3600/660 = 5.45$ seconds, and hence the pressure release stage lasts only about $t_{prel} = 5.45\,10/360 = 0.15$ seconds.

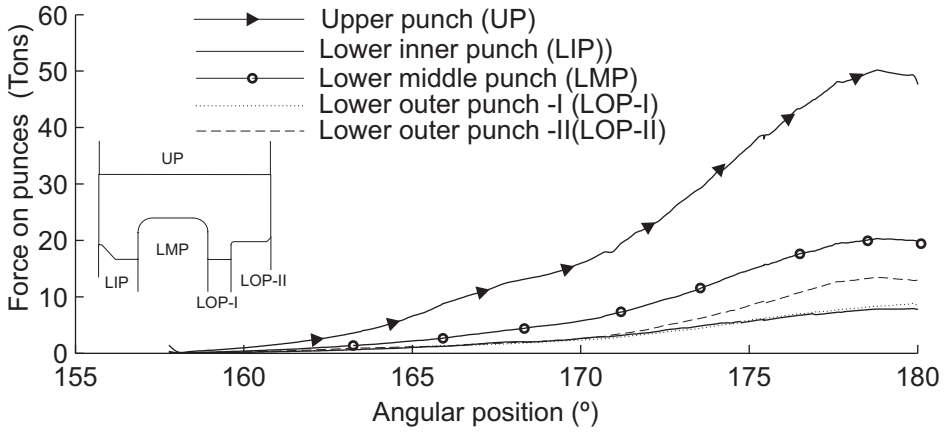

Figure 5.20 *Evolution of computed force on punches.*

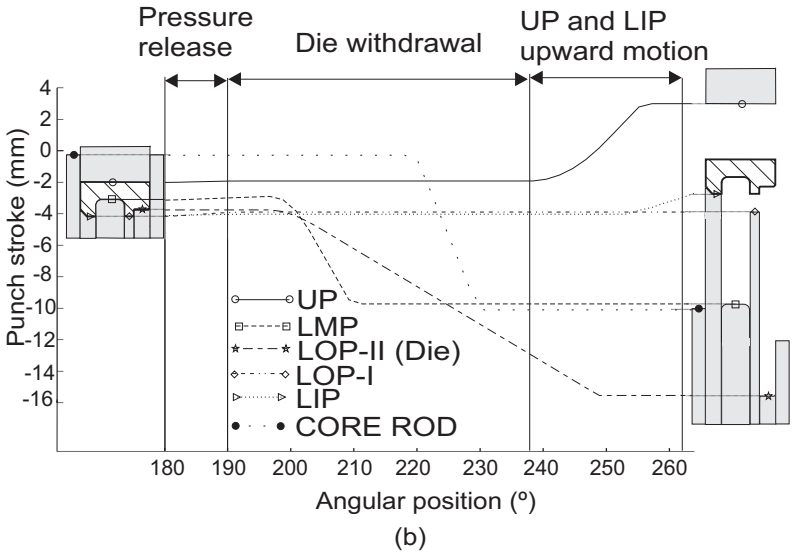

Figure 5.21 *Typical tooling motion profile for the ejection stage.*

(*withdrawal tooling system*) while the two lower punches (LIP and LOP-I) forming the lowest faces remain stationary so as to support the part. In order to release some radial pressure, the withdrawal movement of the die may be accompanied by the downward motion of the core rod and/or the lower middle punch. In the third stage, ranging from 240° to 265°, the upper punch moves up away from the compact and, simultaneously, the lower inner punch lifts the part slightly so that it can be removed by the gripper from the compaction zone.

The finite element results will be also presented according to this division of

the process. First, we shall carry out the simulation of the pressure release stage. The computed cohesion contours corresponding to this analysis will be carefully examined and discussed for different tooling kinematics. If it turns out that no evidence of cracking is detected, then the computation of the subsequent stage will proceed. On the contrary, if de-cohesion patterns are observed in the corresponding contour plot, it is of no practical interest to pursue further the computations, and we shall concentrate rather in ascertaining the root cause of such de-cohesion patterns.

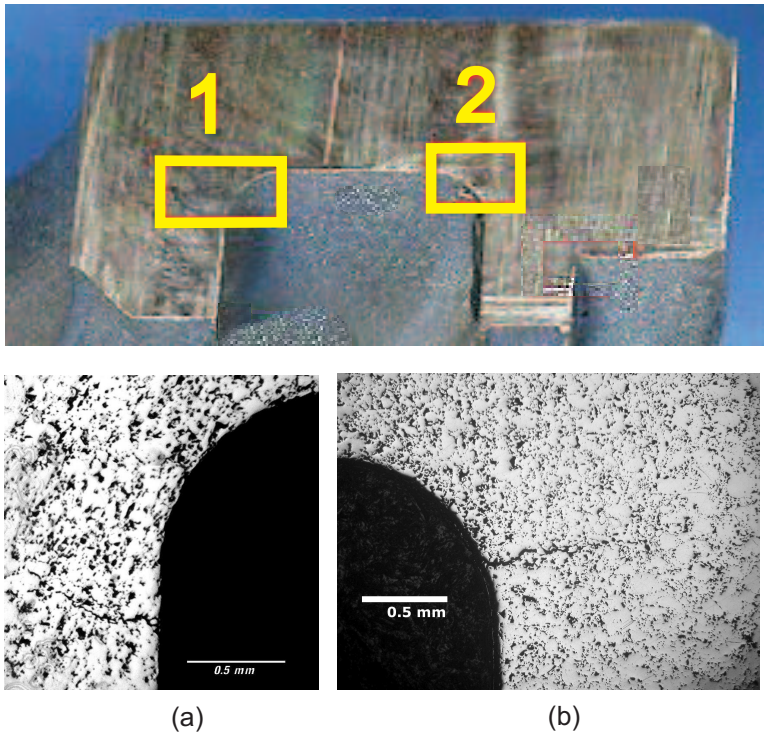

Figure 5.22 *Cross-sectional view showing two cracks detected in the green compact. Microscopic image of: (a) Zone 1 (b) Zone 2*

As anticipated at the outset of this chapter, the part being the target of this study was not finally fabricated exactly following the initial customer's specifications, displayed in figure 5.1, due to difficulties in obtaining a free-defect green compact. Some of the detected defects were visible to the naked eye, and other were only discerned after microscopic examination. A microscopic view of two of these observed cracks is shown in figure 5.22. We should point out, however, that the ensuing discussion is not intended to set up a systematic comparison between experimentally recorded crack images and computed cohesion contours. The retrospective character of the study makes somewhat elusive such rigorous verification of results. Rather, we limit ourselves to *qualitatively examining* , by simple comparison of cohesion contours, the adequacy of *alternative* ejection processes. Consider

two alternative routes A and B for ejecting the part from the die cavity. If, for instance, the cohesion computed using the ejection route A remains unaltered during the process, whereas the predicted cohesion contours using ejection schedule B shows clear signs of cracking, we can legitimately say that ejection schedule A is, *comparatively*, more appropriate than ejection route B. However, we should refrain from *categorically* concluding that ejection schedule A leads to a free defect part, as this would require confirmation from experience.

5.4.0.1 Pressure release

The finite element analysis of the pressure release stage is *restarted*[12] from the solution (using "true" punch displacement curves, see section 5.3.2) obtained at the end of the computation of the pressing stage. In the sequel, two different sequences of tooling motion are examined.

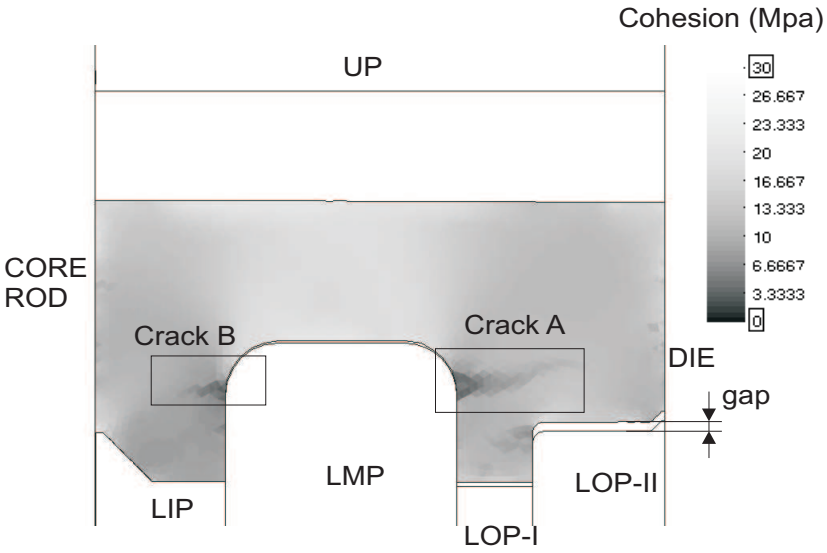

Figure 5.23 *Contour plot of cohesion at the end of pressure release stage. Total axial unloading case.*

.

First, we consider a scenario in which the upper punch moves up away from the compact and the lower platens remain fixed. Every PM practitioner knows that this practice represents conditions likely to generate a defective part and, thus, is by no means adequate, especially when dealing with relatively thin parts. Nevertheless, we shall momentarily overlook such practical recommendation and

[12] As alluded to in section 4.1, a *restart facility* in the simulation code provides the flexibility in automatically initiating the analysis from any point in the computational cycle. In restarting the analysis, some parameters controlling the solution algorithm can be changed. For instance, for the ejection stage, kinematic description is restricted to the *small strain regime* and the remeshing utility is disabled.

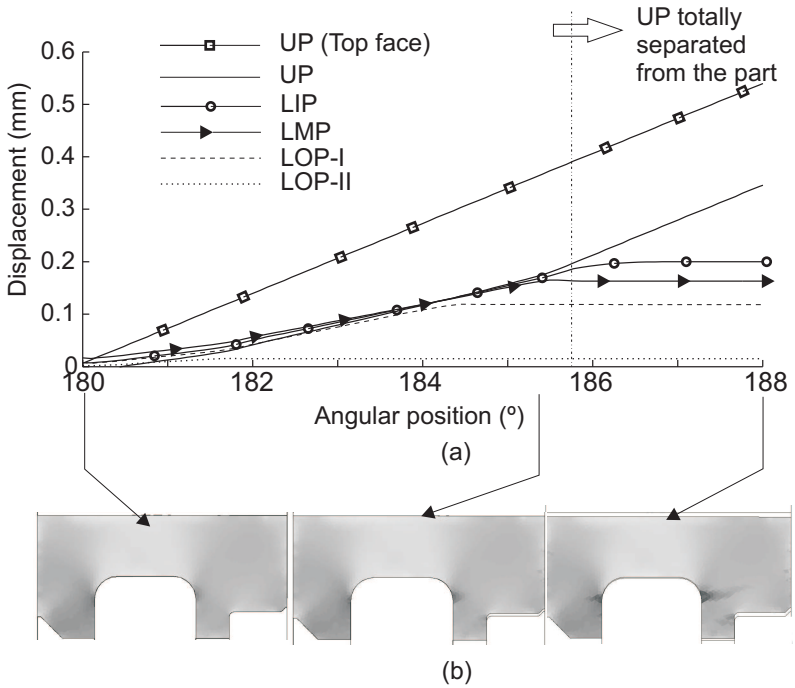

Figure 5.24 *Total axial unloading case. (a) Displacement of the working ends of lower and upper punches, together with the displacement of the top face of the upper punch, as a function of the angular position. (b) Sequence of contour plots of cohesion.*

.

evaluate the ability of the model in reproducing the typology of cracks arising in these situations. Then, this case will be compared with one in which the upper punch maintains a certain level of axial pressure and the motions of the lower punch platens are accurately controlled so as to reduce the detrimental effects of unbalanced punch deflections.

Procedure I: Total axial unloading (no *hold-down* force)

In figure 5.23, we show the computed contour plot of cohesion at the end of the pressure release stage in the case in which the upper punch moves up 0.6 *mm* away from the compact and the lower platens remain fixed. Recall (see chapter 4) that crack locations are identified as those areas affected by a *local decrease of cohesion*. Examination of the contour plot of figure 5.23 clearly reveals two de-cohesion patterns, labelled therein as "crack A" and "crack B", being loss of cohesion especially intense along the former. In the sequel, we concentrate thus on describing the formation and ascertaining the root cause of the horizontal crack A.

A glance at the tooling dimensions shown in figure 5.3 indicates that the lower inner punch LIP is larger, by a factor of almost ten, than the lower outer punch LOP-II. This fact is reflected in the graphs of vertical displacement of punch work-

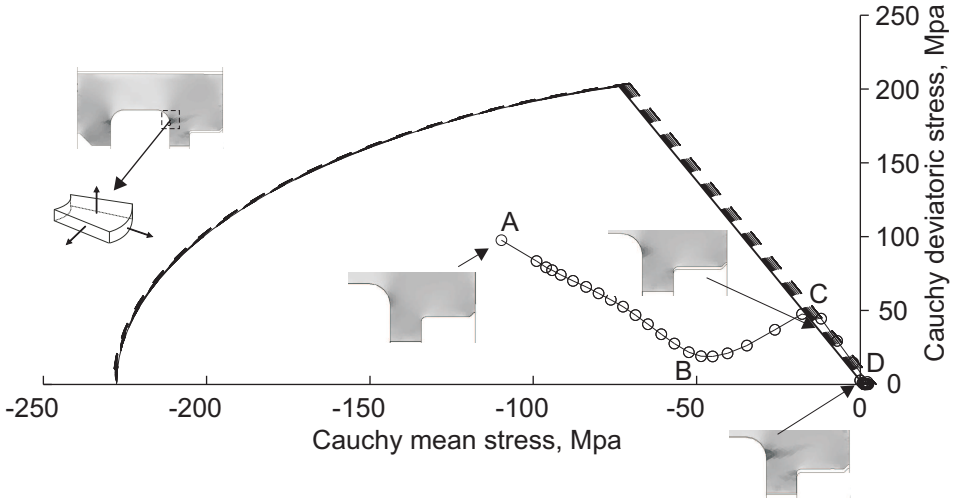

Figure 5.25 *Stress trajectory in the mean-deviatoric plane at a point located in the area affected by the de-cohesion pattern labelled as "Crack A" in figure 5.23.*

.

ing ends versus the angular position contained in figure 5.24.a. The LIP experiences the greatest total deflection - approximately 0.2 *mm* -, in contrast to the almost negligible change in dimensions of the lower outer punch LOP-II. This means that the compact moves with the lower inner punch and, consequently gaps are generated between the working ends of the lower outer punches and the compact, as can be observed in figure 5.23. In this process, the outer flange is partially gripped between the LMP outer wall and the LIP-I inner wall, due to friction effects. The combination of this restraining action and the upward movement of the LIP places in tension the corner region and the crack is therefore induced. The propagation of this crack can be visualized in the sequence of cohesion contours displayed in figure 5.24.b.

In order to corroborate the physical origin of this de-cohesion pattern, the stress history at a point located in the affected area is plotted in the mean-deviatoric stress plane (see figure 5.25). The stress state at the beginning of axial unloading is located at point A. As axial unloading progresses, it moves toward the tensile region (first quadrant) following the path ABC (elastic regime). At point C, however, it encounters the Drucker-Prager failure line, which represents the limited ability of the green compact to resist tensile stresses. Continued strain (of tensile nature), provoked by the aforementioned uneven tooling deflection, induces continued plastic yielding and thus a local decrease of cohesion (*strain softening*), causing the stress state to travel along the failure line towards the origin (point D). No anomalous oscillations, due for instance to an unsatisfactory reproduction of the tool-powder contact behavior, are observed. This indicates that numerical flaws do not pollute the response, and, therefore, the de-cohesion pattern can be ascribed definitely to the aforementioned mechanical cause.

Procedure II: Balanced deflection of lower punches (with *hold-down* force)

The foregoing scenario represents working conditions quite similar to that encountered in press machines whose upper rams are actuated exclusively by mechanical drives. One of the major disadvantages of those presses is the sudden release of force occurring after the rotating drive member reaches the bottom dead center ($\varphi = 180°$). However, we mentioned earlier that the analyzed part was manufactured in a press machine in which, during the post-pressing operations, the upper punch is operated by a separate hydraulically drive system. This mechanism allows to apply a certain downward pressure during withdrawal of the die, the so-called *hold down* or *counter- pressure*. In the numerical simulation presented in the following, the upper punch is gradually lifted until the axial force on the upper punch is set to 10 Tons. The CNC press machines also offers the possibility of accu-

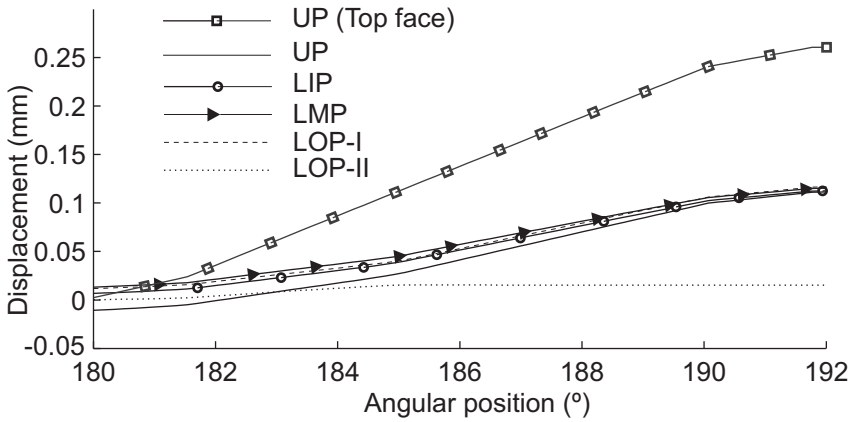

Figure 5.26 *Balanced deflection of lower punches case (hold-down force). Displacement of the working ends of lower punches, as well as the displacement of the top face of the upper punch, as a function of the angular position.*

.

rately controlling the position of the lower rams. In order to compensate for the unbalanced punch deflections, the lower inner punch LIP, which is the largest one, descends 0.05 mm, whereas the lower outer punch LOP-I moves 0.04 mm upward. The LMP and die platens are kept fixed. Figure 5.26 displays the computed vertical displacement, as a function of the angular position, of the punch working ends together with the displacement of the top face of the upper punch. According to the graph corresponding to the UP top face, the imposed reduction in axial force requires to move the upper punch 0.25 mm upward. The displacement curves corresponding to the working ends of the UP, LIP, and LMP-I meet at the end of the pressure release stage, a fact that indicates that the motions prescribed at the bottom of the LIP and LMP-I have proved efficient in compensating for the differences in elastic deflection between punches. The relative uniformity exhibited by the cohesion distribution computed at the end of pressure release stage, displayed

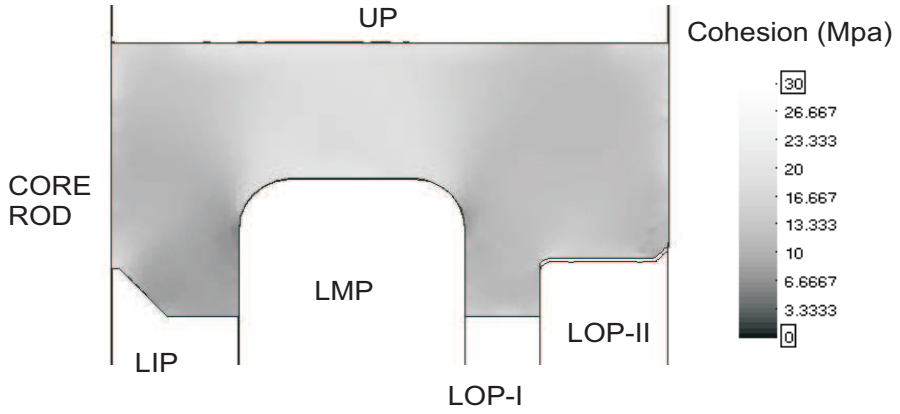

Figure 5.27 *Contour plot of cohesion at the end of pressure release stage. Balanced deflection of lower punches case.*

.

in figure 5.27, confirms also this efficiency since, in contrast to the contour plot computed in the previous situation of uncontrolled punch deflection (figure 5.23), *no appreciable evidences of loss of cohesion are detected.*

5.4.0.2 Withdrawal of the die

Using as starting point the results obtained at the end of the pressure release stage, we tackle now the analysis of the die withdrawal phase. Three different ejection procedures are numerically tested. In these three alternatives, the compact is held between the upper punch and the two lower punches forming the lowest faces of the compact (LIP and LOP-I), which act, thus, as supporting punches as the die is withdrawn.

Option a: Held stationary the LMP and the core rod.

We shall explore first the consequences of keeping fixed the lower middle punch and the core rod as the die is lowered. The tooling motion profile corresponding to this situation is depicted in figure 5.28. This diagram is accompanied by a sequence of three contour plots of cohesion computed at different times during the process. In the rightmost plot, which is shown also - in magnified form - in figure 5.29.a, a horizontal de-cohesion path stemming from the outer wall is observed. This de-cohesion pattern certainly exhibits a distinctly crack-like appearance. However, the factor or factors that provoke its development are not readily apparent. In order to identify these factors, and eventually clarify the physical origin, if any, of this localized loss of cohesion, we shall propose two alternative, physically plausible hypothesis.

The first hypothesis considers that the computed crack is due to the effects of *elastic strain release in the radial direction.* The observed mechanical degradation arises when the top face of the die is approximately flush with the top face of the

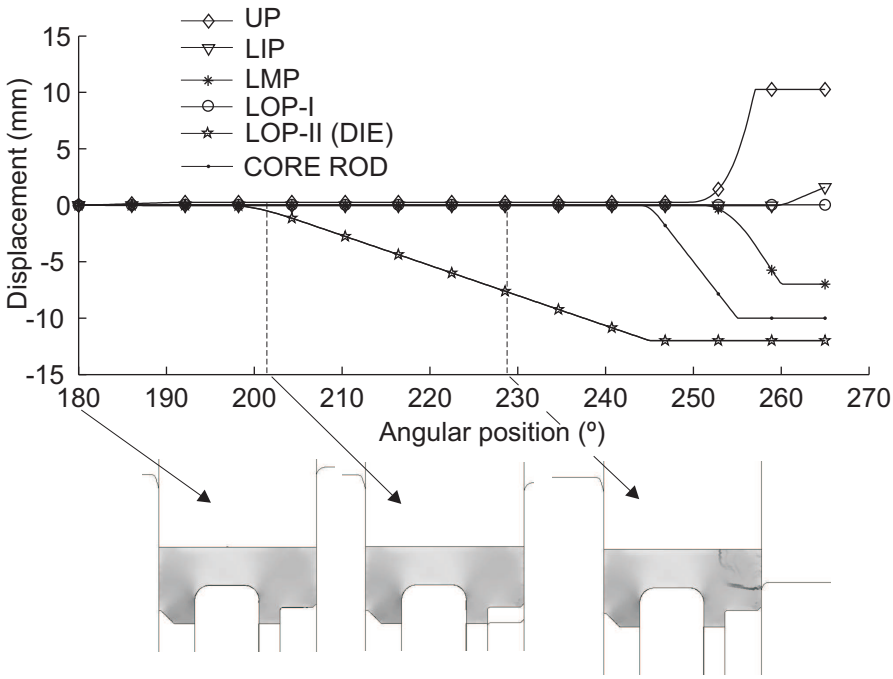

Figure 5.28 *Prescribed punch displacements as a function of the angular position, together with a sequence of contour plots of computed cohesion. Case in which the LMP and the core rod are held stationary.*

.

lower middle punch, that is, when the main body of the part is clear of the die. The radial expansion of the main body coupled with the radial force exerted on the portion of outer surface still restrained by the die tends to *shear* the compact along the radial direction, as pictorially depicted in figure 5.29.b. Accordingly, this presumably *shear-mode* (or *mode-II*) crack can be eliminated by reducing the level of radial stress when withdrawing the die. One possibility to carry out this reduction is, as recommended by Zenger et al. [112], to decrease the degree of confinement of the part by withdrawing the lower middle punch and the core rod. Another possibility to reduce the effects of radial expansion would be to diminish the hold down pressure exerted by the upper punch. However, this practice may conflict with the requirements for avoiding the crack promoting effect, described previously, of uncontrolled punch deflections.

The other hypothesis advocates that the root cause of the numerically predicted crack is the "stepped" character of the die. As already mentioned, the lower outer punch LOP-II is mounted on the die platen. Thus, as the die descends to free the part, the LOP-II inevitably moves down away from the compact. This separation leaves the external portion of the compact vertically unsupported and, consequently, frictional downward forces between the die and the compact may tend

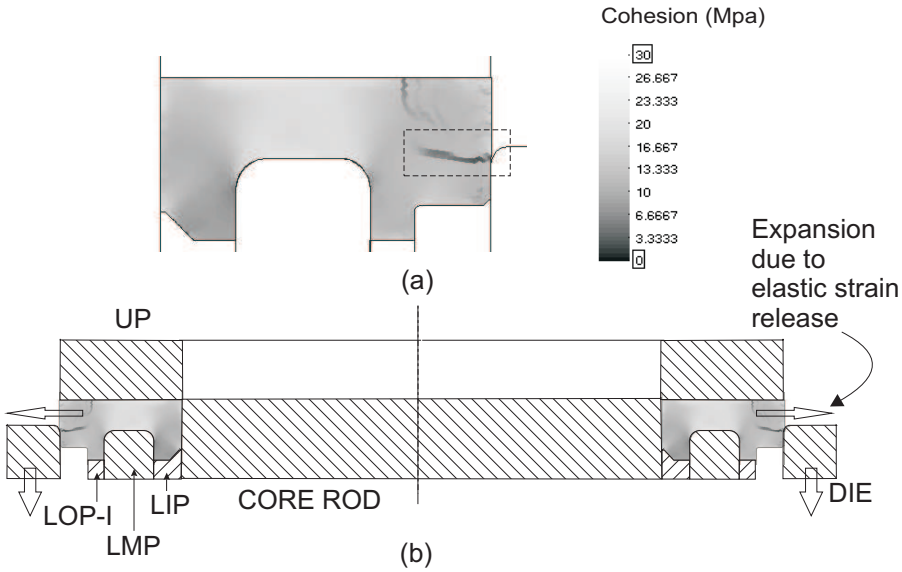

Figure 5.29 *(a) Contour plot of computed cohesion at $\phi = 203°$ for the case in which the LMP and the core rod are held stationary. (b) Schematic representation of the effect of elastic strain release.*

.

to *pull apart* the main body and the bottom section. According to this hypothesis, thus, the horizontal crack develops predominantly under *opening or mode-I loading conditions*. In turn, the bending deformation caused by these frictional forces would also explain consistently the formation of the other discernable de-cohesion path (see figure 5.29.a), located at the top face of the part.

In order to ascertain which hypothesis is more consistent, we shall carry out two additional finite element analysis of the die withdrawal stage. In the first one, the lower middle punch and the core rod accompany the die in its downward motion so as to release some elastic radial strain. In the second one, the lower inner punch is kept fixed so that it can support the part while the die descends.

Option b: Withdrawing the core rod and the LPM simultaneously

The tooling displacement diagram, together with a sequence of three contour plots of cohesion, corresponding to this case are shown in figure 5.30. For ease of visualization, an enlarged view of the contour plot at $\varphi = 230°$ is displayed in figure 5.31.a. Details of crack propagation through the mesh employed in the calculations can be appreciated in figure 5.31.b. A qualitative comparison of the contour plot in figure 5.31.a with that contained in figure 5.29 leads immediately to the conclusion that withdrawing the lower middle punch and the core rod has not proved effective in eliminating the observed cracks. Both contour plots exhibits the same de-cohesion patterns, being the only discernable effect a slight decrease

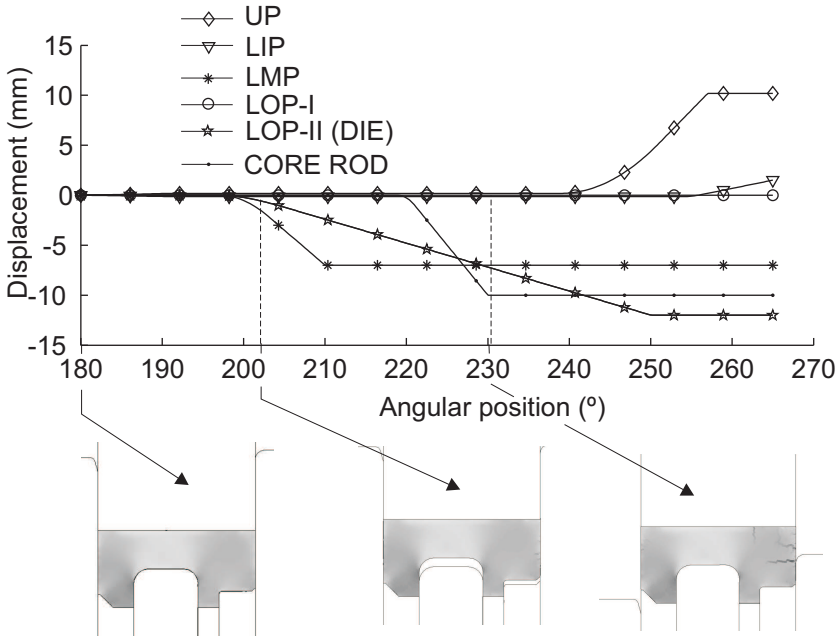

Figure 5.30 *Prescribed punch displacements as a function of the angular position, together with a sequence of contour plots of computed cohesion. Case in which the LMP and the core rod are withdrawn simultaneously with the die.*

.

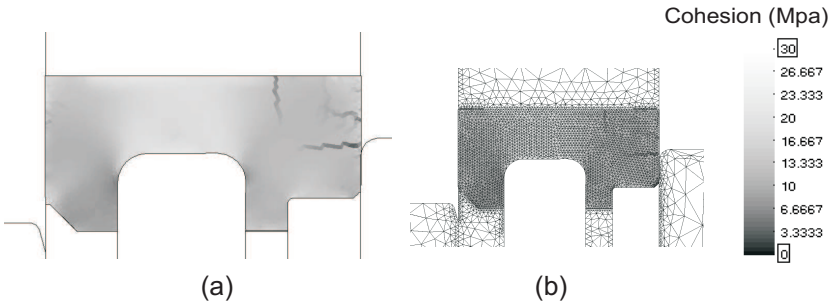

Figure 5.31 *(a) Contour plot of computed cohesion at $\phi = 230°$. Case in which the LMP and the core rod are withdrawn simultaneously with the die. for the kinematics shown in figure 5.28, for $\phi = 230°$. (b) The same contour plot showing the mesh used in the computations.*

in the intensity of the degradation along these paths.

Option c: Holding stationary the LOP-II.

The modeling of this scenario requires to consider a tooling arrangement different from the one described in section 5.2. Rather than attached to the die platen,

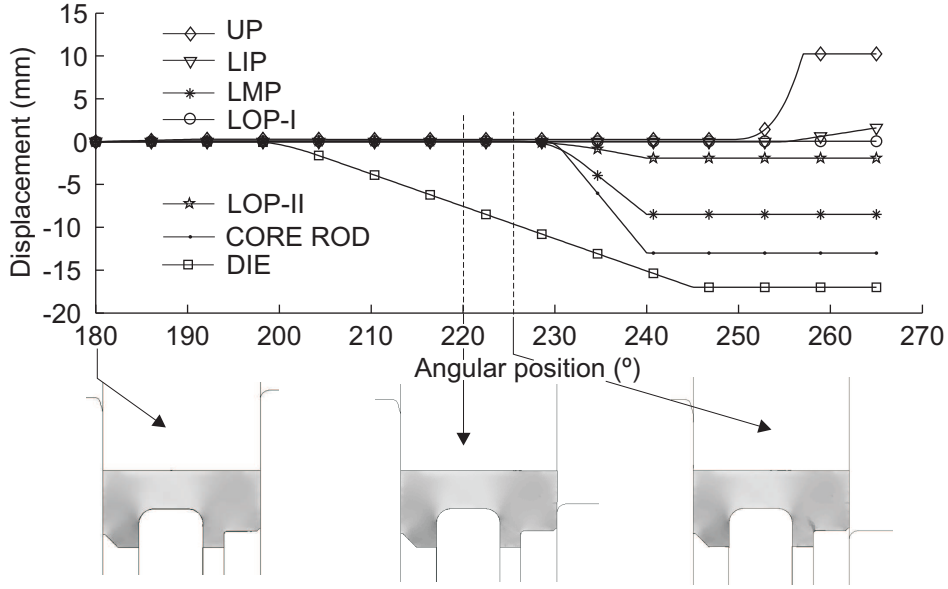

Figure 5.32 *Prescribed punch displacements as a function of the angular position, together with a sequence of contour plots of computed cohesion. Case in which the LOP-II moves independently from the die.*

the LOP-II is assumed to be mounted on an independent platen so that it can support the compact during the downward motion of the die platen. Consequently, in this ejection schedule the part is fully supported by the four lower punches, as indicated in the diagram of tooling displacements shown in figure 5.32. Below this diagram we show the cohesion distribution at three different times during the die withdrawal. The central plot depicts a situation in which the top face of the die is practically flush with the working end of the LMP, which is the relative position of die and LMP at which the de-cohesion patterns reported in the preceding simulations were detected. In this case, by contrast, the cohesion distribution exhibits a relatively uniform aspect and no evidence of intense loss of cohesion is observed. This fact clearly substantiates the second hypothesis advanced previously. Thus, we can conclude from the numerical simulations carried out that the *root cause of the numerically predicted cracks* (shown in figure 5.29.a) lies in the "stepped" character of the die.

Incidentally, examination of the rightmost contour plot in figure 5.32 (displayed in magnified form in figure 5.33.a) shows a vertical, slightly leaned inwards, de-cohesion path that develops at the junction between the levels formed by the LOP-I and the LOP-II. Although the primary goal in studying this ejection schedule was to merely confront the hypothesis advanced at the onset of the discussion, rather than rigorously investigate the defects formed in producing the part using this

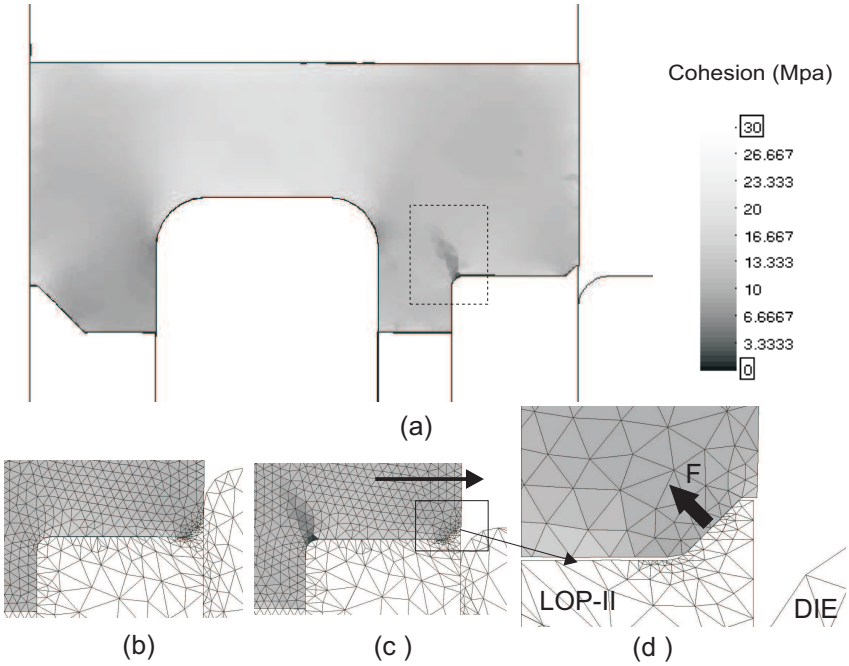

Figure 5.33 *(a) Contour plot of computed cohesion at $\varphi = 226^{\circ}$. Case in which the LOP-II moves independently from the die. (b) (c) Enlarged views of the zone at which the crack is formed (d) Schematic representation of the force generated on the protruding rim due to radial expansion.*

tooling arrangement[13], it may prove instructive to, at least superficially, inquire about the root cause of this de-cohesion pattern.

A plausible explanation for this localized loss of cohesion may lie in the particular geometry of the LOP-II. Inspection of the plots in figures 5.33.b and 5.33.c indicates that loss of cohesion in the corner region occurs right after the compact is totally freed from the radial restraint imposed by the die. The top surface of the LOP-II is not completely horizontal, but it has a vertical protruding feature (0.2 mm height, see figure 5.1) at the outer edge. As the compact emerges from the die, it tends to expand radially due to elastic strain release. The radial expansion of the lower portion of the part, however, is hindered to some extent by the protruding feature. This restriction generates a lifting force (see figure 5.33.d), that, considering that the leg section is restrained by the radial action of the LOP-II and the LMP, induces bending of the part. The computed de-cohesion path might be ascribed thus to the effects of such bending deformation.

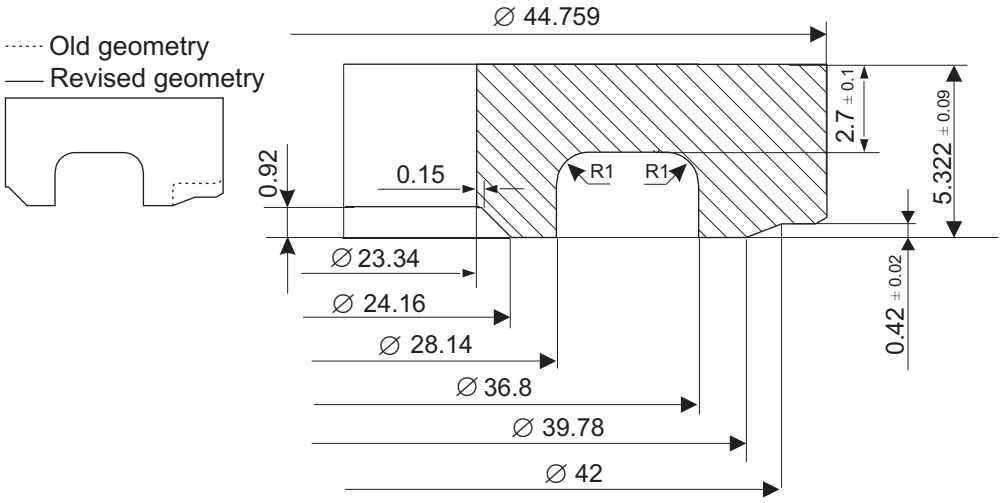

Figure 5.34 *Revised geometry (dimensions in mm).*

5.4.1 Revised design

Figure 5.34 shows the *revised design* of the part. The only modification with respect to the original design is that the difference in length between the levels previously formed by the LOP-I and LOP-II has been diminished considerably. Furthermore, a tapered surface has eliminated the abruptness of the cross-sectional change. The main implication of this geometry modification is that it dispenses with the need for two separate lower outer punches. Accordingly, the two thin-walled lower outer punches LOP-I and LOP-II employed in shaping the part in its original conception are replaced by a single, more massive, *lower outer punch*, abbreviated LOP, with a tapered top surface. Observe that this modification is totally consistent with the hypothesis put forward in the previous section for explaining the difficulties in producing a free-defect part using the "stepped die" tooling configuration.

	UP	LIP	LMP	LOP	DIE	CORE ROD
f	1	0.043	0.234	0.019	0.173	0.233

Table 5.10 *Motion scale factors used for pressing the modified part.*

The pressing kinematics is defined by the motion scale factors tabulated in table 5.10. The determination of the starting conditions and the analysis of the pressing stage proceed along the same lines described in section 5.3.1. We bypass thus such details and concentrate exclusively on presenting the computed results corresponding to the ejection stage.

[13]In practice, this tooling arrangement with an independently movable LOP-II was not tested due to equipment limitations.

Procedure I: Total axial unloading (no *hold-down* force)

In order to evaluate again the ability of the model in reproducing the typology of cracks arising in situations of unbalanced punch deflections, we consider first a case in which the upper punch moves up away from the compact and the lower platens remain fixed. In figure 5.36, the graphs of the computed displacement of punch working ends versus the angular position are displayed. Below this diagram, we show a sequence of contour plots of computed cohesion. A horizontal de-cohesion path emanating from the junction corner and propagating outwards through the section change is easily detected in these plots.

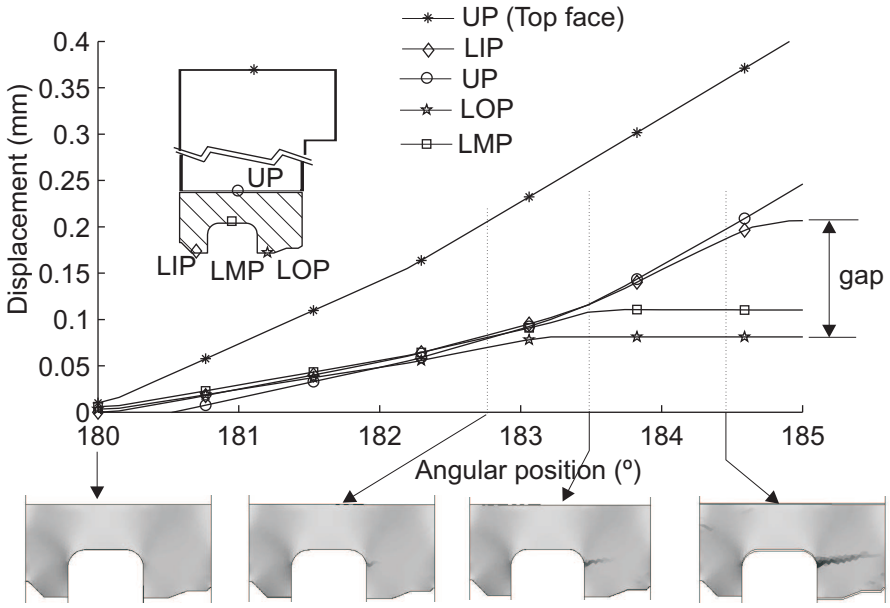

Figure 5.35 *Total axial unloading case (modified part). (a) Displacement of the working ends of lower and upper punches, together with the displacement of the top face of the upper punch, as a function of the angular position. (b) Sequence of contour plots of cohesion.*

.

The reasoning behind this localized mechanical degradation is essentially the same outlined in section 5.4.0.1 for explaining the formation of the de-cohesion pattern labelled as "Crack A" (see figure 5.23). In this case, however, cracking is markedly more intense that in the one shown previously in figure 5.23. At the end of the pressure release stage (see figure 5.36), the computed de-cohesion path spans the whole section, a fact that suggests that fracture is imminent. This can be readily explained from the punch displacement diagram displayed in figure 5.36. The difference between the deflections experienced by the lower inner punch and the lower outer punch in compressing the modified part is more pronounced that in the original part case (see figure 5.24, curves LIP, LOP-I), due to the greater cross-

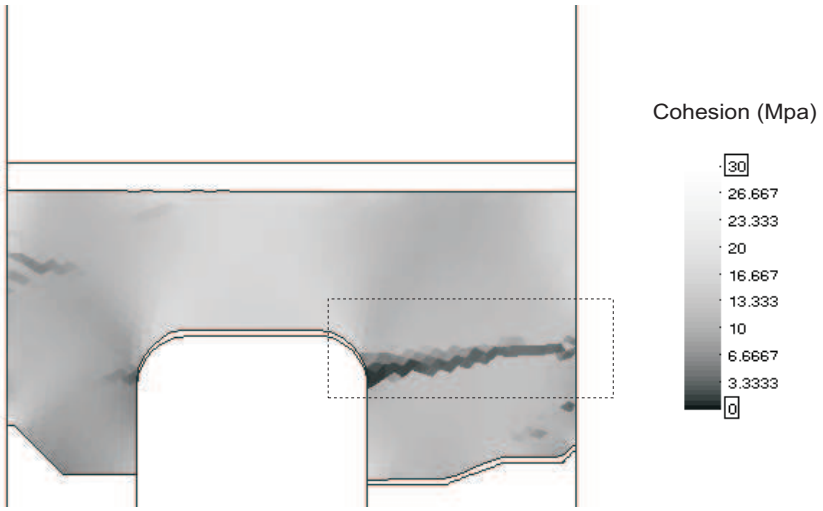

Figure 5.36 *Contour plot of cohesion at the end of pressure release stage. Total axial unloading case (modified part)*

.

sectional area of the LOP in comparison to the LOP-I. *Bending deformation is therefore accentuated, and this results, in turn, in an intensification of the cracking process.*

Procedure II: Balanced deflection of lower punches (with hold-down force)

We carry out now the finite element analysis of a pressure release stage in which the lower outer punch and the lower middle punch are programmed to move upward 0.08 mm and 0.06 mm while maintaining a hold down force of 10 Tons. Figure 5.37 shows the evolution of the computed displacement of the punch working ends. The curves corresponding to the lower punches gradually approach each other, eventually meeting at $\varphi = 192°$. This indicates that gaps between the lower punch ends and the compact have been eliminated. In addition, examination of the contour plot of cohesion displayed in figure 5.38 shows that the programmed punch strokes *have also proved effective in totally mitigating the crack reported when studying the unbalanced deflection case* (figure 5.36).

The conditions computed at the end of the above presented pressure release stage are used as starting conditions for simulating the rest of the ejection process. The tooling motions according to which the part was finally manufactured are displayed in figure 5.39. First the die is lowered so as to free the part. The downward motion of the die is followed by the withdrawal of the core rod and the lower middle punch. Finally, the upper punch moves up away from the compact and the lower inner punch is slightly lifted so as to ready the part for being removed by the gripper. The cohesion distribution computed at four different positions are

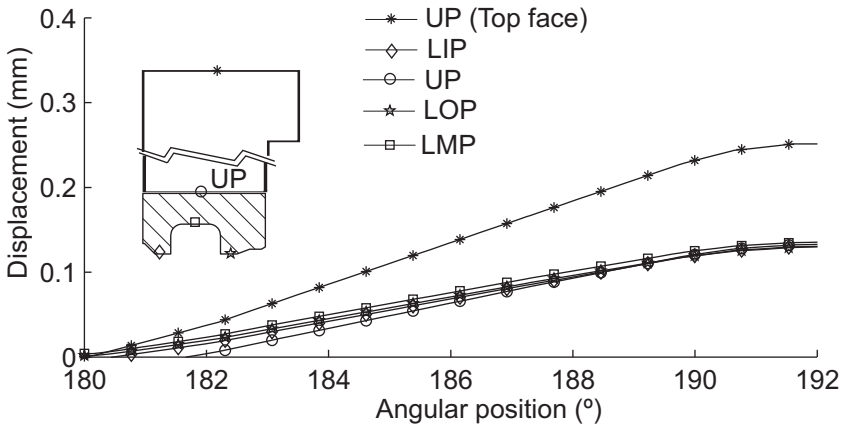

Figure 5.37 *Balanced deflection of lower punches case (modified part). (a) Displacement of the working ends of lower and upper punches, together with the displacement of the top face of the upper punch, as a function of the angular position.*

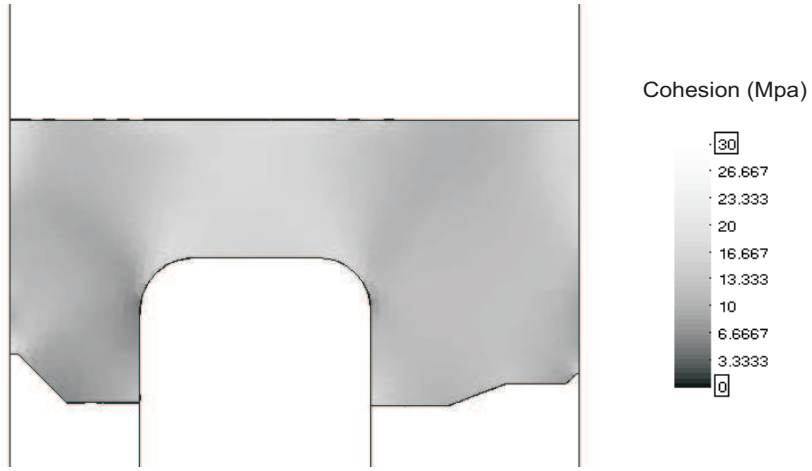

Figure 5.38 *Contour plot of cohesion at the end of pressure release stage. Balanced deflection of lower punches case (modified part).*

shown also in figure 5.39. It is apparent that the cohesion field remains unaffected during the ejection process. *The model predictions, therefore, are in accordance with experimental evidence and confirm the benefits of manufacturing the part according to the revised design.*

5.5 Conclusions

This chapter was devoted to discuss several aspects concerning the numerical simulation of the compaction of an axisymmetric multilevel part in an advanced CNC

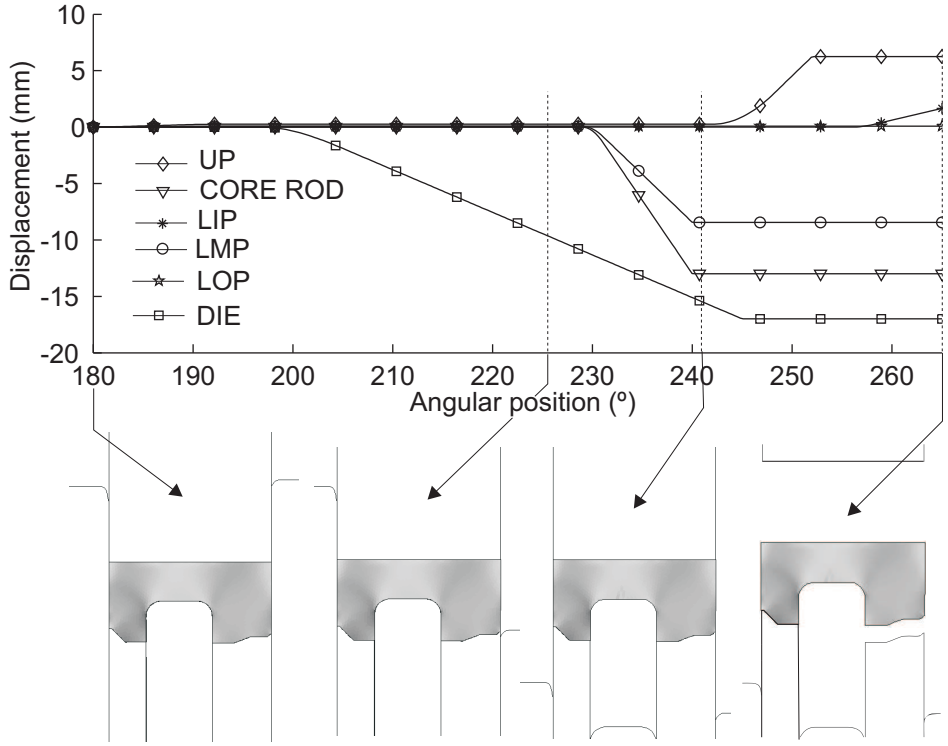

Figure 5.39 *Prescribed punch displacements as a function of the angular position, together with a sequence of contour plots of computed cohesion (modified part).*

press machine. Emphasis on the first part of the chapter was placed on conveying the relevance of an *accurate characterization of the tooling set and the external actions* acting on it if one whishes to obtain a satisfactory computed response. It was shown that numerical predictions of density distributions using, as prescribed conditions on tools, *theoretical* or *nominal* motions can result in substantial disagreement with experimental measurements. It is therefore essential to possess a proper knowledge on the CNC press performance so as to be aware of potential sources of deviations from nominal tooling motions. Unawareness of such factors may promote the tendency of rationalizing discrepancies as being due to flaws either in the constitutive model or in the algorithmic procedure used to compute the response and, thus, one would be tempted in this case to either refine the constitutive equation or to increase the accuracy of the approximation so as to bring numerical predictions into agreement with experimental values. But one does not increase the strength of a chain by improving the strong links. Further refinements of these aspects of the model would be in vain, and rather than embarking on these mathematically and computationally challenging research efforts, one should concentrate task of revising the available input data and the characterization of the tool set.

An aspect that has also received special consideration is that of the optimization of the pressing sequence. It was shown that the problem can be posed mathematically as a nonlinear constrained optimization problem. It was argued that the solution of this problem can be approximated by the solution of a similar problem defined in terms of density predictions provided by an elementary "column model". The validity of this statement was assessed by a finite element simulation, which finally corroborated the optimum character of the pressing route calculated on the basis of the elementary column model. As explained, in instances in which friction effects play a dominant role in determining density gradients, this column model-based procedure may fail in determining a pressing sequence close to the "ideal" tooling motion. Therefore, caution is required in extending this methodology to the design of parts of considerable height.

To date, the modeling of the pressing stage and the densification phenomenon have been the focus of the vast majority of research efforts in the field. Both the abovementioned assessment of the impact of accurately representing the tool set and the external actions and the determination of optimum tooling motion were carried out in terms of density values attained at the end of the pressing stage, and hence, they are essentially further contributions to this research aspect. By contrast, the analysis of the *formation of cracks during the ejection stage* lies outside the scope of conventional finite elements studies of the compaction process, and can be considered thereby as an original and innovative part of this chapter.

Observations made in this study are in qualitative agreement with experimental evidences. The absence of easily discernable de-cohesion patterns in the cohesion distribution computed at the end of the ejection phase - in the modified part case, see figure 5.39-, provides convincing proof of the consistency of the computed results. Numerical simulation of several ejection routes have illustrated the difficulties encountered in manufacturing the part according to the original design. Scrutiny of the computed cohesion distributions resulting from such simulations have allowed us to give physically plausible reasons for explaining such difficulties.

The overall impression gained is that the judicious interpretation of cohesion distributions predicted by the model can provide satisfactory answers to practical questions related to the design of an adequate ejection route. However, this is not intended to suggest that the model can predict *with certainty*, in any circumstances, the formation and development of cracks. In principle, the numerical simulation of a given ejection route attempts to answer the question: will this ejection route lead to a free-defect part ? But such a question demands a categorical *yes or no* answer; there is no flexibility and the risk of arriving at wrong conclusions is thus high. Except in some *pathological* cases, such as the uncontrolled punch deflections (see figures 5.23 and 5.36), we should theferore refrain from drawing definite conclusions from a single simulation. A more fruitful strategy consists in running several analysis for different *alternative* ejection procedures, and limiting ourserlves to answer the question: which of these ejection procedures represents more favorable conditions for ejecting the part safely from the die? The case study presented in this chapter has demonstrated that this question can be consistently answered by our approach.

The advantages of employing FE simulations of the ejection process becomes especially apparent when alternative tooling arrangements are to be tested. Design and manufacturing of the new tooling, together with the changeover of the die set, are time-consuming and costly tasks. Prior to undertaking these operations, several FEM analysis can be performed to evaluate the feasibility of the operation.

The capacity to predict crack formation and its implication at the design stage are not the only issues to be considered when using the numerical model. Normally, the definite sequence of ejection is achieved by trial-and-error procedures guided by the operator's intuitive experience. This means the that the "how" is finally in hands of the operator. But intuition is difficult to characterize if the "how" is achieved without a mechanically grounded understanding of the "why". Numerical simulations can serve the useful purpose of clarifying the reason behind the appropriateness of the ejection route empirically found, so as to establish practical recommendations that will facilitate the ejection of similar parts. Last but not least, numerical FEM simulations have the added benefit of illustrating the process by attractive graphics. The visualization of cracks as de-cohesion patterns is particularly appealing, since it does not require a profound knowledge on the mathematical basis of the model. Computed displaced shape displayed in conjunction with contour plots of cohesion may be of considerable assistance in both fueling the interest of uninitiated practitioners and stimulating the intuition of experienced PM technologists.

Chapter 6

Concluding remarks

The primary goal of this work was to explore the possibilities of numerically simulating crack formation during the post-pressing stages in uniaxial die compaction processes. A phenomenological approach was adopted to mathematically represent the behavior of our *target system*, which comprises both the powder contained in the die cavity and the tooling employed to consolidate the powder into the final shape. Research effort has been focused on constructing a large strain elasto-plastic constitutive model able to describe, in an unified manner, both the densification of the powder under compressive stress states and the formation of cracks during the post-pressing operations. The innovative part of our modeling is mainly connected with the characterization of the latter phenomenological aspect, i.e: cracking.

6.1 On the general features of the proposed constitutive model

For the purpose of modeling the material behavior in stress space, the elastic domain is bounded by three surfaces intersecting non-smoothly, namely, an elliptical cap -associated with hardening behavior-, and two classical Von Mises and Drucker-Prager yield surfaces. The truly original feature of the formulation is the use of a *parabolic plastic potential function* to describe the plastic flow on the Drucker-Prager failure surface. The introduction of this non-classical plastic potential function has proved successful in reproducing the experimentally observed plastic isochoric behavior in the shear regime, while avoiding the acclaimed numerical shortcomings appearing when jointly using traditional pure isochoric flow rules and implicit integration procedures. However, the constitutive implications of the practically pure dilatational deformation occurring when the updated stress state lies close to the vertex of the Drucker-Prager has not been fully explored. To further improve the confidence in the proposed constitutive model, this aspect should be subjected to close scrutiny in future developments.

6.1.1 The fracture modeling

A classical strain localization approach has been adopted for modeling the cracking phenomenon. Incorporation of a *softening law* - relating cohesion and accumulated plastic shear strain - permits the representation of macroscopic cracks as high gradients of inelastic strains concentrated along bands of finite thickness. In turn, a novel, thermodynamically consistent calibration procedure has been used to relate material parameters involved in this softening law to fracture energy values obtained experimentally on Distaloy AE specimens. The convergence studies carried out in dealing with the Brazilian test case indicates that the proposed regularization of the softening law, although not very elaborated, seems to alleviate the problem of lack of convergence upon refinement of the finite element mesh. The other main factor that rendered the choice of a classical strain localization approach objectionable is the mesh-induced directional bias of the computed cracks - the propagating localization band tends to follow certain preferred directions dictated by the mesh. However, it was argued that this criticism is blunted if viewed in the light of the aim and purpose of our investigation. Our primary concern was to capture any evidence of macroscopic cracking, but without a compelling necessity of giving an accurate and detailed description of the crack growth conditions. In this respect, results presented in chapters 4 and 5 have certainly demonstrated the ability of the model in revealing evidence of macroscopic defects and in qualitatively evaluating the influence, in the formation of cracks, of variations in the input data (material parameters, tooling kinematics, etc). A more realistic representation of the physical discontinuity would require to abandon this elementary approach in favor of one the various sophisticated - viz. more complex -, material failure modeling techniques that have, in recent years, successfully superseded the smeared crack approach in other fields of solid mechanics. Such refinements will be fruitless, however, unless other more elementary aspects of the model, equally relevant to the accuracy of the predictions, are also improved. Accordingly, moving to more sophisticated approaches for representing the cracking process is not regarded as a priority, at least in the short term.

6.1.2 The thermodynamic framework

Although certainly not an original contribution of this work, the mathematical form of the constitutive relationships describing the other phenomenological aspects - elastic and hardening behavior - has been derived with the same rigor and care as the softening law. In fact, one of the distinguishing features of this work is that the formulation of the constitutive model is entirely cast within a rational *thermodynamic framework*. The foremost motivation in such a thermodynamic soundness was to originate our considerations from the most general standpoint possible, with a view towards future extensions of the model. For example, the paucity of experimental results concerning fracture energy compelled us to make some restrictive assumptions and eventually consider only one internal variable for capturing the softening behavior of the green compact. One internal variable may appear too simplistic for accounting for the effects of the whole range of micromechani-

cal events occurring at the damage zone. Consequently, flaws in these restrictive assumptions may be uncovered as more experimental data become available, and this may dictate the eventual incorporation of additional internal variables. The thermodynamically consistent structure of the constitutive equation will facilitate considerably the seamless accommodation in the model of these new variables.

Another motivation was to ensure the satisfaction of the second law of the thermodynamics, an aspect often disregarded by many researchers in the field. Compatibility with the second law does not imply that the response predicted by our model is in closer agreement with experimental observations than responses computed using other models not embedded in a thermodynamic framework, but rather provides the confidence that thermodynamically unreasonable results -"negative dissipation" - are not produced in loading situations different from that used for calibrating the model. The demonstration of the consistency of the proposed constitutive model with the second law of thermodynamics, carried out in appendix C, can be considered also as an original contribution of this work.

6.2 On the integration of the constitutive equation

Due to the presence of strain softening and the non-linear, tightly coupled character of the governing equations, standard procedures turned out to be inadequate for carrying out the (implicit) numerical integration of the constitutive equation, and we were thus compelled to develop an alternative, apparently novel, method for dealing with this problem. The proposed *local* integration procedure has the intuitive flavor of a *fractional step method* (FSM), since it is based on the *decoupling* of the evolution equations for the the plastic strains and the internal variables. The algorithmic structure underlying this methodology has been discussed in a thorough manner, placing special emphasis on the issues of convergence and existence of solution. In particular, it has been shown that the solution of the return-mapping algorithm has an unique solution for any conceivable stress state trial. Another remarkable feature is that plastic consistency is restored in a maximum of three iterations of the FSM predictor-corrector scheme, except when the trial stress is projected onto the Drucker-Prager yield surface. In this case, nevertheless, it has been rigorously proved that the sequence defined by the predictor-corrector scheme converges *unconditionally* to the solution, with a linear rate of convergence. Concerning the global iteration scheme, the introduction of the IMPLEX (implicit-explicit) integration procedure has proved crucial in avoiding the adverse effects of softening-induced non-positive definite algorithmic elastoplastic moduli, exhibited typically by purely implicit, standard integration schemes. Furthermore, it has become evident that, if used in conjunction with an adequate adaptive time stepping scheme, the IMPLEX procedure offers an efficient solution to the trade-off between robustness and computational time requirements.

6.3 On the robustness of the solution algorithm

Numerical experience indicates that the main cause of convergence difficulties is the inaccurate computation of the powder-tooling contact response. Too large time steps, an inadequate mesh, specially at regions of stress concentration, or the combination of these two factors may imply a poor enforcement of the impenetrability constraint. Small amounts of interpenetration can be tolerated without serious consequences in the compression regime (pressing stage). By contrast, contact inaccuracies are particularly detrimental under tensile stress conditions (ejection stage). The synergistic combination of the effects of innacuracies in computing the contact response and the dilatational deformation associated to stress states lying close to the apex of the Drucker-Prager yield surface induces severe distorsion of the mesh at the boundary of the powder body, with consequent negative impact on the performance of the global algorithm. This fact dictated the choice of the more computationally costly -in comparison with the penalty approach- augmented lagranian strategy for computing the contact response in the simulation of the ejection process.

6.4 On the simulation technology

The numerical simulation of the compaction of an axisymmetric multilevel part in an advanced CNC press machine has enabled us to appreciate the extreme importance of accurately characterizing the geometry of the tool set and the external actions acting on it. Although the assessment of the effect of the innacurate representation of tooling motions was carried out in terms of final density distributions -cracking is not a readily quantifiable phenomenon-, similar considerations apply to the simulation of the formation of cracks during the ejection stage. One should regard, accordingly, the problem from a broader perspective, more in concordance with the systemic conception adopted in this work, and not remain exclusively within the confines of powder constitutive modeling, since discrepancies between observed and calculated responses may be attributable to an inadequate modeling of the tooling sub-system and the environmental actions, rather than in an unsatisfactory representation of the powder behavior.

The multilevel part case-study has served also to exemplify the use of the model as a tool for supporting and guiding - but never supplanting - engineer judgement in a practical problem. It has become apparent that the judicious interpretation of cohesion distributions can considerably assist in understanding the underlying physical mechanisms that control the occurrence of cracks during the ejection process. Useful insight can be squeezed from simple qualitative comparisons of cohesion contours obtained from simulation of alternative ejection routes. The proposed computational model is certainly not perfect, as no engineering analysis is, and it may fail in answering some practical questions. But, as clearly evidenced throughout this work, it can provide satisfactory answers to many others, which is, in our opinion, sufficient justification for its use.

Appendix A

Mathematical aspects of the continuum formulation

A.1 Large strain kinematics

We regard the powder sub-system as a deformable body $\mathcal{B}$ consisting of continuously distributed material occupying, at a reference time t_0, a region Ω_0 of $\mathbb{R}^n$ $(n = 2, 3)$. As is customary, we designate the position vector $\mathbf{X}$, with respect to a fixed origin O, of the particle $X \in \mathcal{B}$ in the *reference configuration* Ω_0 as the label of this particle throughout the deformation process. We assume that the deformation at time t relative to the reference configuration is given by the one-to-one $\mathcal{C}^2$ mapping

$$\boldsymbol{\varphi} : \Omega_0 \to \Omega_t \subset \mathbb{R}^n. \tag{A.1.1}$$

Hence, we can write the position vector, with respect to a fixed origin o, of particle $X \in \mathcal{B}$ in the so-called *current configuration* Ω_t as

$$\mathbf{x} = \boldsymbol{\varphi}\left(\mathbf{X}, t\right). \tag{A.1.2}$$

We introduce a coordinate system in the reference configuration Ω_0, defined by its origin *0* and a set of orthogonal basis vectors $\{\bar{\mathbf{E}}_A\}$ $(A = 1, 2, 3)$, and another coordinate system in the current configuration Ω_t, with its origin in o and orthogonal basis vectors $\{\bar{\mathbf{e}}_a\}$, $(a = 1, 2, 3)$. Thus, it can be written $\mathbf{X} = \mathbf{X}^A \bar{\mathbf{E}}_A$ and $\mathbf{x} = x^a \bar{\mathbf{e}}_a$ [1], where the summation convention for two repeated indices holds.

A line element $\mathbf{dX}$ placed on point $\mathbf{X}$ in Ω_0 transforms into a line element $\mathbf{dx}$ placed on $\mathbf{x}$ in Ω_t according to the linear mapping[2]

$$\mathbf{dx} = \mathbf{F}\left(\mathbf{X}, t\right) \cdot \mathbf{dX}. \tag{A.1.3}$$

[1] Convention index used throughout this appendix follows *Marsden and Hughes* [63]. Upper case letters refer to the reference configuration Ω_0 and lower case for the current configuration Ω_t. Index placement (superindex and subindex) will be discussed later.

[2] More precisely, $\mathbf{F}$ is a linear mapping from the *tangent space* of Ω_0 at $\mathbf{X}$ to the *tangent space* of Ω_t at $\mathbf{x}$, i.e. $\mathbf{F} : T_X(\Omega_0) \to T_x(\Omega_t)$ [73, 63].

The second-order tensor $\mathbf{F}(\mathbf{X},t)$ is called the *deformation gradient* of $\boldsymbol{\varphi}$ [63], and it can be defined, in abstract form, as

$$\mathbf{F}\left(\mathbf{X},t\right)=\frac{\partial\boldsymbol{\varphi}\left(\mathbf{X},t\right)}{\partial\mathbf{X}}, \tag{A.1.4}$$

or through its components along the basis vectors $\{\bar{\mathbf{E}}_A\}$ and $\{\bar{\mathbf{e}}_a\}$ as

$$F_A^a(\mathbf{X},t)=\frac{\partial\varphi^a(\mathbf{X},t)}{\partial X^A}. \tag{A.1.5}$$

Impenetrability of matter, i.e. no two particles can occupy the same place in space at a given time, requires $J=det(\mathbf{F})>0$. The gradient tensor $\mathbf{F}$ is, therefore, a non-singular second-order tensor and hence admits the local *polar decomposition*

$$\mathbf{F}(\mathbf{X})=\mathbf{R}(\mathbf{X})\cdot\mathbf{U}(\mathbf{X})=\mathbf{V}(\mathbf{x})\cdot\mathbf{R}(\mathbf{X}), \tag{A.1.6}$$

where $\mathbf{R}(\mathbf{X})$ is an orthogonal *rotation* tensor and $\mathbf{U}(\mathbf{X})$ and $\mathbf{V}(\mathbf{x})$ are symmetric positive-definite *stretch* tensors. The so-called right Cauchy-Green tensor is defined as

$$\mathbf{C}(\mathbf{X})=\mathbf{F}^T(\boldsymbol{\varphi}\left(\mathbf{X}\right))\cdot\mathbf{F}\left(\mathbf{X}\right)=\left(\mathbf{R}(\mathbf{X})\cdot\mathbf{U}(\mathbf{X})\right)^T\cdot\mathbf{R}(X)\cdot\mathbf{U}(X)=\mathbf{U}^2(X), \tag{A.1.7}$$

or in component form (omitting explicit indication of the argument)

$$C_{AB}=g_{ab}F_A^aF_B^b, \tag{A.1.8}$$

where g_{ab} is the matrix of the metric tensor associated with the inner product in the spatial configuration Ω_t. Since we are using cartesian coordinates system, we have $g_{ab}=\delta_{ab}$, being δ_{ab} the second-order *Kronecker* delta. In fact, the placement of the suffix (superscript or subscript) is irrelevant for the value of tensor components in the setting of a cartesian representation (e.g., $F_A^a=F_{aA}=F^{aA}$). However, in order to distinguish the *covariant* and *contra-variant* character of tensors, we shall attempt to keep the natural position of indices of tensor components. Therefore, Eq.(A.1.8) indicates that the right Cauchy-Green tensor $\mathbf{C}$ with components C_{AB} is a covariant tensor (of rank 2)[3].

We shall employ as material strain measure the *Green-Lagrange* strain tensor, defined in the reference configuration Ω_0 as

$$\mathbf{E}(\mathbf{X})=\frac{1}{2}\left(\mathbf{C}(\mathbf{X})-\mathbf{G}\left(\mathbf{X}\right)\right)\qquad\text{or}\qquad E_{AB}=\frac{1}{2}\left(C_{AB}-G_{AB}\right). \tag{A.1.9}$$

[3]In a general coordinate system, the right Cauchy-Green tensor defined by $\mathbf{C}=\mathbf{F}^T\mathbf{F}$ can be regarded as a linear mapping $\mathbf{C}:T_X(\Omega_0)\rightarrow T_X(\Omega_0)$, with component representation C_B^A. The *associated* tensor [63] of $\mathbf{C}$ is a covariant tensor $\mathbf{C}^\flat:T_X(\Omega_0)\rightarrow T_X^*(\Omega_0)$ ($T_X^*(\Omega_0)$ is the dual space of $T_X(\Omega_0)$) with components $C_{AB}=G_{CA}C_B^C$, G_{CA} being the matrix of the metric tensor in Ω_0. Thus, rigorously speaking, components defined in Eq.(A.1.5) corresponds to $\mathbf{C}^\flat$ rather than to $\mathbf{C}$. We make no such a distinction herein and assume that all strain tensors are *covariant* tensors.

Note that for a local rigid motion $\mathbf{C} = \mathbf{G}$ and therefore an unstrained state corresponds to $\mathbf{E}(\mathbf{X}) = \mathbf{0}$. In analogous manner, the strained state is characterized in the current configuration Ω_t by the so-called Almansi strain tensor

$$\mathbf{e}(\mathbf{x}) = \frac{1}{2}\left(\mathbf{g}(\mathbf{x}) - \mathbf{b}^{-1}(\mathbf{x})\right), \tag{A.1.10}$$

where $\mathbf{b}^{-1}$ is called the *Finger* deformation tensor, whose components are

$$(\mathbf{b}^{-1})_{ab} = \left(\mathbf{F}^{-1}\right)^{A}_{\ a}\left(\mathbf{F}^{-1}\right)^{B}_{\ b} G_{AB}. \tag{A.1.11}$$

Both $\mathbf{e}$ and $\mathbf{b}^{-1}$ are symmetric positive-definite covariant tensor defined in the current configuration Ω_t.

A remark concerning notation is in order here. Recall that $\mathbf{G}$ and $\mathbf{g}$ are the metric tensors in Ω_0 and Ω_t, respectively. Since both possess the same matrix representation in the setting of rectangular cartesian coordinates (the identity matrix), for simplicity in notation we often make $\mathbf{g} = \mathbf{1}$ and $\mathbf{G} = \mathbf{1}$, where $\mathbf{1}$ is the second-order identity tensor. Then, we can write $\mathbf{E} = \frac{1}{2}(\mathbf{C} - \mathbf{1})$ and $\mathbf{e} = \frac{1}{2}(\mathbf{1} - \mathbf{b}^{-1})$, with the understanding that the object $\mathbf{1}$ has different meaning in each case. Likewise, the deformation gradient of a motionless body may be expressed as $\mathbf{F} = \mathbf{1}$, being $\mathbf{1}$ interpreted here as a two-point identity tensor relating Ω_0 and Ω_t. Index notation proves to be useful when ambiguity is to be removed (e.g. $F^a_{\ A} = \delta^a_{\ A}$).

The *push-forward* and *pull-back* transformation induced by $\boldsymbol{\varphi}$, which relate tensorial fields between both configurations [63], are denoted by $\varphi_*(\bullet)$ and $\varphi^*(\bullet)$, respectively. The components of the push-forward of a covariant[4] second-order tensor defined in Ω_0 are given by

$$\left(\varphi_*(\bullet)\right)_{ab} = \left(\mathbf{F}^{-1}\right)^{A}_{\ a}\left(\mathbf{F}^{-1}\right)^{B}_{\ b}(\bullet)_{AB}, \tag{A.1.12}$$

or in direct notation[5]

$$\varphi_*(\bullet) = \mathbf{F}^{-T}\cdot(\bullet)\cdot\mathbf{F}^{-1}, \tag{A.1.13}$$

whereas the components of the pull-back of a covariant second-order tensor defined in Ω_t can be written as

$$\left(\varphi^*(\bullet)\right)_{AB} = F^a_{\ A}F^b_{\ B}(\bullet)_{ab}, \tag{A.1.14}$$

or

$$\varphi^*(\bullet) = \mathbf{F}^{T}\cdot(\bullet)\cdot\mathbf{F}. \tag{A.1.15}$$

Therefore, in view of (A.1.8) and (A.1.11), the right Cauchy-Green tensor $\mathbf{C}$ and the Finger deformation tensor $\mathbf{b}^{-1}$ can be regarded as the pull-back of the metric tensor

[4]The definition of the operators $\varphi_*(\bullet)$ and $\varphi^*(\bullet)$ depends on their arguments. The pull-back, for instance, of a contra-variant tensor in Ω_t is defined as $\left(\varphi^*(\bullet)\right)^{AB} = \left(\mathbf{F}^{-1}\right)^{A}_{\ a}\left(\mathbf{F}^{-1}\right)^{B}_{\ b}(\bullet)^{ab}$. Since covariant indices can only contract with contra-variant indices, it can be established a rule for defining $\varphi_*(\bullet)$ and $\varphi^*(\bullet)$ for tensors of any rank [63]. Roughly speaking, a covariant spatial index, for instance, would *transform* into a covariant material index via $F^a_{\ A}$, i.e. $T_{\cdots a}F^a_{\ A} = T_{\cdots A}$.

[5]Recasting the pull-back and push-forward operations in direct notation is a common practice in solid mechanics literature, and we also adopt it. However, we have to bear in mind that it lacks of any geometric sense (it is a consequence of the over-reliance on the cartesian structure, see Ref. [63]), and only definitions in component form Eq.(A.1.12) and Eq.(A.1.14) are strictly valid.

in Ω_t, $\mathbf{C} = \varphi^*(\mathbf{g})$, and the push-forward of the metric tensor in Ω_0, $\mathbf{b}^{-1} = \varphi_*(\mathbf{G})$, respectively. Furthermore, it can be shown that the Almansi strain tensor is the spatial counterpart of the Green-Lagrange tensor

$$\mathbf{e} = \varphi_*(\mathbf{E}) \qquad \text{or} \qquad e_{ab} = (\varphi_*(\mathbf{E}))_{ab} = \left(\mathbf{F}^{-1}\right)^A_a \left(\mathbf{F}^{-1}\right)^B_b E_{AB}. \tag{A.1.16}$$

The spatial *velocity gradient* $\mathbf{l}$ is a covariant second-order tensor defined by[6]

$$l_{ab} = g_{ac}\frac{\partial v^c}{\partial x^b} = \frac{\partial}{\partial t}\left(\frac{\partial x^c}{\partial X^B}\right)\frac{\partial X^B}{\partial x^b} = g_{ac}\dot{F}^c_B \left(\mathbf{F}^{-1}\right)^B_b, \tag{A.1.17}$$

where v^c denotes the components of the *spatial velocity*, or in abstract notation

$$\mathbf{l}(\mathbf{x}) = \dot{\mathbf{F}}\left(\boldsymbol{\varphi}^{-1}(\mathbf{x}, t)\right)\mathbf{F}^{-1}(\mathbf{x}, t), \tag{A.1.18}$$

being $\dot{\mathbf{F}}$ the derivative of $\mathbf{F}$ with respect to time holding $\mathbf{X}$ fixed. The spatial velocity gradient is not a valid candidate for inclusion in the spatial description of motion due to the requirement of frame-indifference of any constitutive model [9]. Nevertheless, its symmetric part, called the *rate of deformation tensor*

$$\mathbf{d}(\mathbf{x}) = \frac{1}{2}(\mathbf{l}(\mathbf{x}) + \mathbf{l}^T(\mathbf{x})), \tag{A.1.19}$$

does conform with the definition of objective spatial tensor[7].Furthermore, the rate of deformation tensor $\mathbf{d}$ can be interpreted as the *Lie derivative*[8] of the Almansi strain tensor:

$$\mathbf{d} = \mathcal{L}_v\mathbf{e} = \varphi_*\left(\frac{\partial\varphi^*(\mathbf{e})}{\partial t}\right) = \varphi_*\left(\frac{\partial\mathbf{E}}{\partial t}\right). \tag{A.1.20}$$

A.1.0.1 Multiplicative decomposition

The standard local multiplicative decomposition of the deformation gradient into plastic and elastic parts[9] reads

$$\mathbf{F} = \hat{\mathbf{F}}_e \cdot \mathbf{F}_p \qquad \text{or} \qquad F^a_A = (\hat{\mathbf{F}}_e)^a_{\hat{A}}(\mathbf{F}_p)^{\hat{A}}_A. \tag{A.1.21}$$

Although $\hat{\mathbf{F}}_e$ and $\mathbf{F}_p$ cannot be considered as gradients of any deformation mapping, some kinematic relationship can be derived in analogy with the strain measures given in Eq.(A.1.7), Eq.(A.1.9), Eq.(A.1.10) and Eq.(A.1.11). In the reference

[6] Following a frequent abuse of notation $\mathbf{x} = \boldsymbol{\varphi}(X, t) = \mathbf{x}(\mathbf{X}, t)$ and $\mathbf{X} = \boldsymbol{\varphi}^{-1}(\mathbf{x}, t) = \mathbf{X}(\mathbf{x}, t)$.

[7] $\mathbf{d}$ transforms according to $\mathbf{d}^+ = \mathbf{Q}\mathbf{d}\mathbf{Q}^T$ under a superposed rigid body motion, defined by the rotation tensor $\mathbf{Q}$, of the spatial configuration.

[8] Since tensor fields on the reference configuration remain unaltered under spatially superposed rigid body motions, $\mathbf{e}$ is firstly *pulled backward* from the spatial to the reference configuration, yielding $\mathbf{E}$, and then differentiated ($\dot{\mathbf{E}}$) prior to being *pushed forward* to the current configuration [63].

[9] To identify those tensorial fields associated to the intermediate configuration $\hat{\Omega}_t$, we use a *hat* on both the tensorial quantity and the corresponding index

configuration Ω_0, the plastic counterparts of the right Cauchy-Green tensor and the Green-Lagrange tensor are defined as

$$\mathbf{C}_p = \mathbf{F}_p^T \cdot \mathbf{F}_p \qquad \text{or} \qquad (\mathbf{C}_p)_{AB} = (\mathbf{F}_p)^{\hat{A}}_{\ A} (\mathbf{F}_p)^{\hat{B}}_{\ B} \hat{G}_{\hat{A}\hat{B}}, \tag{A.1.22}$$

$$\mathbf{E}_p = \frac{1}{2}(\mathbf{C}_p - \hat{\mathbf{G}}) \qquad \text{or} \qquad (\mathbf{E}_p)_{AB} = \frac{1}{2}\left((\mathbf{C}_p)_{AB} - G_{AB}\right). \tag{A.1.23}$$

where $\hat{G}_{\hat{A}\hat{B}} = \delta_{\hat{A}\hat{B}}$ is the metric defined in $\hat{\Omega}_t$. Similarly, the elastic right Cauchy-Green $\hat{\mathbf{C}}_e$ and Green-Lagrange $\hat{\mathbf{E}}_e$ tensors, and the plastic Finger deformation and Almansi strain tensors, $\hat{\mathbf{b}}_p^{-1}$ and $\hat{\mathbf{e}}_p$, respectively, all of them defined in the intermediate configuration $\hat{\Omega}_t$, are given by

$$\hat{\mathbf{C}}_e = \hat{\mathbf{F}}_e^T \cdot \hat{\mathbf{F}}_e \qquad \text{or} \qquad (\hat{\mathbf{C}}_e)_{\hat{A}\hat{B}} = (\hat{\mathbf{F}}_e)^{a}_{\ \hat{A}} (\hat{\mathbf{F}}_e)^{b}_{\ \hat{B}} g_{ab}, \tag{A.1.24}$$

$$\hat{\mathbf{E}}_e = \frac{1}{2}(\hat{\mathbf{C}}_e - \hat{\mathbf{G}}) \qquad \text{or} \qquad (\hat{\mathbf{E}}_e)_{\hat{A}\hat{B}} = \frac{1}{2}((\hat{\mathbf{C}}_e)_{\hat{A}\hat{B}} - \hat{G}_{\hat{A}\hat{B}}), \tag{A.1.25}$$

$$\hat{\mathbf{b}}_p^{-1} = \hat{\mathbf{F}}_p^{-T} \cdot \hat{\mathbf{F}}_p^{-1} \qquad \text{or} \qquad (\hat{\mathbf{b}}_p^{-1})_{\hat{A}\hat{B}} = (\hat{\mathbf{F}}_p^{-1})^{A}_{\ \hat{A}} (\hat{\mathbf{F}}_p^{-1})^{B}_{\ \hat{B}} G_{AB}, \tag{A.1.26}$$

$$\hat{\mathbf{e}}_p = \frac{1}{2}(\hat{\mathbf{G}} - \hat{\mathbf{b}}_p^{-1}) \qquad \text{or} \qquad (\hat{\mathbf{e}}_p)_{\hat{A}\hat{B}} = \frac{1}{2}(\hat{G}_{\hat{A}\hat{B}} - (\hat{\mathbf{b}}_p^{-1})_{\hat{A}\hat{B}}). \tag{A.1.27}$$

Finally, the spatial elastic finger deformation tensor $\mathbf{b}_e^{-1}$ and the elastic Almansi strain tensor $\mathbf{e}_e$ take the form

$$\mathbf{b}_e^{-1} = \hat{\mathbf{F}}_e^{-T} \cdot \hat{\mathbf{F}}_e^{-1} \qquad \text{or} \qquad (\mathbf{b}_e^{-1})_{ab} = (\hat{\mathbf{F}}_e^{-1})^{\hat{A}}_{\ a} (\hat{\mathbf{F}}_e^{-1})^{\hat{B}}_{\ b} \hat{G}_{\hat{A}\hat{B}}, \tag{A.1.28}$$

$$\mathbf{e}_e = \frac{1}{2}(\mathbf{g} - \mathbf{b}_e^{-1}) \qquad \text{or} \qquad (\mathbf{e}_e)_{ab} = \frac{1}{2}(g_{ab} - (\mathbf{b}_e^{-1})_{ab}). \tag{A.1.29}$$

A valuable relationship may be derived from Eq.(A.1.10), Eq.(A.1.29) and Eq.(A.1.27)

$$\begin{aligned} e_{ab} - (\mathbf{e}_e)_{ab} &= \frac{1}{2}((\mathbf{b}_e^{-1})_{ab} - (\mathbf{b}^{-1})_{ab}) \\ &= \frac{1}{2}(\hat{\mathbf{F}}_e^{-1})^{\hat{A}}_{\ a} (\hat{G}_{\hat{A}\hat{B}} - (\hat{\mathbf{b}}_p^{-1})_{\hat{A}\hat{B}}) (\hat{\mathbf{F}}_e^{-1})^{\hat{B}}_{\ b} \\ &= (\hat{\mathbf{F}}_e^{-1})^{\hat{A}}_{\ a} (\hat{\mathbf{e}}_p)_{\hat{A}\hat{B}} (\hat{\mathbf{F}}_e^{-1})^{\hat{B}}_{\ b}. \end{aligned} \tag{A.1.30}$$

Consider that $\hat{\mathbf{F}}_e$ is expressed as

$$\hat{\mathbf{F}}_e = \hat{\mathbf{I}} + \hat{\mathbf{J}}_e \qquad \text{or} \qquad (\hat{\mathbf{F}}_e)^{a}_{\ \hat{A}} = \delta^{a}_{\ \hat{A}} + (\hat{\mathbf{J}}_e)^{a}_{\ \hat{A}}. \tag{A.1.31}$$

The assumption of infinitesimal elastic strains implies that each component of tensor $\hat{\mathbf{J}}_e$ is small compared with unity $|(\hat{\mathbf{J}}_e)^{a}_{\ \hat{A}} \ll 1|$. Consequently, we neglect terms $\mathcal{O}(\|\hat{\mathbf{J}}_e\|)$ and accept the approximation

$$\hat{\mathbf{F}}_e = \hat{\mathbf{I}} \qquad \text{or} \qquad (\hat{\mathbf{F}}_e)^{a}_{\ \hat{A}} = \delta^{a}_{\ \hat{A}}. \tag{A.1.32}$$

The same holds for $\hat{\mathbf{F}}_e^{-1}$. Expanding $\hat{\mathbf{F}}_e^{-1} = (\hat{\mathbf{I}} + \hat{\mathbf{J}}_e)^{-1}$ in a Taylor's series and neglecting again terms $\mathcal{O}(\|\hat{\mathbf{J}}_e\|)$, we have

$$(\hat{\mathbf{F}}_e^{-1})^{\hat{A}}_{\ a} = \delta^{\hat{A}}_a. \tag{A.1.33}$$

Consequently, all tensorial objects defined in the intermediate configuration are translated into spatial objects by applying identity mappings[10] between both configurations.

By substituting Eq.(A.1.33) in Eq.(A.1.30), we obtain

$$e_{ab} - (\mathbf{e}_e)_{ab} = (\hat{\mathbf{F}}_e^{-1})^{\hat{A}}_{\ a}(\hat{\mathbf{F}}_e^{-1})^{\hat{B}}_{\ b}(\hat{\mathbf{e}}_p)_{\hat{A}\hat{B}} = \delta^{\hat{A}}_a\delta^{\hat{B}}_b(\hat{\mathbf{e}}_p)_{\hat{A}\hat{B}}\ . \tag{A.1.34}$$

The right-hand side term of Eq.(A.1.34) has no explicit references to any elastic measure (it can be constructed only in terms of $\mathbf{F}_p$) and consequently it can be identified as the plastic Almansi strain tensor

$$(\mathbf{e}_p)_{ab} = \delta^{\hat{A}}_a\delta^{\hat{B}}_b(\hat{\mathbf{e}}_p)_{\hat{A}\hat{B}}\ . \tag{A.1.35}$$

By virtue of (A.1.34) and (A.1.35)

$$\mathbf{e}(\mathbf{x}) = \mathbf{e}_e(\mathbf{x}) + \mathbf{e}_p(\mathbf{x}), \tag{A.1.36}$$

i.e. the additive decomposition of the spatial strain tensor into plastic and elastic parts holds under the assumption of infinitesimal elastic strains and arbitrary plastic deformations.

Dually, in the reference configuration Ω_0, the difference between the total Green-Lagrange strain tensor $\mathbf{E}$ and its plastic counterpart $\mathbf{E}_p$ yields

$$\mathbf{E} - \mathbf{E}_p = \varphi^*(\mathbf{e}_e) \qquad \text{or} \qquad E_{AB} - (\mathbf{E}_p)_{AB} = F^a_{\ A}F^b_{\ B}(\mathbf{e}_e)_{ab}, \tag{A.1.37}$$

which shows that $\mathbf{E}-\mathbf{E}_p$ is a material strain tensor induced from the elastic Eulerian tensor $\mathbf{e}_e$ via a pull-back transformation. We shall denote $\mathbf{E}_e = \mathbf{E} - \mathbf{E}_p$, although acknowledging that $\mathbf{E}_e$ is not intrinsically an elastic tensor, as both $\hat{\mathbf{F}}_e$ and $\mathbf{F}_p$ are coupled geometrically in its definition. A useful expression can be also derived from the above relations:

$$\begin{aligned}\mathbf{E} - \mathbf{E}_p = \varphi^*(\mathbf{e}_e) = \varphi^*(\mathbf{e} - \mathbf{e}_p) = \varphi^*(\mathbf{e}) - \varphi^*(\mathbf{e}_p) = \mathbf{E} - \varphi^*(\mathbf{e}_p)\\ \Rightarrow \mathbf{E}_p = \varphi^*(\mathbf{e}_p)\,.\end{aligned} \tag{A.1.38}$$

Rate form expressions of the decoupling of plastic and elastic effects are also of considerable assistance in the formulation of the constitutive model. By inserting Eq.(A.1.21) in Eq.(A.1.17), we get upon rearrangement

[10] The "*hatted*" uppercase indices (in $\hat{\Omega}_t$) and the lower case indices (in Ω_t) of the component tensors are interchangeable. Applying, for instance, the identity tensor whose components are $\delta^{\hat{A}}_a$ is equivalent to transform the covariant intermediate index $\hat{A}$ of the argument into the covariant spatial index a.

$$\mathbf{l} = \mathbf{l}_e + \hat{\mathbf{F}}_e \cdot \hat{\mathbf{l}}_p \cdot \hat{\mathbf{F}}_e^{-1}, \tag{A.1.39}$$

or in components

$$l_{ab} = (\mathbf{l}_e)_{ab} + g_{ac}(\hat{\mathbf{F}}_e)^c_{\hat{A}}(\hat{\mathbf{F}}_e^{-1})^{\hat{B}}_b(\hat{\mathbf{l}}_p)^{\hat{A}}_{\hat{B}}, \tag{A.1.40}$$

where $\mathbf{l}_e$ stands for the spatial elastic velocity gradient, defined, in analogy with Eq.(A.1.17), as

$$(\mathbf{l}_e)_{ab} = g_{ac}(\dot{\hat{\mathbf{F}}}_e)^c_{\hat{A}}(\hat{\mathbf{F}}_e^{-1})^{\hat{A}}_b, \tag{A.1.41}$$

and $\hat{\mathbf{l}}_p$ is the plastic velocity gradient (embedded in the intermediate configuration $\hat{\Omega}_t$)

$$(\hat{\mathbf{l}}_p)^{\hat{A}}_{\hat{B}} = (\dot{\mathbf{F}}_p)^{\hat{A}}_A(\hat{\mathbf{F}}_p^{-1})^A_{\hat{B}}. \tag{A.1.42}$$

Again, assumptions (A.1.32) and (A.1.33) permit the second term of the right-hand side of Eq.(A.1.40) to be expressed solely through terms depending on $\mathbf{F}_p$ and, hence, it can identified as the plastic velocity gradient $\mathbf{l}_p$, whose components are therefore given by

$$(\mathbf{l}_p)_{ab} = g_{ac}\delta^c_{\hat{A}}\delta^{\hat{B}}_b(\hat{\mathbf{l}}_p)^{\hat{A}}_{\hat{B}}. \tag{A.1.43}$$

The preceding definitions implicates that the additive decomposition holds for the velocity gradient tensor, i.e. $\mathbf{l}(\mathbf{x}) = \mathbf{l}_e(\mathbf{x}) + \mathbf{l}_p(\mathbf{x})$ and, obviously also for its symmetric part $\mathbf{d}$

$$\mathbf{d} = \mathbf{d}_e + \mathbf{d}_p. \tag{A.1.44}$$

Furthermore, it can be easily verified that the plastic and elastic parts of the rate of deformation tensor are the Lie derivative of the plastic and elastic Almansi strain tensors, i.e.

$$\mathbf{d}_p = \mathcal{L}_v\mathbf{e}_p \qquad \text{and} \qquad \mathbf{d}_e = \mathcal{L}_v\mathbf{e}_e\ , \tag{A.1.45}$$

respectively.

A.1.1 Structure of the free energy function

The dependence of the free energy function per unit reference volume ψ on the elastic deformation $\hat{\mathbf{F}}_e$ can be specified in different configurations and in different functional forms, provided that they satisfy the restriction placed by objectivity, i.e. ψ must be unaffected by rotations of the deformed configuration Ω_t:

$$\hat{\psi}(\hat{\mathbf{F}}_e, \boldsymbol{\xi}^h, \boldsymbol{\xi}^s) = \hat{\psi}(\mathbf{Q} \cdot \hat{\mathbf{F}}_e, \boldsymbol{\xi}^h, \boldsymbol{\xi}^s), \tag{A.1.46}$$

where $\mathbf{Q}$ is an arbitrary orthogonal tensor. The polar decomposition (A.1.6) for the elastic part of the gradient deformation reads

$$\hat{\mathbf{F}}_e = \hat{\mathbf{R}}_e \cdot \hat{\mathbf{U}}_e. \tag{A.1.47}$$

By taking $\mathbf{Q}^T = \hat{\mathbf{R}}_e$ and upon substitution of Eq.(A.1.47) in Eq.(A.1.46), we get

$$\hat{\psi}(\hat{\mathbf{F}}_e, \boldsymbol{\xi}^h, \boldsymbol{\xi}^s) = \hat{\psi}(\hat{\mathbf{U}}_e, \boldsymbol{\xi}^h, \boldsymbol{\xi}^s), \tag{A.1.48}$$

that is, ψ must depend only on the stretching part of $\hat{\mathbf{F}}_e$. In particular, in view of definition (A.1.25) of the elastic Green-Lagrange tensor, we may write

$$\psi = \hat{\psi}(\hat{\mathbf{E}}_e, \boldsymbol{\xi}^h, \boldsymbol{\xi}^s). \tag{A.1.49}$$

The functional form of ψ is further restricted by the isotropy of the elastic response, which implies a functional form of the type:

$$\psi = \hat{\psi}(I_{\hat{\mathbf{E}}_e}, II_{\hat{\mathbf{E}}_e}, III_{\hat{\mathbf{E}}_e}, \boldsymbol{\xi}^h, \boldsymbol{\xi}^s), \tag{A.1.50}$$

where $I_{\hat{\mathbf{E}}_e}$, $II_{\hat{\mathbf{E}}_e}$ and $III_{\hat{\mathbf{E}}_e}$ are the principal invariants of $\hat{\mathbf{E}}_e$, given by the following expressions:

$$I_{\hat{\mathbf{E}}_e} = \hat{\mathrm{tr}}\, \hat{\mathbf{E}}_e = (\hat{\mathbf{E}}_e)^{\hat{A}\hat{B}}(\hat{\mathbf{E}}_e)_{\hat{A}\hat{B}}, \tag{A.1.51}$$

$$II_{\hat{\mathbf{E}}_e} = \hat{\mathrm{tr}}\, \hat{\mathbf{E}}_e \cdot \hat{\mathbf{E}}_e = (\hat{\mathbf{E}}_e)^{\hat{A}}_{\hat{B}}(\hat{\mathbf{E}}_e)^{\hat{B}}_{\hat{A}}, \tag{A.1.52}$$

$$III_{\hat{\mathbf{E}}_e} = \det(\hat{\mathbf{E}}_e). \tag{A.1.53}$$

In order to revert to a spatial formulation in terms of the elastic strain tensor $\mathbf{e}_e$, we must find expressions $I_{\hat{\mathbf{E}}_e} = f(\mathbf{e}_e)$, and so forth, which, as it may be surmised from definitions (A.1.51), (A.1.52),(A.1.53), and the relationship:

$$(\hat{\mathbf{E}}_e)_{\hat{A}\hat{B}} = (\hat{\mathbf{F}}_e)^a_{\hat{A}}(\mathbf{e}_e)_{ab}(\hat{\mathbf{F}}_e)^b_{\hat{B}}, \tag{A.1.54}$$

is a somewhat cumbersome task in a general context of unrestricted elastic strain magnitude. However, the approximation

$$(\hat{\mathbf{E}}_e)_{\hat{A}\hat{B}} \approx \delta^a_{\hat{A}}\delta^b_{\hat{B}}(\mathbf{e}_e)_{ab} \tag{A.1.55}$$

holds for the small elastic strain regime, as it is inferred following the same reasoning applied in derivation (A.1.35). In the light of this simplification, we may identify the invariants of $\hat{\mathbf{E}}_e$ and $\mathbf{e}_e$, and legitimately express the energy function per unit reference volume as a function of $\mathbf{e}_e$:

$$\psi = \psi(\mathbf{e}_e, \boldsymbol{\xi}^h, \boldsymbol{\xi}^s) = \psi(I_{\mathbf{e}_e}, II_{\mathbf{e}_e}, III_{\mathbf{e}_e}, \boldsymbol{\xi}^h, \boldsymbol{\xi}^s). \tag{A.1.56}$$

Proposition A.1.1. *The rate of change of the free energy function is given by*

$$\dot{\psi} = \frac{\partial \psi}{\partial \boldsymbol{e}_e} : \boldsymbol{d}_e + \frac{\partial \psi}{\partial \xi^h_\alpha}\dot{\xi}^h_\alpha + \frac{\partial \psi}{\partial \xi^s_\beta}\dot{\xi}^s_\beta, \tag{A.1.57}$$

where $\boldsymbol{d}_e$ is the elastic part of the rate of deformation tensor (see Eq.(A.1.45)).

Proof. The internal variables $\xi^h_\alpha,\ \alpha = 1,2\ldots n_{ih}$, and $\xi^s_\beta,\ \beta = 1,2\ldots n_{is}$ are scalar values and, hence, they can be differentiated with respect to time directly. The time derivative of ψ, holding $\boldsymbol{\xi}^h$ and $\boldsymbol{\xi}^s$ fixed, requires further manipulation. Using the chain rule and the identity (A.1.45), we get

$$\begin{aligned}\left.\frac{\partial\psi}{\partial t}\right|_{\boldsymbol{\xi}=const} &= \frac{\partial\psi}{\partial(\mathbf{e}_e)_{ab}}\,\frac{\partial(\mathbf{e}_e)_{ab}}{\partial(\mathbf{E}_e)_{AB}}\,\frac{\partial(\mathbf{E}_e)_{AB}}{\partial t}\\ &= \frac{\partial\psi}{\partial(\mathbf{e}_e)_{ab}}\,\underbrace{\left(\mathbf{F}^{-1}\right)^A_a\left(\mathbf{F}^{-1}\right)^B_b\frac{\partial(\mathbf{E}_e)_{AB}}{\partial t}}_{\mathcal{L}_v\mathbf{e}_e=\mathbf{d}_e}\\ &= \frac{\partial\psi}{\partial(\mathbf{e}_e)_{ab}}\,(\mathbf{d}_e)_{ab}\,.\end{aligned} \tag{A.1.58}$$

□

Suppose that at time t_0 ($\mathbf{x} = \mathbf{X}$) the Cauchy stress field is given by:

$$\boldsymbol{\sigma}(\mathbf{x},t_0) = \boldsymbol{\sigma_0}(\mathbf{X}). \tag{A.1.59}$$

This initial stress field cannot be directly summed to (2.4.5), since it represents initial forces (defined in Ω_0) measured per unit reference area. This notion of stress coincides with the definition of the second Piola-Kirchhoff stress tensor, denoted by $\boldsymbol{S}$, hence $\boldsymbol{S}_0(\mathbf{X}) = \boldsymbol{\sigma_0}(\mathbf{X})$. The Kirchhoff stress tensor $\boldsymbol{\tau}$ is, in turn, the push-forward of the second Piola-Kirchhoff stress tensor. Therefore, the current stress state can be written as:

$$\boldsymbol{\tau}(\mathbf{x},t) = \varphi_*(\boldsymbol{S}_0) + \boldsymbol{c_e} : \mathbf{e}_e = \mathbf{F}\cdot\boldsymbol{S}_0\cdot\mathbf{F}^T + \boldsymbol{c_e} : \mathbf{e}_e. \tag{A.1.60}$$

For completeness, it would be pertinent to analyze if the stress field (A.1.60) is compatible with the existence of an elastic free energy function. Observe that one of the fundamental assumption stated in Section (2.3) was that the free energy function depends on $\mathbf{F}$ solely through its elastic part $\hat{\mathbf{F}}_e$. It is obvious that this assumption does not hold for a non stress-free reference configuration, since the deformation gradient itself is involved in the definition. In the following proposition, an expression for the elastic free energy is derived for this particular case of non stress-free reference configuration.

Proposition A.1.2. Under the assumption of small elastic strain, the Kirchhoff stress tensor $\boldsymbol{\tau}(\mathbf{x})$ given by

$$\boldsymbol{\tau} = \overbrace{\mathbf{F}\cdot\boldsymbol{S}_0\cdot\mathbf{F}^T}^{\boldsymbol{\tau}_0} + \boldsymbol{c_e} : \mathbf{e}_e, \tag{A.1.61}$$

can be obtained as the derivative, with respect to $\mathbf{e}_e$, of the following elastic free energy function:

$$\psi_e = \overbrace{\boldsymbol{\tau}_0 : \mathbf{e}_e}^{\psi_{e0}} + \frac{1}{2}\mathbf{e}_e : \boldsymbol{c_e} : \mathbf{e}_e, \tag{A.1.62}$$

where $\boldsymbol{S}_0(\mathbf{X})$ denotes the initial stress field.

Proof. Differentiation of the second term of the right-hand side of Eq.(A.1.62) involves no difficulty. Attention is confined to the first term ψ_{e0}. Inserting the multiplicative decomposition (A.1.21) in the expression of ψ_{e0}, we get

$$\begin{aligned}\psi_{e0} = F^a_A F^b_B \boldsymbol{S}_0{}^{AB}(\mathbf{e}_e)_{ab} &= (\hat{\mathbf{F}}_e)^a_{\hat{A}}(\hat{\mathbf{F}}_e)^b_{\hat{B}}(\mathbf{e}_e)_{ab}\overbrace{\boldsymbol{S}_0{}^{AB}(\mathbf{F}_p)^{\hat{A}}_A(\mathbf{F}_p)^{\hat{B}}_B}^{(\hat{\boldsymbol{S}}_0)^{\hat{A}\hat{B}}} \\ &= (\hat{\mathbf{F}}_e)^a_{\hat{A}}(\hat{\mathbf{F}}_e)^b_{\hat{B}}(\mathbf{e}_e)_{ab}(\hat{\boldsymbol{S}}_0)^{\hat{A}\hat{B}}.\end{aligned} \tag{A.1.63}$$

Note that tensor $\hat{\boldsymbol{S}}_0$ is independent of any elastic measure. Thus, taking the derivative of Eq.(A.1.63) with respect to $\mathbf{e}_e$, it gives

$$\frac{\partial \psi_{e0}}{\partial (\mathbf{e}_e)_{cd}} = (\hat{\boldsymbol{S}}_0)^{\hat{A}\hat{B}}\left((\hat{\mathbf{F}}_e)^c_{\hat{A}}(\hat{\mathbf{F}}_e)^d_{\hat{B}} + (\mathbf{e}_e)_{ab}\frac{\partial (\hat{\mathbf{F}}_e)^a_{\hat{A}}(\hat{\mathbf{F}}_e)^b_{\hat{B}}}{\partial (\mathbf{e}_e)_{cd}}\right). \tag{A.1.64}$$

By using the chain rule, and identities (A.1.54) and (A.1.25),

$$\frac{\partial (\bullet)}{\partial (\mathbf{e}_e)_{cd}} = \frac{\partial (\bullet)}{\partial (\hat{\mathbf{C}}_e)_{\hat{E}\hat{F}}}\frac{\partial (\hat{\mathbf{C}}_e)_{\hat{E}\hat{F}}}{\partial (\hat{\mathbf{E}}_e)_{\hat{C}\hat{D}}}\frac{\partial (\hat{\mathbf{E}}_e)_{\hat{C}\hat{D}}}{\partial (\mathbf{e}_e)_{cd}} = 2\frac{\partial (\bullet)}{\partial (\hat{\mathbf{C}}_e)_{\hat{C}\hat{D}}}(\hat{\mathbf{F}}_e)^c_{\hat{C}}(\hat{\mathbf{F}}_e)^d_{\hat{D}}. \tag{A.1.65}$$

Inserting Eq.(A.1.65) in Eq.(A.1.64), it yields

$$\begin{aligned}\frac{\partial \psi_{e0}}{\partial (\mathbf{e}_e)_{cd}} &= (\hat{\boldsymbol{S}}_0)^{\hat{A}\hat{B}}\left((\hat{\mathbf{F}}_e)^c_{\hat{A}}(\hat{\mathbf{F}}_e)^d_{\hat{B}} + 2(\hat{\mathbf{F}}_e)^c_{\hat{C}}(\hat{\mathbf{F}}_e)^d_{\hat{D}}(\mathbf{e}_e)_{ab}\frac{\partial (\hat{\mathbf{F}}_e)^a_{\hat{A}}(\hat{\mathbf{F}}_e)^b_{\hat{B}}}{\partial (\hat{\mathbf{C}}_e)_{\hat{C}\hat{D}}}\right) \\ &= (\hat{\boldsymbol{S}}_0)^{\hat{A}\hat{B}}(\hat{\mathbf{F}}_e)^c_{\hat{A}}(\hat{\mathbf{F}}_e)^d_{\hat{B}}\left(1 + 2(\mathbf{e}_e)_{ab}\frac{\partial (\hat{\mathbf{F}}_e)^a_{\hat{C}}(\hat{\mathbf{F}}_e)^b_{\hat{D}}}{\partial (\hat{\mathbf{C}}_e)_{\hat{C}\hat{D}}}\right).\end{aligned} \tag{A.1.66}$$

By considering the definition (A.1.24) of $\hat{\mathbf{C}}_e$,

$$\frac{\partial (\hat{\mathbf{C}}_e)_{\hat{C}\hat{D}}}{\partial (\hat{\mathbf{C}}_e)_{\hat{E}\hat{F}}} = \frac{\partial ((\hat{\mathbf{F}}_e)^a_{\hat{C}}(\hat{\mathbf{F}}_e)^b_{\hat{D}})}{\partial (\hat{\mathbf{C}}_e)_{\hat{E}\hat{F}}}g_{ab} = \delta^{\hat{E}}_{\hat{C}}\delta^{\hat{F}}_{\hat{D}}. \tag{A.1.67}$$

Hence,

$$\frac{\partial ((\hat{\mathbf{F}}_e)^a_{\hat{C}}(\hat{\mathbf{F}}_e)^b_{\hat{D}})}{\partial (\hat{\mathbf{C}}_e)_{\hat{E}\hat{F}}} = g^{ab}\delta^{\hat{E}}_{\hat{C}}\delta^{\hat{F}}_{\hat{D}}. \tag{A.1.68}$$

Inserting (A.1.68) in (A.1.66), we finally get

$$\frac{\partial \psi_{e0}}{\partial (\mathbf{e}_e)_{cd}} = (\boldsymbol{\tau}_0)^{cd}(1 + 2(\mathbf{e}_e)_{ab}g^{ab}), \tag{A.1.69}$$

or in compact notation

$$\frac{\partial \psi_{e0}}{\partial \mathbf{e}_e} = \boldsymbol{\tau}_0(1 + 2\mathrm{tr}\,\mathbf{e}_e). \tag{A.1.70}$$

Under the assumption of small elastic strain, $1 \gg 2\mathrm{tr}\,\mathbf{e}_e$. Therefore:

$$\frac{\partial \psi_{e0}}{\partial \mathbf{e}_e} \approx \boldsymbol{\tau}_0, \tag{A.1.71}$$

as asserted. □

A.1.2 Lie derivative of some spatial tensors

The following identities are useful in the linearization of the governing equations.

Proposition A.1.3. *The Lie derivative of the metric tensor* $\boldsymbol{g}$ *is given by*

$$(\mathcal{L}_v \boldsymbol{g})_{ab} = 2\, d_{ab}, \tag{A.1.72}$$

where d_{ab} *is the component matrix of the rate of deformation tensor.*

Proof. By using definition (A.1.20) of Lie derivative, we get

$$\begin{aligned}(\mathcal{L}_v \mathbf{g})_{ab} &= \left(\varphi_* \left(\frac{\partial \varphi^*(\mathbf{g})}{\partial t}\right)\right)_{ab} \\ &= \left(\mathbf{F}^{-1}\right)^C_{\ a} \left(\mathbf{F}^{-1}\right)^D_{\ b} \frac{\partial}{\partial t}(F^c_{\ C} F^d_{\ D} g_{cd}) \\ &= \left(\mathbf{F}^{-1}\right)^C_{\ a} \left(\mathbf{F}^{-1}\right)^D_{\ b} (\dot{F}^c_{\ C} F^d_{\ D} g_{cd} + F^c_{\ C} \dot{F}^d_{\ D} g_{cd}) \\ &= \left(\mathbf{F}^{-1}\right)^C_{\ a} \dot{F}^c_{\ C} g_{cb} + \left(\mathbf{F}^{-1}\right)^D_{\ b} \dot{F}^d_{\ D} g_{ad}.\end{aligned} \tag{A.1.73}$$

Finally, inserting the definition of the spatial velocity gradient $\mathbf{l}$ (see Eq.(A.1.17)) in Eq.(A.1.73) yields

$$(\mathcal{L}_v \mathbf{g})_{ab} = l_{ba} + l_{ab} = 2 d_{ab}. \tag{A.1.74}$$

□

Proposition A.1.4. *The Lie derivative of the inverse of the metric tensor* $\boldsymbol{g}^{-1}$ *is given by*

$$(\mathcal{L}_v \boldsymbol{g}^{-1})^{ab} = -2 \overbrace{g^{ac} g^{bd}}^{(\boldsymbol{I})^{abcd}} d_{cd} = -2 (\boldsymbol{I})^{abcd} d_{cd}. \tag{A.1.75}$$

Proof. This relation follows immediately from differentiation[11] of the identity $g^{ab}\, g_{bc} = \delta^a_c$ and the result presented in proposition (A.1.3):

$$\begin{aligned}&\mathcal{L}_v(\mathbf{g}^{-1} \cdot \mathbf{g}) = (\mathcal{L}_v \mathbf{g}^{-1})^{ab} g_{bc} + g^{ab} (\mathcal{L}_v \mathbf{g})_{bc} = 0 \\ &\Rightarrow\ (\mathcal{L}_v \mathbf{g}^{-1})^{ae} = -g^{ab}\, g^{ec} (\mathcal{L}_v \mathbf{g})_{bc} = -2\, g^{ab}\, g^{ec} d_{bc}.\end{aligned} \tag{A.1.76}$$

□

The foregoing results can be exploited to obtain the Lie derivatives of the fourth order tensors involved in the definition of the elasticity tensor (see Eq.(2.4.4)):

$$\boldsymbol{c_e} = \kappa^e\, \boldsymbol{I}_{\rm vol} + 2\, \mu^e\, \boldsymbol{I}_{\rm dev} = (\kappa^e - \frac{2}{3}\mu^e)\, \boldsymbol{I}_{\rm vol} + 2\, \mu^e\, \boldsymbol{I}_{\rm sym},$$

namely, the volumetric tensor

$$(\boldsymbol{I}_{\rm vol})^{abcd} = (\mathbf{1} \otimes \mathbf{1})^{abcd} = (\mathbf{g}^{-1} \otimes \mathbf{g}^{-1})^{abcd} = g^{ab} g^{cd}, \tag{A.1.77}$$

[11] Note that the Lie derivative satisfies the standard *product rule*, i.e. $\mathcal{L}_v(A \cdot B) = \mathcal{L}_v A \cdot B + A \cdot \mathcal{L}_v B$. This assertion is proved by considering that $\varphi^*(A \cdot B) = \varphi^*(A) \cdot \varphi^*(B)$ [63].

the fourth order identity[12] tensor,

$$(\boldsymbol{I})^{abcd} = g^{ac} g^{bd}, \tag{A.1.78}$$

and the *symmetric* fourth order identity tensor

$$(\boldsymbol{I}_{\text{sym}})^{abcd} = \frac{1}{2}((\boldsymbol{I})^{abcd} + (\boldsymbol{I})^{abdc}) = \frac{1}{2}(g^{ac} g^{bd} + g^{ad} g^{bc}). \tag{A.1.79}$$

Observe that in the definition of the elasticity tensor, only *fully contravariant* tensors are involved. This follows from the fact that the elasticity tensor is an operator that takes strain measures, which are regarded as covariant second-order tensors, to stress quantities, which are contravariant.

Proposition A.1.5. *The Lie derivative of the (fully contravariant) fourth order volumetric tensor is expressible as:*

$$\mathcal{L}_v \boldsymbol{I}_{vol} = \overset{\triangledown}{\boldsymbol{I}}_{vol} : \boldsymbol{d}, \tag{A.1.80}$$

where the components of the sixth order tensor $\overset{\triangledown}{\boldsymbol{I}}_{vol}$ *are given by the following formula:*

$$(\overset{\triangledown}{\boldsymbol{I}}_{vol})^{abcdef} = -2(g^{ab}(\boldsymbol{I})^{cdef} + g^{cd}(\boldsymbol{I})^{abef}). \tag{A.1.81}$$

Proof. In virtue of the product rule of differentiation, we can write

$$(\mathcal{L}_v \boldsymbol{I}_{\text{vol}})^{abcd} = (\mathcal{L}_v(\mathbf{g}^{-1} \otimes \mathbf{g}^{-1}))^{abcd} = (\mathcal{L}_v \mathbf{g}^{-1})^{ab} g^{cd} + g^{ab} (\mathcal{L}_v \mathbf{g}^{-1})^{cd}. \tag{A.1.82}$$

Finally, using property (A.1.75), the above equation takes the form

$$\begin{aligned} (\mathcal{L}_v \boldsymbol{I}_{\text{vol}})^{abcd} &= (-2\,(\boldsymbol{I})^{abef}\, d_{ef})\, g^{cd} + g^{ab}\, (-2\,(\boldsymbol{I})^{cdef}\, d_{ef}) \\ &= -2\,(g^{cd}(\boldsymbol{I})^{abef} + g^{ab}(\boldsymbol{I})^{cdef}) d_{ef}. \end{aligned} \tag{A.1.83}$$

□

The following identity can be inferred from definition (A.1.81):

$$(\mathcal{L}_v \boldsymbol{I}_{\text{vol}})^{abcd}\, e_{cd} = -2\,(\operatorname{tr} \mathbf{e}\,(\boldsymbol{I})^{abef} + g^{ab} e^{ef}) d_{ef}, \tag{A.1.84}$$

where $\mathbf{e}$ denotes any second order covariant tensor.

[12] The denomination "identity" may appear a misnomer herein. Strictly speaking, the fourth order identity tensor relating second order quantities in the spatial configuration is defined as $(\boldsymbol{I})^{ab}_{cd} = \delta^a_c \delta^b_d$. As stated earlier, in the context of cartesian coordinate system the components of g^{ab}, g_{ab} and δ^a_b are the same (the Kronecker Delta). However, we shall strive in this appendix to maintain this distinct treatment because although their components are equal, the underlying meaning of each tensor is different. For instance, whereas the Lie derivative of the metric $\mathcal{L}_v(g^{ab}\bar{\mathbf{e}}_a \otimes \bar{\mathbf{e}}_b) = 2\mathbf{d}$, the Lie derivative $\mathcal{L}_v(\delta^a_b \bar{\mathbf{e}}_a \otimes \bar{\mathbf{e}}^b) = 0$ vanishes.

Proposition A.1.6. *The Lie derivative of the (fully contravariant) fourth order identity tensor is given by:*

$$\mathcal{L}_v \boldsymbol{I} = \overset{\triangledown}{\boldsymbol{I}} : \boldsymbol{d}. \tag{A.1.85}$$

Here the the sixth order tensor $\overset{\triangledown}{\boldsymbol{I}}$ *has components:*

$$(\overset{\triangledown}{\boldsymbol{I}})^{abcdef} = -2(g^{ac}(\boldsymbol{I})^{bdef} + g^{bd}(\boldsymbol{I})^{acef}). \tag{A.1.86}$$

Proof. This proof follows exactly the same lines as the proof of proposition A.1.5. □

Proposition A.1.7. *The Lie derivative of the (fully contravariant) symmetric fourth order identity tensor can be expressed as:*

$$\mathcal{L}_v \boldsymbol{I}_{sym} = \overset{\triangledown}{\boldsymbol{I}}_{sym} : \boldsymbol{d}. \tag{A.1.87}$$

where the components of the sixth-order tensor $\overset{\triangledown}{\boldsymbol{I}}_{sym}$ *are given by:*

$$(\overset{\triangledown}{\boldsymbol{I}}_{sym})^{abcdef} = -2(g^{df}(\boldsymbol{I}_{sym})^{abce} + g^{cf}(\boldsymbol{I}_{sym})^{abde}). \tag{A.1.88}$$

Proof. It follows from the definition (A.1.79) of $\boldsymbol{I}_{\mathrm{sym}}$ that

$$(\mathcal{L}_v \boldsymbol{I}_{\mathrm{sym}})^{abcd} = \frac{1}{2}((\mathcal{L}_v \boldsymbol{I})^{abcd} + (\mathcal{L}_v \boldsymbol{I})^{abdc}). \tag{A.1.89}$$

Substituting Eq.(A.1.85) into the above equation yields

$$\begin{aligned}(\mathcal{L}_v \boldsymbol{I}_{\mathrm{sym}})^{abcd} &= -2\,\frac{1}{2}(g^{ac}(\boldsymbol{I})^{bdef} + g^{bd}(\boldsymbol{I})^{acef} \\ &\quad + g^{ad}(\boldsymbol{I})^{bcef} + g^{bc}(\boldsymbol{I})^{adef})d_{ef} \\ &= -(g^{ac}g^{be}g^{df} + g^{bd}g^{ae}g^{cf} \\ &\quad + g^{ad}g^{be}g^{cf} + g^{bc}g^{ae}g^{df})d_{ef}.\end{aligned} \tag{A.1.90}$$

Upon rearranging terms, we finally obtain

$$\begin{aligned}(\mathcal{L}_v \boldsymbol{I}_{\mathrm{sym}})^{abcd} &= -(g^{df}\,(\overbrace{g^{ac}g^{be} + g^{bc}g^{ae}}^{2\,(\boldsymbol{I}_{\mathrm{sym}})^{abce}}) + g^{cf}\,(\overbrace{g^{bd}g^{ae} + g^{ad}g^{be}}^{2\,(\boldsymbol{I}_{\mathrm{sym}})^{abde}}))\,d_{ef} \\ &= -2(g^{df}(\boldsymbol{I}_{\mathrm{sym}})^{abce} + g^{cf}(\boldsymbol{I}_{\mathrm{sym}})^{abde})\,d_{ef}.\end{aligned} \tag{A.1.91}$$

□

The following identity can be deduced from definition (A.1.88):

$$(\mathcal{L}_v \boldsymbol{I}_{\mathrm{sym}})^{abcd} e_{cd} = -2\,(e^{af}g^{be} + g^{ae}e^{bf})\,, \tag{A.1.92}$$

where **e** denotes any symmetric second order covariant tensor.

A.1.2.1 Spatial elasticity tensor

The Lie derivative of the elasticity tensor can be written in terms of the quantities defined in the preceding discussion:

$$\begin{aligned}\mathcal{L}_v \boldsymbol{c_e} &= \kappa^e \, \mathcal{L}_v \boldsymbol{I}_{\rm vol} + 2\,\mu^e \, (\mathcal{L}_v \boldsymbol{I}_{\rm sym} - \frac{1}{3}\mathcal{L}_v \boldsymbol{I}_{\rm vol}) + \frac{\partial \boldsymbol{c_e}}{\partial \xi^h}\,\dot{\xi}^h \\ &= \left((\kappa^e - \frac{2}{3}\mu^e)\, \overset{\triangledown}{\boldsymbol{I}}_{\rm vol} + 2\,\mu^e \, \overset{\triangledown}{\boldsymbol{I}}_{\rm sym} \right) : \mathbf{d} \, + \, \frac{\partial \boldsymbol{c_e}}{\partial \xi^h}\,\dot{\xi}^h .\end{aligned} \tag{A.1.93}$$

A result of much interest is the double contraction of $\mathcal{L}_v \boldsymbol{c_e}$ and the elastic Almansi strain tensor. The following proposition addresses this question.

Proposition A.1.8. *Let $\boldsymbol{e}_e$ be the Almansi stress tensor and $\boldsymbol{c_e}$ the fourth order elasticity tensor, both defined in the spatial configuration. Then, the double contraction of the Lie derivative of $\boldsymbol{c_e}$ and $\boldsymbol{e}_e$ can be expressed as:*

$$\mathcal{L}_v \boldsymbol{c_e} : \boldsymbol{e}_e = \mathbf{a_e}(\boldsymbol{e}_e) + \frac{\partial \boldsymbol{c_e}}{\partial \xi^h} : \boldsymbol{e}_e \dot{\xi}^h, \tag{A.1.94}$$

where the components of the fourth order tensor $\mathbf{a_e}$ are given by:

$$\begin{aligned}(\mathbf{a_e})^{abef} = -2 \Big(&\big(\kappa^e - \frac{2}{3}\mu^e\big)\big(g^{ab}(\boldsymbol{e}_e)^{ef} + tr\,\boldsymbol{e}_e(\boldsymbol{I})^{abef}\big) \\ &+ 2\,\mu^e \big((\boldsymbol{e}_e)^{af} g^{be} + (\boldsymbol{e}_e)^{bf} g^{ae}\big)\Big).\end{aligned} \tag{A.1.95}$$

Proof. This follows immediately from substituting identities (A.1.84) and (A.1.92) into Eq.(A.1.93). □

For the sake of notational compactness, it proves advantageous to express $\mathbf{a_e}(\mathbf{e}_e)$ in symbolic notation. This task is not obvious, since the last term of the right hand side of Eq.(A.1.95) cannot be constructed using conventional symbolic operators. Thus, we are compelled to introduce a new operator, denoted symbolically as $\boldsymbol{\mathcal{I}}_s(\bullet)$ and defined by the following relation

$$(\boldsymbol{\mathcal{I}}_s(\mathbf{e}))^{abef} = \frac{1}{2}\big(e^{af} g^{be} + e^{bf} g^{ae}\big), \tag{A.1.96}$$

where $\mathbf{e}$ stands for any second order symmetric tensor. This operator has the following remarkable properties. Let $\mathbf{d}$ and $\mathbf{e}$ be symmetric second order tensors. Then, it follows from Eq.(A.1.96) that

$$\boldsymbol{\mathcal{I}}_s(\mathbf{e}) : \mathbf{d} = \frac{1}{2}\big(\mathbf{e}\cdot\mathbf{d} + \mathbf{d}\cdot\mathbf{e}\big) = sym(\mathbf{e}\cdot\mathbf{d}). \tag{A.1.97}$$

Furthermore,

$$\boldsymbol{\mathcal{I}}_s(\mathbf{1}) = \boldsymbol{I}_{\rm sym}. \tag{A.1.98}$$

i.e., when acting on the identity tensor $\mathbf{1}$, it produces the fourth order symmetric identity tensor $\boldsymbol{I}_{\rm sym}$, previously defined in Eq.(A.1.79). Therefore, according to Eq.(A.1.95) and Eq.(A.1.96), the tensor $\mathbf{a_e}$ can be symbolically written as

$$\mathbf{a_e}(\mathbf{e}_e) = -2\left(\left(\kappa^e - \frac{2}{3}\mu^e\right)\left(\mathbf{1}\otimes\mathbf{e}_e + \operatorname{tr}\mathbf{e}_e\boldsymbol{I}\right) + 2\,\mu^e\,\boldsymbol{\mathcal{I}}_s(\mathbf{e}_e)\right). \tag{A.1.99}$$

A.1.2.2 Fully covariant tensors

The tensorial objects appearing in the foregoing developments were regarded as fully contravariant. However, in the formulation of the constitutive equation, *fully covariant* fourth-order tensors may come also into play. For instance, the plastic flow vector is aligned with the rate of deformation tensor, which is a strain measure and hence it is considered as a fully covariant tensor. Hence, if one wants to relate through an affine transformation the plastic flow vector $\boldsymbol{m}$ (covariant) to the Kirchhoff stress tensor $\boldsymbol{\tau}$ (contravariant), the corresponding fourth-order operator $\boldsymbol{A}$ must be fully covariant: .

$$m_{ab} = A_{abcd}\,\tau^{cd} + B_{cd}. \tag{A.1.100}$$

Here our interest is confined to devise an expression for the Lie derivative of a fully covariant fourth order tensor of the type

$$\boldsymbol{A} = A_{vol}\boldsymbol{I}_{\rm vol} + A_{dev}\boldsymbol{I}_{\rm dev}. \tag{A.1.101}$$

To remove ambiguity and explicitly indicate the covariant nature of this tensor, it proves helpful to write the above equation in component form:

$$A_{abcd} = (A_{vol} - \frac{1}{3}A_{dev})(\boldsymbol{I}_{\rm vol})_{abcd} + A_{dev}(\boldsymbol{I}_{\rm sym})_{abcd}, \tag{A.1.102}$$

where

$$(\boldsymbol{I}_{\rm vol})_{abcd} = (\mathbf{1}\otimes\mathbf{1})_{abcd} = (\mathbf{g}\otimes\mathbf{g})_{abcd} = g_{ab}g_{cd}, \tag{A.1.103}$$

$$(\boldsymbol{I}_{\rm sym})_{abcd} = \frac{1}{2}((\boldsymbol{I})_{abcd} + (\boldsymbol{I})_{abdc}) = \frac{1}{2}(g_{ac}g_{bd} + g_{ad}g_{bc}). \tag{A.1.104}$$

The derivation of the Lie derivative of the covariant volumetric fourth-order tensor $\boldsymbol{I}_{\rm vol}$ and the covariant symmetric identity tensor $\boldsymbol{I}_{\rm sym}$ proceeds along the same lines discussed for their contravariant counterparts (see Eqs. (A.1.81) and (A.1.88)). Since no new insight is to be gained from this derivations, we simply quote the final result:

$$(\mathcal{L}_v\boldsymbol{I}_{\rm vol})_{abcd} = 2\big(g_{ab}(\boldsymbol{I})^{ef}_{cd} + g_{cd}(\boldsymbol{I})^{ef}_{ab}\big)d_{ef}, \tag{A.1.105}$$

$$(\mathcal{L}_v\boldsymbol{I}_{\rm sym})_{abcd} = 2(\delta^f_d(\boldsymbol{I}_{\rm sym})^e_{abc} + \delta^f_c(\boldsymbol{I}_{\rm sym})^e_{abd}), \tag{A.1.106}$$

where

$$(\boldsymbol{I})^{de}_{ab} = \delta^d_a\delta^e_b, \quad (\boldsymbol{I})^e_{abc} = g_{ab}\delta^e_c, \quad (\boldsymbol{I}_{\rm sym})^e_{abc} = \frac{1}{2}\big((\boldsymbol{I})^e_{abc} + (\boldsymbol{I})^c_{abe}\big). \tag{A.1.107}$$

We reiterate that, when using Cartesian coordinates, raising or lowering indices do not affect the values of tensor components. Therefore, from a comparison of Eq.(A.1.105) and Eq.(A.1.81), and also Eq.(A.1.106) and Eq.(A.1.88), we can conclude that the expressions for the Lie derivative of $\boldsymbol{I}_{\text{vol}}$ and $\boldsymbol{I}_{\text{sym}}$ when those tensors are regarded as covariants are identical to the corresponding Lie derivatives when $\boldsymbol{I}_{\text{vol}}$ and $\boldsymbol{I}_{\text{sym}}$ are considered contravariant, except for the sign. We can exploit this analogy to directly derive the covariant counterpart of Eq.(A.1.95):

$$\mathcal{L}_v \boldsymbol{A} : \boldsymbol{\tau} = \mathbf{a}_\tau(A_{vol}, A_{dev}, \boldsymbol{\tau}) : \mathbf{d} + \frac{\partial \boldsymbol{A}}{\partial t} : \boldsymbol{\tau}, \tag{A.1.108}$$

being $\mathbf{a}_\tau$ a fourth order tensor given by the following formula

$$\mathbf{a}_\tau(A_{vol}, A_{dev}, \boldsymbol{\tau}) = 2\left(\left(A_{vol} - \frac{1}{3}A_{dev}\right)\left(\mathbf{1} \otimes \boldsymbol{\tau} + \operatorname{tr}\boldsymbol{\tau}\boldsymbol{I}\right) + 2\,A_{dev}\,\boldsymbol{\mathcal{I}}_s(\boldsymbol{\tau})\right), \tag{A.1.109}$$

and $\boldsymbol{\tau}$ any contravariant second order tensor.

A.2 Governing equation in generalized stresses

The aim of this section is to show that the set of governing equations can be cast into the following reduced format:

$$\dot{\boldsymbol{\Sigma}} = \boldsymbol{A}(\boldsymbol{\Sigma}, \dot{\mathbf{E}}) + \sum_{\beta=1}^{3} \dot{\lambda}^\beta \boldsymbol{\Xi}_\beta(\boldsymbol{\Sigma}), \tag{A.2.1}$$

wherein $\boldsymbol{\Sigma}$ denotes a *generalized stress* variable and $\boldsymbol{A}$ and $\boldsymbol{\Xi}_\beta$, $(\beta = 1, 2, 3)$ are as yet undetermined functions of $\boldsymbol{\Sigma}$ and $\dot{\mathbf{E}}$.

For this purpose, we first derive the rate form of the elastic relationship $\boldsymbol{\tau} = \boldsymbol{\tau}_0 + \boldsymbol{c_e} : \mathbf{e}_e$ by applying the Lie derivative:

$$\begin{aligned} \mathcal{L}_v\boldsymbol{\tau} &= \overbrace{\mathcal{L}_v\boldsymbol{\tau}_0}^{=0} + \mathcal{L}_v\boldsymbol{c_e} : \mathbf{e}_e + \boldsymbol{c_e} : \mathcal{L}_v\mathbf{e}_e \\ &= \mathcal{L}_v\boldsymbol{c_e} : \mathbf{e}_e + \boldsymbol{c_e} : (\mathcal{L}_v\mathbf{e} - \mathcal{L}_v\mathbf{e}_p) \\ &= \mathcal{L}_v\boldsymbol{c_e} : \mathbf{e}_e + \boldsymbol{c_e} : (\mathbf{d} - \mathbf{d}_p). \end{aligned} \tag{A.2.2}$$

As stated in section A.1.2.1 (see Eq.(A.1.95)), the Lie derivative of $\boldsymbol{c_e}$ can be expressed in terms of the rate of deformation tensor and the rate of change of the internal hardening variable. Substituting Eq.(A.1.95) into the above equation yields

$$\begin{aligned} \mathcal{L}_v\boldsymbol{\tau} &= \overbrace{\mathbf{a}_\mathbf{e}(\mathbf{e}_e) : \mathbf{d} + \frac{\partial \boldsymbol{c_e}}{\partial \xi^h} : \mathbf{e}_e\,\dot{\xi}^h}^{\mathcal{L}_v\boldsymbol{c_e}:\mathbf{e}_e} + \boldsymbol{c_e} : (\mathbf{d} - \mathbf{d}_p) \\ &= \left(\boldsymbol{c_e} + \mathbf{a}_\mathbf{e}(\mathbf{e}_e)\right) : \mathbf{d} - \boldsymbol{c_e} : \mathbf{d}_p + \frac{\partial \boldsymbol{c_e}}{\partial \xi^h} : \mathbf{e}_e\,\dot{\xi}^h, \end{aligned} \tag{A.2.3}$$

where the fourth order tensor $\mathbf{a_e}(\mathbf{e}_e)$ has been defined in Eq.(A.1.95).

The evolution of the vector of internal variables can be expressed in compact format as

$$\dot{\boldsymbol{\xi}} = \begin{bmatrix} \dot{\xi}^h \\ \dot{\xi}^s \end{bmatrix} = \dot{\lambda}^1 \begin{bmatrix} -2\xi^h s_2^2 p \\ 0 \end{bmatrix} + \dot{\lambda}^2 \begin{bmatrix} 0 \\ 2q \end{bmatrix} = \sum_{\beta=1}^{3} \dot{\lambda}^\beta \mathbf{h}_\beta, \tag{A.2.4}$$

where $\mathbf{h}_\beta$ is defined as

$$\mathbf{h}_1 = \begin{bmatrix} -2\xi^h s_2^2 p \\ 0 \end{bmatrix}, \quad \mathbf{h}_2 = \begin{bmatrix} 0 \\ 2q \end{bmatrix}, \quad \mathbf{h}_3 = \begin{bmatrix} 0 \\ 0 \end{bmatrix}. \tag{A.2.5}$$

In section 2.3, it was established that any state function at current time t is expressible as a function of the point values of $\mathbf{F}$, the driving variable, and the strain-like state variables $\{\mathbf{e}_e, \boldsymbol{\xi}\}$. Nevertheless, the description can be conceived alternatively in terms of $\mathbf{F}$ and a set of *stress-like variables*, namely $\boldsymbol{\tau}$ (or $\boldsymbol{S}$) and $\mathbf{r}$. Although within the framework of classical associative plasticity the *stress-like internal variable* vector $\mathbf{r}$ is identified as the thermodynamic *conjugate variable* to $\boldsymbol{\xi}$, one need not to assign a particular thermodynamic meaning to $\mathbf{r}$ [13]. Variable $\mathbf{r}$ can be any stress-like state function provided that the operator $\boldsymbol{D}$ defined through the expression

$$\dot{\mathbf{r}} = \boldsymbol{D} \cdot \dot{\boldsymbol{\xi}}, \tag{A.2.6}$$

is invertible. The choice

$$\mathbf{r} = \begin{bmatrix} s_1 \\ c \end{bmatrix}, \tag{A.2.7}$$

fulfils this condition, since the associated operator

$$\boldsymbol{D} = \begin{bmatrix} \dfrac{\partial s_{1\mathrm{h}}}{\partial \xi^h} & 0 \\ \dfrac{\partial c_{\mathrm{h}}}{\partial \xi^h} & H \end{bmatrix}, \tag{A.2.8}$$

is invertible whenever $\dfrac{\partial s_{1\mathrm{h}}}{\partial \xi^h} \neq 0$ and $H \neq 0$ [14]. The derivatives $\dfrac{\partial s_{1\mathrm{h}}}{\partial \xi^h} > 0$ and $\dfrac{\partial c_{\mathrm{h}}}{\partial \xi^h} > 0$ quantify how the elliptical cap and the Drucker-Prager surfaces evolves upon a change of the internal hardening variable. Thus, they can be regarded as *hardening moduli*. The other component of $\boldsymbol{D}$ is the *softening modulus* $H < 0$, defined in *Eq.*(2.5.79). The operator $\boldsymbol{D}$ is therefore referred to as the *generalized plastic moduli*.

The rate form Eq.(A.2.3) of the elastic constitutive relation combined with flow rule for the plastic strains (see Eq.(3.1.9)) and the evolution equation (A.2.4) lead

[13] As explained in Appendix C.1, the multisurface nature of our model renders the identification of these conjugate variables a difficult task.

[14] In Eq.(2.3.3) it was stated that the softening mechanism was not active for lower levels of densification, i.e. $H = 0$. In these circumstances, however, the role of the interval softening variable ξ^s is irrelevant and we can simply write $\boldsymbol{\xi} = \xi^h$ and $\mathbf{r} = s_1$.

to the following equation:

$$\begin{aligned}\mathcal{L}_v\boldsymbol{\tau} &= (\boldsymbol{c_e}+\mathbf{a_e}):\mathbf{d}-\sum_{\beta=1}^{3}\dot{\lambda}^{\beta}\,\boldsymbol{c_e}:\boldsymbol{m}^{\beta}+\sum_{\beta=1}^{3}\dot{\lambda}^{\beta}\,\frac{\partial \boldsymbol{c_e}}{\partial \xi^h}:\mathbf{e}_e\,h_{1\beta}\\ &= (\boldsymbol{c_e}+\mathbf{a_e}):\mathbf{d}+\sum_{\beta=1}^{3}\dot{\lambda}^{\beta}\,\big(\frac{\partial \boldsymbol{c_e}}{\partial \xi^h}:\mathbf{e}_e\,h_{1\beta}-\boldsymbol{c_e}:\boldsymbol{m}^{\beta}\big).\end{aligned} \tag{A.2.9}$$

Factoring out the elasticity tensor $\boldsymbol{c_e}$ in the second term of the right-hand side of the above, we get

$$\begin{aligned}\mathcal{L}_v\boldsymbol{\tau} &= (\boldsymbol{c_e}+\mathbf{a_e}):\mathbf{d}+\boldsymbol{c_e}:\sum_{\beta=1}^{3}\dot{\lambda}^{\beta}\,\big(\overbrace{\boldsymbol{c_e}^{-1}:\frac{\partial \boldsymbol{c_e}}{\partial \xi^h}:\mathbf{e}_e\,h_{1\beta}-\boldsymbol{m}^{\beta}}^{-\overset{\triangle}{\boldsymbol{m}}_{\beta}}\big)\\ &= (\boldsymbol{c_e}+\mathbf{a_e}):\mathbf{d}-\boldsymbol{c_e}:\sum_{\beta=1}^{3}\dot{\lambda}^{\beta}\,\overset{\triangle}{\boldsymbol{m}}_{\beta}.\end{aligned} \tag{A.2.10}$$

Remark A.2.1. It is worthwhile to digress briefly and examine in depth the structure of Eq.(A.2.9). In particular, we are interested in underlying those aspects that make this formulation different from that of classical infinitesimal plasticity, as presented, for instance, in Simo[93]. The first distinctive feature is the use of objective rates (Lie derivative) in lieu of standard differentiation . Another difference is the coupling between elastic and plastic behavior, which is manifested by the term in Eq.(A.2.9) involving the derivative with respect of ξ^h of $\boldsymbol{c_e}$. By using definition (2.4.4) of the elasticity tensor $\boldsymbol{c_e}$, the last term of Eq.(A.2.10) can be expanded in the following manner:

$$\begin{aligned}\overset{\triangle}{\boldsymbol{m}}_{\beta} &= -\boldsymbol{c_e}^{-1}:\frac{\partial \boldsymbol{c_e}}{\partial \xi^h}:\mathbf{e}_e\,h_{1\beta}+\boldsymbol{m}^{\beta}\\ &= -\big(\frac{1}{9\kappa^e}\,\boldsymbol{I}_{\mathrm{vol}}+\frac{1}{2\mu^e}\boldsymbol{I}_{\mathrm{dev}}\big):\big(\frac{\partial \kappa^e}{\partial \xi^h}\mathrm{tr}\,\mathbf{e}_e+2\frac{\partial \mu^e}{\partial \xi^h}dev\,\mathbf{e}_e\big)\,h_{1\beta}+\boldsymbol{m}^{\beta}\\ &= \big(-\frac{1}{3\,\kappa^e}\frac{\partial \kappa^e}{\partial \xi^h}\,\mathrm{tr}\,\mathbf{e}_e\,h_{1\beta}+\frac{1}{3}\mathrm{tr}\,\boldsymbol{m}^{\beta}\big)\,\mathbf{1}+\big(-\frac{1}{\mu^e}\frac{\partial \mu^e}{\partial \xi^h}\,dev\,\mathbf{e}_e\,h_{1\beta}+dev\,\boldsymbol{m}^{\beta}\big).\end{aligned} \tag{A.2.11}$$

As it can be inferred from definition (A.2.5), the following relation between $h_{1\beta}$ and the plastic flow vector $\boldsymbol{m}^{\beta}$ holds:

$$h_{1\beta}=\delta_{e\beta}\xi^h\mathrm{tr}\,\boldsymbol{m}^{\beta}. \tag{A.2.12}$$

Taking the trace of Eq.(A.2.11) and inserting Eq.(A.2.12), we obtain

$$\begin{aligned}\mathrm{tr}\,\overset{\triangle}{\boldsymbol{m}}_{\beta} &= \mathrm{tr}\,\boldsymbol{m}^{\beta}\big(1-\frac{1}{\kappa^e}\frac{\partial \kappa^e}{\partial \xi^h}\,\mathrm{tr}\,\mathbf{e}_e\,\delta_{e\beta}\,\xi^h\big)\\ &= \mathrm{tr}\,\boldsymbol{m}^{\beta}\big(1-\frac{\partial \log\kappa^e}{\partial \xi^h}\,\mathrm{tr}\,\mathbf{e}_e\,\delta_{e\beta}\,\xi^h\big).\end{aligned} \tag{A.2.13}$$

To determine the relative influence of the contribution due to non-linear elasticity in the direction of the plastic flow vector $\boldsymbol{m}^{\beta}$, one has to evaluate the derivative $\partial \log \kappa^e / \partial \xi^h$. The elastic bulk modulus can be expressed in terms of the Young's modulus E^e through Eq.(2.4.2). Then, using the exponential curve fit (2.5.60) for E^e (the Poisson's ratio is regarded as constant) one obtains the following analytical expression for κ^e:

$$\kappa^e(\xi^h) = \frac{1}{3(1-2\nu^e)} E^e(\xi^h) = \frac{1}{3(1-2\nu^e)} \frac{\eta_0}{\xi^h} E_0 e^{B_E(\xi^h - \eta_0)}. \tag{A.2.14}$$

Differentiation of $\log \kappa^e$ then yields

$$\frac{\partial \log \kappa^e}{\partial \xi^h} = \frac{\partial}{\partial \xi^h}(\log \frac{\eta_0}{\xi^h}) + B_E = B_E - \frac{1}{\xi^h}. \tag{A.2.15}$$

Inserting Eq.(A.2.15) in Eq.(A.2.13) leads to

$$\operatorname{tr} \overset{\triangle}{\boldsymbol{m}}_{\beta} = \operatorname{tr} \boldsymbol{m}^{\beta} \big(1 - \operatorname{tr} \mathbf{e}_e \, (\xi^h \, B_E - 1)\big). \tag{A.2.16}$$

As seen in section 2.5.4, for a typical Distaloy AE the adjustable constant $B_E \approx 9$. Thus, according to Eq.(A.2.16), the effect of non-linear elasticity (dependence of $\boldsymbol{c_e}$ upon ξ^h) can be viewed as an alteration of the direction of the plastic flow vector $\boldsymbol{m}^{\beta}$ of order

$$\operatorname{tr} \mathbf{e}_e \, (\xi^h \, B_E - 1) \backsim 10 \operatorname{tr} \mathbf{e}_e, \tag{A.2.17}$$

i.e., one order of magnitude greater than the elastic strains.

The other difference lies on the fact that the rate of deformation tensor $\mathbf{d}$ is not solely multiplied by $\boldsymbol{c_e}$ in Eq.(A.2.10), but an additional fourth order tensor $\mathbf{a_e}$ appears. This is a direct consequence of the hyperelastic nature of the free energy function. In the course of pure elastic deformation, the plastic multipliers vanish and Eq.(A.2.10) reduces to $\mathcal{L}_v \boldsymbol{\tau} = (\boldsymbol{c_e} + \mathbf{a_e}(\mathbf{e}_e)) : \mathbf{d}$. If one discards the term $\mathbf{a_e}$, then a typical hypoelastic correlation is recovered, $\mathcal{L}_v \boldsymbol{\tau} = \boldsymbol{c_e} : \mathbf{d}$. This tensorial quantity $\mathbf{a_e}$ stems, as set forth in Eq.(A.1.95), from the objective differentiation of $\boldsymbol{c_e}$. Taking into account property Eq.(A.1.98) of the operator $\boldsymbol{\mathcal{I}}_s(\bullet)$, we can write

$$\begin{aligned} \boldsymbol{c_e} + \mathbf{a_e}(\mathbf{e}_e) &= \big((\kappa^e - \frac{2}{3}\mu^e)\, \mathbf{1} \otimes \mathbf{1} + 2\mu^e \boldsymbol{I}_{\mathrm{sym}}\big) \\ &\quad - 2\Big(\big(\kappa^e - \frac{2}{3}\mu^e\big)\big(\mathbf{1} \otimes \mathbf{e}_e + \operatorname{tr} \mathbf{e}_e \boldsymbol{I}\big) + 2\,\mu^e \boldsymbol{\mathcal{I}}_s(\mathbf{e}_e)\Big) \\ &= \big(\kappa^e - \frac{2}{3}\mu^e\big)\big(\mathbf{1} \otimes (\mathbf{1} - 2\,\mathbf{e}_e) - 2\mathrm{tr}\, \mathbf{e}_e \boldsymbol{I}\big) + 2\,\mu^e \boldsymbol{\mathcal{I}}_s(\mathbf{1} - 2\,\mathbf{e}_e). \end{aligned} \tag{A.2.18}$$

Since $\|\mathbf{e}_e\| \ll 1$, it becomes evident from the above expression that the influence of $\mathbf{a_e}(\mathbf{e}_e)$ is not significant in comparison with $\boldsymbol{c_e}$.

On the other hand, substitution of Eq.(A.2.4) in Eq.(A.2.6) yields the following result for the rate of the stress-like internal variable:

$$\dot{\mathbf{r}} = \sum_{\beta=1}^{3} \dot{\lambda}^{\beta} \boldsymbol{D} \cdot \mathbf{h}_{\beta}. \tag{A.2.19}$$

The desired result of phrasing the constitutive equations into a single rate equation emerges by, first, performing a pull-back transformation on equation Eq.(A.2.10):

$$\begin{aligned}\varphi^*(\mathcal{L}_v\boldsymbol{\tau}) =&\varphi^*(\boldsymbol{c_e}+\mathbf{a_e}):\varphi^*(\mathbf{d})-\varphi^*(\boldsymbol{c_e}):\sum_{\beta=1}^{3}\dot\lambda^\beta\,\varphi^*\big(\overset{\triangle}{\boldsymbol{m}}_\beta\big)\\ \Rightarrow\ \dot{\boldsymbol{S}} =&(\boldsymbol{C_e}+\mathbf{A_e}):\dot{\mathbf{E}}-\boldsymbol{C_e}:\sum_{\beta=1}^{3}\dot\lambda^\beta\,\overset{\triangle}{\boldsymbol{M}}_\beta\end{aligned}\tag{A.2.20}$$

where $\boldsymbol{C_e}$, $\mathbf{A_e}$ and $\overset{\triangle}{\boldsymbol{M}}_\beta$ are the material counterparts of the spatial quantities $\boldsymbol{c_e}$, $\mathbf{a_e}$ and $\overset{\triangle}{\boldsymbol{m}}_\beta$, respectively. Then, by defining the *generalized stress* variable [92] as $\boldsymbol{\Sigma}=(\boldsymbol{S},\mathbf{r})$, Eqs. (A.2.19) and (A.2.20) can be finally cast as:

$$\dot{\boldsymbol{\Sigma}}=\boldsymbol{A}(\boldsymbol{\Sigma},\dot{\mathbf{E}})+\sum_{\beta=1}^{3}\dot\lambda^\beta\boldsymbol{\Xi}_\beta(\boldsymbol{\Sigma}),\tag{A.2.21}$$

where $\boldsymbol{A}(\boldsymbol{\Sigma},\dot{\mathbf{E}})=\big((\boldsymbol{C_e}+\mathbf{A_e}):\dot{\mathbf{E}},\mathbf{0}\big)$ and $\boldsymbol{\Xi}_\beta(\boldsymbol{\Sigma})=\big(-\boldsymbol{C_e}:\overset{\triangle}{\boldsymbol{M}}_\beta,\boldsymbol{D}\cdot\mathbf{h}_\beta\big)$.

The above equation, supplemented with the initial conditions $\boldsymbol{\Sigma}(t_0)=(\boldsymbol{S}_0,\mathbf{r}(\boldsymbol{\xi}_0))$, constitutes the initial value ODE system which governs the local behavior of the powder. The components of the generalized stress tensor $\boldsymbol{\Sigma}$ are the dependent variables and the rate of the Green-Lagrange strain tensor $\dot{\mathbf{E}}$ is the source term. The evolution of $\boldsymbol{\Sigma}$ is further restricted by the loading/unloading and consistency conditions, which in terms of $\boldsymbol{\Sigma}$ are written as

$$\dot\lambda^\beta\geq 0,\quad \phi^\beta(\boldsymbol{\Sigma})\leq 0,\tag{A.2.22}$$

$$\dot\lambda^\beta\phi^\beta(\boldsymbol{\Sigma})=0,\qquad(\text{no sum on }\beta),\tag{A.2.23}$$

$$\dot\lambda^\beta\dot\phi^\beta(\boldsymbol{\Sigma})=0,\qquad(\text{no sum on }\beta).\tag{A.2.24}$$

A.3 Continuum elastoplastic tangent moduli

During intervals of plastic loading, the plastic multipliers $\dot\lambda^\mu$ belonging to the *active set of constraints* $\mathbb{J}^{act}$ [93], i.e. $\dot\lambda^\mu>0$, can be obtained from the consistency condition $\dot\phi^\mu=0,\ \mu\in\mathbb{J}^{act}$:

$$\dot\phi^\mu=\frac{\partial\phi^\mu}{\partial\boldsymbol{\tau}}:\mathcal{L}_v\boldsymbol{\tau}+\frac{\partial\phi^\mu}{\partial\mathbf{r}}\cdot\dot{\mathbf{r}}=0,\ \ \mu\in\mathbb{J}^{act}.\tag{A.3.1}$$

Upon rearrangement, substitution of Eq.(A.2.10) and Eq.(A.2.19)into the above equation gives

$$\begin{aligned}\dot\phi^\mu&=\frac{\partial\phi^\mu}{\partial\boldsymbol{\tau}}:(\boldsymbol{c_e}+\mathbf{a_e}):\mathbf{d}-\sum_{\beta\in\mathbb{J}^{act}}\big(\overbrace{\frac{\partial\phi^\mu}{\partial\boldsymbol{\tau}}:\boldsymbol{c_e}:\overset{\triangle}{\boldsymbol{m}}_\beta-\frac{\partial\phi^\mu}{\partial\mathbf{r}}\cdot\boldsymbol{D}\cdot\mathbf{h}_\beta}^{N_{\mu\beta}}\big)\dot\lambda^\beta\\ &=\frac{\partial\phi^\mu}{\partial\boldsymbol{\tau}}:(\boldsymbol{c_e}+\mathbf{a_e}):\mathbf{d}-\sum_{\beta\in\mathbb{J}^{act}}N_{\mu\beta}\,\dot\lambda^\beta=0.\end{aligned}\tag{A.3.2}$$

Assuming that the component matrix of $N_{\mu\beta}$, defined as

$$N_{\mu\beta} = \frac{\partial \phi^{\mu}}{\partial \boldsymbol{\tau}} : \boldsymbol{c_e} : \overset{\triangle}{\boldsymbol{m}}_{\beta} - \frac{\partial \phi^{\mu}}{\partial \mathbf{r}} \cdot \boldsymbol{D} \cdot \mathbf{h}_{\beta}, \tag{A.3.3}$$

is invertible, the expression for the plastic multiplier $\dot{\lambda}^{\mu},\ \mu \in \mathbb{J}^{act}$ takes the following explicit form:

$$\dot{\lambda}^{\mu} = \sum_{\beta \in \mathbb{J}^{act}} N^{-1}_{\mu\beta} \big(\frac{\partial \phi^{\beta}}{\partial \boldsymbol{\tau}} : (\boldsymbol{c_e} + \mathbf{a_e}) \big) : \mathbf{d}, \quad \mu \in \mathbb{J}^{act}. \tag{A.3.4}$$

Inserting Eq.(A.3.4) into Eq.(A.2.10) yields a relation between the Lie derivative of the Kirchhoff stress and the rate of deformation tensor:

$$\mathcal{L}_v \boldsymbol{\tau} = \boldsymbol{c_{ep}} : \mathbf{d}, \tag{A.3.5}$$

where

$$\boldsymbol{c_{ep}} = \Big(\big(\boldsymbol{c_e} + \mathbf{a_e} \big) - \sum_{\beta} \sum_{\mu} N^{-1}_{\mu\beta}\, \boldsymbol{c_e} : \overset{\triangle}{\boldsymbol{m}}_{\mu} \otimes \frac{\partial \phi^{\beta}}{\partial \boldsymbol{\tau}} : (\boldsymbol{c_e} + \mathbf{a_e}) \Big), \quad \mu, \beta \in \mathbb{J}^{act}. \tag{A.3.6}$$

The fourth order tensor $\boldsymbol{c_{ep}}$ denotes is the *continuum elastoplastic tangent moduli* in the spatial configuration.

A.4 Derivation of the IMPLEX algorithmic elastoplastic tangent moduli

The spatial algorithmic tangent moduli is the fourth-order tensor satisfying:

$$\mathcal{L}_v \tilde{\boldsymbol{\tau}}_{n+1} = \tilde{\boldsymbol{c}}_{\boldsymbol{ep},n+1} : \mathcal{L}_v \mathbf{e}_{n+1} = \tilde{\boldsymbol{c}}_{\boldsymbol{ep},n+1} : \mathbf{d}_{n+1}. \tag{A.4.1}$$

wherein $\tilde{\boldsymbol{\tau}}_{n+1}$ is the stress tensor obtained from the following stress-update formula Eq.(3.3.20). We begin by defining the IMPLEX plastic strain tensor:

$$\tilde{\mathbf{e}}_{p,n+1} = \breve{\mathbf{e}}_{p,n} + \sum_{\beta=1}^{3} \Delta \tilde{\lambda}^{\beta}_{n+1} \tilde{\boldsymbol{m}}^{\beta}_{n+1}. \tag{A.4.2}$$

Using the definition (3.2.18) of trial stress, Eq.(3.3.20) can be rephrased as

$$\begin{aligned} \tilde{\boldsymbol{\tau}}_{n+1} &= \mathbf{F}_{n+1} \cdot \boldsymbol{S}_0 \cdot \mathbf{F}^{T}_{n+1} + \tilde{\boldsymbol{c}}_{\boldsymbol{e},n+1} : (\mathbf{e}_{n+1} - \tilde{\mathbf{e}}_{p,n+1}) \\ &= \mathbf{F}_{n+1} \cdot \boldsymbol{S}_0 \cdot \mathbf{F}^{T}_{n+1} + \tilde{\boldsymbol{c}}_{\boldsymbol{e},n+1} : \tilde{\mathbf{e}}_{e,n+1}. \end{aligned} \tag{A.4.3}$$

Applying the Lie derivative to the above expression leads to

$$\mathcal{L}_v \tilde{\boldsymbol{\tau}}_{n+1} = \mathbf{F}_{n+1} \cdot \overbrace{\frac{\partial \boldsymbol{S}_0}{\partial t_{n+1}}}^{=0} \cdot \mathbf{F}^{T}_{n+1} + \mathcal{L}_v \tilde{\boldsymbol{c}}_{\boldsymbol{e},n+1} : \tilde{\mathbf{e}}_{e,n+1} + \tilde{\boldsymbol{c}}_{\boldsymbol{e},n+1} : (\mathbf{d}_{n+1} - \mathcal{L}_v \tilde{\mathbf{e}}_{p,n+1}). \tag{A.4.4}$$

An expression for the second term on the right-hand side of the preceding equation is elaborated in section (A.1.2.1). The result takes the form

$$\begin{aligned}\mathcal{L}_v \boldsymbol{c_e} : \tilde{\mathbf{e}}_{e,n+1} &= \mathbf{a_e}(\tilde{\mathbf{e}}_{e,n+1}) : \mathbf{d}_{n+1} + \overbrace{\frac{\partial \tilde{\xi}^h_{n+1}}{\partial t_{n+1}}}^{=0} \frac{\partial \tilde{\boldsymbol{c}}_{\boldsymbol{e},n+1}}{\partial \xi^h} : \tilde{\mathbf{e}}_{e,n+1} \\ &= \mathbf{a_e}(\tilde{\mathbf{e}}_{e,n+1}) : \mathbf{d}_{n+1},\end{aligned} \tag{A.4.5}$$

where the fourth order tensor $\mathbf{a_e}$ is defined through equation Eq.(A.1.99). Note that the derivative $\partial \tilde{\xi}^h_{n+1}/\partial t_{n+1}$ vanishes in virtue of the extrapolated character of $\tilde{\xi}^h_{n+1}$, that is, $\tilde{\xi}^h_{n+1}$ does not depend on the deformation state at t_{n+1}.

The rightmost term in Eq.(A.4.4) can be expanded using Eq.(A.4.2):

$$\begin{aligned}\mathcal{L}_v \tilde{\mathbf{e}}_{p,n+1} &= \mathcal{L}_v \breve{\mathbf{e}}_{p,n} + \sum_{\beta=1}^{3} \overbrace{\frac{\partial \Delta\tilde{\lambda}^\beta_{n+1}}{\partial t_{n+1}}}^{=0} \tilde{\boldsymbol{m}}^\beta_{n+1} + \sum_{\beta=1}^{3} \Delta\tilde{\lambda}^\beta_{n+1} \mathcal{L}_v \tilde{\boldsymbol{m}}^\beta_{n+1} \\ &= \mathbf{F}_{n+1} \cdot \overbrace{\frac{\partial \mathbf{E}_{p,n}}{\partial t_{n+1}}}^{=0} \cdot \mathbf{F}^T_{n+1} + \sum_{\beta=1}^{3} \Delta\tilde{\lambda}^\beta_{n+1} \mathcal{L}_v \tilde{\boldsymbol{m}}^\beta_{n+1} \\ &= \sum_{\beta=1}^{3} \Delta\tilde{\lambda}^\beta_{n+1} \mathcal{L}_v \tilde{\boldsymbol{m}}^\beta_{n+1}.\end{aligned} \tag{A.4.6}$$

Hence, the task of obtaining the Lie derivative of $\tilde{\mathbf{e}}_{p,n+1}$ reduces to finding the Lie derivative of the plastic flow vectors associated to each surface, since

$$\partial \Delta\tilde{\lambda}^\beta_{n+1}/\partial t_{n+1} = 0.$$

The simplicity afforded by the use of the IMPLEX stress-update scheme is again manifest. In the context of a standard implicit integration procedure, the tightly coupled character of the governing equations may make the determination of a closed-form expression for the term $\partial \Delta\lambda^\beta_{n+1}/\partial t_{n+1}$ prohibitively complicated.

Applying the Lie derivative to the affine transformation Eq.(3.3.15) relating the plastic flow vector and the Kirchhoff stress tensor yields

$$\begin{aligned}\mathcal{L}_v \tilde{\boldsymbol{m}}^\beta_{n+1} &= \mathcal{L}_v(\tilde{\boldsymbol{A}}^\beta_{n+1} : \tilde{\boldsymbol{\tau}}_{n+1}) + \mathcal{L}_v \tilde{\boldsymbol{B}}^\beta_{n+1} \\ &= \mathcal{L}_v \tilde{\boldsymbol{A}}^\beta_{n+1} : \tilde{\boldsymbol{\tau}}_{n+1} + \tilde{\boldsymbol{A}}^\beta_{n+1} : \mathcal{L}_v \tilde{\boldsymbol{\tau}}_{n+1} + \mathcal{L}_v \tilde{\boldsymbol{B}}^\beta_{n+1}.\end{aligned} \tag{A.4.7}$$

According to the geometric issues pointed out in section (A.1.2), stress tensors are regarded as contravariant, whereas strain measures are covariant. The plastic flow vector $\tilde{\boldsymbol{m}}^\beta_{n+1}$ has the same tensorial character as the plastic strain tensor, that is, $\tilde{\boldsymbol{m}}^\beta_{n+1}$ is also covariant. Therefore, the fourth-order tensor $\tilde{\boldsymbol{A}}^\beta_{n+1}$ takes contravariant quantities to covariant quantities. Then, it follows that $\tilde{\boldsymbol{A}}^\beta_{n+1}$ is a *fully covariant* tensor (in contrast to the elasticity tensor $\tilde{\boldsymbol{c}}_{\boldsymbol{e},n+1}$, which is *fully contravariant*).

A general expression for the double contraction of a *fully covariant* fourth order tensor and a contravariant second order tensor is given in Eq.(A.1.108) of section A.1.2.2. Specializing this general expression for the case $A_{dev} = (\tilde{\boldsymbol{A}}^{\beta}_{n+1})_{dev} = 2$ and $A_{vol} = (\tilde{\boldsymbol{A}}^{\beta}_{n+1})_{vol} = 1/3\tilde{u}^{\beta}_{n+1}$ leads to the following result:

$$\begin{aligned}\mathcal{L}_v\tilde{\boldsymbol{A}}^{\beta}_{n+1} : \tilde{\boldsymbol{\tau}}_{n+1} &= \mathbf{a}_\tau(\tilde{u}^{\beta}_{n+1}, \tilde{\boldsymbol{\tau}}_{n+1}) : \mathbf{d}_{n+1} + \frac{\partial \tilde{u}^{\beta}_{n+1}}{\partial t_{n+1}} \frac{\partial \tilde{\boldsymbol{A}}^{\beta}_{n+1}}{\partial \tilde{u}^{\beta}_{n+1}} \\ &= \mathbf{a}_\tau(\tilde{u}^{\beta}_{n+1}, \tilde{\boldsymbol{\tau}}_{n+1}) : \mathbf{d}_{n+1},\end{aligned} \tag{A.4.8}$$

where

$$\mathbf{a}_\tau(\tilde{u}^{\beta}_{n+1}, \tilde{\boldsymbol{\tau}}_{n+1}) = 2\left(\frac{1}{3}(\tilde{u}^{\beta}_{n+1} - 2)\big(\mathbf{1} \otimes \tilde{\boldsymbol{\tau}}_{n+1} + \operatorname{tr}\tilde{\boldsymbol{\tau}}_{n+1}\boldsymbol{I}\big) + 4\,\boldsymbol{\mathcal{I}}_s(\tilde{\boldsymbol{\tau}}_{n+1})\right). \tag{A.4.9}$$

The remaining term in Eq.(A.4.7) is given by

$$\mathcal{L}_v\tilde{\boldsymbol{B}}^{\beta}_{n+1} = \frac{\partial \tilde{v}^{\beta}_{n+1}}{\partial t_{n+1}}\,\mathbf{1} + \tilde{v}^{\beta}_{n+1}\mathcal{L}_v\mathbf{1}. \tag{A.4.10}$$

The first term on the right-hand side of the above equation is zero, since $\tilde{v}^{\beta}_{n+1}$ depends upon $\tilde{\xi}^{h}_{n+1}$ and $\tilde{\xi}^{h}_{n+1}$. The second term involves the Lie derivative of the *covariant* identity tensor, that is, the metric tensor. Then, according to Eq.(A.1.72), Eq.(A.4.10) can be written as

$$\mathcal{L}_v\tilde{\boldsymbol{B}}^{\beta}_{n+1} = 2\,\tilde{v}^{\beta}_{n+1}\mathbf{d}_{n+1}. \tag{A.4.11}$$

Inserting Eq.(A.4.11) and Eq.(A.4.8) into Eq.(A.4.7) yields

$$\mathcal{L}_v\tilde{\boldsymbol{m}}^{\beta}_{n+1} = \big(\mathbf{a}_\tau(\tilde{u}^{\beta}_{n+1}, \tilde{\boldsymbol{\tau}}_{n+1}) + 2\,\tilde{v}^{\beta}_{n+1}\big) : \mathbf{d}_{n+1} + \tilde{\boldsymbol{A}}^{\beta}_{n+1} : \mathcal{L}_v\tilde{\boldsymbol{\tau}}_{n+1}. \tag{A.4.12}$$

The derivative $\mathcal{L}_v\tilde{\mathbf{e}}_{p,n+1}$ is then obtained by using the above in Eq.(A.4.6)

$$\begin{aligned}\mathcal{L}_v\tilde{\mathbf{e}}_{p,n+1} = &\Big(\sum_{\beta=1}^{3}\Delta\tilde{\lambda}^{\beta}_{n+1}\big(\mathbf{a}_\tau(\tilde{u}^{\beta}_{n+1}, \tilde{\boldsymbol{\tau}}_{n+1}) + 2\,\tilde{v}^{\beta}_{n+1}\big)\Big) : \mathbf{d}_{n+1} \\ &+ \Big(\sum_{\beta=1}^{3}\Delta\tilde{\lambda}^{\beta}_{n+1}\tilde{\boldsymbol{A}}^{\beta}_{n+1}\Big) : \mathcal{L}_v\tilde{\boldsymbol{\tau}}_{n+1}.\end{aligned} \tag{A.4.13}$$

After substituting (A.4.13) and (A.4.5) into Eq.(A.4.4), an expression for the *spatial algorithmic tangent tensor* is finally achieved by collecting terms involving $\mathcal{L}_v\tilde{\boldsymbol{\tau}}_{n+1}$ and $\mathbf{d}_{n+1}$:

$$\begin{aligned}&\left(\boldsymbol{I} + \tilde{\boldsymbol{c}}_{\boldsymbol{e},n+1} : \sum_{\beta=1}^{3}\Delta\tilde{\lambda}^{\beta}_{n+1}\tilde{\boldsymbol{A}}^{\beta}_{n+1}\right) : \mathcal{L}_v\tilde{\boldsymbol{\tau}}_{n+1} \\ &= \left(\mathbf{a}_{\mathbf{e}}(\tilde{\mathbf{e}}_{e,n+1}) + \tilde{\boldsymbol{c}}_{\boldsymbol{e},n+1} : \Big(\boldsymbol{I} - \sum_{\beta=1}^{3}\Delta\tilde{\lambda}^{\beta}_{n+1}\big(\mathbf{a}_\tau(\tilde{u}^{\beta}_{n+1}, \tilde{\boldsymbol{\tau}}_{n+1}) + 2\,\tilde{v}^{\beta}_{n+1}\boldsymbol{I}\big)\Big)\right) : \mathbf{d}_{n+1} \Rightarrow\end{aligned} \tag{A.4.14}$$

$$\tilde{\boldsymbol{c}}_{\boldsymbol{ep},n+1} = \tilde{\boldsymbol{R}}_{n+1}^{-1} : \left(\mathbf{a}_{\mathbf{e}}(\tilde{\mathbf{e}}_{e,n+1}) + \tilde{\boldsymbol{c}}_{\boldsymbol{e},n+1} : \left(\boldsymbol{I} - \sum_{\beta=1}^{3} \Delta\tilde{\lambda}_{n+1}^{\beta} \tilde{\boldsymbol{z}}_{n+1}^{\beta}(\tilde{\boldsymbol{\tau}}_{n+1}) \right) \right), \quad \text{(A.4.15)}$$

where

$$\tilde{\boldsymbol{R}}_{n+1} = \boldsymbol{I} + \tilde{\boldsymbol{c}}_{\boldsymbol{e},n+1} : \sum_{\beta=1}^{3} \Delta\tilde{\lambda}_{n+1}^{\beta} \tilde{\boldsymbol{A}}_{n+1}^{\beta}, \quad \text{(A.4.16)}$$

and

$$\tilde{\boldsymbol{z}}_{n+1}^{\beta}(\tilde{\boldsymbol{\tau}}_{n+1}) = \mathbf{a}_{\tau}(\tilde{u}_{n+1}^{\beta}, \tilde{\boldsymbol{\tau}}_{n+1}) + 2\,\tilde{v}_{n+1}^{\beta} \boldsymbol{I}. \quad \text{(A.4.17)}$$

Appendix B

Analytical study of the compaction of a cylindrical specimen

B.1 Pressing stage

This appendix is intended to provide some insight into the underlying inelastic large strain theory. It can be skipped by the expert reader, whereas for the uninitiated reader it may result of great assistance to grasp the theory and to acquire some familiarity with terms like deformation gradient, rate of deformation tensor or plastic flow rule, which are not of common usage in the daily engineering practice.

For this purpose, consider a cylindrical reference configuration Ω_0 (that may be identified with the die cavity) of height H and radius R. The body is deformed by prescribed displacements on its upper and lateral surfaces. The height and radius at any deformed state (current configuration Ω_t) are given by the functions $h = h(t)$ and $r = r(t)$, respectively. The deformation throughout the domain is assumed homogeneous, and it is characterized by the following deformation mapping:

$$\begin{aligned} \tilde{x}^1 &= \frac{r(t)}{R}\tilde{X}^1 = \Lambda_r(t)\tilde{X}^1 \\ \tilde{x}^2 &= \frac{h(t)}{H}\tilde{X}^2 = \Lambda_z(t)\tilde{X}^2 \\ \tilde{x}^3 &= \tilde{X}^3, \end{aligned} \tag{B.1.1}$$

where $\{\tilde{x}^a\}$ and $\{\tilde{X}^A\}$ denote cylindrical coordinate systems and Λ_r and Λ_z are the stretches. Inasmuch as the metric tensor associated to a cylindrical coordinate system is not the identity, it is convenient to revert to a cartesian coordinate system

by employing the following transformation:

$$\begin{aligned} X^1 &= \tilde{X}^1 \\ X^2 &= \tilde{X}^2 \\ X^3 &= \tilde{X}^3 \tilde{X}^1, \end{aligned} \tag{B.1.2}$$

(the same transformation holds for the coordinate system $\{\tilde{x}^a\}$), with $\tilde{X}^3 = 0$. The deformation mapping in these coordinate systems can be written as

$$\begin{aligned} x^1 &= \varphi^1(\mathbf{X}, t) = \Lambda_r(t) X^1 \\ x^2 &= \varphi^2(\mathbf{X}, t) = \Lambda_z(t) X^2 \\ x^3 &= \varphi^3(\mathbf{X}, t) = \frac{x^1}{X^1} X^3 = \Lambda_r(t) X^3. \end{aligned} \tag{B.1.3}$$

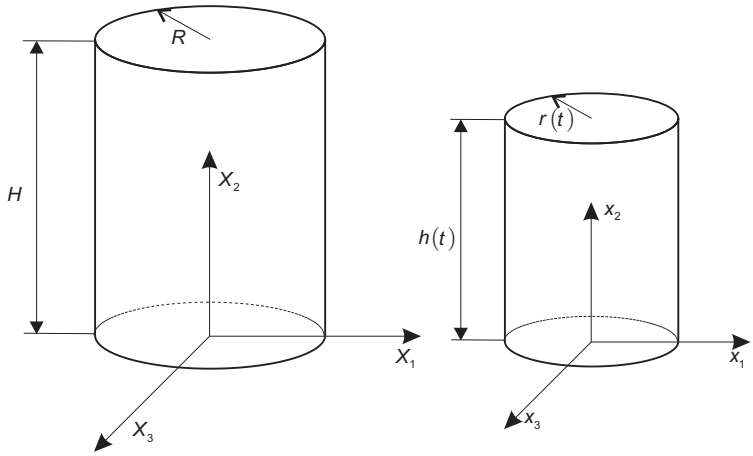

Figure B.1

The collection of kinematics measures defined in section 2.2 can be straightforwardly derived from the above mapping. The matrix of the deformation gradient tensor $\mathbf{F}$, defined in (2.2.3), is given by

$$\mathbf{F} = \begin{bmatrix} \Lambda_r(t) & 0 & 0 \\ 0 & \Lambda_z(t) & 0 \\ 0 & 0 & \Lambda_r(t) \end{bmatrix} = \operatorname{diag}(\Lambda_r, \Lambda_z, \Lambda_r), \tag{B.1.4}$$

where $\operatorname{diag}(\bullet, \bullet, \bullet)$ is the shorthand notation for a diagonal matrix. The Green-Lagrange and the Almansi strain tensors have the following expressions:

$$\mathbf{E} = \frac{1}{2}\left(\mathbf{F}^T \cdot \mathbf{F} - \mathbf{1}\right) = \frac{1}{2}\operatorname{diag}(\Lambda_r^2 - 1, \Lambda_z^2 - 1, \Lambda_r^2 - 1), \tag{B.1.5}$$

$$\mathbf{e} = \frac{1}{2}\left(\mathbf{1} - \mathbf{F}^{-T}\cdot\mathbf{F}^{-1}\right) = \frac{1}{2}\mathrm{diag}\,(1-\Lambda_r^{-2}, 1-\Lambda_z^{-2}, 1-\Lambda_r^{-2}), \tag{B.1.6}$$

respectively.
The rate of deformation tensor assumes the form:

$$\mathbf{d} = sym(\mathbf{l}) = \mathbf{l} = \dot{\mathbf{F}}\cdot\mathbf{F}^{-1} = \mathrm{diag}\,(\frac{\dot{\Lambda}_r}{\Lambda_r}, \frac{\dot{\Lambda}_z}{\Lambda_z}, \frac{\dot{\Lambda}_r}{\Lambda_r}). \tag{B.1.7}$$

The volumetric and deviatoric parts of $\mathbf{d}$ are of crucial importance in the formulation of the constitutive model. They are expressible as

$$\mathrm{tr}\,\mathbf{d} = 2\frac{\dot{\Lambda}_r}{\Lambda_r} + \frac{\dot{\Lambda}_z}{\Lambda_z}, \tag{B.1.8}$$

$$dev\,\mathbf{d} = \frac{1}{3}(\frac{\dot{\Lambda}_r}{\Lambda_r} - \frac{\dot{\Lambda}_z}{\Lambda_z})\,\mathrm{diag}\,(1,-2,1) \Rightarrow \|dev\,\mathbf{d}\| = \sqrt{\frac{2}{3}}|\frac{\dot{\Lambda}_r}{\Lambda_r} - \frac{\dot{\Lambda}_z}{\Lambda_z}|. \tag{B.1.9}$$

Suppose now that the deformation is such that the material is subjected to a monotonically increasing compressive state, which ensures that the stress remains on the elliptical cap surface throughout the deformation. In such situation, the plastic counterpart of the rate of deformation tensor (see section 2.5.3) takes the form

$$\mathbf{d}_p = \dot{\lambda}^e\left(2dev\,\boldsymbol{\tau} + \frac{2}{3}s_2^2 p\mathbf{1}\right), \tag{B.1.10}$$

or in volumetric and deviatoric components

$$\mathrm{tr}\,\mathbf{d}_p = 2\dot{\lambda}^e s_2^2 p, \tag{B.1.11}$$

$$\|dev\,\mathbf{d}_p\| = 2\dot{\lambda}^e q. \tag{B.1.12}$$

One of the basic assumption listed earlier (section 2.2.1), and in which relies in some extent the simplicity of the formulation, states that the magnitude of the recoverable strains are small in comparison with the permanent strain acquired during the pressing stage ($\mathbf{d} \approx \mathbf{d}_p$). Therefore, it may be legitimately written the following approximation:

$$\mathrm{tr}\,\mathbf{d} \approx \mathrm{tr}\,\mathbf{d}_p \;\Rightarrow\; 2\frac{\dot{\Lambda}_r}{\Lambda_r} + \frac{\dot{\Lambda}_z}{\Lambda_z} \approx 2\dot{\lambda}^e s_2^2 p, \tag{B.1.13}$$

$$\|dev\,\mathbf{d}\| \approx \|dev\,\mathbf{d}_p\| \;\Rightarrow\; \sqrt{\frac{2}{3}}|\frac{\dot{\Lambda}_r}{\Lambda_r} - \frac{\dot{\Lambda}_z}{\Lambda_z}| \approx 2\dot{\lambda}^e q. \tag{B.1.14}$$

Dividing Eq.(B.1.14) by Eq.(B.1.13), the dependence on the plastic multiplier $\dot{\lambda}^e$ is eliminated:

$$\frac{\sqrt{\frac{2}{3}}|\frac{\dot{\Lambda}_r}{\Lambda_r} - \frac{\dot{\Lambda}_z}{\Lambda_z}|}{2\frac{\dot{\Lambda}_r}{\Lambda_r} + \frac{\dot{\Lambda}_z}{\Lambda_z}} \approx \frac{q}{s_2^2 p} \tag{B.1.15}$$

The usefulness of approximation (B.1.15) lies on the fact that it relates directly kinematic measures (stretch ratios) with stress states. For an axial die compaction (with perfectly rigid die), the radial stretch ratio is the unity at any time $\Lambda_r = 1$. Hence, expression (B.1.15) reads in this case

$$q \approx -\sqrt{\frac{2}{3}} s_2^2 p. \tag{B.1.16}$$

Furthermore, a physical meaning can be attached to variable s_2 if one takes into account that

$$p = \frac{1}{3}(\tau_z + 2\tau_r) = \frac{1}{3}\tau_z(1 + 2k_{tr}), \tag{B.1.17}$$

$$q = \sqrt{\frac{2}{3}}|\tau_z - \tau_r| = \sqrt{\frac{2}{3}}\tau_z(1 - k_{tr}), \tag{B.1.18}$$

where k_{tr} is the *pressure transmission coefficient*, defined as the ratio between the radial pressure exerted on the die τ_r and the axial stress τ_z. Inserting (B.1.17) and (B.1.18) in (B.1.16), one gets

$$s_2 \approx \sqrt{\frac{3(1 - k_{tr})}{1 + 2k_{tr}}}, \tag{B.1.19}$$

an expression which reveals that, ignoring the influence of elastic strains, the elliptic cap parameter s_2 depends solely on the pressure transmission coefficient, and, therefore, it can be easily calibrated in a uniaxial die compaction test by monitoring axial and radial pressures throughout the test.

The other parameter governing the size of the elliptical cap surface, s_1, admits an immediate interpretation in the context of an isostatic test. In an such test, the same pressure is applied in the axial and radial direction ($\tau_z = \tau_r$), hence $q = 0$. According to approximation (B.1.14), this hydrostatic condition corresponds in terms of prescribed displacements to:

$$\frac{\dot{\Lambda}_r}{\Lambda_r} = \frac{\dot{\Lambda}_z}{\Lambda_z}, \tag{B.1.20}$$

and the Jacobian determinant J takes the form

$$J = \det(\mathbf{F}) = \Lambda_z^3. \tag{B.1.21}$$

Since the deviatoric stress magnitude q is zero, and by virtue of plastic consistency, the stress state is constrained to lie on the interception point of the elliptical cap surface and the mean stress axis. Hence,

$$p = \frac{1}{3}\mathrm{tr}\,\boldsymbol{\tau} = \frac{1}{3}(\tau_z + 2\tau_r) = \tau_z = -s_1. \tag{B.1.22}$$

The above expression can be recast in terms of Cauchy, or true, stresses:

$$s_1 = -\tau_z = -J\sigma_z = -\Lambda_z^3\sigma_z. \tag{B.1.23}$$

Hence, the s_1 parameter can be obtained directly in an isostatic test by measuring the hydrostatic pressure applied to the cell for each level of density. Nevertheless, if it is not possible to carry out such experiment, s_1 can be calibrated indirectly from an uniaxial die compaction test through the following expression

$$s_1 = -\sqrt{\frac{2}{3}s_2^2 + 1}\ \ p, \tag{B.1.24}$$

which has been deduced by simply inserting the yield condition $\phi^e = 0$ in Eq.(B.1.16).

B.2 Assessment of the smallness of elastic strains

The above particular case of isotropic furnishes a suitable framework for the assessment of the hypothesis of elastic small strains. First, the gradient of deformation (B.1.4) in this case takes the form

$$\mathbf{F} = \overbrace{\mathrm{diag}\,(\Lambda_r, \Lambda_z, \Lambda_r)}^{\Lambda_z=\Lambda_r=\Lambda} = \Lambda\,\mathrm{diag}\,(1,1,1). \tag{B.2.1}$$

In virtue of the multiplicative decomposition A.1.21, we may legitimately write

$$\mathbf{F} = \mathbf{F}_e \cdot \mathbf{F}_p = \Lambda_e \Lambda_p \mathrm{diag}\,(1,1,1), \tag{B.2.2}$$

where the stretches Λ_e and Λ_p are associated to the elastic and plastic deformation, respectively. The elastic Almansi strain tensor, given in Eq.(A.1.29), can be written as

$$\mathbf{e}_e = \frac{\Lambda_e^2 - 1}{2\,\Lambda_e^2}\mathrm{diag}\,(1,1,1). \tag{B.2.3}$$

Taking the trace of the above expression, we obtain

$$\mathrm{tr}\,\mathbf{e}_e = 3\frac{\Lambda_e^2 - 1}{2\,\Lambda_e^2}. \tag{B.2.4}$$

Similarly, the elastic counterpart of the rate of deformation tensor reads

$$\mathbf{d}_e = \dot{\mathbf{F}}_e \cdot \mathbf{F}_e^{-1} = \frac{\dot{\Lambda}_e}{\Lambda_e}\mathrm{diag}\,(1,1,1), \tag{B.2.5}$$

and its trace

$$\mathrm{tr}\,\mathbf{d}_e = 3\,\frac{\dot{\Lambda}_e}{\Lambda_e}. \tag{B.2.6}$$

The following results is crucial for the assessment of the hypothesis of small strain:

Proposition B.2.1. *In a monotonic (hydrostatic compressive) loading history the ratio between relative density and internal hardening variable is bounded by*

$$\frac{\eta}{\xi^h} \leq \boldsymbol{e}^{\frac{s_1}{\kappa^e}}. \tag{B.2.7}$$

Proof. First, let the definition of ξ^h be recast in terms of $\mathbf{d}$ and $\mathbf{d}_e$, i.e.

$$\xi^h = \eta_0 \, e^{-\int_{t_0}^{t} \operatorname{tr} \mathbf{d}_p \, dt} = \eta_0 \, e^{-\int_{t_0}^{t} \operatorname{tr} \mathbf{d} \, dt} \, e^{\int_{t_0}^{t} \operatorname{tr} \mathbf{d}_e \, dt} \tag{B.2.8}$$

Taking into account that, by definition, the relative density is given by

$$\eta = \eta_0 \, e^{-\int_{t_0}^{t} \operatorname{tr} \mathbf{d} \, dt}, \tag{B.2.9}$$

then Eq.(B.2.8) can be expressed as

$$\frac{\eta}{\xi^h} = e^{-\int_{t_0}^{t} \operatorname{tr} \mathbf{d}_e \, dt}. \tag{B.2.10}$$

It follows from Eq.(B.2.6) that the integral in Eq.(B.2.10) can be evaluated as:

$$\int_{t_0}^{t} \operatorname{tr} \mathbf{d}_e \, dt = \int_{t_0}^{t} 3 \, \frac{\dot{\Lambda}_e}{\Lambda_e} \, dt = 3 \log \Lambda_e(t), \tag{B.2.11}$$

Expanding the above expression around $\Lambda_e(t_0) = 1$, we get

$$\int_{t_0}^{t} \operatorname{tr} \mathbf{d}_e \, dt = -3 \, (\sum_{k=1}^{\infty} \frac{(1-\Lambda_e)^k}{k}) \leq 0, \quad \text{for} \quad \Lambda_e \leq 1. \tag{B.2.12}$$

The concept of expansion is also employed for expressing $\operatorname{tr} \mathbf{e}_e$ as a polynomial:

$$\operatorname{tr} \mathbf{e}_e = 3 \frac{\Lambda_e^2 - 1}{2 \, \Lambda_e^2} = -3 \, (\sum_{k=1}^{\infty} \frac{k+1}{2} (1-\Lambda_e)^k) \leq 0 \quad \text{for} \quad \Lambda_e \leq 1. \tag{B.2.13}$$

Subtracting Eq.(B.2.12) from Eq.(B.2.13), we get upon rearrangement

$$\operatorname{tr} \mathbf{e}_e - \int_{t_0}^{t} \operatorname{tr} \mathbf{d}_e \, dt = -3 \, (\sum_{k=1}^{\infty} (\frac{1-k}{2} (1-\Lambda_e)^k). \tag{B.2.14}$$

From the above equation, it follows that

$$|\operatorname{tr} \mathbf{e}_e| \geq |\int_{t_0}^{t} \operatorname{tr} \mathbf{d}_e \, dt|. \tag{B.2.15}$$

The condition of plastic consistency indicates that $p = -s_1$. Considering the constitutive relationship $p = \kappa^e \operatorname{tr} \mathbf{e}_e$, we finally get

$$\begin{aligned} \frac{\eta}{\xi^h} &= e^{-\int_{t_0}^{t} \operatorname{tr} \mathbf{d}_e \, dt} = e^{|\int_{t_0}^{t} \operatorname{tr} \mathbf{d}_e \, dt|} \\ &\leq e^{|\operatorname{tr} \mathbf{e}_e|} = e^{\frac{s_1}{\kappa^e}}. \end{aligned} \tag{B.2.16}$$

□

B.3 Release of axial pressure

This appendix is intended to analytically study the stress state on a cylindrical specimen during the gradual removal of the upper punch. In particular, our interest lies in deriving an expression whereby the radial pressure exerted by the die on the compact is related to the upper punch axial pressure.

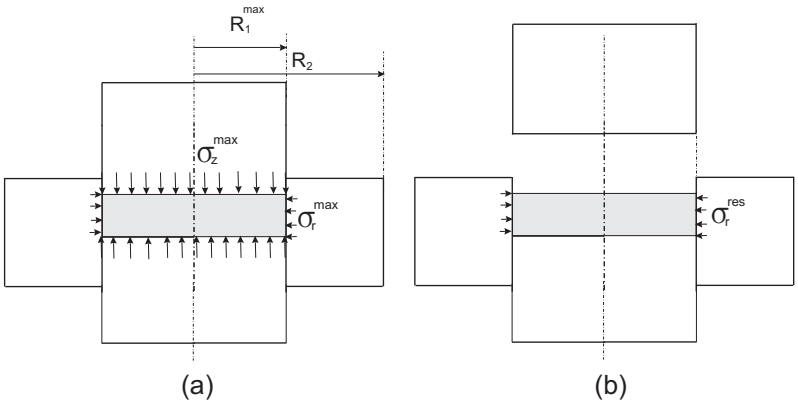

Figure B.2 *Compaction of a cylindrical specimen. (a) End of pressing stage. (b) Total removal of the upper punch.*

The powder is pressed by the downward motion of the upper punch while the lower punch and the die remain stationary. Friction effects are neglected by considering either a cylindrical specimen with a small height to diameter ratio or a sufficiently efficient lubrication. The stress at the end of the pressing stage is characterized by its radial and axial components[1] σ_r^{max} and σ_z^{max}, respectively. During pressing, the specimen tends to expand radially. The extent of such expansion at the end of the pressing stage depends upon the maximum radial pressure σ_r^{max} and the characteristics of the die. As the die is viewed as an isotropic elastic body, with Young's modulus E_{tool} and Poisson's ratio ν_{tool}, the magnitude of this expansion can be expressed[2] as

$$\frac{R_1^{max} - R_1^0}{R_1^0} = -\frac{\sigma_r^{max}}{K_{tool}}, \tag{B.3.1}$$

where R_1^0 is the initial inner radius of the die. The constant K_{tool} is a measure of the stiffness of the die in the radial direction. In practice, this constant has to be obtained by undertaking a linear finite element analysis (see figure B.3). In the absence of such computations, K_{tool} may be alternatively estimated on the basis of a stress analysis of a thick walled cylinder submitted to the action of uniformly

[1] As already pointed out, the hypothesis of small strains can be legitimately used in describing the deformation state during the post-pressing operations by simply taking as *reference configuration* the placement of the body at the end of the pressing stage. Consequently, the Kirchhoff stress tensor $\boldsymbol{\tau}$ appearing in the constitutive equations can be directly replaced by the Cauchy or *true* stress tensor $\boldsymbol{\sigma}$.

[2] It is further assumed that this expansion is approximately uniform along the axial direction.

distributed internal pressure (Timoshenko [101]):

$$\frac{1}{K_{tool}} = \frac{R_1}{E_{tool}} \left(\frac{R_1^2 + R_2^2}{R_2^2 - R_1^2} + \nu_{tool} \right). \tag{B.3.2}$$

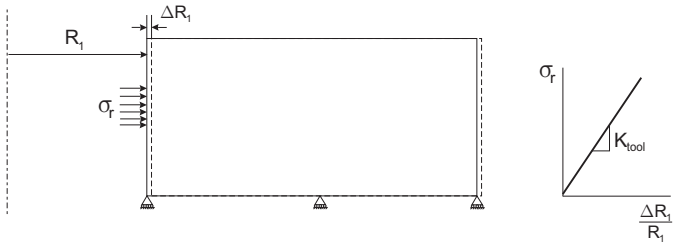

Figure B.3 *Stiffness of the die in the radial direction.*

Gradual removal of axial pressing force causes radial pressure to decrease and, as a consequence, the die tends to revert to its initial dimensions. However, the compact offers some resistance to the contracting tendency of the inner surface of the die. For a given decrease in axial pressure $\Delta\sigma_z = \sigma_z - \sigma_z^{max}$, the corresponding decrease in radial pressure $\Delta\sigma_r = \sigma_r - \sigma_r^{max}$ can be easily obtained by presuming that elastic conditions prevail on the compact during this process. Indeed, according to the Hooke's law (see Eq.(2.4.5) in 2.4), the radial component of the strain tensor can be written as

$$\epsilon_r = \frac{R_1 - R_1^{max}}{R_1^0} = \frac{1}{E^e}(\Delta\sigma_r - \nu^e(\Delta\sigma_\theta + \Delta\sigma_z)). \tag{B.3.3}$$

where $R_1 - R_1^{max}$ symbolizes the contraction of the die . The radial stress is assumed to be constant along the radial direction. Hence, in virtue of the momentum balance equation, we have

$$\frac{\partial\sigma_r}{\partial r} + \frac{\sigma_r - \sigma_\theta}{r} = 0 \;\Rightarrow\; \sigma_r = \sigma_\theta, \tag{B.3.4}$$

where σ_θ denotes the circumferential stress. Inserting the above result into Eq.(B.3.3), we can write

$$\frac{R_1 - R_1^{max}}{R_1^0} = \frac{1}{E^e}((1 - \nu^e)\Delta\sigma_r - \nu^e\Delta\sigma_z). \tag{B.3.5}$$

The contraction of the die is related to the decrease in radial pressure through the constant K_{tool}. Therefore,

$$-\frac{\Delta\sigma_r}{K_{tool}} = \frac{1}{E^e}((1 - \nu^e)\Delta\sigma_r - \nu^e\Delta\sigma_z). \tag{B.3.6}$$

Finally, upon rearrangement, it follows from the above that:

$$\Delta\sigma_r = M_{ul}\Delta\sigma_z, \tag{B.3.7}$$

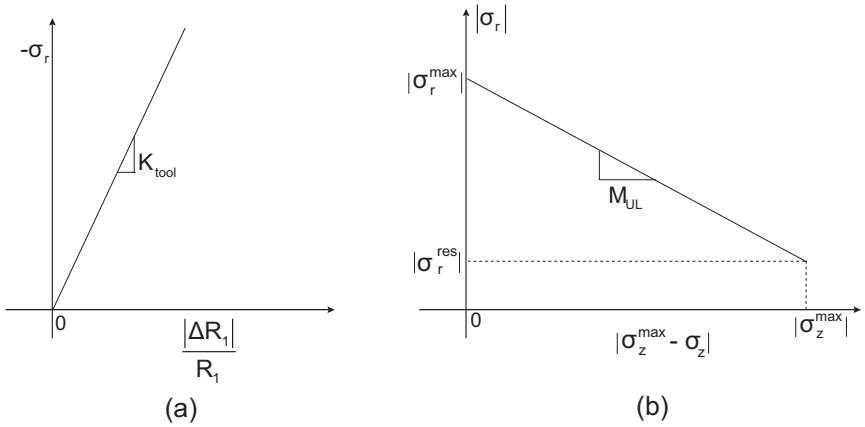

Figure B.4 *(a) Radial pressure as a function of the radial expansion of the compact. The (constant) slope K_{tool} depends on the elastic properties of the powder and on the elastic properties and geometry of the die. (b) Radial pressure as a function of the decrease in axial pressure.*

where

$$M_{ul} = \frac{\nu^e}{(1-\nu^e) + \dfrac{E^e}{K_{tool}}}. \tag{B.3.8}$$

The parameter M_{ul} gives an indication of how the decrease in axial load affects the magnitude of the pressure exerted on the die. The dependence of M_{ul} on the value of the Young's modulus of the compact is depicted in figure B.5.a, for a die stiffness[3] $K_{tool} = 470600 MPa$. According to this graph, a change in almost one order of magnitude in E^e, from $20000\,MPa$ to $160000\,MPa$, induces a change in M_{ul} of 0.1. In the limiting case of total release of axial load, the pressure exerted on the die can be derived from Eq.(B.3.7) by setting $\Delta\sigma_z = -\sigma_z^{max}$:

$$\sigma_r^{res} = \sigma_r^{max} - M_{ul}\sigma_z^{max}. \tag{B.3.9}$$

In order to gain additional insight into the representation and interpretation of stress histories in the $p-q$ plane (deviatoric vs. mean stress), it proves instructive to plot the evolution of the stress state during the gradual release of axial load on this plane (see figure B.5.b.). The path emanates from point A, which corresponds to the end of the pressing stage, and, therefore, lies on the elliptical yield surface. Then the stress state traces a piecewise linear path ABC. A noteworthy feature of this path is the kink exhibited at point B, which arises because of the positiveness of the deviatoric stress measure (see Eq.(B.1.18)). At this point, consequently, $\sigma_r = \sigma_z$, whereas at point C we have $\sigma_z = 0$. The equation for the slope L_{ul} can be obtained by inserting Eq.(B.3.9) in Eqs. Eq.(B.1.17) and Eq.(B.1.18). After some

[3]This value corresponds to the stiffness computed in the example shown in section 4.3.

manipulation, we get

$$L_{ul} = \frac{\sqrt{6}(1 - M_{ul})}{1 + 2M_{ul}}. \tag{B.3.10}$$

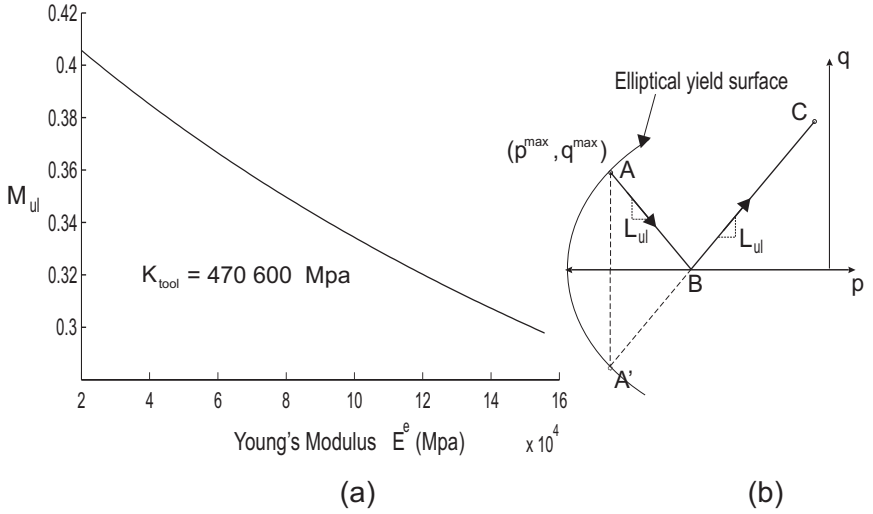

Figure B.5 *(a) Ratio decrease in radial pressure to decrease in axial pressure during axial load release (M_{ul}) as a function of the Young's modulus of the green compact. (b) Representation on the $p - q$ plane (mean-deviatoric stresses) of the path traced by the stress during axial load release.*

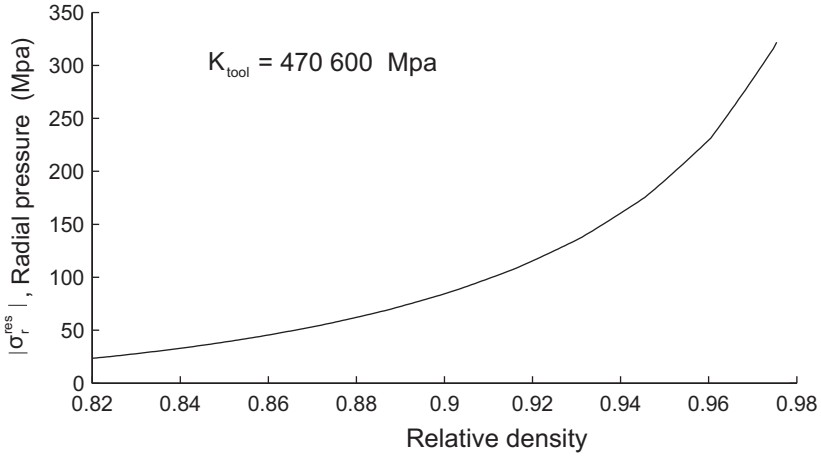

Figure B.6 *Radial stress upon total removal of applied axial force versus final density for Distaloy AE powder. Analytical prediction for a die radial stiffness $K_{tool} = 470600 MPa$.*

By means of Eqs. (B.1.16) to (B.1.19), the axial and radial stresses at the end

of the pressing stage are expressible in terms of the attained (relative) density η [4]:

$$\sigma_z^{max} = \frac{\eta}{\eta_0}\sqrt{\frac{2s_2^2(\eta)+3}{3}}\, s_1(\eta), \tag{B.3.11}$$

$$\sigma_r^{max} = k_{tr}(\eta)\sigma_z^{max} = \frac{3-s_2^2(\eta)}{2s_2^2(\eta)+3}\sigma_z^{max}(\eta), \tag{B.3.12}$$

where η_0 is the fill relative density. Thus, a relation between radial stress and final density can be constructed by combining (B.3.11), (B.3.12) and (B.3.9). This relation is plotted in figure B.6 for the Distaloy AE powder used for calibrating the model in Chapter 2.

[4] As customary, we invoke the approximation $\xi^h \approx \eta$, that is, the internal hardening variable is practically identified with the relative density.

Appendix C

Thermodynamic aspects

C.1 Fulfilment of the Clausius-Duhem inequality

In section 2.3, the existence of a Helmholtz free energy function ψ was postulated. The additive decomposition for this free energy function was also set forth, $\psi = \psi_0 + \psi_e + \psi_p$. Thus far, however, only the functional form of its elastic counterpart $\psi_e = \psi_e(\xi^h)$ has been outlined (see Eq.(2.4.1)). In the establishment of the hardening and softening laws, we were compelled by mathematical difficulties to disregard this aspect, and these constitutive laws were presented as simple empirical correlations, without invoking any thermodynamic potential for their derivation. Thus, it is natural to inquire at this point whether this view toward pragmatism has not induced a thermodynamic inconsistency in our formulation or, in other words, our constitutive model does satisfy the requirement of positive dissipation (see Eq.(2.3.7)):

$$\mathcal{D} = \boldsymbol{\tau} : \mathbf{d}_p - \overbrace{(\frac{\partial \psi_e}{\partial \xi^h} + \frac{\partial \psi_p}{\partial \xi^h})\dot{\xi}^h}^{\dot{\psi}_h} - \overbrace{\frac{\partial \psi_p}{\partial \xi^s}\dot{\xi}^s}^{\dot{\psi}_s} \geq 0. \tag{C.1.1}$$

The associated character of the plastic flow on the elliptical cap and the Von Mises surface, together with the remarks made in section 2.5.3 regarding the plastic flow on the Drucker-Prager surface, ensures the positiveness of the rate of plastic work per unit reference volume $\boldsymbol{\tau} : \mathbf{d}_p$. The term $\dot{\psi}_s$ accounts for the release of energy associated with softening. In this case, the thermodynamic conjugate $\dfrac{\partial \psi_p}{\partial \xi^s}$ of the internal softening variable ξ^s can be readily identified as the variable c_s, defined in Eq.(2.5.78):

$$\frac{\partial \psi_p}{\partial \xi^s} = c_s = c_0(e^{\frac{H_0(\xi^s - \xi^{s0})}{c_0}} - 1). \tag{C.1.2}$$

Since $\dot{\psi}_s \leq 0$, the worst conceivable circumstances for the satisfaction of inequality

(C.1.1) is when $\dot{\psi}_s = 0$. Therefore, inequality (C.1.1) reduces to

$$\boldsymbol{\tau} : \mathbf{d}_p \geq \frac{\partial \psi_e}{\partial \xi^h}\dot{\xi}^h + \frac{\partial \psi_p}{\partial \xi^h}\dot{\xi}^h, \tag{C.1.3}$$

i.e., the rate at which energy is *stored* in the powder structure cannot exceed the rate at which plastic work is supplied.

As stated by Eq.(2.5.60), the material becomes stiffer as densification progresses. This is reflected also in an increase of internal energy, given by the first term of the right hand side of inequality (C.1.3):

$$\frac{\partial \psi_e}{\partial \xi^h}\dot{\xi}^h = \frac{1}{2}(3\frac{\partial \kappa^e}{\partial \xi^h}\mathrm{tr}^2\,\mathbf{e}_e + 2\frac{\partial \mu^e}{\partial \xi^h}\,dev\,\mathbf{e}_e : dev\,\mathbf{e}_e)\dot{\xi}^h. \tag{C.1.4}$$

Albeit the increase of the bulk and shear modulus, represented by the derivatives $\frac{\partial \kappa^e}{\partial \xi^h}$ and $\frac{\partial \mu^e}{\partial \xi^h}$, is of the same order as the hardening parameter $\frac{\partial s_1}{\partial \xi^h}$, they have weighting factors which are quadratic in the elastic strains, a fact that renders the energetic contribution $\frac{\partial \psi_e}{\partial \xi^h}$ negligible in comparison with the other term of $\dot{\psi}_h$. Therefore, attention is restricted to prove that

$$\mathcal{D} = \boldsymbol{\tau} : \mathbf{d}_p - \frac{\partial \psi_p}{\partial \xi^h}\dot{\xi}^h \geq 0. \tag{C.1.5}$$

The task of verifying (C.1.5) following a rigorous and sound procedure would require to devise a closed-form analytical expression for ψ_p, so that the set of hardening laws $c_\mathrm{h} = c_\mathrm{h}(\xi^h)$, $c_v = c_v(\xi^h)$ and $s_1 = s_1(\xi^h)$ could be derived by differentiation of ψ_p with respect to ξ^h. In the work of Bier et al.[7], for instance, this task is accomplished by assuming the additive split of the plastic free energy into several parts, each one of them accounting for a different hardening mechanism. Their constitutive model is amenable to such decomposition because they employ an unique function for describing the yield condition and, hence, any transformation of the yield surface in stress space can be easily associated with a combination of simple isotropic (expansion), kinematic (translation) and distortional (change of shape) hardening mechanism.

In our case, the hardening behavior is not represented by an unique function, but by three evolving surfaces, a fact that makes rather difficult to define separately pure expansions, translations and distortions of the yield condition. The derivation of an analytical form for ψ_p, hence, could become prohibitively complicated, if not impossible. It is necessary, thus, to retrace the analysis from a more pragmatic perspective, appealing to physical insight and intuition.

Note that our primary concern is not to obtain an expression for ψ_p, but to prove the validity of inequality (C.1.5). With this in mind, consider an alternative constitutive model characterized solely by an elliptical yield function (figure C.1, dashed curve). The flow rule and the equations governing the size of the ellipse are the same as those of the original model. A loading history is imposed on both materials, the one representing the powder and the other one replicating

the behavior of an idealized *symmetric* material, in such a way that the internal hardening variable ξ^h evolves identically in both cases from ξ^h to $\xi^h+\Delta\xi^h$. We also assume the existence of a free energy function per unit reference volume, denoted by $\tilde{\psi}$, for the idealized symmetric material. Due to interlocking of rough grains, cold welding of particles and other microscopic events macroscopically correlated with a strain-hardening tendency, the internal energy in the powder material increases by an amount

$$\Delta\psi = \psi(\xi^h + \Delta\xi^h) - \psi(\xi^h), \tag{C.1.6}$$

and in the idealized material

$$\Delta\tilde{\psi} = \tilde{\psi}(\xi^h + \Delta\xi^h) - \tilde{\psi}(\xi^h). \tag{C.1.7}$$

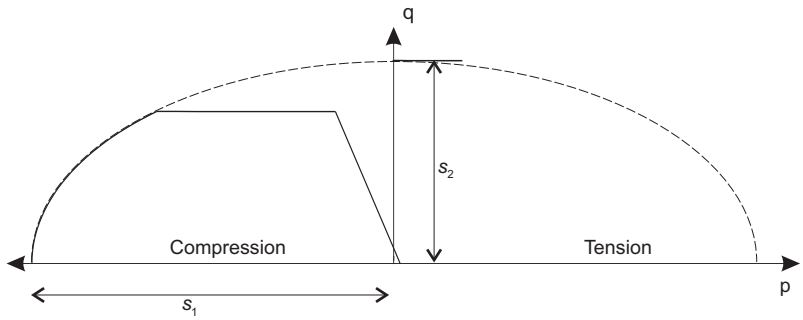

Figure C.1 *Yield condition in the $p-q$ plane for the multisurface model (solid line) and for an idealized symmetrical model (dashed line).*

According to the empirical correlations $s_1 = s_1(\xi^h)$ and $c_\mathrm{h} = c_\mathrm{h}(\xi^h)$, given in Eq.(2.5.53) and Eq.(2.5.56), respectively, for a typical iron based Distaloy AE powder, an increase of ξ^h from, say 0.8 to 0.9, is accompanied by an increase of the hydrostatic yield stress in compression of approximately 125 MPa, whereas the increase of yield stress encountered on stress reversal is just 10 MPa. This gives a ratio increase of strength in (hydrostatic) compression to increase of strength in (hydrostatic) tension of $125/10 = 12.5$. By contrast, the raise of strength predicted by the elliptical model is the same in compression and tension. Concerning the energy stored in the powder structure, it seems reasonable to expect also a similar trend, hence

$$\Delta\tilde{\psi} > \Delta\psi, \tag{C.1.8}$$

i.e., in the idealized material the increase of the cohesive forces binding the powder particles are greater than that in the real material, and this is manifested by a greater amount of stored internal energy.

This line of reasoning can be exploited further by introducing a third idealized constitutive model, that we shall referr to as model C. The yield condition of this model is exactly the same as in the idealized model presented above, henceforth labelled as model B, but no distortional hardening will be considered, i.e., the eccentricity of the ellipse is independent of ξ^h, as illustrated in figure C.2.a. From

this peculiarity, and arguing as above, it can be deduced that the yield stress predicted by model C will be equal or greater than that predicted by model B for any loading path (figure C.2.b), inasmuch as $(s_2)_C \geq (s_2)_B$. This implies that

$$\Delta\hat{\psi} > \Delta\tilde{\psi}, \tag{C.1.9}$$

where $\hat{\psi}$ denotes the Helmholtz free energy function per unit reference volume associated to model C.

An interesting conclusion can be drawn from inequalities (C.1.9) and (C.1.8): for the same increment $\Delta\xi^h$ in the internal hardening variable, the increase in internal energy $\Delta\hat{\psi}$ corresponding to model C is an *upper bound* of the increase in internal energy $\Delta\psi$ corresponding to the original model. The same conclusion can be couched in terms of dissipation: the dissipation associated to model C is a *lower bound* of the dissipation associated to the original model, $\hat{\mathcal{D}} \leq \mathcal{D}$. Therefore, if we show that $\hat{\mathcal{D}} > 0$, where $\hat{\mathcal{D}}$ is the dissipation function for model C, the thermodynamic consistency of the original multisurface model is ensured. The usefulness of our analysis becomes evident at this point. Only a hardening mechanism, an expansion characterized by the variable s_1, is active in model C, which can be categorized a simple *isotropic* hardening model. Therefore, the identification of the thermodynamic conjugate of ξ^h in such model is comparatively an easy task, as we show in the following discussion.

Let us write the dissipation function for model C as

$$\hat{\mathcal{D}} = \boldsymbol{\tau} : \mathbf{d}_p - \frac{\partial\hat{\psi}}{\partial\xi^h}\dot{\xi}^h. \tag{C.1.10}$$

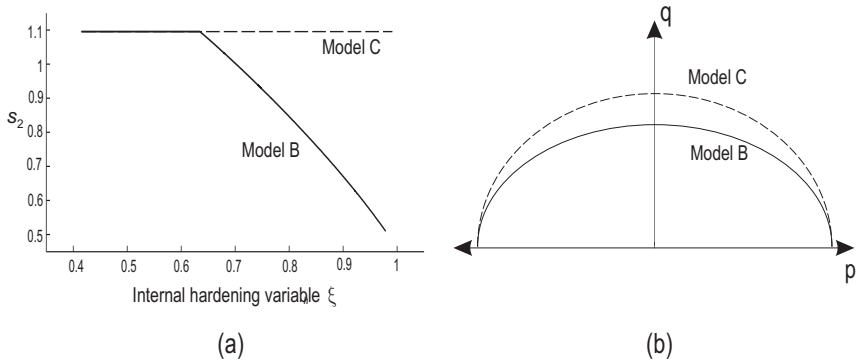

Figure C.2 *(a) Eccentricity of the ellipse for idealized models B and C. (B) Yield condition for models B and C .*

In order to avoid a lengthy derivation, we shall recast the definition of the internal hardening variable in a more suitable format. Recall that ξ^h was defined as a function of the length of the trajectory in the plastic strain space through

expression:

$$\xi^h(t) = \xi^{h0}\, e^{-\int_{t_0}^{t} \mathrm{tr}\,\mathbf{d}_p\, dt} \quad . \tag{C.1.11}$$

The exponential format of Eq.(C.1.11) was aimed at defining an internal variable reminiscent of the relative density. For our purpose it is convenient to dispense with this exponential structure and define the internal hardening variable simply as

$$\hat{\xi}^h(t) = \int_{t_0}^{t} -\mathrm{tr}\,\mathbf{d}_p\, dt \Longrightarrow \dot{\hat{\xi}}^h = -\mathrm{tr}\,\mathbf{d}_p = -\frac{\dot{\xi}^h}{\xi^h}. \tag{C.1.12}$$

Note that the physical meaning of the internal hardening variable is not altered by this transformation. Equation (C.1.10) in terms of $\hat{\xi}^h$ becomes

$$\hat{\mathcal{D}} = \boldsymbol{\tau} : \mathbf{d}_p - \frac{\partial \hat{\psi}}{\partial \xi^h}\dot{\xi}^h = \boldsymbol{\tau} : \mathbf{d}_p - \frac{\partial \hat{\psi}}{\partial \hat{\xi}^h}\dot{\hat{\xi}}^h. \tag{C.1.13}$$

It only remains to choose the thermodynamic conjugate of $\hat{\xi}^h$. Taking into account that $\mathrm{tr}\,\mathbf{d}_p$, and hence $\hat{\xi}^h$, is directly related with inelastic volumetric changes, a natural candidate for the conjugate of $\hat{\xi}^h$ is the hydrostatic yield stress in compression, the state variable s_1:

$$\frac{\partial \hat{\psi}}{\partial \hat{\xi}^h} = s_1(\hat{\xi}^h). \tag{C.1.14}$$

To complete the analysis, Eqs. (C.1.14) and (C.1.12) are substituted in Eq.(C.1.13), and by rearranging terms, we obtain

$$\hat{\mathcal{D}} = \boldsymbol{\tau} : \mathbf{d}_p + s_1 \mathrm{tr}\,\mathbf{d}_p = (p + s_1)\mathrm{tr}\,\mathbf{d}_p + dev\,\boldsymbol{\tau} : dev\,\mathbf{d}_p. \tag{C.1.15}$$

By using the flow rule (2.5.25) in Eq.(C.1.14), we get

$$\hat{\mathcal{D}} = 2\dot{\lambda}^e\,(s_2^2\, p\,(p + s_1) + q^2). \tag{C.1.16}$$

Finally, to study the sign of Eq.(C.1.16), the norm of the deviatoric stress q is expressed as a function of p and s_1, yielding

$$\hat{\mathcal{D}} = 2\dot{\lambda}^e\,(s_2^2\, p\,(p + s_1) + s_2^2(s_1^2 - p^2)) = 2\dot{\lambda}^e s_2^2 s_1 (p + s_1). \tag{C.1.17}$$

Since $\dot{\lambda}^e \geq 0$ and $|p| \leq s_1$, it follows from Eq.(C.1.17) that $\hat{\mathcal{D}} \geq 0$. Thus, the requirement of positive dissipation is satisfied by model C and, as we stated above, this provides the assurance that our multisurface constitutive model is consistent with the second law of the thermodynamics.

References

[1] Agelet de Saracibar, C., Chiumenti, M., Valverde, Q., and Cervera, M. (2006). On the orthogonal subgrid scale pressure stabilization of finite deformation j2 plasticity. *Computer Methods in Applied Mechanics and Engineering*, 195:1224–1251.

[2] Arifiaa, A. K., Gethin, D. T., and Lewis, R. W. (1998). Finite element simulation and experimental validation for multilevel powder compact. *Powder Metallurgy*, 3:123–131.

[3] Aulia, T. B. (2000). Strain localization and fracture energy of high strength concrete under uniaxial compression. *LACER*, 5:221–240.

[4] Belytschko, T., Fish, J., and Engelmann, B. E. (1988). A finite element with embedded localization zones. *Computer Methods in Applied Mechanics and Engineering*, 70:59–89.

[5] Belytschko, T., Liu, W. K., and Moran, B. (2001). *Nonlinear Finite Elements for Continua and Structures*. John Wiley and Sons Ltd., New York.

[6] Belytschko, T. and Mish, K. (2001). Computability in non-linear solid mechanics. *International Journal for Numerical Methods in Engineering*, 52:3–21.

[7] Bier, W. and Hartmann, S. (2006). A finite strain constitutive model for metal powder compaction using a unique and convex single surface yield function. *European Journal of Mechanics*, 25:1009–1030.

[8] Blasco, J., Codina, R., and Huerta, A. (1998). A fractional-step method for the incompressible navier-stokes equations related to a predictor-multicorrector algorithm. *International Journal for Numerical Methods in Engineering*, 28:1391–1419.

[9] Bonet, J. and Wood, R. D. (1997). *Nonlinear Continuum Mechanics for Finite Element Analysis*. Cambridge University Press, Cambridge.

[10] Borst, R. (2001). Some recent issues in computational failure mechanics. *International Journal for Numerical Methods in Engineering*, 52:63–95.

[11] Borst, R., Remmers, J. J. C., Needleman, A., and Abellan, M. (2004). Discrete vs smeared crack models for concrete fracture: bridging the gap. *International journal for numerical and analytical methods in geomechanics*, 28:583–607.

[12] Brekelmans, W. A. M., Janssen, J. D., and de Ven, A. A. F. V. (1991). An eulerian approach for die compaction processes. *International Journal for Numerical Methods in Engineering*, 31:509–524.

[13] Brewin, P. and Federzoni, L. (2006). Dienet: conclusions and achievements. *Powder Metallurgy*, 49:8–10.

[14] Broek, D. (1988). *The Practical Use of Fracture Mechanics*. Kluwer Academic Publishers.

[15] Brown, S. B. and Weber, G. G. A. (1988). A constitutive model for the compaction of metal powders. *Modern Developments in Powder Metallurgy*, 18:465–476.

[16] Cante, J. C. (1995). *Simulación numérica de procesos de compactación de pulvimateriales. Aplicación de técnicas de cálculo paralelo.* PhD thesis, Technical University of Cataluña, Barcelona.

[17] Cante, J. C., Oliver, J., González, C., Calero, J. A., and Benítez, F. (2005). On numerical simulation of powder compaction processes: powder transfer modelling and characterisation. *Powder Metallurgy*, 48:85–92.

[18] Cervera, M., Chiumenti, M., and Agelet de Saracibar, C. (2004). Softening, localization and stabilization: capture of discontinuous solutions in j2 plasticity. *International Journal for Numerical and Analytical Methods in Geomechanics*, 28:373–393.

[19] Chong, E. and Zak, S. (2001). *An introduction to optimization*. Wiley, New York.

[20] Chtourou, H., Gakwaya, A., and Guillot, M. (2002a). Modeling of the metal powder compaction process using the cap model. part ii: Numerical implementation and practical applications. *International Journal of Solids and Structures*, 39:1077–1096.

[21] Chtourou, H., Guillota, M., and Gakwaya, A. (2002b). Modeling of the metal powder compaction process using the cap model. part i: Experimental material characterization and validation. *International Journal of Solids and Structures*, 39:1059–1075.

[22] Cocks, A. C. F. and Sinka, I. C. (2006). Constitutive modelling of powder compaction -i. theoretical concepts. *Mechanics of Materials*, 39:392–403.

[23] Codina, R. (2000). A nodal-based implementation of a stabilized finite element method for incompressible flow problems. *International Journal for Numerical Methods in Engineering*, 33:737–766.

[24] Cook, R. (1995). *Finite element modeling for stress analysis*. John Wiley and Sons., New York.

[25] Coube, O. (1998). *Modelling and numerical simulation of powder die compaction with consideration of cracking*. PhD thesis, University Pierre et Marie Curie, Paris VI, Paris.

[26] Coube, O. and Riedel, H. (2000). Numerical simulation of metal powder die compaction with special consideration of cracking. *Powder Metallurgy*, 43:123–131.

[27] Crisfield, M. A. (1991). *Non-linear Finite Element Analysis of Solids and Structures, Volume 1: Essentials*. John Wiley and Sons Ltd., Chichester.

[28] Cunningham, J. C. (2005). *Experimental Studies and Modeling of the Roller Compaction of Pharmaceutical Powders*. PhD thesis, Drexel University.

[29] Degnan, C. C., Kennedy, A. R., and Shipway, P. H. (2007). Relationship between physical structure and machinability of green compacts. *Powder Metallurgy*, 50:14–20.

[30] Desai, C. S. (2001). *Mechanics of Materials and Interfaces: the disturbed state concept*. CRC Press, New York.

[31] Doremus, P., Toussaint, F., and Alvain, O. (2001). Simple tests and standard procedure for the characterization of green compacted powder. In *Recent developments in Computer Modeling of Powder Metallurgy Processes*, pages 277–285, IOS press. A. Zavaliangos and A. Lapter.

[32] Duxbury, P. and Li, X. (1996). Development of elasto-plastic material models in a natural coordinate system. *Computer Methods in Applied Mechanics and Engineering*, 135:283–306.

[33] Erhart, T., Wall, W. A., and Ramm, E. (2005). A robust computational approach for dry powders under quasi-static and transient impact loadings. *Computer Methods in Applied Mechanics and Engineering*, 194:4115–4134.

[34] Etse, G. and Willam, K. J. (1994). A fracture-energy based constitutive formulation for inelastic behavior of plain concrete. *Journal of Engineering Mechanics*, 120:1983–2011.

[35] Ferguson, B. and Krauss, T. (1991). Modeling ejection of die pressed parts. In *Proceedings of the 1991 Powder Metallurgy Conference and Exhibition*, pages 147–164, London.

[36] Fleck, N. A. (1995). On the cold compaction of powders. *Journal of the Mechanics and Physics of Solids*, 43:1409–1431.

[37] Gethin, D. T., Kran, V. D., Lewis, R. W., and Ariffin, A. K. (1994). An investigation of powder compaction processes. *International Journal of Powder Metallurgy*, 30:385–389.

[38] Grassl, P. and Jiràsek, M. (2006). Damage-plastic model for concrete failure. *International Journal of Solids and Structures*, 43:7166–7196.

[39] Groover, M. P. (2002). *Fundamentals of modern manufacturing: Materials, Processes and Systems*. Wiley.

[40] Hartmann, S., Oliver, J., Cante, J. C., Weyler, R., and Hernández, J. A. (2009). A contact domain method for large deformation frictional contact problems. part 2: Numerical aspects. *Computer Methods in Applied Mechanics and Engineering*, 198:2607–2631.

[41] Hearn, E. J. (2000). *Mechanics of Materials I*. Butterworth-Heinemann, Oxford.

[42] Hill, R. (1950). *The Mathematical Theory of Plasticity*. Oxford University Press, London.

[43] Hirschhorn, J. S. (1969). *Introduction to powder metallurgy*. American powder metallurgy institute, New York.

[44] Hjiaj, M., Fortin, J., and Saxcé, G. (2003). A complete stress update algorithm for the non-associated drucker-prager model including treatment of the apex. *International Journal of Engineering Science*, 41:1109–1143.

[45] Hoffman, J. D. (2001). *Numerical Methods for Engineers and Scientists*. Marcel Dekker.

[46] Holzapfel, G. A. (2000). *Nonlinear solid mechanics*. Wiley, Chichester.

[47] Idelsohn, S. R., Oñate, E., and del Pin, F. (2004). The particle finite element method: a powerful tool to solve incompressible flows with free-surfaces and breaking waves. *Internation Journal for Numerical Methos in Engineering*, 61:964–989.

[48] Jonsén, P. (2006). *Fracture and stress in powder compacts*. PhD thesis, Luleå University of Technology, Luleå, Sweden.

[49] Jonsén, P. and Häggblad, H. (2007). Fracture energy based constitutive models for tensile fracture of metal powder compacts. *International Journal of Solids and Structures*, 44:6398–6411.

[50] Jonsén, P., Häggblad, H.-A., and Sommer, K. (2007). Tensile strength and fracture energy of pressed metal powder by diametral compression test. *Powder Technology*, 176:148–155.

[51] Kachanov, L. (1971). *Foundations of Theory of Plasticity*. North-Holland, Amsterdam.

[52] Kergadallan, J., Puente, G., Doremus, P., and Pavier, E. (1997). Compression of an axisymmetric part with an instrumented press. In *Proceedings of an International Workshop on Modelling of Metal Powder Forming Processes*, pages 277–285, Grenoble.

[53] Khan, A. S. and Huang, S. (1995). *Continuum Theory of Plasticity.* Wiley, New York.

[54] Khoei, A. R. and Lewis, R. W. (1999). Adaptive finite element remeshing in a large deformation analysis of metal powder forming. *Internation Journal for Numerical Methos in Engineering*, 45:801–820.

[55] Khoei, A. R., Shamloo, A., and Azami, A. R. (2006). Extended finite element method in plasticity forming of powder compaction with contact friction. *International Journal of Solids and Structures*, 43:5421–5448.

[56] Kuhl, E., Ramm, E., and Willam, K. (2000). Failure analysis of elasto-plastic material models on diferent levels of observation. *International Journal of Solids and Structures*, 37:7259–7280.

[57] Kwon, Y. S., Chung, S. H., Sanderow, H. I., Kim, H. I., and German, R. (2003). Numerical analysis and optimization of die compaction process. In Federation, M. P. I., editor, *Advances in Powder Metallurgy and Particulate Materials*, pages 37–50, New Jersey. Princeton.

[58] Larsson, R., Steinmann, P., and Runesson, K. (1998). Finite element embedded localization band for finite strain plasticity. *Mechanics of cohesive-frictional materials*, 4:171–194.

[59] Lewis, R. W. and Khoei, A. R. (2001). Numerical analysis of strain localization in metal powder-forming processes. *Internation journal for numerical methos in engineering*, 52:489–501.

[60] Lubarda, V. A. (2002). *Elastoplasticity Theory.* CRC Press.

[61] Lubliner, J. (1990). *Plasticity Theory.* McMillan, New York.

[62] Mähler, L. and Runesson, K. (2003). Constitutive modeling of cold compaction and sintering of hardmetal. *Journal of Engineering Materials and Technology*, 125:191–199.

[63] Marsden, J. E. and Hugues, T. J. R. (1994). *Mathematical foundations of elasticity.* Dover, New York.

[64] Martin, C. L. (2003). Unloading of powder compacts and their resulting tensile strength. *Acta Metall.*, 51:4589–4602.

[65] Mase, G. T. (1999). *Continuum mechanics for engineers.* CRC Press, Boca Raton.

[66] Mediavilla, J., Peerlings, R. H. J., and Geers, M. G. D. (2006). Discrete crack modelling of ductile fracture drivenby non-local softening plasticity. *International Journal for Numerical Methods in Engineering*, 66:661–688.

[67] Metal Powder Industry Federation (2002). *MPIF Standard 31. Definition of Terms for Metal Powder Compacting Presses and Tooling.* Metal Powder Industry Federation, Princeton.

[68] Moran, B., Ortiz, M., and Shih, C. F. (1990). Formulation of implicit finite element methods for multiplicative finite deformation plasticity. *International Journal for Numerical Methods in Engineering*, 29:483–514.

[69] Mosbah, P. (1995). *Etude expérimentale et modélisation du comportement de poudres métalliques au cours du compactage en matrice fermée*. PhD thesis, Université Joseph Fourier-Grenoble I.

[70] Mosler, J. and Meschke, G. (2004). Embedded crack vs. smeared crack models: A comparison of elementwise discontinuous crack path approaches with emphasis on mesh bias. *Computer Methods in Applied Mechanics and Engineering*, 193:3351–3375.

[71] Nocedal, J. and Wright, S. J. (1999). *Numerical optimization*. Springer, New York.

[72] O'Dowd, N. (2003). Lectures on fundamentals of elastic, elastic-plastic and creep fracture. Advanced fracture mechanics. Department of Mechanical Engineering.Imperial College London.

[73] Ogden, R. (1997). *Non-linear elastic deformations*. Dover, New York.

[74] Oliver, J. (1989). A consistent characteristic length for smeared cracking models. *International Journal for Numerical Methods in Engineering*, 28:461–474.

[75] Oliver, J. (1996). Modelling strong discontinuities in solid mechanics via strain softening constitutive equations. *Internation journal for numerical methos in engineering*, 39:3575–3600.

[76] Oliver, J. (2000). On the discrete constitutive models induced by strong discontinuity kinematics and continuum constitutive equations. *International Journal of Solids and Structures*, 37:7207–7229.

[77] Oliver, J., Cante, J. C., Weyler, R., González, C., and Hernández, J. A. (2007). *Computational Plasticity*, chapter Particle Finite Element Methods in Solid Mechanics. Springer.

[78] Oliver, J., Hartmann, S., Cante, J. C., Weyler, R., and Hernández, J. A. (2009). A contact domain method for large deformation frictional contact problems. part 1: Theoretical basis. *Computer Methods in Applied Mechanics and Engineering*, 198:2591–2606.

[79] Oliver, J., Huespe, A. E., Blanco, S., and Linero, D. L. (2006). Stability and robustness issues in numerical modeling of material failure with the strong discontinuity approach. *Computer Methods in Applied Mechanics and Engineering*, 195:7093–7114.

[80] Oliver, J., Huespe, A. E., and Cante, J. C. (2008). An implicit/explicit integration scheme to increase computability of non-linear material and contact/friction problems. *Computer Methods in Applied Mechanics and Engineering*, 197:1865–1889.

[81] Oliver, J., Oller, S., and Cante, J. C. (1996). A plasticity model for simulation of industrial powder compaction processes. *Journal of Solids and Structures*, 33:3161–3178.

[82] Oller, S. (1998). *Un modelo de daño continuo para materiales friccionales*. PhD thesis, Technical University of Cataluña, Barcelona.

[83] Pavier, E. (1998). *Caracterisation du comportement d'une poudre de fer pour le procede de compression en matrice*. PhD thesis, L'Institut National Polytechnique de Grenoble.

[84] Pavier, E. and Dorémus, P. (1996). Mechanical behavior of a lubricated iron powder. *In: Powder Metallurgy PM96. Advances in Powder Metallurgy and Particulate Materials*, 6:27–40.

[85] Pedregal, P. (2003). *Introduction to optimization*. Springer-Verlag, New York.

[86] Procopio, A. T. and Zavaliangos, A. (2005). Simulation of multi-axial compaction of granular media from loose to high relative densities. *Journal of the Mechanics and Physics of Solids*, 53:1523–1551.

[87] Quarteroni, A., Sacco, R., and Saleri, F. (2000). *Numerical Mathematics*. Springer, New York.

[88] Reddy, B. D. (1998). *Introductory Functional Analysis*. Springer-Vedag, New York.

[89] Riera, M. D. (1999). *Comportamiento elastoplástico de compactos pulvimetalúrgicos*. PhD thesis, Technical University of Cataluña, Barcelona.

[90] Rossi, R., Alves, M. K., and Qureshi, H. A. A. (2007). A model for the simulation of powder compaction processes. *Journal of Materials Processing Technology*, 182:286–296.

[91] Simo, J., Oliver, J., and Armero, F. (1993). An analysis of strong discontinuities induced by strain softening in rate-independent inelastic solids. *Computational Mechanics*, 12:277–296.

[92] Simo, J. C. (1999). *Topics on the numerical analysis and simulation of plasticity. In Handbook of Numerical Analysis, Ciarlet PG, Lions JL (eds), volume III*. Elsevier Science Publisher, Amsterdam.

[93] Simo, J. C. and Hughes, T. J. R. (1998). *Computational inelasticity*. Springer, New York.

[94] Sinka, I. C. and Cocks, A. C. F. (2007). Constitutive modelling of powder compaction -ii. evaluation of material data. *Mechanics of Materials*, 39:404–416.

[95] Sinka, I. C., Cocks, A. C. F., and Tweed, J. H. (2001). Constitutive data for powder compaction modelling. *Journal of Engineering Materials and Technology*, 123:176–183.

[96] Stevenson, R. W. (1990). *ASM Handbook, Vol. 7- Powder Metallurgy*, chapter P/M Copper-Based Alloys. ASM International.

[97] Storåkers, B., Fleck, N. A., and McMeeking, R. M. (1999). The viscoplastic compaction of composite powders. *Journal of Mechanics and Physics of Solids*, 47:785–815.

[98] Strang, G. (1988). *Linear Algebra and Its Applications*. Brooks Cole.

[99] Tahir, S. M. and Ariffin, A. K. (2006). Fracture in metal powder compaction. *International Journal of Solids and Structures*, 43:1528–1542.

[100] Thümmler, F. and Oberacker, R. (1993). *Introduction to powder metallurgy*. The Institute of Materials, London.

[101] Timoshenko, S. P. (1941). *Strength of Materials, part II. Advanced theory and problems*. Van Nostrand.

[102] Timoshenko, S. P. and Goodier, J. N. (1970). *Theory of Elasticity*. McGraw-Hill.

[103] T.M. Krauss, G.J. Petrus, B. F. (1991). Die compaction process design part 2: Fem simulation. In *Proceedings of the 1991 Powder Metallurgy Conference and Exhibition*, pages 110–121, London.

[104] Tszeng, T. C. and Wu, W. T. (1996). A study of the coefficients in yield functions modeling metal powder deformation. *Acta Metall.*, 44:3543–3552.

[105] Vrech, S. M. and Etse, G. (2006). Geometrical localization analysis of gradient-dependent parabolic drucker-prager elastoplasticity. *International Journal of Plasticity*, 22:943–964.

[106] Wagle, G. S. (2000). *Numerical investigation of constitutive models for the powder compaction process*. PhD thesis, The Pennsylvania State University, Pennsylvania.

[107] Wanga, Q. Z., Jiaa, X. M., Koub, S. Q., Zhangb, Z. X., and Lindqvistb, P. A. (2003). The flattened brazilian disc specimen used for testing elastic modulus, tensile strength and fracture toughness of brittle rocks: analytical and numerical results. *International Journal of Rock Mechanics and Mining Sciences*, 41:245–253.

[108] Weber, G. G. and Brown, S. B. (1989). Simulation of the compaction of powder components. *Advances in Powder Metallurgy and Particulate Materials*, 1:106–118.

[109] Weyler, R. (2000). *Simulación numérica de procesos de compactación y extrusión de materiales pulverulentos*. PhD thesis, Technical University of Cataluña, Barcelona.

[110] Wriggers, P. (2006). *Computational Contact Mechanics*. Springer.

[111] Yanenko, N. N. (1971). *The Method of Fractional-Steps*. Springer, Berlin.

[112] Zenger, D. and Cai, H. (1997). *Handbook of the Common Cracks in Green P/M Compacts*. Metal Powder Industry Federation, Worcester.

[113] Zienkiewicz, O. C. and Taylor, R. L. (1994). *The finite element method. Volumes 1 and 2*. McGraw-Hill.